Reactivity and Properties of Au/TiO_2 Nanocatalysts

Monica McEntee
Chesapeake, VA

B.S. Chemistry, Virginia Tech, 2010
B.S. Mathematics, Virginia Tech, 2010

A Dissertation presented to the Graduate Faculty
of the University of Virginia in Candidacy for the Degree of
Doctor of Philosophy

Department of Chemistry

University of Virginia
March, 2015

Abstract:

Gold particles with diameters in the nanometer range in contact with reducible oxide supports exhibit catalytic activity at temperatures well below 273 K. Many studies have suggested that the catalytic activity occurs at interface sites between the metal and the support. Here, using infrared (IR) spectroscopy, I show the oxidation of CO, ethylene, and carboxylic acids (acetic, propionic and butyric acid) on a Au/TiO_2 catalyst with ~3 nm diameter Au nanoparticles in order to further explore the role of the Au/TiO_2 interface. At the interface, the first step in all the oxidation processes is the dissociation of O_2 at the Au-Ti^{4+} dual site, where one dioxygen O atom is bonded to the Au and the other O is bonded to the Ti^{4+} site of the metal oxide support, to form activated O adatoms on the surface. Then for ethylene and the carboxylic acids, in sequential steps, acidic C-H bonds are activated, followed by C-O and C-C (for acid oxidation) bond scission yielding adsorbed ketenylidene, $Au_2C=C=O$, an exotic species formed just before full oxidation. The kinetics and full mechanisms are discussed.

Additionally, I explore the effect of the metal oxide support, TiO_2, on ~3 nm Au nanoparticles by adsorbing donor molecules (CH_4, C_2H_6 and C_3H_8) and separately an acceptor molecule (SF_6) on only the TiO_2 support. In order to observe the effect these molecules have on the Au nanoparticles, CO is initially adsorbed on only the Au sites. As donor or acceptor molecules adsorb on the TiO_2, IR spectroscopy is used to observe the frequency change in the Au-CO IR absorbance bands. For donor/TiO_2 adsorption, electrons transfer from the TiO_2 to the Au causing a redshift; whereas, for acceptor/TiO_2 adsorption, electrons transfer from the Au nanoparticles to the TiO_2 support causing a blueshift in the IR frequency. In comparison, electron transfer was not observed on a Au/SiO_2 catalyst. Additional methods confirm these results.

Acknowledgements:

I would particularly like to thank my primary advisor Dr. John T. Yates, Jr. for not only advising and teaching me how to become a better researcher, but also for helping me become a complete scientist, who connects with people through collaborations and conferences and who opens their mind to new ideas and opportunities. I would also like to thank my secondary advisor Dr. Ian Harrison for all of his insightful discussions and his “you’ve got this” pep talks whenever I was stressed or nervous about presenting in front of a group.

The other people who have been there for me throughout my graduate school are those in both the Yates and Harrison group including Dr. Isabel Green (for teaching me the IR system used in this work), Dr. Ana Stevanovic (for collaborating on a paper with me and for being a great friend), Dr. Lynn Mandeltort, Dr. Scott Donald, Dr. Mahesh Rajappan, Dr. Zhen Zhang, Isla Cooke, Dr. Matt Reish, Shiliang Ma, Yifeng Song and any other members that I have worked with. Thank you all for making my time in graduate school an enjoyable experience.

My research would not have been as complete without the help of collaborators from outside of the Chemistry Department. I would particularly like to thank Dr. Wenjie Tang and Professor Matthew Neurock (for performing all of the DFT calculations presented in this work), Dr. Nadir Faradzhev and Dr. Tom Lucatorto (from NIST), Dr. Jun Wang and Dr. Peter Maksymovych (from Oak Ridge National Laboratory), Matthew Schneider (for his TEM imaging), Professor Linda Columbus, Steve Kalman and any other people I have forgotten to mention that I was fortunate enough to work and produce exciting science with during my time in graduate school.

Additional people I would like to thank, who helped and/or supported me, are Dr. Dina Bai (for all of her “computer genius” and support), Dr. Jeff Shabanowitz and all of the faculty and staff in the Chemistry Department here at the University of Virginia. I also would like to thank my family and friends, in particular, Mom, Dad, Mark (brother) and Renee (sister) for all of the support and love they give me every day.

Last (but not least!), I would like to thank my boyfriend, Dr. Jason Navin. Thank you for comforting me during Candidacy Exams, calming me down before group meetings with John and for always being there for me. Anyone else I forgot to mention I would just like to say thank you and God bless you.

Table of Contents

Chapter 1: Introduction

1.1 Heterogeneous Catalysis: History of the Field with an Emphasis on Au Supported on Metal Oxides

1.1.1 History of Heterogeneous Catalysis and Surface Science

The history of heterogeneous catalysis spans as far back as 1796 when M. van Marum first studied the dehydrogenation of alcohols using metals.[1] Soon after in the early 1800's, J. W. Döbereiner and M. Faraday discovered platinum surfaces glow in an atmosphere of air and hydrogen.[2-4] J. J. Berzelius coined the name for these types of reactions and this area of research in 1836: *catalysis*.[5] The definition of catalysis (used today) came later in 1894 from W. Ostwald, who said "catalysis is the acceleration of a slowly proceeding chemical reaction through the presence of a foreign substance… [and] at the end of the reaction the foreign substance can be considered as removed [and reused]."[6-9] Ostwald later won the Nobel Prize in 1909 for his work in catalysis involving the discovery of ammonia oxidation to make nitric oxide and nitric acid catalyzed using platinum metal.[10]

Later, in the early 1900's, Fritz Haber won the Nobel Prize for his discovery of the Haber process for N_2 activation to make NH_3 at catalytic levels using an iron catalyst. This was used in World War I to make explosives from N_2. Later on, the process was developed along with W. Nernst and C. Bosch to industrially synthesize NH_3 as a fertilizer, which now utilizes about 5% of the world's power for its production and allows more than a billion people to be fed than would otherwise be possible.[11] Haber did not stop there; he also theorized how the reaction mechanism to form ammonia (NH_3) on the catalyst would happen. He rationalized that the first step in the process would involve adsorption (Figure 1.1(1)). In 1915, Langmuir developed the well-established adsorption model that states a gas molecule can "stick" (or adsorb) to a surface site and that each site can contain only one molecule.[12]

Since the adsorption model has been widely accepted, scientists have found various different types of adsorption correlating to the binding energies/forces of molecules to the surface. Adsorption can be categorized into three main types: physisorption, associative chemisorption and dissociative chemisorption. Physisorption involves the molecule binding to the surface through weak interactions such as van der Waals or London forces, and the molecule does not form or break any bonds. Associative chemisorption occurs when a molecule binds to the surface atom or atoms and the chemical bond strengths are changed to form bonds with the surface atoms with no bond breaking. Lastly, dissociative chemisorption occurs when the molecule binds to the surface and the molecular bonds break to form new bonds with the surface atoms.

Once the molecule adsorbs onto the surface, three different processes can happen: reaction with a neighboring molecule or surface, diffusion, or desorption. With enough energy, one molecule adsorbed on the surface can react with a second molecule on a neighboring site to form a product. In 1925, H. S. Taylor theorized that not all surface sites are the same (as thought by Langmuir), and that certain sites can accelerate a reaction, which are called active sites.[13] These sites have been known to occur at step edges and kinks, where the coordination number of neighboring atoms is low, on single crystal metals. The atoms in these low coordination number sites are unstable and want to react or bond to other molecules to make more stable structures. These sites might be far away, from where the molecule initially adsorbs, which means the reaction might never occur if the molecule stays immobile. However, molecules with enough energy to move from site to site across a surface could eventually reach the active sites and react with other molecules to form products. The process of moving across the surface from one adsorption site to another is called diffusion (Figure 1.1(2)). Once a product is made, it could stay adsorbed to the surface or it could leave the surface to the gas phase. Holloway and Beeby[14] developed a model in 1975 for molecules leaving the surface, which is called desorption (Figure 1.1(3)). This process not only occurs with product molecules but also with molecules that could desorb before reacting with other molecules on the surface to form products. By measuring and calculating the adsorption, diffusion and desorption energies of molecules on surfaces, we can understand reaction mechanisms and tailor catalysts to enhance the efficiency, selectivity and rates of product formation.

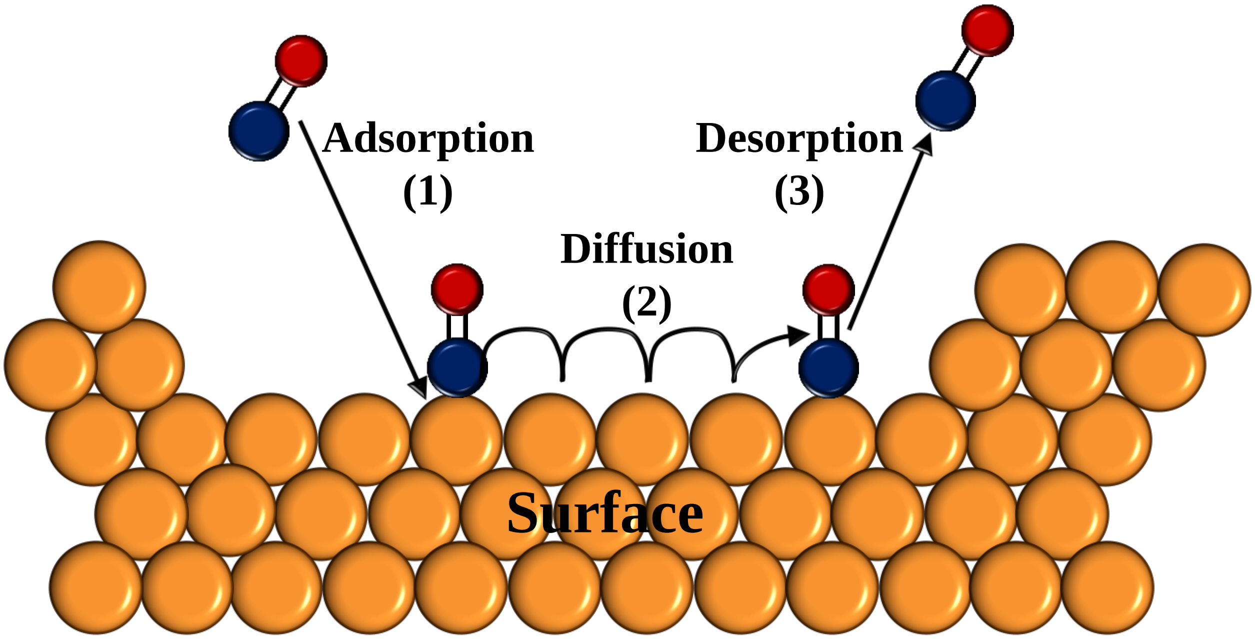

Figure 1.1 (1) Binding or "sticking" of a molecule from the gas phase to a surface is called adsorption; (2) Movement of a molecule from one site on the surface to another is called diffusion; and (3) Detachment of a molecule from the surface to the gas phase is called desorption.

1.1.2 History of Supported Gold Nanoparticles

The next 12 years of heterogeneous catalysis research encompassed work involving structure, morphology, active sites and electronic properties of single crystal metals and metal oxides. One metal in particular was known to be inert in its bulk (single crystal) form due to full d-band electron orbitals,[15] and that metal was *gold*. However, in 1987, M. Haruta and his colleagues discovered that when Au is reduced to nanometer diameter sizes supported on metal oxides, the Au exhibits enhanced catalytic activity for CO oxidation to form CO_2 at temperatures below 0°C.[16] Since this discovery, other studies have been done in order to determine where the active sites are on these catalysts and the mechanisms involved in product formation. The first studies included particle size and shape dependent experiments[17,18] where the optimal size and shape for the highest CO_2 conversion rates were ~3 nm diameter hemispherical Au particles. As the particles increased in diameter > 3 nm, the catalytic activity decreased. The results of these experiments provided the first evidence that the reaction was taking place at the Au perimeter sites.

In 2007, Rodriguez *et al.*[19] inverted the catalyst with metal oxide (in this case, TiO_2 and CeO_2) nanoparticles supported on a Au (111) single crystal surface. After measuring the water gas shift reaction (WGS, $CO + H_2O \rightarrow CO_2 + H_2$) H_2 formation vs the fraction of Au covered with metal oxide, the largest amount of H_2 molecules produced occurred when 20-30% of the Au sites were covered with metal oxide. The clean Au (111) surface was catalytically inactive for the WGS reaction, and when the Au (111) surface was covered with more than 30% of metal oxide, the catalytic activity decreased with increasing metal oxide coverage.[19] Thus, the metal oxide was necessary along with the Au for the reaction to occur. They found that the water dissociated on the metal oxide and O adatoms reacted with CO molecules adsorbed on the Au sites.[19] Therefore, the reaction had to take place at the metal oxide/Au interface.

Fujitani *et al.*,[20] in 2009, studied the H_2-D_2 exchange reaction and found that the HD formation rate decreased as the mean Au particle size increased for each sample (with a constant Au loading); in addition, the HD formation turnover frequency (TOF) per perimeter site stayed the same as the Au particle size increased. A decrease in HD formation rate with increasing Au particle size suggests H_2 and D_2 dissociate and subsequently exchange at the Au perimeter, and the constant TOF per perimeter site infers the electronic properties (such as molecular binding and activation energies) are unchanged as the Au particle size increases. Therefore, we can conclude that the active sites for the reaction are unchanged but are fewer in number as the Au particle size increases.

Other groups arrived at the same conclusions, that for these types of catalysts, the reactions occur at the interface between the metal and metal oxide, for various reactions. Behm *et al.*[21] found catalytic activity is proportional to the perimeter length of the Au/TiO_2 interface for CO oxidation. Using both experiments and theoretical calculations, Camellone *et al.*[22] discovered that methanol oxidation to form formaldehyde, CH_2O, occurs at the Au/TiO_2 interface through a CH_3OH-O_2 intermediate. Our group has further contributed to the fundamental understanding of these types of reactions and mechanisms on Au/TiO_2 catalysts. Here I report on not only different oxidation reactions including CO oxidation, ethylene oxidation and carboxylic acid oxidation and their mechanisms on Au/TiO_2, but I also report on the electronic properties of the Au/TiO_2 interface.

1.1.3 Structure and Electron Properties of Metal Oxide Supports: TiO_2 vs SiO_2

Many metals in the presence of ambient air produce stable structures in the form of metal oxides. For example, William Gregor discovered titanium in 1791 in a black sandy mineral that was later found to be made up of a mixture of iron oxide (Fe_2O_3) and titanium dioxide (TiO_2).[23]

Four years later, Martin H. Klaproth tried to make pure titanium metal, but he could only make TiO_2.[23] Since then, TiO_2 has been found to be an attractive model metal oxide due to its catalytic and photocatalytic properties, low cost, high abundance, high surface area and reducibility.

Arguably, the two most commonly used TiO_2 crystal structures are rutile and anatase. Single crystal rutile TiO_2(110) has been extensively studied experimentally and theoretically owing to the fact that rutile (110) is the most thermally stable and abundant face structure on single crystal and nanoparticle TiO_2 surfaces.[24-26] Rutile is a body-centered tetragonal crystal system consisting of each Ti cation bonded to six O anions (Figure 1.2, top). The surface contains alternating rows of bridging oxygens bonded to only two Ti cations, which have coordination numbers of six, and rows of 5-fold coordinate Ti cations. Similarly, anatase (101) is the most common anatase face for nanoparticles, and it also has a tetragonal crystal system; however, the surface is ridged (Figure 1.2, bottom). The surface also has alternating rows of bridging oxygens and 5-coordinate Ti cations similar to rutile (110). In this thesis, we use commercial TiO_2 P25, which is a mixture of ~75% anatase and ~25% rutile nanoparticles, and it will be described in more detail in Chapter 2.

These two structures are unique in that they are not always stoichiometric. Both structures usually have sites that are missing atoms such as O vacancies, which are also called defect sites.[27,28] These sites can form on the surface at bridging O sites or in the bulk. At these O vacancy sites, excessive negative charge can be trapped or can move from site to site.[28] Thus, these sites are also called charge carrier sites. In catalysis and photocatalysis, these sites can increase the rate of a reaction by increasing the binding energies of a reactant to the surface, transferring charge to an adsorbed molecule or allowing movement of charge carriers from the bulk to the surface active sites.

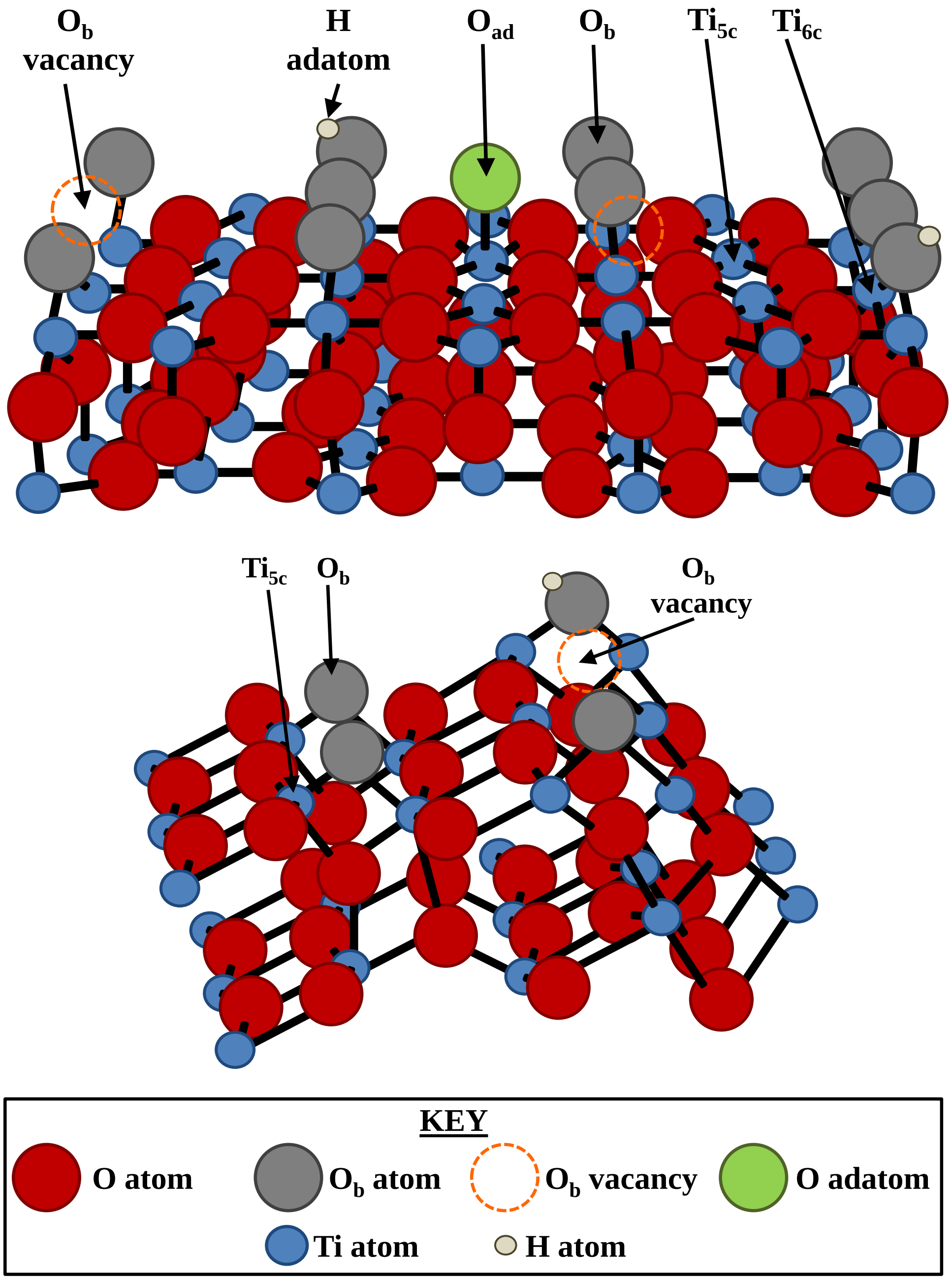

Figure 1.2 Representation of the TiO_2 rutile (110) (top) and anatase (101) (bottom) surface including oxygen vacancies at the bridge sites (O_b, dotted circles), hydrogen adatoms (H, small light gray circles), oxygen adatoms (O_{ad}, green circles), bridging oxygen (O_b, grey circles), and titanium atoms with 5-fold coordination (Ti_{5c}, blue circles) and 6-fold coordination (Ti_{6c}, blue circles).

Not all metal oxides have these significant electronic properties. One such oxide is silicon dioxide, SiO_2. SiO_2 has a tetrahedral coordinate crystal system, where every Si cation is bonded to four O anions. This system is stoichiometric and does not contain O vacancies because Si has only one oxidation state of 4+, unlike Ti, which has two oxidation states of 4+ and 3+. Thus, when an O vacancy is formed, the Ti^{4+} cations convert to Ti^{3+} cations; whereas, oxygen vacancy formation would make SiO_2 unstable and just fall apart. Thus, SiO_2 is called an irreducible oxide and a poor charge carrier catalyst as will be discussed further in later chapters.

Using the accumulated knowledge collected about these two oxides, important discoveries can be found about the role of metal oxide supports in the mechanisms of catalytic reactions on Au supported TiO_2 and SiO_2 catalysts. This thesis reports on the kinetics and mechanisms involved in various oxidation reactions and the electronic processes associated with Au/TiO_2 and Au/SiO_2 catalysts.

1.1.4 Future of the Field: Dopants and Bimetallics

Numerous studies have been conducted to elucidate the electronic properties and the origin of catalytically active sites on TiO_2; and, even though there is still a great deal more to be learned about this system, scientists have an extensive understanding of the structural and electronic properties of this metal oxide semiconductor. Therefore, the next step in producing more efficient and selective catalysts is to optimize and tune the properties of TiO_2 to help facilitate faster reaction rates, product selectivity, etc. Two emerging fields that can accomplish this goal are dopants and bimetallics in or on TiO_2, respectively.

Dopants in TiO_2 are atoms (e.g. V, N, La, etc.) that replace a small fraction of the Ti or O atoms in the lattice structure. These elements can change both the geometric structure and the electronic properties of the material.[29,30] Advantages to changing the geometric structure include creating more oxygen vacancies, which are known to be catalytically active sites for various reactions; exposing more uncoordinated metal atoms to the surface to allow for stronger binding sites; and, producing new adsorption sites by the dopants themselves, which could also enhance molecular binding or be catalytically active.

Not only can dopants affect structure, but they can also affect electronic properties. An electron acceptor (e.g. La^{3+} replacing Ti^{4+}) dopant provides fewer electrons to the lattice, which makes the material electron deficient. Horia Metiu and his colleagues call this kind of material a Lewis acid material.[30] If the surface has Lewis acid character, then a Lewis base (i.e. electron donating) adsorbate molecule can bind more strongly to the surface, which enhances electron transfer processes from the adsorbate to the oxide to other possible molecules or sites. Likewise, when an electron donor (e.g. V^{5+} replacing Ti^{4+}) dopant adds electrons to the lattice, the material becomes electron rich, and Lewis acid (e.g. O_2) adsorbate molecules bind more strongly to the surface.[30] In the case of O_2 activation, the electron rich V-doped TiO_2 transfers electrons to the $2\pi^*$ antibonding orbital of the O_2 molecule weakening the O-O bond and lowering the activation energy barrier for dissociation. Tailoring doped metal oxides to enhance selective reactions is the next logical step to the production of cheap, efficient and clean catalysts.

Another way to enhance catalytic activity using these types of catalysts is by anchoring not just metal nanoparticles, but bimetallic nanoparticles to the TiO_2 support. Recent studies have shown that Au/TiO_2 and Pd/TiO_2 do not synthesize H_2O_2 from H_2 and O_2; however, bimetallic Au/Pd nanoparticles supported on TiO_2 easily synthesize H_2O_2.[31] Another Au/Pd/TiO_2 catalyst was used to oxidize primary alcohols to produce aldehydes.[32] The mechanisms are still a mystery and need to be understood in order to create future catalysts. The electron transfer processes from one metal site to the next could help pave the way to new research areas in electronics, catalysis and photovoltaic cells.

1.2 Infrared Spectroscopy and Its Uses

1.2.1 History and Development of Infrared (IR) Spectroscopy

Coblentz was the first to obtain an IR spectrum in 1905.[33] Since then, IR spectroscopy has become a powerful technique for chemical species identification. In 1940, Terenin and Kasparov were the first to use IR spectroscopy to study adsorbates on surfaces particularly NH_3 on iron-distributed silica aerogel.[33] Not long after, Eischens *et al.*[34] studied CO chemisorbed on metals and metal oxides supported on SiO_2 and Al_2O_3 powders. The original IR instrument has been enhanced over the years as well from only being able to use liquid samples to solid samples using Nujol as a mulling agent in 1943 to samples using KBr in 1952 to finally samples in a liquid argon matrix in 1954.[33] As time went on, techniques with better signal to noise ratios and the ability to take a broad range of frequencies at once were developed such as attenuated total reflection (ATR) and Fourier transform IR (FTIR) spectroscopy.

1.2.2 Infrared Spectroscopy: Design

In order to determine what happens to reactants in the presence of a catalyst (i.e. what intermediates and products are produced, what electron transfer processes occur, where are the catalytically active sites, etc.), we employ infrared (IR) spectroscopy to study the reactions on the surface of the catalyst and mass spectrometry (MS) to observe the gas phase products coming off the surface of the catalyst in a vacuum chamber, which will be described in more detail in Chapter 2. Infrared spectroscopy is the spectroscopic measurement of the interaction between IR light and a chemical species or material. The most commonly used IR system setup (and what we use) includes a Fourier transform infrared (FTIR) spectrometer. In a FTIR spectrometer, the measurement of the light is obtained by determining each chemical species' ability to absorb light. In order to measure different chemical species with different adsorption affinities, a broadband light source containing many frequencies of light is used opposed to a monochromatic light beam, which only measures the amount of light adsorbed at one frequency. If only one frequency is used, any species that does not absorb light at that particular frequency is not observed. Thus, a broadband light is used to acquire more information in a shorter time.

Therefore, the FTIR setup starts with this broadband light source, where a broad spectrum of frequencies can be measured, emitting light into a Michelson interferometer. A basic Michelson interferometer consists of two mirrors, a beamsplitter and a detector as shown in Figure 1.3.[35] The broadband light source emits a beam of light that strikes the partially reflective beam splitter, which transmits a fraction of the light towards one of the mirrors (Mirror 1) while the rest of the light is reflected towards a different mirror (Mirror 2). Both mirrors reflect the light to the same point on the beamsplitter, where the combined beams of light then travel to the detector in the form of an interference pattern. The computer processes the raw data, or also called interferogram (light absorption for each mirror position), into a spectrum (absorbance for each frequency). The raw data, which is measured as a function of length, is converted using a Fourier transform algorithm into data measured as a function of wavenumber (cm^{-1}).

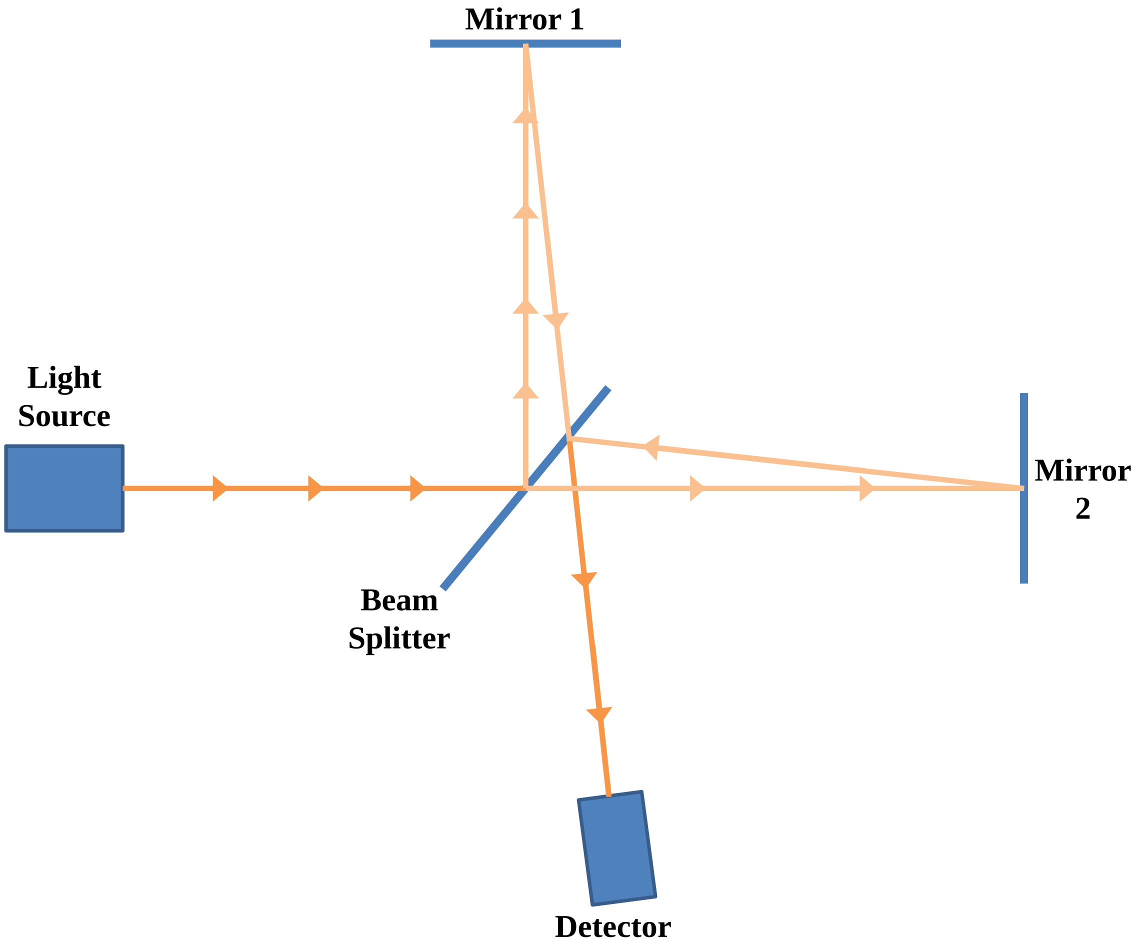

Figure 1.3 Schematic of a basic Michelson Interferometer and the path the light travels to reach the detector.

Several different FTIR spectroscopy techniques have been developed in order to analyze different types of materials. A few types include transmission infrared (TIR), diffuse reflectance IR Fourier transform (DRIFT) and reflection-absorption infrared spectroscopy (RAIRS) as shown in Figure 1.4. TIR is the most straightforward technique where the light transmits through sample and collects into the detector; DRIFTS measures the diffusely reflected IR light from the surface; and, RAIRS measures the reflected light from the surface at grazing incidence. The advantage to using TIR and DRIFTS is that these techniques can be used to study powders, which allow light to transmit through and reflect off these diffuse particles; on the other hand, RAIRS can be used to measure single crystals, which do not allow for light to transmit through them. In our studies, we use Au/TiO_2 nanoparticle catalysts, and therefore, we use TIR methods to measure and observe chemical reactions throughout the entire powder, not just at the surface, which is one disadvantage of DRIFTS.

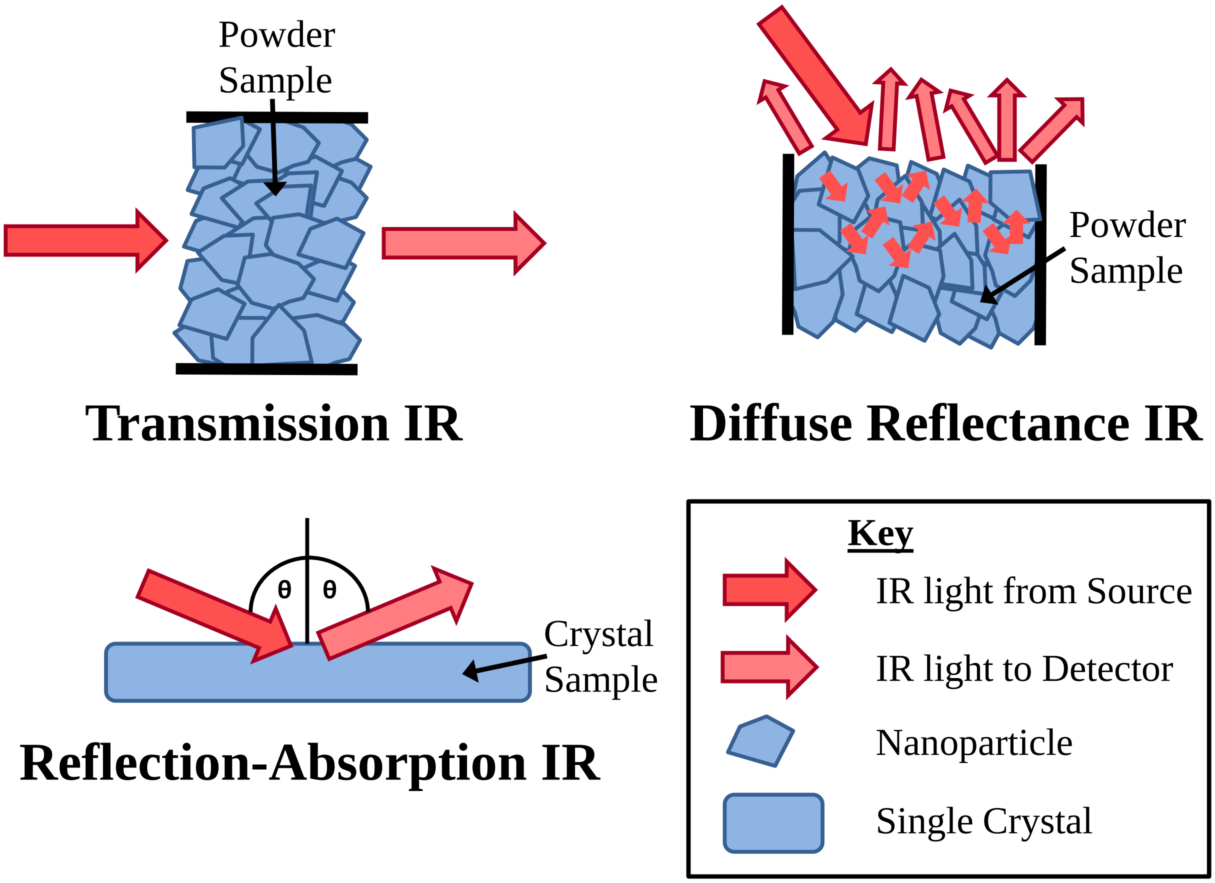

Figure 1.4 Different types of FTIR techniques and their setups: Transmission IR (Top Left), Diffuse Reflectance IR (Top Right) and Reflection-Absorption IR (Below Left).

1.2.3 Infrared Spectroscopy: Uses and Methods

Since the first IR spectrum was measured, many analysis methods using this technique have been formed to help determine the chemical identification of species on the surface, the kinetics and activation energies of a chemical reaction and the electron transfer processes that occur when molecules are adsorbed onto the surface. Here we discuss the specific IR analysis methods and their significance that we use in the following chapters.

Two methods that we use to identify adsorbed species on the surface are band frequency uniqueness and isotopic-labelling studies. The broadband light source that we employ is mid-IR light, which encompasses frequencies in the range 4000-400 cm^{-1}. Therefore, if the chemical species being measured has a net change in its dipole moment in this range, then the IR light will be absorbed by the species and a band will appear in the IR spectrum. This means modes with non-zero dipole derivatives with respect to mode displacement ("motion") are IR active and modes with zero dipole derivatives are IR inactive (e.g N≡N stretch). The absorption is measured using Beer's Law[36] where,

$$T = \frac{I}{I_0} = e^{-\varepsilon l c} \qquad (1.1)$$

$$A = -\ln\left(\frac{I}{I_0}\right) = -\ln(e^{-\varepsilon l c}) = \varepsilon l c \qquad (1.2)$$

where T is the transmission of light, I is the intensity of transmitted light, I_0 is the intensity of the incident light, ε is the molar absorptivity, l is the path length, c is the concentration of the material and A is the absorbance. Using these two equations, we can not only differentiate multiple chemical species, but we can also observe information about the absorption coverage (concentration) of molecules on the surface.

Since chemical species can contain different chemical bonds that are IR active, multiple chemical species can be identified on the surface or in the gas phase by the different frequencies they produce in the IR spectrum. Furthermore, the same species adsorbed on different sites can also be differentiated because electron transfer processes occur between the species and the support differently depending on the binding site creating an IR frequency shift. For example, CO adsorbed on TiO_2 has an absorbance frequency at 2179 cm^{-1}, while CO adsorbed on Au has a broad absorbance frequency at ~2100 cm^{-1}.[37]

Unfortunately, complex reactions can make species identification difficult, especially when multiple chemical species contain similar IR frequencies. In order to prove that the species believed to be at a certain frequency is present, isotopically labeled experiments are performed. Molecules containing their heavier complement isotopes have a shift in their IR frequency as understood by the simple harmonic oscillator equation. When a "harmonic" system is displaced from its equilibrium position, a restoring force is applied that is directly proportional to the dislocation. Applying Newton's 2nd Law of motion to the simple harmonic oscillator force law,[38] yields the following results,

$$F = \mu a = \mu \frac{d^2x}{dt^2} = -kx \qquad (1.3)$$

$$x(t) = A\cos(\omega t + \theta) \qquad (1.4)$$

$$\omega = \sqrt{\frac{k}{\mu}} = \frac{2\pi}{\tau} \qquad (1.5)$$

$$\nu = \frac{1}{\tau} = \frac{1}{2\pi}\sqrt{\frac{k}{\mu}} \qquad (1.6)$$

where μ is the reduced mass (e.g. $\mu = \frac{m_1 m_2}{m_1 + m_2}$ for a diatomic molecule), a is acceleration, x is dislocation, t and τ are time and mode period, k is the force constant, ω is the angular frequency, and ν is the frequency. From equation 1.6, we can deduce that heavier isotopes will downshift the IR frequency. We particularly exchange ^{12}C-labeled molecules with ^{13}C-labeled molecules,

^{16}O-labeled molecules with ^{18}O-labeled molecules, and H-labeled molecules with D-labeled molecules in the experiments presented in this thesis.

Other information can be acquired from an IR spectrum such as kinetic data during a reaction. The integrated area under the curve of an IR absorbance frequency is proportional to the concentration of the chemical species that that frequency identifies. Therefore, when a product forms over a period of time during a chemical reaction, the integrated absorbance area can be plotted vs time. Based on kinetic theory,[39] depending on the order of the reaction, the rate of the reaction, k, can be determined by fitting a line to the curve mentioned above. In our case, all of the reactions we studied were fitted to first order kinetic equations shown below,

$$y = y_0 + Ae^{-kt} \qquad (1.7)$$

$$y = y_0 + A(1 - e^{-kt}) \approx y_0 + Akt \qquad (1.8)$$

where y is the integrated absorbance area, y_0 is the integrated absorbance area before reaction, k is the rate constant, and t is time. Equation 1.7 fits a first-order exponential rate decay, and equation 1.8 fits a first-order linear initial rate. These equations were used to determine the rate of reactant molecule consumption and the rate of product molecule formation at a constant temperature, respectively. A set of experiments at different temperatures can then be performed, and the $k(T)$ values can be recorded in order to determine the activation energy for that reaction as shown by the manipulation of the Arrhenius equation[39] below,

$$k = Ae^{\frac{-E_a}{k_B T}} \qquad (1.9)$$

$$\ln(k) = \ln\left(Ae^{\frac{-E_a}{k_B T}}\right) = \ln(A) - \frac{E_a}{k_B T} \qquad (1.10)$$

where E_a is the activation energy and k_B is the Boltzmann constant. Plotting the $ln(k)$'s vs $1/T$ creates a linear line, and the slope of that line can give you the E_a value.

The last two IR analysis methods we use give unique information about the electron processes occurring on the surface and in the bulk of the material. The first method relates to the background rise of the entire IR absorbance spectrum. It has been well established that for metal oxide semiconductor catalysts, defect sites are present above the Fermi level and just below the conduction band.[40,41] The IR radiation excites electrons in these defect sites into the conduction band as a continuum of states, which causes the background absorbance rise.[40,41] Therefore, we can probe electron transfer of adsorbed molecules as they donate or accept electrons to or from these sites, respectively, by the increase or decrease of the IR background rise.

The other method for analyzing electron transfer is measuring frequency shifts of the molecules. When a molecule gains or loses electrons, depending on if the electrons occupy a bonding or anti-bonding molecular orbital, the bond can either weaken or strengthen causing unique shifts in the IR frequency. Electric field effects can also change the IR frequency, as will be explained in more detail in later chapters. Thus, using this powerful technique, IR spectroscopy, we can look at many aspects of the catalyst, the reaction molecules and even the role of electrons in these systems.

References

1. Campbell, I. M. *Catalysis at surfaces;* Springer: **1988**, 1-10.

2. Kauffman, G. B. Johann Wolfgang Döbereiner's Feuerzeug. *Platinum Metals Review* **1999**, *43*, 122-128.

3. Burwell Jr, R. L. Heterogeneous catalysis before 1934. *Catalysis* **1894**, 3-12.

4. Faraday, M. On the Mutual Action of Sulphuric Acid and Naphthaline, and on a New Acid Produced. *Philosophical Transactions of the Royal Society of London* **1826**, 140-162.

5. Berzelius, J. J. *Årsberättelse om framstegen i fysik och kemi;* Norstedt: **1840**, 245.

6. Stohmann, F. Über dem Wärmewerth der Bestandtheile der Nahrungsmittel. *Zeitschrift fur Biologie* **1894**, *31*, 364-391.

7. Ertl, G.; Gloyna, T. Catalysis-From philosopher's stone to Wilhelm Ostwald. *Zeitschrift fur Physikalische Chemie-International Journal of Research in Physical Chemistry & Chemical Physics* **2003**, *217*, 1207-1219.

8. Ostwald, W. Definition der Katalyse. *Zeitschrift für Physikalische Chemie* **1894**, *15*, 705-706.

9. Rodnyi, N. I.; Solov, J. I.; Wächtler, E. *Wilhelm Ostwald [Vil'gel'm Ostval'd, dt.][Von] NI Rodnyj u. Ju. I. Solowjew;* **1977**.

10. Hunt, L. The ammonia oxidation process for nitric acid manufacture. *Platinum Metals Review* **1958**, *2*, 129-134.

11. Smil, V. *Enriching the earth: Fritz Haber, Carl Bosch, and the transformation of world food production;* MIT press: **2004**, 61-82.

12. Langmuir, I. Modelisation of adsorption. *Physical Review* **1915**, *6*, 79-80.

13. Taylor, H. S. A theory of the catalytic surface. *Proceedings of the Royal Society of London.Series A* **1925**, *108*, 105-111.

14. Holloway, W.; Beeby, J. The theory of atomic desorption within the harmonic approximation. *Journal of Physics C: Solid State Physics* **1975**, *8*, 3531.

15. Hammer, B.; Norskov, J. Why gold is the noblest of all the metals. *Nature* **1995**, *376*, 238-240.

16. Haruta, M.; Kobayashi, T.; Sano, H.; Yamada, N. Novel gold catalysts for the oxidation of carbon monoxide at a temperature far below 0 ^{o}C. *Chemistry Letters* **1987**, 405-408.

17. Haruta, M.; Tsubota, S.; Kobayashi, T.; Kageyama, H.; Genet, M. J.; Delmon, B. Low-Temperature Oxidation of CO over Gold Supported on TiO_2, α-Fe_2O_3, and Co_3O_4. *Journal of Catalysis* **1993**, *144*, 175-192.

18. Haruta, M. Size-and support-dependency in the catalysis of gold. *Catalysis Today* **1997**, *36*, 153-166.

19. Rodriguez, J.; Ma, S.; Liu, P.; Hrbek, J.; Evans, J.; Perez, M. Activity of CeO_x and TiO_x nanoparticles grown on Au(111) in the water-gas shift reaction. *Science* **2007**, *318*, 1757-1760.

20. Fujitani, T.; Nakamura, I.; Akita, T.; Okumura, M.; Haruta, M. Hydrogen dissociation by gold clusters. *Angewandte Chemie* **2009**, *121*, 9679-9682.

21. Kotobuki, M.; Leppelt, R.; Hansgen, D.; Widmann, D.; Behm, R. Reactive oxygen on a Au/TiO_2 supported catalyst. *Journal of Catalysis* **2009**, *264*, 67-76.

22. Farnesi Camellone, M.; Zhao, J.; Jin, L.; Wang, Y.; Muhler, M.; Marx, D. Molecular Understanding of Reactivity and Selectivity for Methanol Oxidation at the Au/TiO_2 Interface. *Angewandte Chemie International Edition* **2013**, *52*, 5780-5784.

23. Gázquez, M. J.; Bolívar, J. P.; Garcia-Tenorio, R.; Vaca, F. A Review of the Production Cycle of Titanium Dioxide Pigment. *Materials Sciences and Applications* **2014**, *5*, 441.

24. Diebold, U. The surface science of titanium dioxide. *Surface science reports* **2003**, *48*, 53-229.

25. Fujishima, A.; Zhang, X.; Tryk, D. A. TiO_2 photocatalysis and related surface phenomena. *Surface Science Reports* **2008**, *63*, 515-582.

26. Thompson, T. L.; Yates, Jr., J. T. Surface science studies of the photoactivation of TiO_2 new photochemical processes. *Chemical Reviews* **2006**, *106*, 4428-4453.

27. Xiong, L.; Li, J.; Yang, B.; Yu, Y. Ti^{3+} in the surface of titanium dioxide: generation, properties and photocatalytic application. *Journal of Nanomaterials* **2012**, *2012*, 9.

28. Zhang, Z.; Yates, Jr., J. T. Band bending in semiconductors: chemical and physical consequences at surfaces and interfaces. *Chemical Reviews* **2012**, *112*, 5520-5551.

29. McFarland, E. W.; Metiu, H. Catalysis by doped oxides. *Chemical Reviews* **2013**, *113*, 4391-4427.

30. Metiu, H.; Chrétien, S.; Hu, Z.; Li, B.; Sun, X. Chemistry of lewis acid–base pairs on oxide surfaces. *The Journal of Physical Chemistry C* **2012**, *116*, 10439-10450.

31. Edwards, J. K.; Solsona, B. E.; Landon, P.; Carley, A. F.; Herzing, A.; Kiely, C. J.; Hutchings, G. J. Direct synthesis of hydrogen peroxide from H_2 and O_2 using TiO_2-supported Au–Pd catalysts. *Journal of Catalysis* **2005**, *236*, 69-79.

32. Enache, D. I.; Edwards, J. K.; Landon, P.; Solsona-Espriu, B.; Carley, A. F.; Herzing, A. A.; Watanabe, M.; Kiely, C. J.; Knight, D. W.; Hutchings, G. J. Solvent-free oxidation of primary alcohols to aldehydes using Au-Pd/TiO_2 catalysts. *Science* **2006**, *311*, 362-365.

33. Ryczkowski, J. IR spectroscopy in catalysis. *Catalysis Today* **2001**, *68*, 263-381.

34. Eischens, R.; Pliskin, W.; Francis, S. Infrared spectra of chemisorbed carbon monoxide. *Journal of Chemical Physics* **1954**, *22*, 1786-1787.

35. Atkins, P.; De Paula, J. *Atkins' physical chemistry;* Oxford University Press: **2014**, 480.

36. Miller, F. P.; Vandome, A. F.; McBrewster, J. *Beer-Lambert Law*; VDM Publishing House Ltd, Saarbrüken: **2009**, 154.

37. Green, I. X.; Tang, W.; Neurock, M.; Yates, Jr., J. T. Spectroscopic observation of dual catalytic sites during oxidation of CO on a Au/TiO_2 catalyst. *Science* **2011**, *333*, 736-739.

38. Pain, H. J. *The physics of vibrations and waves;* John Wiley and sons: **2005**.

39. Mortimer, M.; Taylor, P. *Chemical kinetics and mechanism;* Royal Society of Chemistry: **2002**; Vol. 1, 65-79.

40. Panayotov, D. A.; Yates, Jr., J. T. n-Type doping of TiO_2 with atomic hydrogen-observation of the production of conduction band electrons by infrared spectroscopy. *Chemical Physics Letters* **2007**, *436*, 204-208.

41. Panayotov, D. A.; Yates, Jr., J. T. Spectroscopic detection of hydrogen atom spillover from Au nanoparticles supported on TiO_2: Use of conduction band electrons. *The Journal of Physical Chemistry C* **2007**, *111*, 2959-2964.

Chapter 2: Experimental Design and Catalyst Synthesis Procedure

2.1 Vacuum Chamber Setup

The chamber used in these studies consists of a stainless steel high vacuum transmission FTIR cell with a base pressure of ~1x10^{-8} Torr. Top and side schematic views along with their corresponding photographs are shown in Figure 2.1. The IR beam from a commercial Bruker TENSOR 27, FTIR spectrometer is aligned using four external optical mirrors to pass through the center of the cell through two differentially pumped KBr windows to a N_2(*lq*) cooled MCT detector. Both the spectrometer and the MCT detector along with the entire IR beam path are purged constantly with CO_2- and H_2O-free air. A residual gas analyzer (RGA) is connected to the cell for gas analysis of product formation in the gas phase as well as for gas purity tests. The RGA can be separated from the cell by closing a gate valve. On the opposite side of the cell, a MKS I-MAG cold cathode ionization gauge is used to monitor the cell pressure at low pressures (10^{-10}-10^{-3} Torr), and a MKS Baratron capacitance manometer is used for higher-pressure readings (0.001-100 Torr). In order to keep the cell under high vacuum, a turbo-molecular pump in conjunction with a mechanical pump is connected to the cell from below. We have also installed a UV fiber optic cable and holder, which can be used for future photochemistry studies. Installation, optimization and calibration of the fiber optic can be found in Appendix A.

The powdered samples are connected to a manipulator, which consists of a N_2(*lq*) Dewar with Z-direction motion, and are centered in the cell at the IR beam focus. A schematic view and photo of the front of the sample holder is shown in Figure 2.2. The powdered samples are pressed into 7 mm diameter disks on a 0.003-inch thick tungsten grid under 33,500 psi of pressure using a hydraulic press. Each disk contains ~0.005g of material, and two samples can be pressed onto the same grid at a time. Since the manipulator has Z-direction motion, both samples can be analyzed under the same reaction conditions. The grid is screwed into a pair of nickel bars, which are connected to copper rods. These copper rods are connected to a (0-100V, 0-50A) power supply for heating. A K-type thermocouple is spot-welded to the top center of the grid above the samples providing accurate temperature readings to 0.1 K resolution. The thermocouple and electrical power supply are joined to a National Data Acquisition (DAQ) card, which is controlled by a LabVIEW program using a proportional-integral-derivative (PID) method to control heating and cooling of the samples. The samples can be linearly heated and cooled in the temperature range 85-1000 K. This experimental setup was adapted from a cell design by Basu *et al.*,[1] and the design has been widely used by others in the field.[2-4]

The gases are introduced to the cell using a gas manifold system that is attached to the vacuum system and isolated from the cell by a closable gate valve and Swaglok valves. A schematic is shown in Figure 2.3. By opening and closing certain valves, the gas can either be introduced into the cell, pumped away through the mechanical pump without entering the cell or can accumulate into a $N_2(lq)$ trap or gas bulb for storage. Steel tubing can also be used to connect small lecture bottles with attached regulators for direct gas transfer to the system. A leak valve is also connected to the manifold for transferring very small amounts of gas ($\geq 10^{-8}$ Torr) to the cell. In order to measure the pressure in the gas manifold a separate capacitance manometer (0.1-1000 Torr) is installed at the top right corner of the system as shown in Figure 2.3. The glass bulbs, lecture bottles and $N_2(lq)$ trap are all connected using VCR fittings and copper gaskets and can be removed and/or replaced with other gases or liquids.

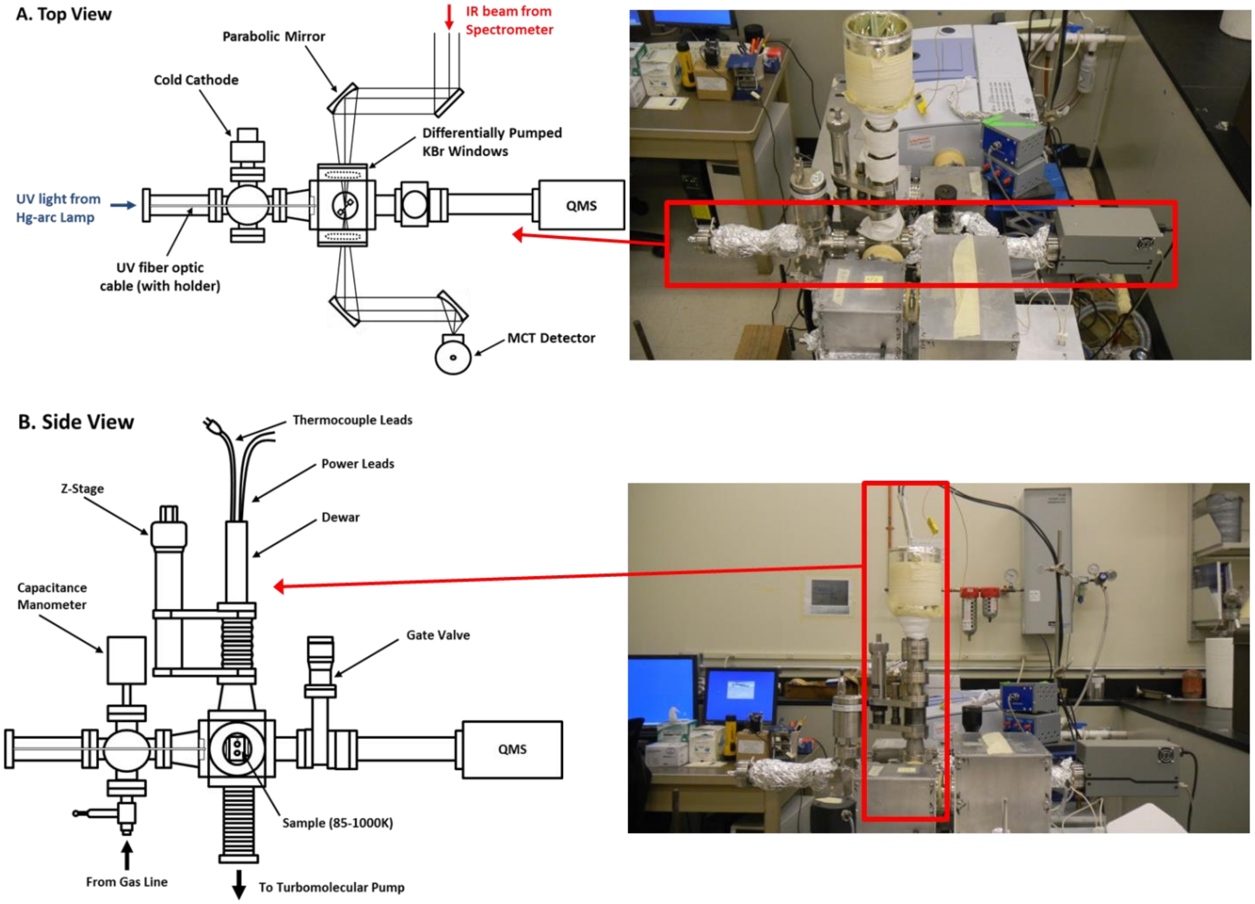

Figure 2.1 (Left) Schematic of (A) top view and (B) side view of the stainless steel vacuum transmission IR cell system; (Right) Photographs of the (A) top view and (B) side view of cell system.

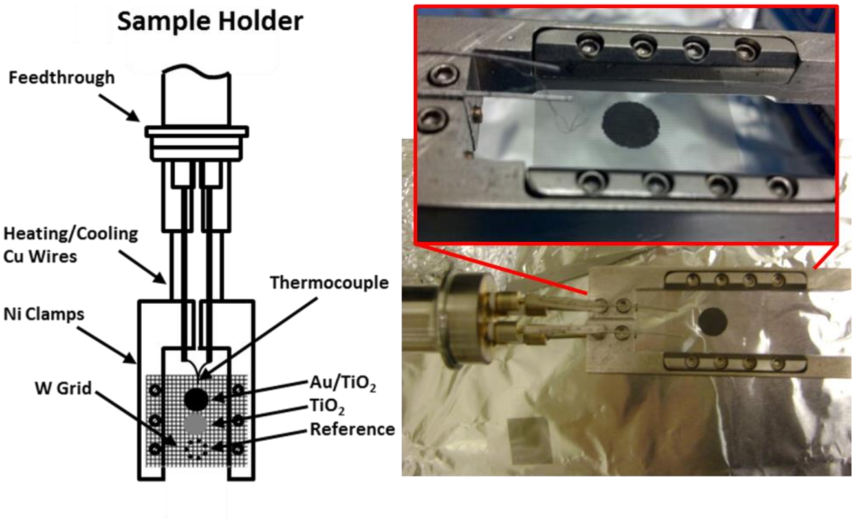

Figure 2.2 (Left) Schematic of the sample holder; (Right) Photographs of the sample holder

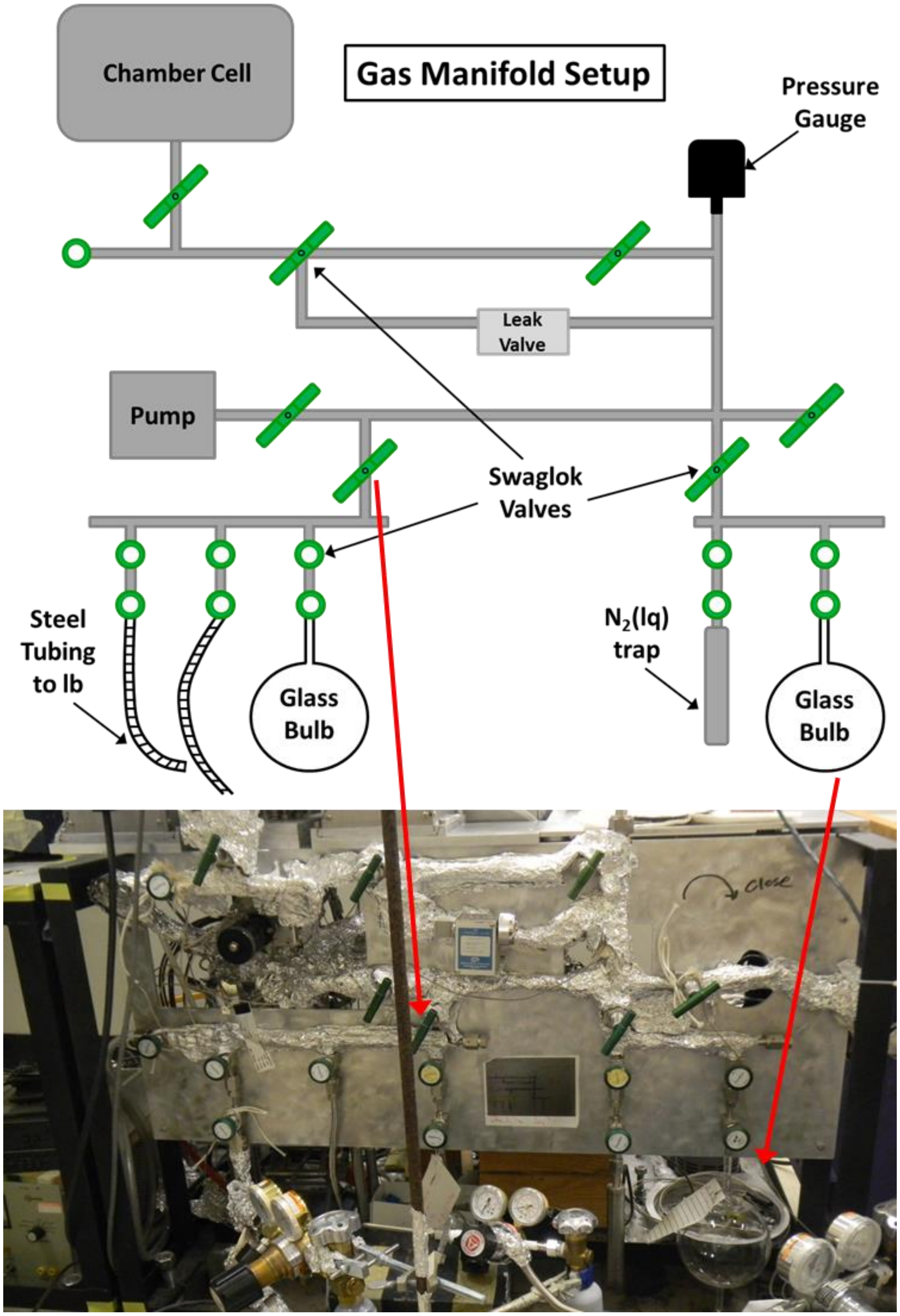

Figure 2.3 (Top) Schematic of the gas manifold; (Bottom) Photograph of the gas manifold

2.2 External GC-MS Setup and Collection Vessel

2.2.1 Collection Vessel

Several of the topics studied in the next chapters include using techniques in addition to TIR spectroscopy and mass spectrometry in order to obtain additional information essential for accurately analyzing the data and for verification of gas purity labels. One of the limitations of mass spectrometry occurs when multiple products are produced and the mass spectrum cannot distinguish between molecules that contain several of the same mass fragments. Therefore, we employ an external gas chromatography mass-spectrometer (GC-MS), which first separates the product molecules depending on size and polarity and then takes a mass spectrum vs time in order to see each separate species that is collected from the IR cell.

The collection vessel and gas extraction setup are depicted in Figure 2.4. We created this simple design using a glass piece connected to Kovar, which was welded to a stainless steel opening of a Swaglok valve. This piece was then glass blown together with a 4 mm thin wall borosilicate glass EPR sample tube (7" L) with a PTFE rubber septum and plastic screw cap attached to the end. In order to extract gas from the collection vessel, a 1 mL Hamilton syringe containing a PTFE plunger tip and PTFE stop valve was employed to ensure a gas-tight seal. Once the syringe pierced the rubber septum and both the vessel and syringe were evacuated, the whole system held a base pressure of ~10^{-7} Torr. The reaction products would then be introduced into the vessel and we would extract the gas and close the stop valve before removing the syringe from the collection vessel. The rubber septum kept a consistent gas tight seal for ~25 punctures of the syringe needle before the vessel would start to leak.

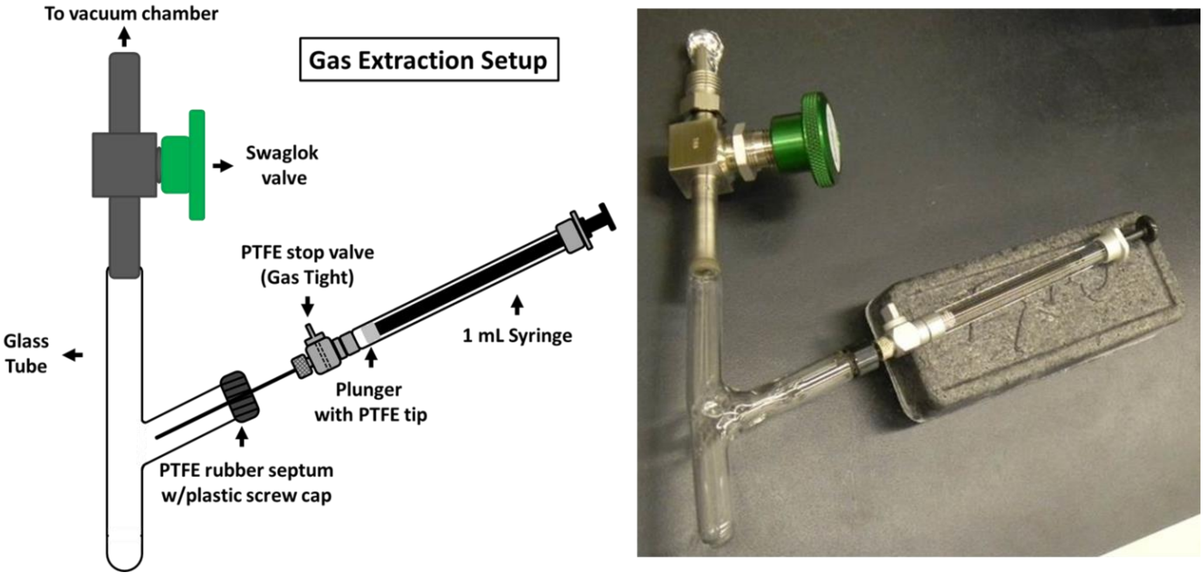

Figure 2.4 (Left) Schematic of collection vessel with syringe inserted through the septum for gas extraction (Right) Photograph of gas extraction setup

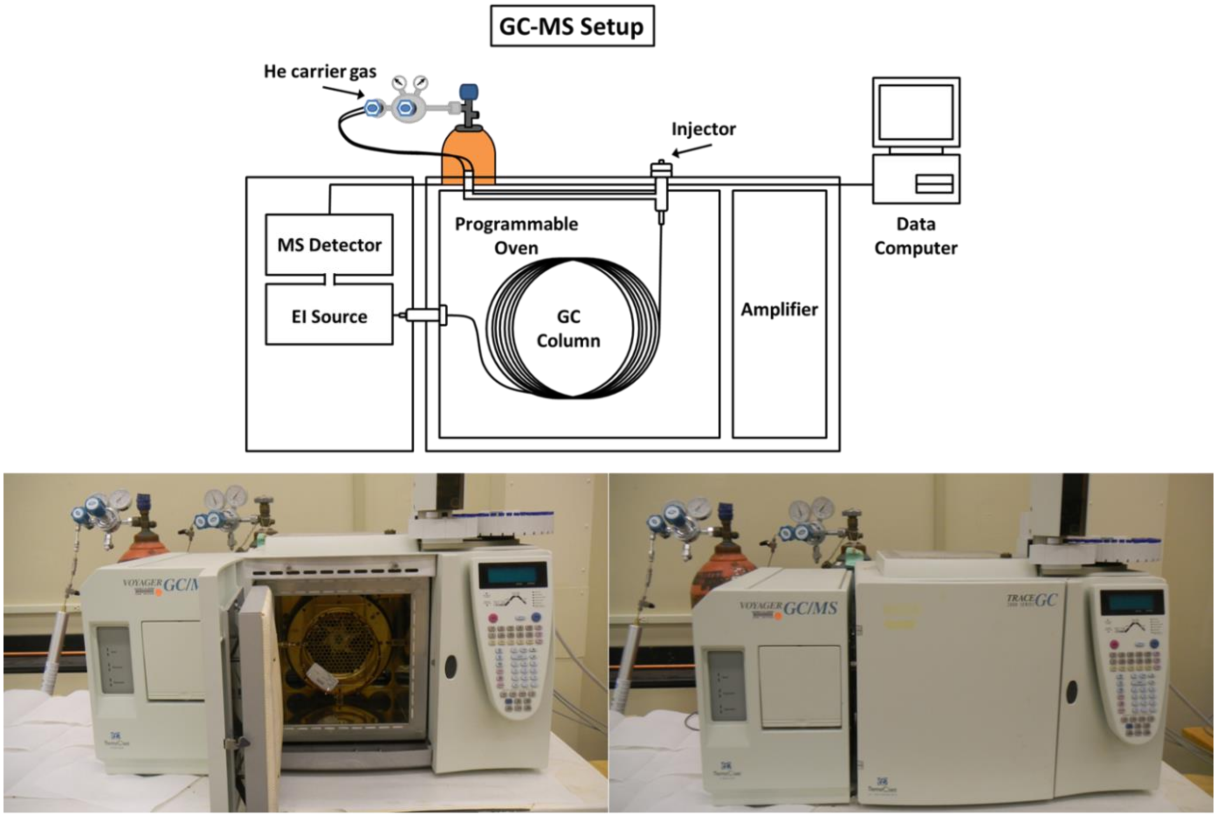

Open Oven Door

Closed Oven Door

Figure 2.5 (Top) Schematic of GC-MS setup (Bottom) Photograph of GC-MS system with (left) oven door open and (right) oven door closed

2.2.2 GC-MS System Setup

The reaction gas (or liquid) in the syringe is transferred to the GC-MS system by inserting the syringe needle into the injector opening and releasing the gas (or liquid) into the system. A schematic and photographs of the GC-MS system setup are shown in Figure 2.5. The sample material (gas or liquid) is vaporized in the GC glass liner first before entering the GC column. The GC column consists of a tube with a stationary phase material, which can be anything between a strongly, polar material to a nonpolar material, covering the walls of the tube. Once the sample is in gas phase, the sample gas along with helium (He) carrier gas enter into the GC column, where the sample gas material separates depending on the size and polarity of the gas product molecules. For example, if the stationary phase is polar, the more polar gas molecules will adsorb and stay longer in the column; whereas, the more, nonpolar molecules will leave the column first. Helium is used as the carrier gas due to its inertness and small size.

After gas separation occurs in the GC column, the gas molecules enter through the GC interface tube into the source, where a filament is heated to produce electrons that collide with the gas molecules and break them into ion fragments. These ions are then repelled into the quadrupole mass analyzer by a repeller plate. The mass analyzer consists of 4 rods with alternating DC and RF voltages to filter ions to the detector, where a current-to-voltage amplifier is used to produce the mass spectrum data seen on the computer. The source and mass analyzer are kept under vacuum using a turbo-molecular pump in conjunction with a mechanical pump to ensure the gas ions detected are from the sample and not the air or other impurities. Calibrations of liquid and gas materials along with applications are shown in Appendix B.

2.3 Nanoparticle Synthesis and Characterization

The Au/TiO_2 sample was home-made following the deposition-precipitation protocol reported by Zanella *et al.*,[5] using hydrogen tetrachloroaurate (III) trihydrate ($HAuCl_4 \cdot 3H_2O$), TiO_2 powder (P25, 49 m^2/g), and urea. The TiO_2 powdered sample was provided by Evonic Industries; the urea (99.5%) and $HAuCl_4 \cdot 3H_2O$ were purchased from Acros. Prior to deposition, the TiO_2 powder was activated at 373 K under 100 mL/min airflow for 24 hours. The Au precursor solution consisted of 4.2×10^{-3}M $HAuCl_4 \cdot 3H_2O$ and 4.2M urea and was kept in dark throughout the synthesis procedure due to the known fact that it decomposes under illumination.[6] The initial pH value of the precursor solution was ~2. Urea was used here to cause a slow release of ammonia to control the acidity of the solution. One gram of activated TiO_2 powder was added to 100 mL of the Au precursor solution for deposition. The mixture was kept at 353 K under vigorous stirring for 8 hours. The pH value of the mixture increased to ~7 by the end of the deposition. The solid (orange color) was then separated from the liquid phase by a centrifuge at 3800 rpm for 20 min. The precipitate was then washed in 100 mL double-deionized (DDI) water at 323 K using vigorous stirring for 10 min and centrifuged again. This washing cycle was repeated 5 times, in an attempt to remove the residual Cl^- anions, which are proposed to compete with O_2 for adsorption sites.[7] The cleaned Au/TiO_2 powdered sample was dried at 373 K for 24 hours under 100 mL/min airflow before installation into the vacuum cell. No chlorine was detected on this sample by Auger spectroscopy measured in a separate UHV system. The maximum Au loading on the catalyst was 8 wt%.

Figure 2.6 shows transmission electron microscopy (TEM) images of the average diameter sizes and shapes of the Au nanoparticles supported on the TiO_2 particles taken after experiments.[8] For the procedure described above, the average Au particle size is ~3 nm as shown by the histogram in Figure 2.6c and the shape is hemispherical in nature with distinct edge facets. The image in Figure 2.6b is looking down the Au(111) plane.

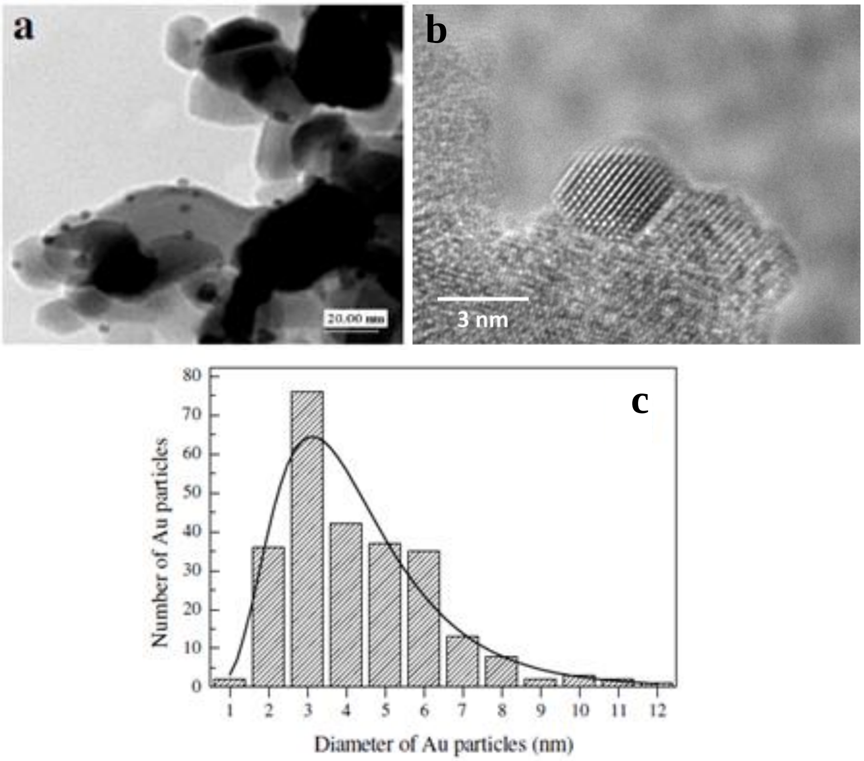

Figure 2.6 (a and b) TEM images of Au/TiO_2 synthesized nanoparticles (c) Histogram of Au particle size. The small circles are Au particles and the big shapes are TiO_2 particles.

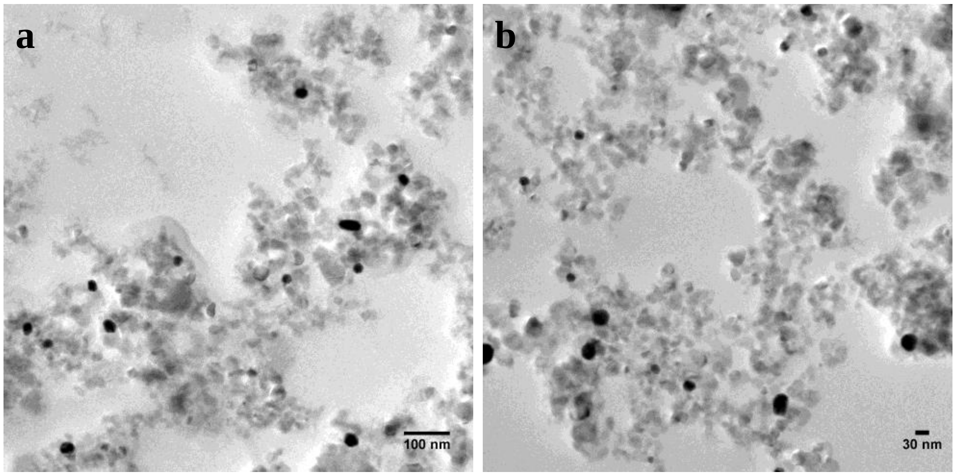

Figure 2.7 TEM images of synthesized larger Au particles supported on TiO_2. The dark shapes are Au nanoparticles and the light shapes are TiO_2 nanoparticles.

We also synthesized larger Au particles on TiO_2 as shown by the TEM images in Figure 2.7. The average Au particle diameter in these powdered samples is ~20-30 nm. In order to synthesize these larger Au particles, we altered the synthesis procedure described above only slightly. We mixed 0.16g of $HAuCl_4$, 1.00g of TiO_2 powder (P25, 49 m^2/g), and 2.53g of urea together with DDI water in a 100 mL volumetric flask as done similarly to the ~3 nm Au/TiO_2 catalyst sample, after drying the TiO_2 in air. The setup is shown in Figure 2.8. With an initial pH of ~2 (as done previously), the mixture was kept at 353 K under vigorous stirring for only 1 hour with the final pH still ~2-3. After exactly 1 hour, the mixture was immediately cooled in an ice bath for 10 minutes. Then as described above, the orange solid mixture was centrifuged and washed 5 times with DDI water. Lastly, it was dried at 373K overnight in airflow before being placed into the vacuum system.

Zanella also provided us with Au/SiO_2 catalyst samples with the average Au diameter particle size of ~3 nm at 1 wt%. He used the same synthesis procedure as the ~3 nm Au/TiO_2 catalyst samples we synthesized.[9]

Figure 2.8 (Left) Nanoparticle synthesis setup including oil bath, yellow thermometer and hot plate; (Right) solid in tube after several washes with DDI water and centrifugation.

References

1. Basu, P.; Ballinger, T.; Yates, Jr., J. T. Wide temperature range IR spectroscopy cell for studies of adsorption and desorption on high area solids. *Review of Scientific Instruments* **1988**, *59*, 1321-1327.

2. Panayotov, D. A.; Yates, Jr., J. T. Spectroscopic detection of hydrogen atom spillover from Au nanoparticles supported on TiO_2: Use of conduction band electrons. *The Journal of Physical Chemistry C* **2007**, *111*, 2959-2964.

3. Stevanovic, A.; Büttner, M.; Zhang, Z.; Yates, Jr., J. T. Photoluminescence of TiO_2: effect of UV light and adsorbed molecules on surface band structure. *Journal of the American Chemical Society* **2011**, *134*, 324-332.

4. Panayotov, D. A.; Morris, J. R. Catalytic degradation of a chemical warfare agent simulant: reaction mechanisms on TiO_2-supported Au nanoparticles. *The Journal of Physical Chemistry C* **2008**, *112*, 7496-7502.

5. Zanella, R.; Giorgio, S.; Henry, C. R.; Louis, C. Alternative methods for the preparation of gold nanoparticles supported on TiO_2. *Journal of Physical Chemistry B* **2002**, *106*, 7634-7642.

6. Zhang, J.; Yu, J.; Zhang, N. Y.; Liu, P.; Chen, H. Preparation of Gold Nanoparticles. *Advanced Materials Research* **2013**, *798*, 223-226.

7. Zhu, H.; Liang, C.; Yan, W.; Overbury, S. H.; Dai, S. Preparation of highly active silica-supported Au catalysts for CO oxidation by a solution-based technique. *The Journal of Physical Chemistry B* **2006**, *110*, 10842-10848.

8. Green, I. X.; Tang, W.; McEntee, M.; Neurock, M.; Yates, Jr., J. T. Inhibition at Perimeter Sites of Au/TiO_2 Oxidation Catalyst by Reactant Oxygen. *Journal of the American Chemical Society* **2012**, *134*, 12717-12723.

9. Zanella, R.; Sandoval, A.; Santiago, P.; Basiuk, V. A.; Saniger, J. M. New preparation method of gold nanoparticles on SiO_2. *The Journal of Physical Chemistry B* **2006**, *110*, 8559-8565.

Chapter 3: Inhibition at Perimeter Sites of Au/TiO_2 Oxidation Catalyst by Reactant Oxygen

(modified from *JACS*, **2012**, 134 (30), pp 12717–12723)

3.1 Introduction

Nanoparticle Au catalysts exhibit extraordinary efficiency and selectivity in key industrial oxidation reactions involving molecular oxygen.[1] Understanding the mechanisms by which these catalysts carry out oxidation reactions will provide valuable insights and guidance toward the design of new catalytic materials. Joining the effort of unraveling the CO oxidation process on the Au/TiO_2 catalyst led by others,[2-6] we have shown spectroscopically that on a catalyst comprised of ∼3 nm Au particles supported on TiO_2 the catalytic activity is localized at the Au perimeter, where dual-catalytic sites involving Au atoms and Ti^{4+} ions work together at very low temperatures to activate molecular oxygen and oxidize both H_2 as well as CO.[7,8] More research is needed as many aspects of the dual-catalytic system are still unclear and under debate.

The charge state of active Au species during the catalytic reaction is one area that has been greatly debated, with different reports citing the active sites as being negative, neutral, or positively charged Au species. For instance, Au clusters deposited on oxide F centers were reported to be negatively charged and highly active for CO oxidation;[6,9-11] other experiments, however, suggest that the active sites for CO oxidation are comprised of partially oxidized (positively charged) Au centers.[12-15] In addition, there are also various reports that suggest as-synthesized cationic Au(III) is not active for CO oxidation at room temperature until reduced to metallic Au[1,16] and that the metallic Au is the active species.[16,17] Previous theoretical calculations of charge effects on Au also provided mixed conclusions as to the relationship between the Au oxidation state and the catalytic activity.[5,18-32]

Two important challenges associated with establishing the charged state of the active sites experimentally are as follows: (1) it was hard to measure the partial charge state (oxidation states between 0 and ±1) of localized Au atoms in situ directly via common techniques such as X-ray photoelectron spectroscopy, X-ray absorption near-edge structure spectroscopy, or Mössbauer spectroscopy until recently;[13,33] and (2) the reactant for the standard catalyst activity test, the CO molecule, is a strong reducing agent for Au nanoparticles at room temperature or lower.[34-36] To avoid these complications, we use the reactant CO molecule as a surface probe at very low temperatures (~120 K) to detect the Au oxidation state during the catalytic reaction and, in addition, to kinetically track the reaction progress via in situ infrared (IR) spectroscopy. At these low temperatures, reduction of cationic Au by CO does not occur during the catalytic reaction.

Green *et al*. previously demonstrated that at temperatures in the range 110–130 K CO molecules adsorbed on the TiO_2 support (CO/TiO_2) are the active species for CO oxidation and are delivered to the dual-catalytic perimeter sites by diffusion across TiO_2.[7] By working at low temperatures the reaction is kinetically simplified via exclusion of higher activation energy processes. In contrast, CO adsorbed on Au sites is essentially unreactive at 120 K.[7] In the work reported here we show that preoxidation of the Au perimeter sites of the Au/TiO_2 catalyst at high temperature (473 K), to produce $Au^{\delta+}$ sites, reduced the CO oxidation activity by a factor of 22 at 120 K (Figure 3.1). The apparent activation energy for CO oxidation over the Au/TiO_2 catalyst increases from 0.16 to 0.27 eV when $Au^{\delta+}$ sites are produced by preoxidation of the catalyst. Density functional theory (DFT) calculations indicate that the origin of the local catalytic inhibition or site poisoning is conversion of Au^0 to $Au^{\delta+}$ at the Au nanoparticle perimeter that results from the strong chemisorption of oxygen atoms at these sites. Understanding the inhibition of the active Au sites in the low-temperature regime provides insight into the mechanism of the CO oxidation reaction on Au/TiO_2 catalysts at higher temperatures, thus coupling low-temperature studies to catalysis at higher temperatures.

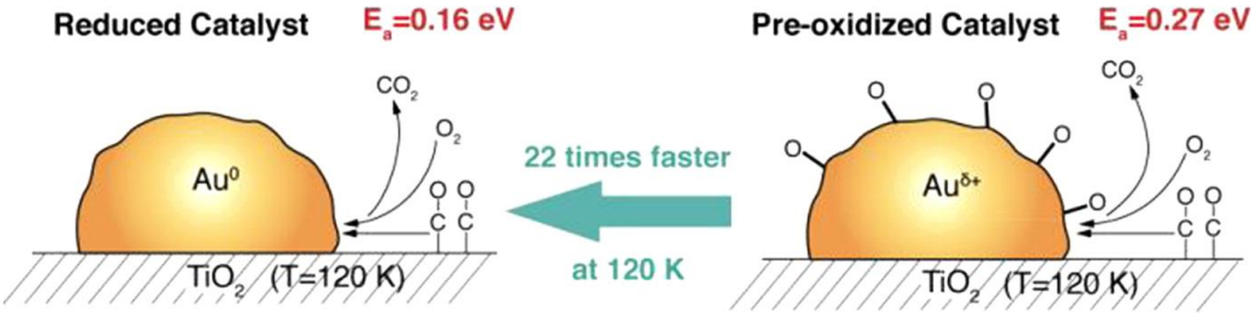

Figure 3.1 Schematic of CO oxidation reaction on (left) reduced Au/TiO_2 and (right) pre-oxidized Au/TiO_2.

3.2 Experimental and Theoretical Procedures

3.2.1 Experimental Procedure

A detailed description of the synthesis procedure and experimental setup can be found in Chapter 2.[7,37] Preoxidation of the catalyst to various stages was carried out at temperatures from 295 to 473 K in 5 Torr of O_2 for 30 min. Prereduction of the catalyst to different degrees was carried out in 0.07 Torr of CO for 5 min at temperatures in the range 120–473 K, as indicated in each experiment reported. All experiments described in this study were carried out on the same catalyst prepared by repeated oxidation in O_2 followed by reduction in CO, i.e., the catalyst was reusable for many experiments. No heating above 473 K was performed to avoid the known effect of sintering of Au nanoparticles.[4,38] Thus, a “fully-oxidized $Au^{\delta+}$/TiO_2 catalyst” and a “fully-reduced Au^0/TiO_2 catalyst” were made by O_2 oxidation or CO reduction at 473 K. Transmission electron microscope measurements of the catalyst after repeated oxidation/reduction cycles show a Au particle size distribution similar to the as-prepared catalyst (2–8 nm diameter, with a most probable diameter of 3 nm, Figure 2.6, Chapter 2).[7,8,39] The catalyst, oxidized and reduced at different temperatures, was cooled to 120 K in vacuum for the CO adsorption and oxidation reaction.

CO adsorption on the catalyst to saturation coverage at temperatures between 110 and 130 K was achieved by backfilling the cell with 0.07 Torr of CO gas. For the CO oxidation studies, after reaching saturation, the CO gas was evacuated from the cell for approximately 10 min to produce one monolayer (ML) coverage. An IR spectrum was taken after 8.6 min of CO evacuation in each experiment and used as the point of time zero for the reaction kinetics study. One Torr of O_2 was then introduced to the cell, and the CO oxidation reaction immediately began. FTIR spectra were taken every minute until the CO/TiO_2 adsorption feature was gone from the IR spectra (~20 min for Au^0/TiO_2 catalyst and ~60 min for $Au^{\delta+}/TiO_2$ catalyst).

3.2.2 Theoretical Model and Parameters

All of the calculations reported herein were carried out using density functional theory (DFT) calculations as implemented in the Vienna *ab initio* Simulation Package (VASP).[40] The core electrons were treated by pseudopotentials built with the projector augmented-wave (PAW) method.[41,42] The valence electrons were described with Kohn-Sham single-electron wave functions and expanded in plane-wave basis with energy cutoff of 400 eV. The exchange-correlation energy was described by the PW91 gradient approximation (GGA) functional.[43] The on-site Coulomb interactions was corrected by the DFT+U method,[44] in which the value of U was chosen to be 4.0 eV in order to generate the experimentally-observed band-gap structure.[45] Spin-polarization was considered for all calculations and was used when necessary. A vacuum gap of 10 Å was used in the *Z*-direction between slabs. The first Brillouin zone was sampled with (2×2×1) k-point mesh.[46] Geometries were considered as optimized when the force on each atom was less than 0.03 eV/Å.

The reaction pathway and activation barriers were found by the nudged elastic band (NEB) method with image climbing,[47] combined with the dimer method.[48] The NEB method was used to follow the minimum energy path between the reactant and product states. When the perpendicular forces on all of the images along the band were lower than 0.1 eV/Å, the dimer method was subsequently used to refine the transition state to the point where the force acting on the transition state dimer was lower than 0.03 eV/ Å.

The Au/TiO_2 system was simulated herein by a Au nanorod supported on a rutile TiO_2(110) surface. The oxide (2 × 3) unit cell has four O–Ti–O trilayers in the Z direction. The atoms in the top two trilayers of the TiO_2 slab were allowed to fully relax, while the atoms in the bottom two trilayers were fixed to their lattice positions. The 3 nm Au particle was simulated by a three-atomic-layers-high Au nanorod as shown in Figure 3.2. All of the Au atoms were allowed to relax in the Z direction. This model has been used previously by other groups and by ourselves to find plausible reaction mechanisms and locate active sites, because the Au nanorod structure is computationally tractable and provides a sample of Au surface sites with different coordination numbers (CN).[7,8,26,49] However, the structure is devoid of Au corner sites, likely causing the calculations to slightly underestimate the actual catalytic reactivity.

The charge state of the Au atoms was analyzed by the Bader charge analysis method.[50,51] Before the catalyst was oxidized, the surface Au atoms were neutral with the exception at the perimeter where the Au atoms bound to the bridge oxygen of the TiO_2 and were slightly positively charged, similar to previous theoretical results for small Au clusters on TiO_2.[27]

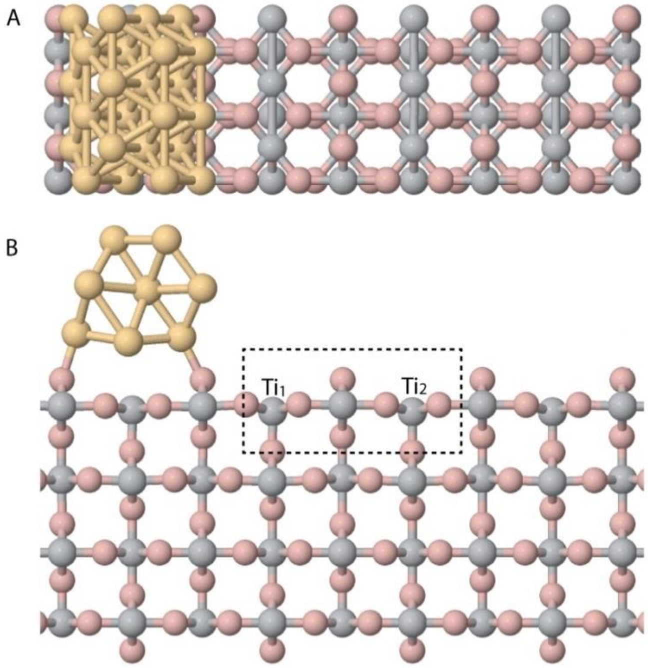

Figure 3.2 The model Au/TiO_2 interface involving a 3x3 Au nano-rod covalently bonded to the bridging oxygen sites on the rutile TiO_2 (110) surface support. A) top view, B) side view.

3.3 Results and Discussion

The stepwise oxidation of the catalyst was carried out to examine the Au^0 to $Au^{\delta+}$ species conversion. Figure 3.3a shows the IR spectra in the CO stretching region of a reduced catalyst preoxidized to different levels. The IR absorption bands at 2179 and 2206 cm^{-1} are assigned to CO adsorbed on Ti^{4+} sites (denoted as CO/TiO_2) because identical bands are observed on a TiO_2 blank sample also held in the IR cell (Figure 3.4). The IR band at ~2106 cm^{-1} is assigned to CO terminally adsorbed on metallic Au^0 sites based on previous investigations (denoted as CO/Au^0).[7,36,52-54] The high-frequency shoulder at ~2126 cm^{-1} is generally assigned to CO adsorbed on positively charged $Au^{\delta+}$ sites ($0 < \delta < 1$, denoted as CO/$Au^{\delta+}$).[36,53-55] As the preoxidation temperature increases from 295 to 473 K, the 2106 cm^{-1} band decreases in absorbance at saturation coverage while the 2126 cm^{-1} band increases in absorbance (Figure 3.3a), indicating a transition from CO/Au^0 species to CO/$Au^{\delta+}$ species under increasingly aggressive oxidation conditions.

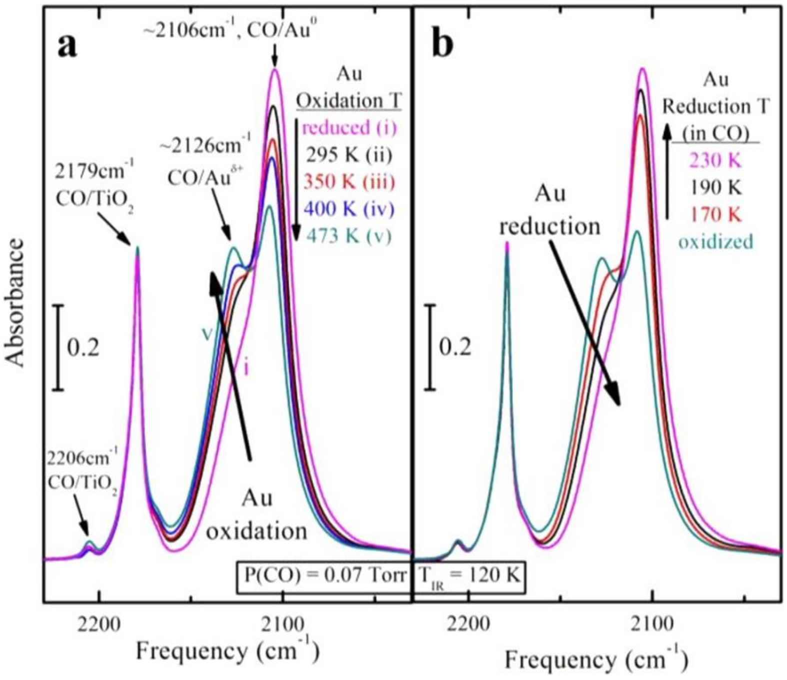

Figure 3.3 IR spectra of 120 K saturated CO adsorption of the Au/TiO$_2$ catalyst surface modification by (a) oxidation in O$_2$ and (b) reduction in CO at different temperatures.

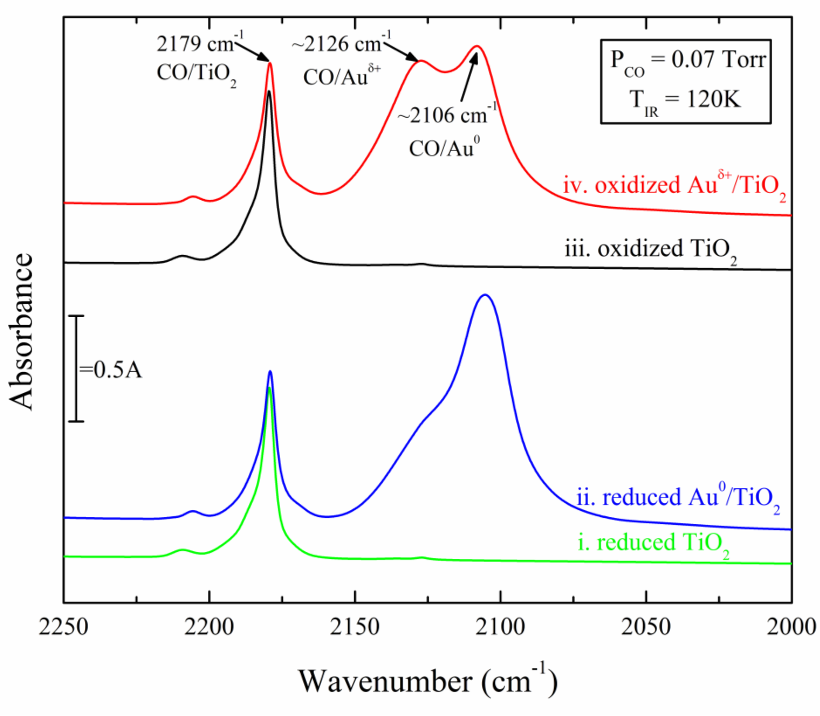

Figure 3.4 IR spectra comparison of CO saturation coverage at 120K on Au/TiO$_2$ and TiO$_2$ blank samples after the same pretreatment. (i. and ii.) After 295K CO reduction followed by 473K evacuation. (iii. and iv.) After 473K O$_2$ oxidation followed by 473K evacuation.

The Au-catalyst preoxidation process was shown to be completely reversible by observation of ν_{CO} during reduction of the oxidized $Au^{\delta+}/TiO_2$ catalyst in gas-phase CO. Figure 3.3b shows the 120 K–CO IR absorption spectra of the preoxidized catalyst reduced at temperatures from 170 to 230 K in 0.07 Torr of CO, where an increase of CO/Au^0 species is accompanied by a decrease of $CO/Au^{\delta+}$ species, just opposite from Figure 3.3a. It is noted that the Au oxidation state produced by pretreatment has no influence on the neighboring CO/TiO_2 species, since the band frequency, band shape, and saturation absorbance of the CO/TiO_2 species remains unchanged upon Au oxidation/reduction. We denote the catalyst in Figure 3.3a(i) as the "fully-reduced Au^0/TiO_2" sample and the catalyst in Figure 3.3a(v) as the "fully-oxidized $Au^{\delta+}/TiO_2$" sample. The CO/Au^{1+} (ν_{CO} = 2186–2159 cm^{-1}),[35,54,56] CO/Au^{3+} ($\nu_{CO} \approx 2207$ cm^{-1}),[56] and $CO/Au^{\delta-}$ (ν_{CO} = 2038–1900 cm^{-1})[55,57] species reported by others on Au nanoparticle catalysts using IR or other measurement techniques[9,10,12] are not found in our IR observations.

To gain quantitative knowledge of the conversion between Au^0 and $Au^{\delta+}$ species, the overlapping CO/Au^0 and $CO/Au^{\delta+}$ bands have been deconvoluted using a Lorentz function in all measurements made during the CO reduction process (part of which are presented in Figure 3.3b). The integrated absorbance of each deconvoluted band is used as a measurement of the amount of the corresponding species on the surface. Figure 3.5 depicts conversion of $CO/Au^{\delta+}$ to CO/Au^0 as a function of increasing reduction temperature in CO. The reduction process starts above 147 K in 0.07 Torr of CO, before which little change in integrated absorbance is observed for either species. The total integrated CO absorbance on the Au^0 and $Au^{\delta+}$ sites remains constant during the reduction (Figure 3.5, right axis), indicating that the saturation coverage of adsorbed CO (1 ML) on the Au nanoparticles is constant for various stages of reduction, and supports the idea that the extinction coefficients of CO/Au^0 species and $CO/Au^{\delta+}$ species are quite similar.

The oxidation/reduction procedures using O_2 and CO provide a very convenient method to reproducibly modify the Au/TiO_2 catalyst.

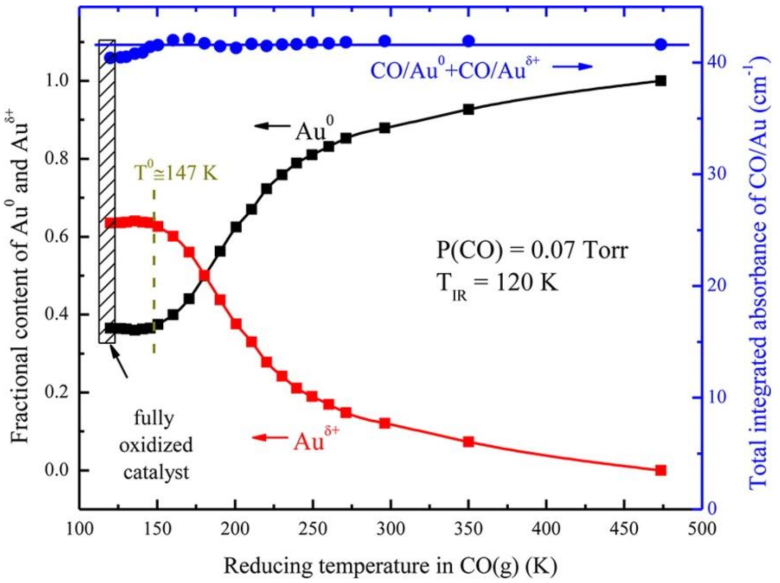

Figure 3.5 (Left axis) Plots of the CO/Au$^{\delta+}$ fractional conversion to CO/Au^0 species monitored by deconvolution of IR bands from Figure 3.2b using the Lorentz ν_{CO} line shape function and comparing the integrated absorbance of each deconvoluted band. (Right axis) Plot of the total integrated IR absorbance of CO/Au$^{\delta+}$ and CO/Au^0 species combined versus catalyst reduction temperature.

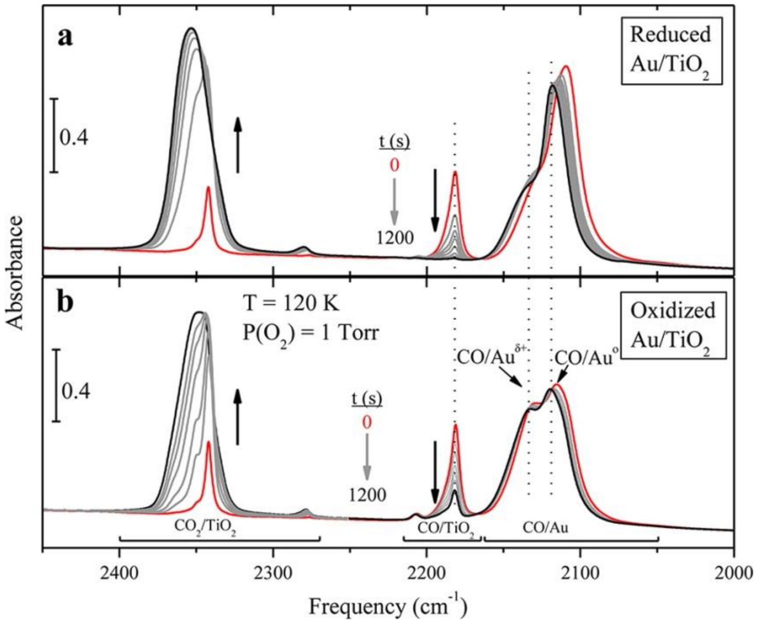

Figure 3.6 Comparison of low-temperature CO oxidation on the (a) reduced Au^0/TiO_2 catalyst and (b) oxidized Au$^{\delta+}$/TiO_2 catalyst.

To determine the kinetic influence of oxidation of the Au/TiO_2 catalyst, we performed low-temperature CO oxidation reactions on the fully reduced catalyst and on the fully oxidized catalyst separately. Infrared spectra taken during the first 1200 s of the two experiments are shown in Figure 3.6. Consistent with our previous findings on Au^0/TiO_2 catalysts,[7] CO/TiO_2 is the main active species undergoing oxidation at 120 K judging by the disappearance of the CO/TiO_2 feature from the IR spectra. An absorption band near 2350 cm^{-1}, corresponding to production of CO_2/TiO_2, is observed to increase. At 120 K, the CO_2 product is captured on the catalyst surface. The CO/Au^0 and CO/$Au^{\delta+}$ bands are slightly blue shifted during the reaction, indicating partial charge transfer by adsorbed oxygen atoms at 120 K. However, these CO/Au^0 and CO/$Au^{\delta+}$ species are not significantly consumed during the CO oxidation reaction due to their limited diffusional motion on Au sites at such low temperature.[7] This small blue shift disappears upon evacuation of O_2 and readsorption of CO at 120 K. The main kinetic difference in the two experiments in Figure 3.6 is the decrease of the rate of CO/TiO_2 consumption (as well as CO_2/TiO_2 generation) on the fully oxidized $Au^{\delta+}/TiO_2$ catalyst. In 1200 s at 120 K, the CO/TiO_2 oxidation reaction is complete on the fully reduced Au^0/TiO_2 catalyst (Figure 3.6a), while ∼20% of CO/TiO_2 remains on the $Au^{\delta+}/TiO_2$ catalyst (Figure 3.6b).

Kinetic plots of the CO/TiO_2 consumption on fully reduced and fully oxidized Au/TiO_2 are shown in Figure 3.7, where a reversibility test for the catalyst during multiple reduction/oxidation cycles is also shown. The CO/TiO_2 oxidation reaction follows accurate first-order kinetics in CO coverage in both cases, indicated by the fitted solid lines in Figure 3.7. The catalyst performance is reproducible for the mild oxidation–reduction cycles used in this study. The first-order CO oxidation rate constant at 120 K is ∼22 times larger on the fully reduced Au^0/TiO_2 catalyst compared to the $Au^{\delta+}/TiO_2$ catalyst, indicating an inhibition effect associated with formation of Au$^{\delta+}$ species. A similar reduction in the CO oxidation rate was also reported on a O_2-treated Au/SiO_2 catalyst working at room temperature.[58] It is noteworthy that the inhibition on Au$^{\delta+}$/TiO_2 is detected by the decrease of the rate of consumption of the CO/TiO_2 species, which is the only participant for CO oxidation at 120 K, showing again the unique activity of dual-catalyst sites at the Au perimeter for CO/TiO_2 oxidation on the Au/TiO_2 catalyst. As shown previously[7] and below, these sites involve Au and Ti centers, which have a special capability to activate molecular O_2 at the perimeter of Au nanoparticles on TiO_2.

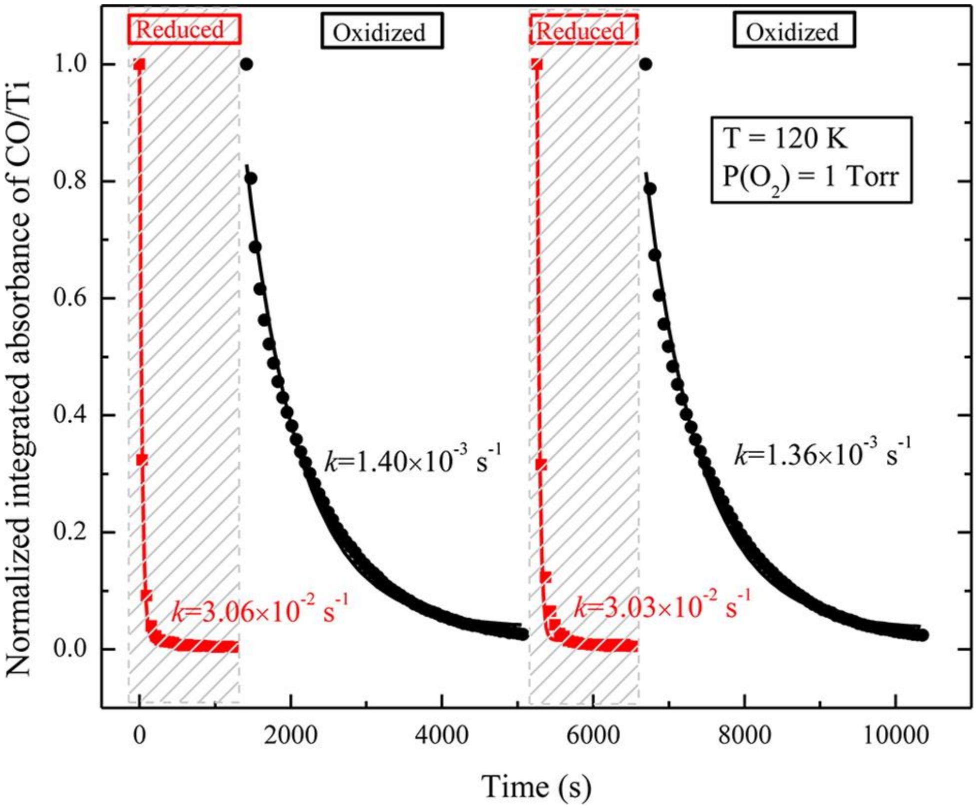

Figure 3.7 Representative kinetic plots of the CO/TiO_2 oxidation process on the fully reduced Au^0/TiO_2 catalyst (red, corresponding to Figure 3.5a) and fully oxidized Au$^{\delta+}$/TiO_2 catalyst (black, corresponding to Figure 3.5b). Solid lines represent the first-order kinetics fit for the experimental data.

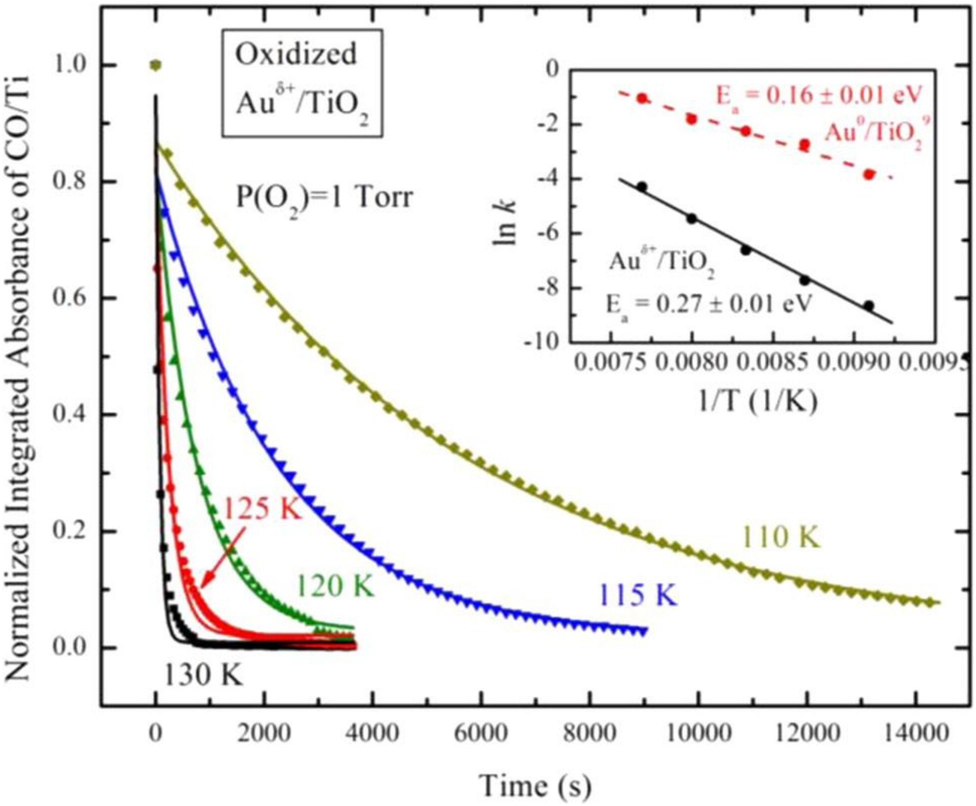

Figure 3.8 Plots of the integrated absorbance of CO/TiO_2 against time during reaction with O_2 at various temperatures fitted to first-order kinetics. (Inset) Arrhenius plot comparing activation energies on Au^0/TiO_2 (red) and $Au^{\delta+}/TiO_2$ (black). Data for Au^0/TiO_2 was taken from ref [7].

Previously we reported the apparent activation energy for CO oxidation on the Au^0/TiO_2 catalyst to be 0.16 ± 0.01 eV.[7] For comparison we carried out a study of the effect of temperature on the CO/TiO_2 oxidation on the fully oxidized $Au^{\delta+}/TiO_2$ catalyst in the temperature range of 110–130 K as shown in Figure 3.8. The resulting apparent activation energy for oxidation of CO/TiO_2 was found to be 0.27 ± 0.01 eV (Figure 3.8 inset), which is a near doubling of apparent activation energy. The ratio of preexponential factors, $A_{ox}/A_{red} \approx 103$, indicates that the O inhibition of Au catalytic activity is likely not due to site blocking by adsorbed O atoms. We postulated previously that the lower activation energy process measured for CO oxidation over the Au^0/TiO_2 catalyst may be heavily influenced by the CO/TiO_2 species' diffusion energy across the TiO_2 surface.[7] The large difference in the pre-exponential factors therefore may indicate that the two Arrhenius plots are likely describing processes that differ in mechanism and activation entropy, where CO oxidation on $Au^{\delta+}$ sites is entropically more favorable. It is worth noting that working at low temperatures is important to see the reduction of catalytic activity associated with the presence of the $Au^{\delta+}$ site. At elevated temperatures near room temperature inhibition by chemisorbed oxygen will not be observed as the CO can migrate to the oxidized Au site and easily reduce it (Figure 3.5).

Density functional theory (DFT) calculations provided detailed insight into the mechanism for CO oxidation at the dual-catalytic sites of the Au^0/TiO_2 perimeter.[7] We carry out similar calculations herein to follow the influence of partially oxidized Au on the oxidation of CO at the dual Au/TiO_2 sites using the same Au/TiO_2 interface model presented in the literature. A detailed charge analysis of the Au sites on the fully reduced Au/TiO_2 surface shows that all of the surface Au atoms are neutral, except for those that are in direct contact with the bridge oxygen atoms of the TiO_2 support which have a charge of ca. +0.1 e.

Some previous theoretical studies have suggested the importance of $Au^{\delta+}$ for CO oxidation on the Au/TiO_2 catalyst.[26-28,30,49] The models that were used examined only the influence of charge transfer between the TiO_2 support and the Au nanoparticles. There are no studies, however, of which we are aware that examine the influence of the preoxidation of Au nanoparticles by chemisorbed oxygen on Au/TiO_2 catalysts. These sites involving chemisorbed oxygen, however, are more likely to be the relevant sites associated with the inhibition phenomena that occur at O_2-rich conditions. We start by examining the Au sites where direct O_2 activation most likely proceeds. Green *et al*. showed previously that O_2 preferentially adsorbs at the perimeter sites along the Au/TiO_2 interface where it is partially activated by its interaction with the Au, thus forming a Ti–O–O–Au, peroxo-type intermediate.[7] Direct activation of O_2 at these perimeter sites, where no assistance by other molecules is involved, proceeds with a barrier of 0.4–0.6 eV (Figure 3.9), resulting in production of O adatoms at the Au perimeter. Once formed, these O adatoms can diffuse to Au sites that are further removed from the perimeter as shown in Figure 3.10. The favorable binding sites for these atomic O species is either on a FCC 3-fold hollow or on the edge bridge site. The binding energies for these chemisorbed O adatoms are from −0.3 to −0.4 eV with respect to one-half of the O_2 molecule in the gas phase, indicating that the O_2 dissociative adsorption is exothermic and chemisorbed O adatoms resulting from O_2 dissociation are stable. The higher activation barriers for O surface diffusion on Au are consistent with the fact that these sites form only at higher preoxidation temperatures (≥295 K). These O adatoms inductively increase the positive charge of the neighboring Au atoms as shown in Figure 3.10 ($Au^{\delta+}$, $\delta = 0.1$–0.3) and directly influence the vibrational frequency of CO adsorbed on these electropositive Au sites. The vibrational frequency calculation results are reported in Figure 3.10. Calculated CO/$Au^{\delta+}$ frequencies reveal a blue shift of +14–23 cm^{-1} from CO/Au^0, which is in very good agreement with the +20 cm^{-1} shift observed experimentally (from ~2106 to ~2126 cm^{-1}, Figure 3.3).

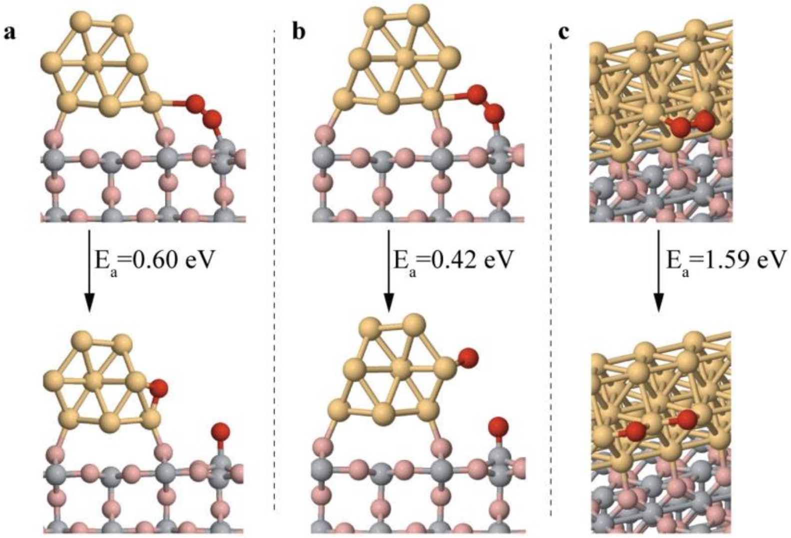

Figure 3.9 Calculated barrier for Au oxidation at different sites.

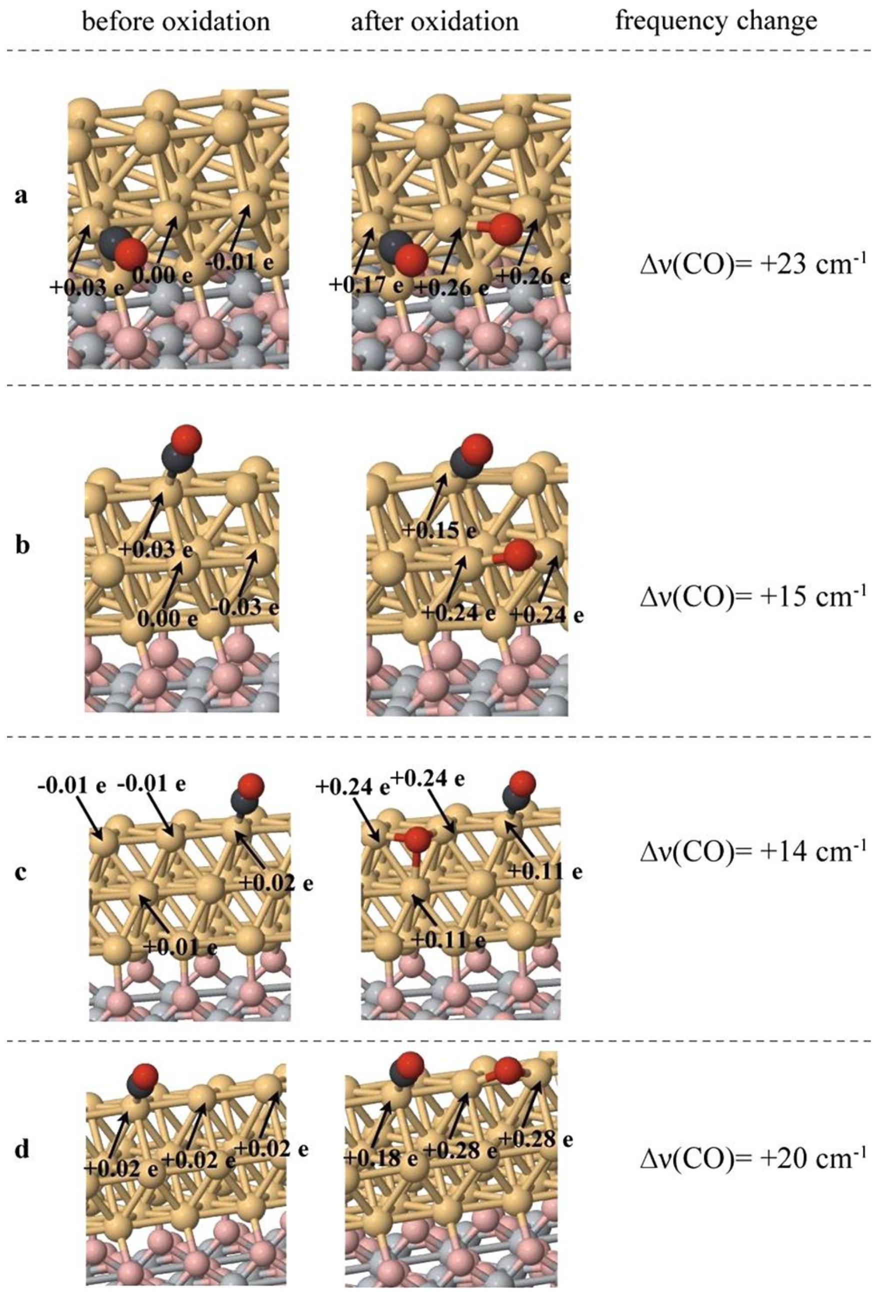

Figure 3.10 Theoretical predictions of the CO vibrational frequency change before and after oxidation. (a–d) Different CO and O adsorption configurations on the Au nanorod.

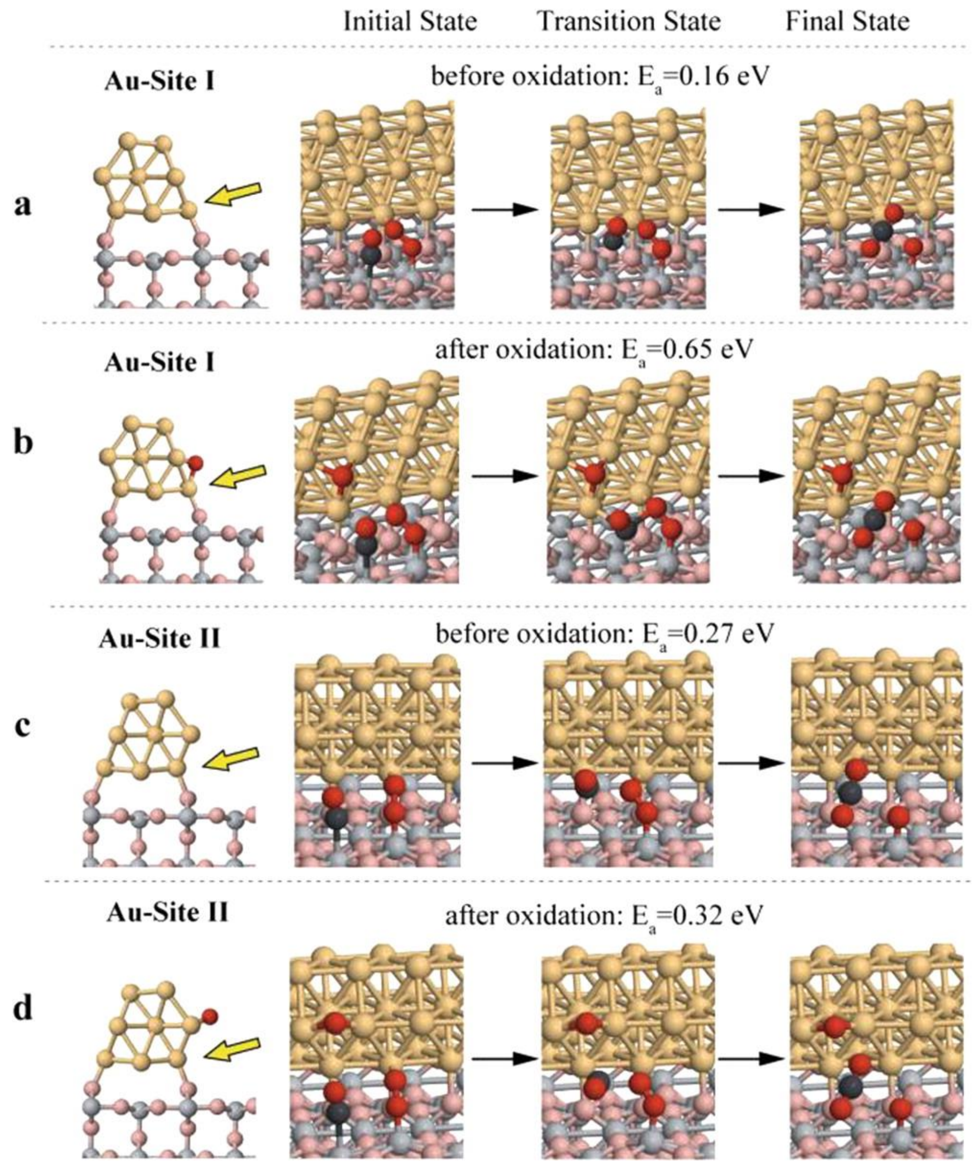

Figure 3.11 Oxygen inhibition effect for O–O bond scission at the Au/TiO_2 perimeter from DFT calculation. (a and b) CO-assisted O_2 dissociation at Au-Site I (a) before and (b) after Au oxidation by an O adatom. (c and d) CO-assisted O_2 dissociation at Au-Site II (a) before and (b) after Au oxidation by an O adatom.

CO oxidation at the Au^0/TiO_2 perimeter was found to follow a path where molecular O_2 is activated in the presence of a nearby CO molecule at a dual-catalytic site via a Au–O–O–Ti precursor.[7,21,26] We examine the two characteristically different perimeter sites, present in our model as shown in Figure 3.11, which reveal the differences that result from the different coordination numbers (CN) of the Au atoms that bind to the TiO_2 support. The first site (site I,

Figure 3.11a) involves a more coordinatively unsaturated Au atom (CN = 6) and is anchored to the support by a TiO_2-bridging oxygen atom. The second site (site II, Figure 3.11c) involves a Au atom with CN = 7 which also interacts with a TiO_2-bridging oxygen atom. The different coordination numbers at these sites provide insights into the behavior of Au atoms with different coordination numbers in contact with the TiO_2 support of actual catalysts. When the Au was not oxidized, the activation energies calculated for the O–O bond scission (assisted by CO at the perimeter) are 0.16 (site I) and 0.27 eV (site II), as shown in Figure 3.11a and 3.11c. The lower barrier for CO oxidation reported at site I is the result of the less-coordinatively saturated Au atom[59] in site I, strongly stabilizing the terminal O of O_2 on TiO_2. Similarly, the higher barrier for CO oxidation at site II, compared to site I, is due to the weaker interaction of Au with O_2 that arises from the increased CN of the Au atom at site II over that at site I. In this case, for the reduced Au^0/TiO_2 catalyst, CO oxidation can proceed at either site at 120 K, with site I being kinetically dominant. The presence of partially oxidized Au atoms that result upon formation of chemisorbed oxygen atoms reduces the ability of $Au^{\delta+}$ to stabilize the CO–O_2 formation in the transition state upon reaction with CO, thus increasing the activation barrier (Figure 3.11b and 3.11d). The CO oxidation activation barrier for $Au^{\delta+}$ at site I is now markedly higher at 0.65 eV as shown in Figure 3.11b. The activation barrier for site II shown in Figure 3.11d is only 0.32 eV. This significant activation barrier increase at site I is the result of the much stronger binding of the chemisorbed oxygen atom due to the lower CN of Au at site I (CN = 6) than at site II (CN = 7). The strong chemisorption of atomic oxygen at site I prohibits site I from carrying out catalytic oxidation, whereas site II can still catalyze CO oxidation at temperatures in the range 110–130 K. Since the preoxidation of the Au/TiO_2 catalyst was performed in 5 Torr of O_2 at elevated temperature (473 K), it is reasonable to assume the majority of perimeter sites are covered with O adatoms after oxidation. In fact, based on the changes in CO/Au^0 and CO/$Au^{\delta+}$ absorbance in Figure 3.5, about 60% of the Au^0 sites on the surface of the Au nanoparticles become $Au^{\delta+}$ sites for the particular size distribution of the Au nanoparticles used in the experiment. As a result, Au–Site I is poisoned whereas Au–Site II becomes the most active site for CO oxidation at low temperatures. Reaction of CO with the first oxygen of O_2 at Au–Site II results in formation of CO_2 and an O adatom on the TiO_2 perimeter. This bound oxygen atom reacts with a second CO molecule on the TiO_2 support to form CO_2 with a barrier of only ~0.1 eV to regenerate the active site.

The result from the theoretical simulations is that formation of strongly chemisorbed oxygen bound to coordinatively unsaturated Au atoms inhibits these sites for low-temperature CO oxidation. The more coordinatively saturated Au atoms associated with bound oxygen atoms can still oxidize CO, but the barrier is increased to 0.32 eV, which is consistent with the experimentally observed inhibition of the Au/TiO_2 catalyst by preoxidation and agrees with the 0.27 eV measured apparent activation energy.

Preoxidation is carried out in a temperature range where Au-based catalytic reactions are usually performed (295–473 K). At these temperatures, $Au^{\delta+}$ species formed from oxygen chemisorption are likely to be involved. The apparent activation energy of 0.27 eV on the $Au^{\delta+}$/TiO_2 catalyst agrees with previously reported 0.2–0.3 eV activation energies for CO oxidation on Au/TiO_2 catalysts measured at higher temperatures (200–350 K).[60,61] While these partially oxidized sites demonstrate reactivity that is consistent with that reported over working catalysts, the higher temperature used here to activate O_2 also promotes diffusion of adsorbed atomic oxygen from the interface where it can react with CO on Au^0 sites. In our low-temperature experiments, the more active Au^0 metal sites at the Au perimeter are only present at temperatures below 200 K. This argument is confirmed by extension of the Arrhenius plots shown in the insert in Figure 3.8, where CO oxidation activity on the $Au^{\delta+}$ sites surpasses the Au^0 sites at 198 K. In the temperature range of $T > 198$ K, CO reacts with the O adatoms on the Au nanorod, constantly reducing the $Au^{\delta+}$ sites to Au^0 sites, and the activity increases above that observed when $Au^{\delta+}$ sites remain unreduced, below 147 K (Figure 3.5). The $Au^{\delta+}$ sites exhibit lower reactivity than Au^0 sites, which is consistent with the results from in situ X-ray absorption studies of CO oxidation over Au/TiO_2 catalysts at higher temperatures.[1,16,17,62,63]

3.4 Conclusion

The activity of Au catalytic sites located at the boundary between Au nanoparticles and a TiO_2 support has been studied experimentally and theoretically in order to understand the influence of oxygen adsorption on the model low-temperature oxidation reaction, $CO + 1/2O_2 \rightarrow CO_2$. As on the reduced Au/TiO_2 catalyst, CO is found to be supplied from TiO_2 sites surrounding the preoxidized Au nanoparticles at catalytic reaction temperatures near 120 K, confirming the general picture of catalytic activity at the nanoparticle perimeter. It is found that on the oxygen-treated catalyst the reaction rate is considerably reduced and the activation energy is nearly doubled by electronic effects which involve induction of positive charge into the perimeter Au atoms by O atom adsorption. Activation of O_2 on the inhibited $Au^{\delta+}$ catalyst is assisted by a neighboring CO molecule at low temperatures. The ability of the catalyst to activate molecular O_2 at dual-perimeter sites involving $Au^{\delta+}$ atoms and neighbor Ti^{4+} ions in the support is retarded significantly for the CN = 6 $Au^{\delta+}$ atoms, causing the catalytic site to shift to the CN = 7 $Au^{\delta+}$ sites. It is likely that the higher temperature and higher O_2 pressure regimes for CO oxidation involve these $Au^{\delta+}$ perimeter sites, where oxidation of Au^0 to $Au^{\delta+}$ by O_2 and reduction of $Au^{\delta+}$ to Au^0 by CO occur constantly.

References

1. Kung, M. C.; Davis, R. J.; Kung, H. H. Understanding Au-catalyzed low-temperature CO oxidation. *Journal of Physical Chemistry C* **2007**, *111*, 11767-11775.

2. Widmann, D.; Behm, R. J. Active Oxygen on a Au/TiO_2 Catalyst: Formation, Stability, and CO Oxidation Activity. *Angewandte Chemie International Edition* **2011**, *50*, 10241-10245.

3. Chen, M.; Goodman, D. The structure of catalytically active gold on titania. *Science* **2004**, *306*, 252-255.

4. Kotobuki, M.; Leppelt, R.; Hansgen, D.; Widmann, D.; Behm, R. Reactive oxygen on a Au/TiO_2 supported catalyst. *Journal of Catalysis* **2009**, *264*, 67-76.

5. Laursen, S.; Linic, S. Geometric and electronic characteristics of active sites on TiO_2-supported Au nano-catalysts: insights from first principles. *Physical Chemistry Chemical Physics* **2009**, *11*, 11006-11012.

6. Wang, J.; Hammer, B. Oxidation state of oxide supported nanometric gold. *Topics in Catalysis* **2007**, *44*, 49-56.

7. Green, I. X.; Tang, W.; Neurock, M.; Yates, Jr., J. T. Spectroscopic observation of dual catalytic sites during oxidation of CO on a Au/TiO_2 catalyst. *Science* **2011**, *333*, 736-739.

8. Green, I. X.; Tang, W.; Neurock, M.; Yates, Jr., J. T. Low-Temperature Catalytic H_2 Oxidation over Au Nanoparticle/TiO_2 Dual Perimeter Sites. *Angewandte Chemie International Edition* **2011**, *50*, 10186-10189.

9. Yan, Z.; Chinta, S.; Mohamed, A. A.; Fackler, J. P.; Goodman, D. W. The role of F-centers in catalysis by Au supported on MgO. *Journal of the American Chemical Society* **2005**, *127*, 1604-1605.

10. Sanchez, A.; Abbet, S.; Heiz, U.; Schneider, W.; Häkkinen, H.; Barnett, R.; Landman, U. When gold is not noble: nanoscale gold catalysts. *The Journal of Physical Chemistry A* **1999**, *103*, 9573-9578.

11. Vijay, A.; Mills, G.; Metiu, H. Adsorption of gold on stoichiometric and reduced rutile TiO_2 (110) surfaces. *Journal of Chemical Physics* **2003**, *118*, 6536-6551.

12. Fu, Q.; Saltsburg, H.; Flytzani-Stephanopoulos, M. Active nonmetallic Au and Pt species on ceria-based water-gas shift catalysts. *Science* **2003**, *301*, 935-938.

13. Fierro-Gonzalez, J. C.; Gates, B. C. Catalysis by gold dispersed on supports: The importance of cationic gold. *Chemical Society Reviews* **2008**, *37*, 2127-2134.

14. Frondelius, P.; Häkkinen, H.; Honkala, K. Formation of gold (I) edge oxide at flat gold nanoclusters on an ultrathin MgO film under ambient conditions. *Angewandte Chemie* **2010**, *122*, 8085-8088.

15. Venezia, A. M.; Pantaleo, G.; Longo, A.; Di Carlo, G.; Casaletto, M. P.; Liotta, F. L.; Deganello, G. Relationship between structure and CO oxidation activity of ceria-supported gold catalysts. *The Journal of Physical Chemistry B* **2005**, *109*, 2821-2827.

16. Calla, J. T.; Bore, M. T.; Datye, A. K.; Davis, R. J. Effect of alumina and titania on the oxidation of CO over Au nanoparticles evaluated by ^{13}C isotopic transient analysis. *Journal of Catalysis* **2006**, *238*, 458-467.

17. Calla, J. T.; Davis, R. J. X-ray absorption spectroscopy and CO oxidation activity of Au/Al_2O_3 treated with NaCN. *Catalysis letters* **2005**, *99*, 21-26.

18. Laursen, S.; Linic, S. Oxidation catalysis by oxide-supported Au nanostructures: The role of supports and the effect of external conditions. *Physical Review Letters* **2006**, *97*, 026101.

19. Molina, L.; Hammer, B. Some recent theoretical advances in the understanding of the catalytic activity of Au. *Applied Catalysis A: General* **2005**, *291*, 21-31.

20. Vilhelmsen, L. B.; Hammer, B. Systematic Study of Au_6 to Au_{12} Gold Clusters on MgO (100) F Centers Using Density-Functional Theory. *Physical Review Letters* **2012**, *108*, 126101.

21. Liu, Z.; Hu, P.; Alavi, A. Catalytic role of gold in gold-based catalysts: a density functional theory study on the CO oxidation on gold. *Journal of the American Chemical Society* **2002**, *124*, 14770-14779.

22. Okazaki, K.; Morikawa, Y.; Tanaka, S.; Tanaka, K.; Kohyama, M. Electronic structures of Au on TiO_2(110) by first-principles calculations. *Physical Review B* **2004**, *69*, 235404.

23. Madsen, G. K.; Hammer, B. Effect of subsurface Ti-interstitials on the bonding of small gold clusters on rutile TiO_2(110). *Journal of Chemical Physics* **2009**, *130*, 044704.

24. Okumura, M.; Kitagawa, Y.; Haruta, M.; Yamaguchi, K. The interaction of neutral and charged Au clusters with O_2, CO and H_2. *Applied Catalysis A: General* **2005**, *291*, 37-44.

25. Okumura, M.; Kitagawa, Y.; Haruta, M.; Yamaguchi, K. DFT studies of interaction between O_2 and Au clusters. The role of anionic surface Au atoms on Au clusters for catalyzed oxygenation. *Chemical Physics Letters* **2001**, *346*, 163-168.

26. Molina, L.; Rasmussen, M.; Hammer, B. Adsorption of O_2 and oxidation of CO at Au nanoparticles supported by TiO_2(110). *Journal of Chemical Physics* **2004**, *120*, 7673-7680.

27. Wang, J.; Hammer, B. Role of Au^+ in Supporting and Activating Au_7 on TiO_2(110). *Physical Review Letters* **2006**, *97*, 136107.

28. Liu, Z.; Gong, X.; Kohanoff, J.; Sanchez, C.; Hu, P. Catalytic Role of Metal Oxides in Gold-Based Catalysts: A First Principles Study of CO Oxidation on TiO_2 Supported Au. *Physical Review Letters* **2003**, *91*, 266102.

29. Boronat, M.; Concepción, P.; Corma, A. Unravelling the nature of gold surface sites by combining IR spectroscopy and DFT calculations. Implications in catalysis. *The Journal of Physical Chemistry C* **2009**, *113*, 16772-16784.

30. Chrétien, S.; Metiu, H. O_2 evolution on a clean partially reduced rutile TiO_2(110) surface and on the same surface precovered with Au_1 and Au_2: The importance of spin conservation. *Journal of Chemical Physics* **2008**, *129*, 074705.

31. Remediakis, I. N.; Lopez, N.; Nørskov, J. K. CO oxidation on gold nanoparticles: Theoretical studies. *Applied Catalysis A: General* **2005**, *291*, 13-20.

32. Tang, D.; Hu, C. DFT insight into CO oxidation catalyzed by gold nanoclusters: charge effect and multi-state reactivity. *The Journal of Physical Chemistry Letters* **2011**, *2*, 2972-2977.

33. van Bokhoven, J. A.; Louis, C.; Miller, J. T.; Tromp, M.; Safonova, O. V.; Glatzel, P. Activation of Oxygen on Gold/Alumina Catalysts: In Situ High-Energy-Resolution Fluorescence and Time-Resolved X-ray Spectroscopy. *Angewandte Chemie* **2006**, *118*, 4767-4770.

34. Li, M.; Wu, Z.; Ma, Z.; Schwartz, V.; Mullins, D. R.; Dai, S.; Overbury, S. H. CO oxidation on Au/$FePO_4$ catalyst: Reaction pathways and nature of Au sites. *Journal of Catalysis* **2009**, *266*, 98-105.

35. Minico, S.; Scire, S.; Crisafulli, C.; Visco, A.; Galvagno, S. FT-IR study of Au/Fe_2O_3 catalysts for CO oxidation at low temperature. *Catalysis letters* **1997**, *47*, 273-276.

36. Dekkers, M.; Lippits, M.; Nieuwenhuys, B. CO adsorption and oxidation on Au/TiO_2. *Catalysis letters* **1998**, *56*, 195-197.

37. Green, I. X.; Tang, W.; McEntee, M.; Neurock, M.; Yates, Jr., J. T. Inhibition at Perimeter Sites of Au/TiO_2 Oxidation Catalyst by Reactant Oxygen. *Journal of the American Chemical Society* **2012**, *134*, 12717-12723.

38. Lee, I.; Joo, J. B.; Yin, Y.; Zaera, F. A yolk@shell nanoarchitecture for Au/TiO_2 catalysts. *Angewandte Chemie* **2011**, *123*, 10390-10393.

39. Zanella, R.; Giorgio, S.; Henry, C. R.; Louis, C. Alternative methods for the preparation of gold nanoparticles supported on TiO_2. *Journal of Physical Chemistry B* **2002**, *106*, 7634-7642.

40. Kresse, G. Dissociation and sticking of H_2 on the Ni(111),(100), and (110) substrate. *Physical Review B* **2000**, *62*, 8295.

41. Blöchl, P. E. Projector augmented-wave method. *Physical Review B* **1994**, *50*, 17953.

42. Kresse, G.; Joubert, D. From ultrasoft pseudopotentials to the projector augmented-wave method. *Physical Review B* **1999**, *59*, 1758.

43. Perdew, J. P.; Wang, Y. Accurate and simple analytic representation of the electron-gas correlation energy. *Physical Review B* **1992**, *45*, 13244.

44. Dudarev, S.; Botton, G.; Savrasov, S.; Humphreys, C.; Sutton, A. Electron-energy-loss spectra and the structural stability of nickel oxide: An LSDA+*U* study. *Physical Review B* **1998**, *57*, 1505.

45. Morgan, B. J.; Watson, G. W. A DFT + *U* description of oxygen vacancies at the TiO_2 rutile (110) surface. *Surface Science* **2007**, *601*, 5034-5041.

46. Monkhorst, H. J.; Pack, J. D. Special points for Brillouin-zone integrations. *Physical Review B* **1976**, *13*, 5188.

47. Henkelman, G.; Uberuaga, B. P.; Jónsson, H. A climbing image nudged elastic band method for finding saddle points and minimum energy paths. *Journal of Chemical Physics* **2000**, *113*, 9901-9904.

48. Henkelman, G.; Jónsson, H. A dimer method for finding saddle points on high dimensional potential surfaces using only first derivatives. *Journal of Chemical Physics* **1999**, *111*, 7010-7022.

49. Laursen, S.; Linic, S. Geometric and electronic characteristics of active sites on TiO_2-supported Au nano-catalysts: insights from first principles. *Physical Chemistry Chemical Physics* **2009**, *11*, 11006-11012.

50. Tang, W.; Sanville, E.; Henkelman, G. A grid-based Bader analysis algorithm without lattice bias. *Journal of Physics: Condensed Matter* **2009**, *21*, 084204.

51. Bader, R. F. *Atoms in Molecules: A Quantum Theory;* Oxford University Press: New York, **1990**.

52. Henao, J. D.; Caputo, T.; Yang, J. H.; Kung, M. C.; Kung, H. H. In situ transient FTIR and XANES studies of the evolution of surface species in CO oxidation on Au/TiO_2. *The Journal of Physical Chemistry B* **2006**, *110*, 8689-8700.

53. Carrettin, S.; Concepción, P.; Corma, A.; Lopez Nieto, J. M.; Puntes, V. F. Nanocrystalline CeO_2 increases the activity of Au for CO oxidation by two orders of magnitude. *Angewandte Chemie International Edition* **2004**, *43*, 2538-2540.

54. Chen, M.; Goodman, D. W. Catalytically active gold: from nanoparticles to ultrathin films. *Accounts of Chemical Research* **2006**, *39*, 739-746.

55. Hao, Y.; Mihaylov, M.; Ivanova, E.; Hadjiivanov, K.; Knözinger, H.; Gates, B. CO oxidation catalyzed by gold supported on MgO: Spectroscopic identification of carbonate-like species bonded to gold during catalyst deactivation. *Journal of Catalysis* **2009**, *261*, 137-149.

56. Mihaylov, M.; Knoezinger, H.; Hadjiivanov, K.; Gates, B. C. Characterization of the oxidation states of supported gold species by IR spectroscopy of adsorbed CO. *Chemie Ingenieur Technik* **2007**, *79*, 795-806.

57. Boccuzzi, F.; Chiorino, A.; Manzoli, M. FTIR study of the electronic effects of CO adsorbed on gold nanoparticles supported on titania. *Surface Science* **2000**, *454*, 942-946.

58. Wu, Z.; Zhou, S.; Zhu, H.; Dai, S.; Overbury, S. H. DRIFTS-QMS study of room temperature CO oxidation on Au/SiO_2 catalyst: Nature and role of different Au species. *The Journal of Physical Chemistry C* **2009**, *113*, 3726-3734.

59. Williams, W. D.; Shekhar, M.; Lee, W.; Kispersky, V.; Delgass, W. N.; Ribeiro, F. H.; Kim, S. M.; Stach, E. A.; Miller, J. T.; Allard, L. F. Metallic Corner Atoms in Gold Clusters Supported on Rutile Are the Dominant Active Site during Water− Gas Shift Catalysis. *Journal of the American Chemical Society* **2010**, *132*, 14018-14020.

60. Okumura, M.; Tsubota, S.; Haruta, M. Vital role of moisture in the catalytic activity of supported gold nanoparticles. *Angewandte Chemie International Edition* **2004**, *43*, 2129-2132.

61. Long, C. G.; Gilbertson, J. D.; Vijayaraghavan, G.; Stevenson, K. J.; Pursell, C. J.; Chandler, B. D. Kinetic Evaluation of Highly Active Supported Gold Catalysts Prepared from Monolayer-Protected Clusters: An Experimental Michaelis− Menten Approach for Determining the Oxygen Binding Constant during CO Oxidation Catalysis. *Journal of the American Chemical Society* **2008**, *130*, 10103-10115.

62. Weiher, N.; Bus, E.; Delannoy, L.; Louis, C.; Ramaker, D.; Miller, J.; Van Bokhoven, J. Structure and oxidation state of gold on different supports under various CO oxidation conditions. *Journal of Catalysis* **2006**, *240*, 100-107.

63. Schwartz, V.; Mullins, D. R.; Yan, W.; Chen, B.; Dai, S.; Overbury, S. H. XAS study of Au supported on TiO_2: Influence of oxidation state and particle size on catalytic activity. *The Journal of Physical Chemistry B* **2004**, *108*, 15782-15790.

Chapter 4: Direct Formation of Acetate from the Partial Oxidation of Ethylene on a Au/TiO_2 Catalyst

(modified from *Topics in Catalysis*, **2013**, 56 (15-17), pp 1512-1524)

4.1 Introduction

Acetic acid is an important industrial feedstock used in the commercial production of polymer precursors such as vinyl acetate and acetic anhydride, with a 2008 world capacity of over 10 million metric tons per year.[1] Most of the synthetic acetic acid is produced by methanol carbonylation ($CH_3OH + CO \rightarrow CH_3COOH$).[1,2] Although efficient, separating the acetic acid product from the liquid reaction mixture is a limitation to the process. Showa Denko K. K., a Japanese chemical company, developed and industrialized a gas-phase direct synthetic method to produce acetic acid from the oxidation of ethylene over a Pd based catalyst in the temperature range of 433–483 K, in 1997.[1,2] This process is environmentally friendlier than the carbonylation route as it involves only a single stage reaction and allows for easy separation of the product. Subsequent efforts in the literature examined other types of Pd catalysts which demonstrated good reactivity for ethylene (C_2H_4) partial oxidation to acetic acid (e.g. ~20 % ethylene conversion rate and 89 % acetic acid selectivity for a Pd supported on Mo–V–Nb/TiO_2 catalyst).[3-5]

The direct oxidation of ethylene to form acetic acid is also interesting scientifically as the elementary steps and their corresponding kinetics will likely provide mechanistic insights into other selective olefin oxidation reactions such as the epoxidation of propylene and ethylene, which typically proceed over supported Au and Ag particles, respectively.[6-8] The question “Why does the oxidation reaction stop at different points on different catalysts?” is an important and rich topic for research. Herein, we report on in situ FTIR observations and theoretical analyses for direct acetate production from ethylene oxidation on a Au/TiO_2 catalyst at temperatures as low as 370 K. There was no evidence for the formation of ethylene oxide either from high sensitivity in situ FTIR or from GC–MS measurements under our mild reaction conditions. The ketenylidene species, however, which is a side product from the partial oxidation of acetate is observed.[9,10] Detailed discussions on the discovery[9] of the ketenylidene intermediate from acetate partial oxidation on a Au/TiO_2 catalyst, as well as the proposed reaction paths,[10] have been previously published. A combination of in situ spectroscopy along with isotopic kinetic experiments and first principle density functional theory (DFT) calculations were used to elucidate the elementary steps and pathways involved in the partial oxidation of ethylene to adsorbed acetate and the lack of ethylene oxide production (Figure 4.1). To the best of our knowledge, this is the first report of direct acetate formation from ethylene oxidation over Au/TiO_2 catalysts.

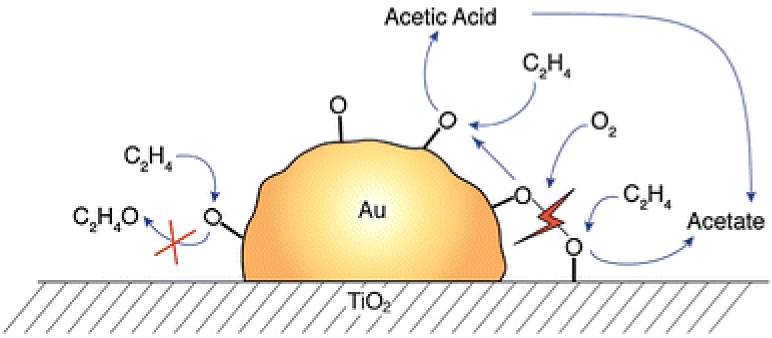

Figure 4.1 Schematic of the C_2H_4 oxidation reaction on Au/TiO_2.

4.2 Experimental Procedure

The experiments were carried out in a high vacuum transmission IR cell that has been described in detail previously,[11-13] combined with an external GC–MS analyzer. A more in depth description of some additional aspects of the experimental setup can be found in Chapter 2. A Au/SiO_2 sample with ~3 nm Au nanoparticle diameter was kindly donated by Dr. Zanella for a comparison study.[14] The catalysts were installed into the vacuum IR cell after synthesis and were activated in ~19 Torr O_2 at 473 K for 90 min before initial use.

To simulate the Au/TiO_2 catalyst, we built a model interface structure which involves a Au nano rod (3 atomic layers high and 3 atomic layers wide) covalently anchored to the bridging oxygen atoms on the surface of a rutile TiO_2(110) slab. All the calculations reported here were carried out using DFT methods and are explained in more detail in Chapter 3, Section 3.2.

4.3 Results and Discussion

4.3.1 FTIR Analysis of the Partial Oxidation of Ethylene to Acetate with GC–MS Analysis for Ethylene Oxide

Figure 4.2 shows the IR spectral development of adsorbed species on the Au/TiO_2 catalyst when it was exposed to a mixture of 0.5 Torr C_2H_4 and 0.5 Torr O_2 at 370 K. Partial oxidation products of ethylene begin to build up on the catalyst surface immediately. The assignments of the observed absorption bands are presented in Figure 4.2. Four bands at 2,985, ~1,520, 1,446, ~1,330 cm^{-1} for $\nu_s(CH_3)$, $\nu_{as}(CO_2)$, $\nu_s(CO_2)$, and $\delta(CH_3)$ respectively indicate the formation of acetate/TiO_2 species.[10,15-17] The gas phase contribution to the IR absorbance was subtracted from the spectra by studies of the gas phase IR background signals separately. No adsorbed ethylene feature was detected at 370 K. The careful comparison of the IR features of acetate adsorption on Au/TiO_2, TiO_2, and Au/SiO_2 under the same conditions, as shown in Figure 4.3, indicates that the acetate species is adsorbed only on the TiO_2 sites as the same characteristic features for acetate on Au/TiO_2 (~1,532, ~1,454, and ~1,338 cm^{-1}) arise in the spectra on TiO_2 but are absent on Au/SiO_2.[10] No partial oxidation products from ethylene were observed on the blank TiO_2 catalyst or on the Au/SiO_2 sample, indicating that the joint presentation of Au and TiO_2 sites is necessary for the partial oxidation of ethylene to form acetate/TiO_2.

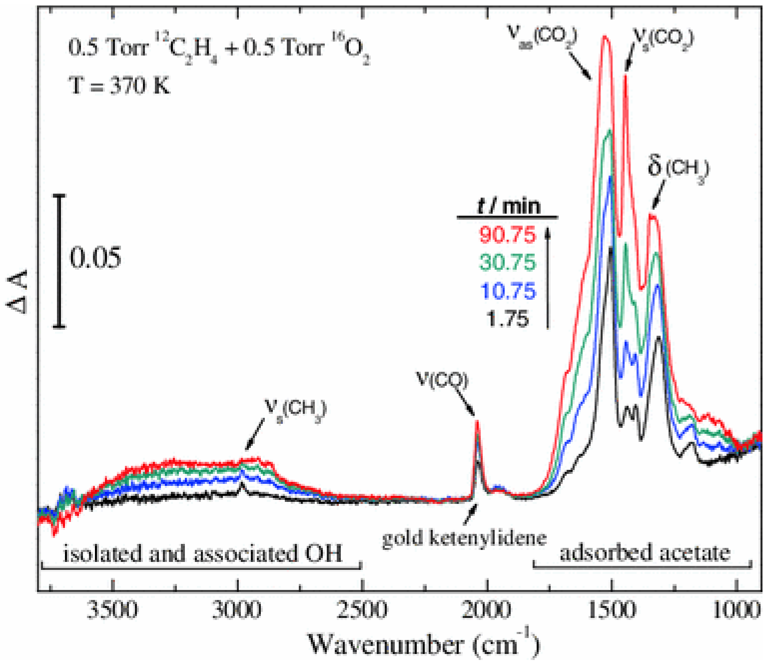

Figure 4.2 IR spectra of C_2H_4 partial oxidation at 370 K, after the reaction has occurred for 1.75 (black curve), 10.75 (dark blue curve), 30.75 (light blue curve), and 90.75 (red curve) minutes.

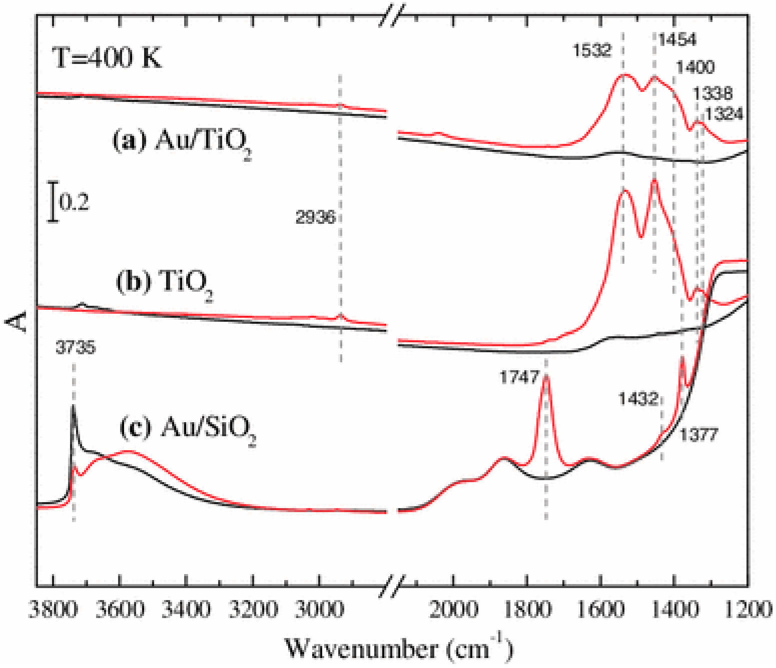

Figure 4.3 IR spectra of acetic acid dissociative adsorption forming acetate on (a). Au/TiO_2; (b). TiO_2; and (c). Au/SiO_2. Black spectra are taken from the clean catalyst surfaces and red spectra are taken from the corresponding catalyst surfaces after acetate formation

In Figure 4.2, the absorption band at 2,040 cm^{-1} is assigned to the υ(CO) vibrational mode of a gold ketenylidene species (Au_2=C=C=O), formed from acetate/TiO_2 partial oxidation at the Au–Ti^{4+} dual perimeter sites. The detailed experimental and theoretical results for the partial oxidation of acetic acid to form the gold ketenylidene intermediate at the Au/TiO_2 interface are reported in references [9,10].

An infrared search for adsorbed ethylene oxide in Figure 4.2 at ~3,016 cm^{-1} (ν(CH_2)) and at ~1,268 cm^{-1} (ring breathing mode) was unsuccessful. An external GC–MS was employed to analyze the gas phase reaction mixture. The GC–MS was calibrated using standard ethylene oxide solution. We determined the GC–MS detection limit to be equivalent to ~3 × 10^{15} ethylene oxide molecules produced in the gas phase in the cell volume. This detectability limit of ~3 × 10^{15} ethylene oxide molecules corresponds to only ~3 % of the perimeter sites around the Au nanoparticles in our Au/TiO_2 catalyst sample. Figure 4.4 shows the absence of detectable gas phase ethylene oxide production at 400 K after 6, 20, 40, 60, 80 and 90 min reaction time. No ethylene oxide was detected at this reaction temperature and up to 473 K. Surprisingly, no acetic acid was detected by the GC–MS either, at Au/TiO_2 temperatures up to 673 K, indicating the acetate/TiO_2 species is strongly bound to the catalyst surface. This is consistent with the IR observation that the acetate/TiO_2 formation slows down and eventually stops, probably because the partial oxidation product blocks dual perimeter Au–Ti^{4+} active sites.

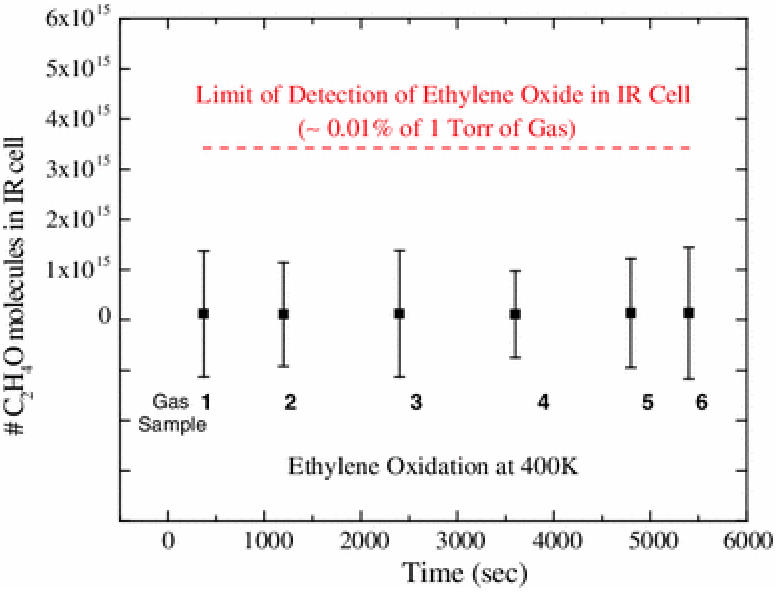

Figure 4.4 GC–MS measurements of ethylene oxide production from ethylene oxidation on Au/TiO_2 at 400 K at P_{O_2}= 0.5 Torr and $P_{C_2H_4}$= 0.5 Torr after: (1). 6 min; (2). 20 min; (3). 40 min; (4). 60 min; (5). 80 min and (6). 90 min. The red dotted line indicates the realistic limit of detection of ethylene oxide molecules in the gas phase in the IR cell, as determined by investigations of standard solutions. The error bars are the GC–MS noise measurements for each gas sample.

4.3.2 Density Functional Theory Simulations of Oxygen Adsorption, Ethylene Adsorption, Acetate Formation

Despite its potential industrial importance and previous studies for olefin epoxidation on Au surfaces and related catalytic systems,[18-23] there are no reported mechanistic studies on the partial oxidation of ethylene to acetic acid over Au/TiO_2 catalysts. Theory was used herein to examine the different elementary steps that may be involved in the oxidation of ethylene at the Au–Ti^{4+} dual perimeter sites as well as at the Au sites. It is currently intractable to model all of the possible sites, intermediates and pathways that may be involved. We have therefore chosen what appear to be possible sites at the Au/TiO_2 interface and steps that may be plausible for the mechanism to proceed. We explicitly try to compare the reaction paths, which occur at both of the interfacial Ti^{4+} and Au sites.

We initially examined possible active sites for ethylene oxidation by calculating the adsorption of C_2H_4 at different sites at the Au/TiO_2 interface. The results indicate that while ethylene preferentially binds in a di-σ mode to the coordinatively unsaturated Au sites with CN = 7 and in a π mode to the Ti sites at the Au/TiO_2 interface, the adsorption is rather weak, with binding energies of −0.48 and −0.24 eV respectively. As a result, C_2H_4 is expected to have a high mobility on the Au/TiO_2 surface at 370 K through either diffusion or adsorption/desorption processes. This is consistent with the lack of C_2H_4 adsorption features observed experimentally by IR.

Previously, we showed that molecular oxygen preferentially adsorbs at the Au–Ti^{4+} dual perimeter sites on Au/TiO_2 to form a strongly coordinated Au–O–O–Ti complex which readily dissociates to form bound O atoms with activation energies of 0.4–0.6 eV, depending on the CN of the Au site (CN = 7 or 8). Oxygen can also be activated at interstitial-Ti defect sites that may form within the proximity of the Au/TiO_2 interface resulting in activation barriers of 0.4–0.6 eV.[24]

The resulting O atoms can diffuse on the Au and Ti sites at the Au/TiO_2 interface with activation barriers that range from 0.2–0.7 eV depending upon the specific nature of the sites involved (Ti vs. Au and the specific coordination number of Au).[25] Thus, under the reaction conditions (0.5 Torr O_2, 370 K), the Au/TiO_2 catalyst is expected to have a significant fraction of mobile O adatoms that can oxidize ethylene.

Theory was used herein to examine the different elementary steps involved in the oxidation of ethylene at the optimal Au–Ti^{4+} dual perimeter sites as well as at the Au sites. As O* binding energies are 4.05 and 4.49 eV on the Au–Au and Ti^{4+}–Au sites, we consider the partial oxidation reactions at both of these sites. The initial states, transition states, and final states for each of these elementary steps at the optimal Au–Ti^{4+} and Au sites are reported in Figures 4.5 and 4.6, respectively. The calculated reaction energies and activation barriers were used to determine the lowest energy paths for the oxidation of ethylene to adsorbed acetate over the active Au–Ti^{4+} sites and Au sites, as shown in the potential energy diagrams in Figure 4.7.

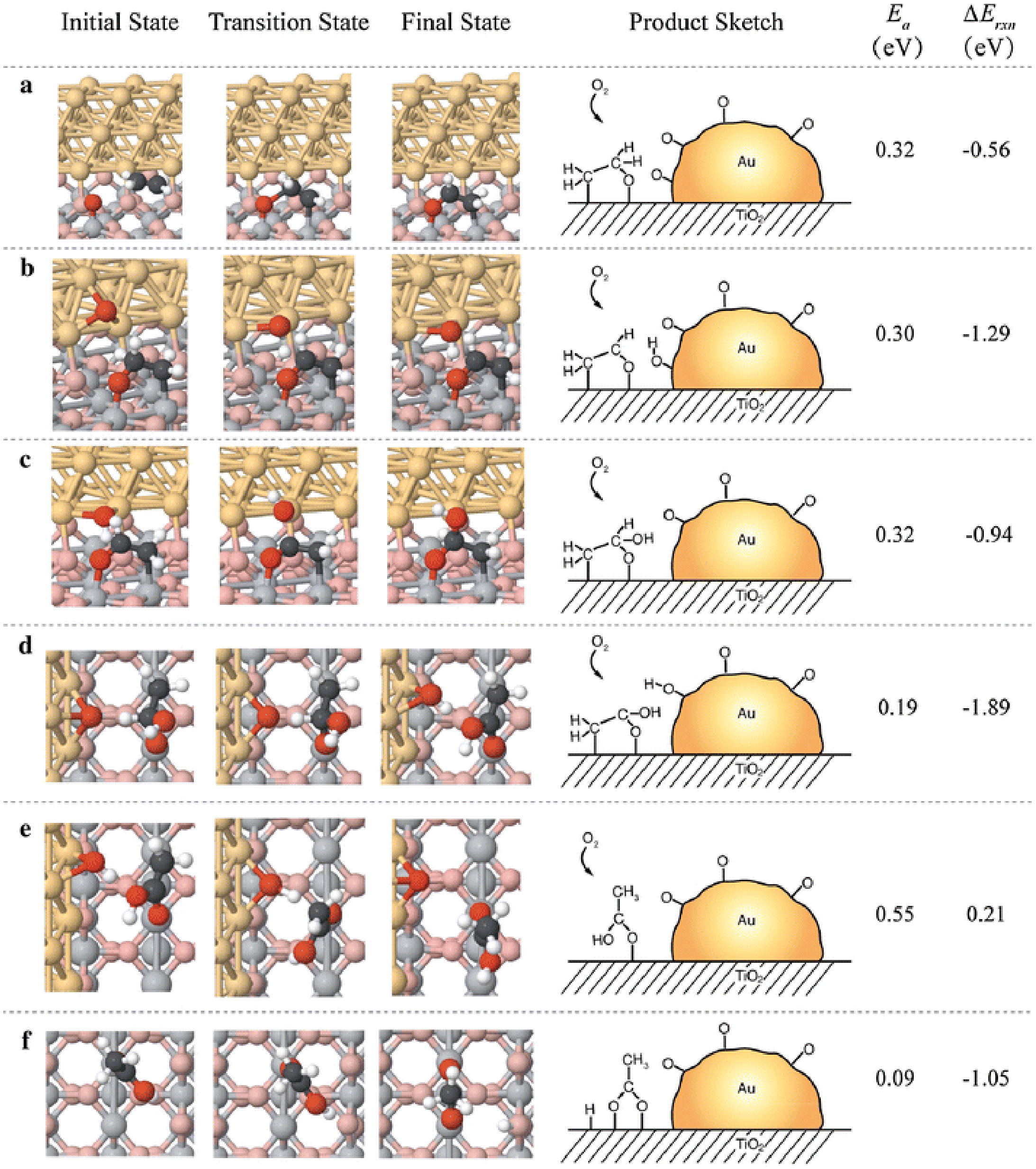

Figure 4.5 C_2H_4 oxidation to acetate at the Au perimeter. The Au atoms and Ti atoms are shown in yellow and grey respectively, whereas the O in the TiO_2 lattice, adsorbed O, C atoms and H atoms are shown in pink, red, black and white respectively. E_a and ΔE_{rxn} refer to the activation barrier and reaction energy for the elementary steps.

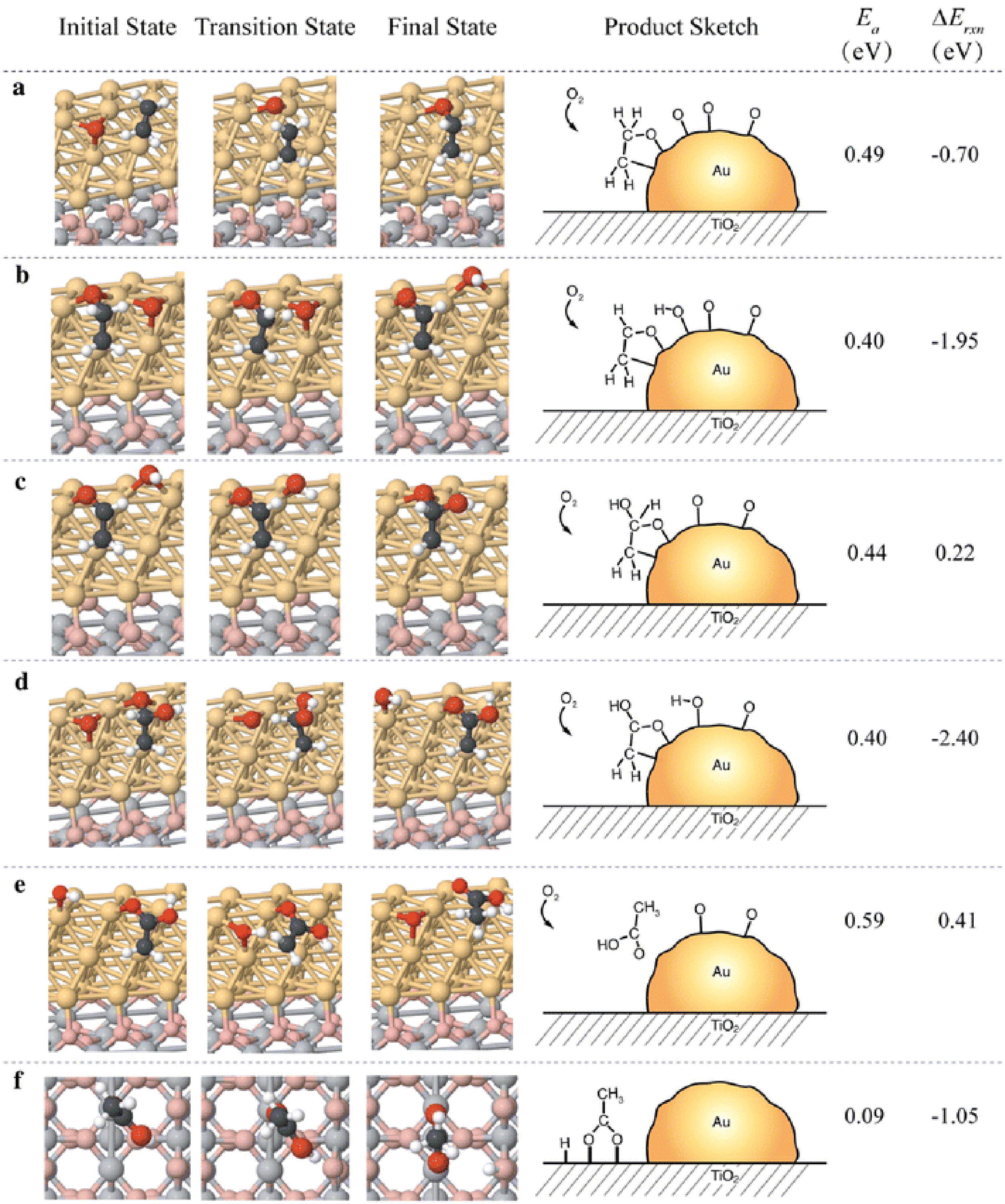

Figure 4.6 C_2H_4 oxidation to acetate on Au sites alone with the final acetate binding to TiO_2. The atom color codes are the same as in Figure 4.5.

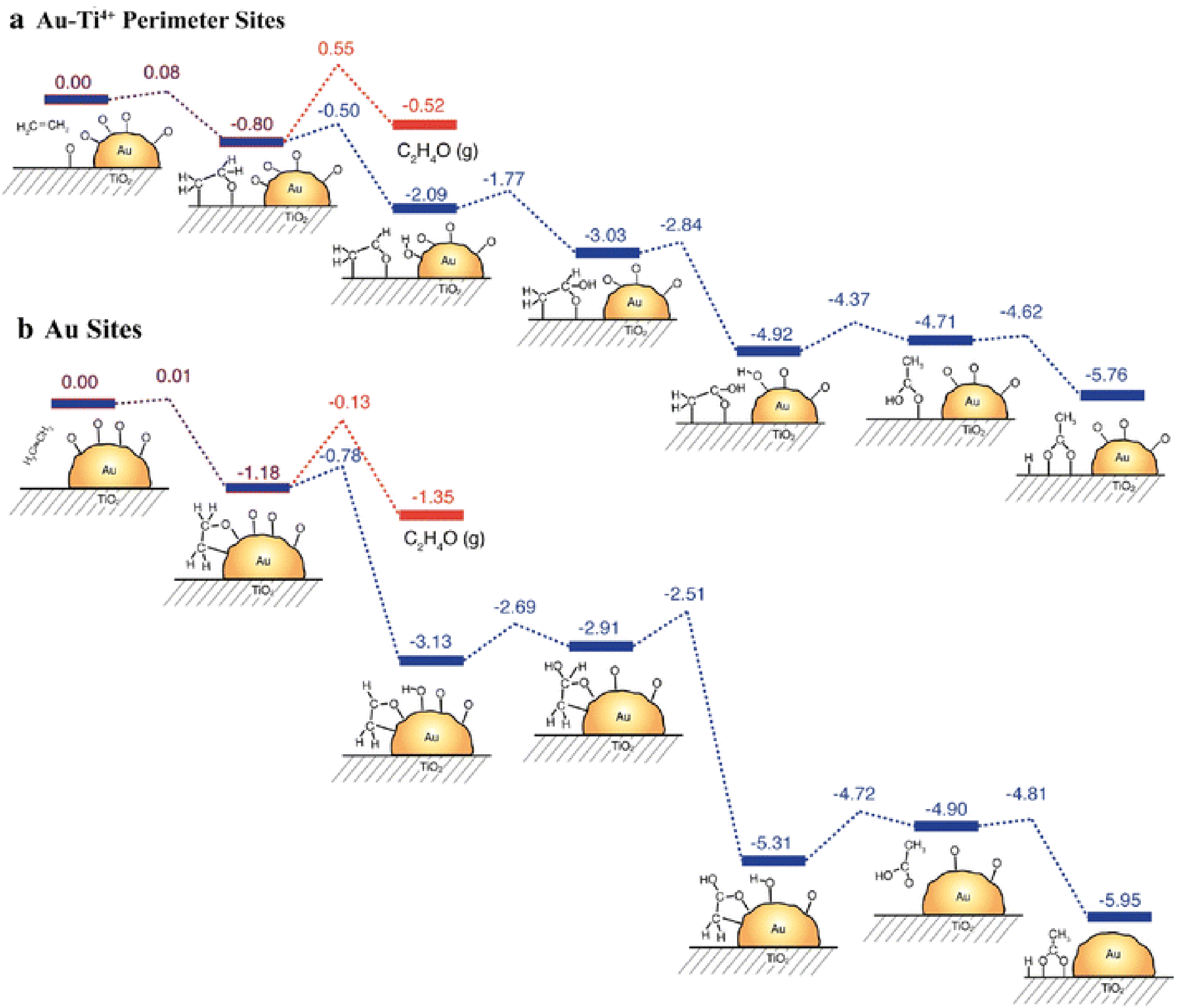

Figure 4.7 Potential energy diagrams for the formation of C_2H_4O and acetate, with respect to the gas phase ethylene. Numbers are in units of eV. Note that in both schemes, O_2 dissociation initially occurs at dual-perimeter sites.

As was reported in the previous section, ethylene weakly adsorbs at the interfacial Au (CN = 7) or the Ti^{4+} sites with adsorption energies of −0.48 and −0.24 eV, respectively. The ethylene that binds to the Ti can react with the active O atom at a vicinal Au–Ti^{4+} site to form the H_2C^*–CH_2O^* oxymetallacycle intermediate as shown in Figure 4.5a (where the * symbol here refers to the atoms in the adsorbate that bind to sites on the Au/TiO_2 surface). The barrier with respect to the gas phase ethylene is only 0.08 eV (and 0.32 eV measured with respect to the adsorbed state).

Ethylene that adsorbs on Au can similarly react with the active O atom on Au as is shown in Figure 4.6a to form the H_2C^*–CH_2O^* oxymetallacycle on the Au–Au site pair resulting in an activation barrier of only 0.01 eV measured with respect to the gas phase (and 0.49 eV with respect to the adsorbed ethylene state). The low barriers for the addition of oxygen to ethylene at both the Au–Ti^{4+} and Au sites reflect the weak binding of O to Au and the O basicity which thus allows it to readily carry out the nucelophilic attack on the ethylene. This is also consistent with previous findings concerning O addition to olefins.[19,22,26,27]

The second reactive O adatom can subsequently be used to activate the C–H bond of the bound CH_2O group of the $H_2C^*CH_2O^*$ oxymetallacycle bound to the Au–Ti^{4+} and Au–Au sites with activation barriers of 0.3 eV (Figure 4.5b) and 0.4 eV (Fig. 4.6b), respectively. This results in the formation of a $H_2C^*CHO^*$ intermediate bound to the surface, and an OH intermediate on Au. The OH* as well as O* that form on Au are weakly bound and thus rather basic.[28] As such, they can readily carry out nucleophilic attack at the unsaturated CH=O* group of the H_2C^*–CHO^* oxymetallacycle intermediate on Au and TiO_2 sites. The attack of OH* on the oxymetallacycle to form the H_2C^*–$CH(OH)O^*$ species involves activation barriers of only 0.32 eV at the Ti^{4+}–Au site (Figure 4.5c) and 0.44 eV at Au–Au sites (Fig. 4.6c). The barriers for the attack of O* are higher than that for OH* as O* is more strongly bound to Au and Ti^{4+}–Au sites.

Regardless of whether O* or OH* adds to the $H_2C^*CHO^*$ intermediate, one must ultimately add a hydrogen to the terminal CH_2 group to form CH_3. The H must initially come from ethylene as this is the only H source. As such the H can be formed by the activation of the C–H bond of one of the adsorbed $C_2H_xO_y^*$ surface intermediates by Au or by oxygen sites present at the Au/TiO_2 interface or by intramolecular hydrogen transfer. Since Au alone cannot activate C–H bonds, the hydrogen must come from either an intramolecular hydrogen transfer or via a sequential surface mediated deprotonation of $H_2C^*–CH(OH)O^*$ by O^* on Au or TiO_2 and subsequent re-protonation of $H_2C^*–C(OH)O$ to form $CH_3–C(OH)O^*$. The intramolecular transfer of the hydrogen from the CH(OH)O moiety of $H_2C^*–CH(OH)O^*$ to the terminal CH_2^* to form $CH_3–C(OH)O^*$ directly is shown in Eq. (4.1):

$$H_2C{*}-CH(OH)O{*} \rightarrow CH_3-C(OH)O{*} \qquad (4.1)$$

This reaction requires rather high barriers of 1.05 and 0.82 eV at the Ti^{4+}–Au and Au–Au sites, respectively. Such intramolecular transfer steps are not typically catalyzed by metal surfaces but instead proceed via separate C–H activation and H-addition steps at the Au/TiO_2 interface.

In the sequential path, the C–H bond of the CH(OH)O moiety on the $H_2C^*–CH(OH)O^*$ species is readily activated by the basic O^* species that is bound to Au, resulting in barriers of 0.19 and 0.40 eV for the reaction shown in Eq. (4.2):

$$H_2C{*}-CH(OH)O{*} + O-Au \rightarrow H_2C{*}-C(OH)O{*} + HO-Au \qquad (4.2)$$

Here where the $H_2C^*–CH(OH)O^*$ resides at the Ti^{4+}–Au and Au–Au sites, respectively (Figures 4.5d, 4.6d). The subsequent hydrogen addition step to the H_2C^* moiety of the bound $H_2C^*–C(OH)O^*$ intermediate proceeds via the reaction shown in Eq. (4.3):

$$H_2C{*}-C(OH)O{*} + HO-Au \rightarrow H_3C-C(OH)O{*} + O-Au \qquad (4.3)$$

The activation barriers for this step were calculated to be 0.55 and 0.59 eV for $H_2C^*–C(OH)O^*$ bound to the Ti^{4+}–Au and Au–Au sites, respectively (Figures 4.5e, 4.6e) suggesting that this step is rather difficult. The resulting acetic acid that forms at the interface readily reacts with the basic O sites on the TiO_2 surface to form the very stable bound acetate intermediate as the barrier is only 0.09 eV, as shown in Figures 4.5f and 4.6f.

The intrinsic activation barriers for all the surface processes described above range from 0.09 to 0.59 eV. The highest barriers appear to involve the protonation of the bound $H_2C^*–C(OH)O^*$

to form the stable acetate surface intermediate shown in Figures 4.5e and 4.6e with barriers of 0.55 and 0.59 eV at the Ti^{4+}–Au and Au–Au sites, respectively. These barriers are consistent with the fact that the ethylene partial oxidation reaction requires a temperature of 370 K to produce the acetate on the oxide. The results here suggest that the protonation of the $H_2C^*C(OH)O^*$ intermediate to produce the bound acetic acid may be the rate-determining step for Au/TiO_2 catalyzed C_2H_4 partial oxidation.

The theoretical results reported here over both Au–Ti^{4+} and Au–Au sites examine a specific sequence of pathways to form the acetate intermediate. While it is clear that the oxymetallacycle is formed, the subsequent C–H activation, H-addition and OH addition steps could occur with an interchange of C–H addition and C–H activation steps. Based on initial screening calculations as well as chemical insights, we chose what appeared to be the most feasible path but these steps could potentially proceed in a different order. While this would change the absolute values of the reported barriers, it should not influence the conclusions.

The DFT calculated potential energy profiles depicted in Figure 4.7 indicate that both the Au–Ti^{4+} as well as the Au–Au sites can effectively carry out the oxidation of ethylene to acetate provided that atomically adsorbed oxygen is present on Au. Green *et al*. have shown previously, however, that the barrier to activate O_2, even on unsaturated Au sites, is very high with activation energies of over 1 eV.[25] O_2 activation however can readily proceed at the dual Au–Ti^{4+} site to form oxygen adatoms that spill over onto the Au, as the barrier is only 0.4 eV. The results indicate that the dual Au–Ti^{4+} site is necessary to activate O_2 and that the reaction would not proceed on TiO_2 or Au/SiO_2 alone. This is consistent with the experimental results shown in Figure 4.3, which clearly reveal that only Au/TiO_2 is active in oxidation of ethylene. The Au–Ti^{4+} sites are thus essential as they produce the reactive O atoms that can subsequently react with ethylene to form acetate. The DFT results presented in Figure 4.7 indicate that the weakly held oxygen atoms that form at both the Au–Ti^{4+} and Au–Au sites are quite basic and readily undergo nucleophilic attack of the coadsorbed ethylene or carry out the activation of weakly acidic C–H bonds. The surface hydroxyl intermediates that form are also important in that they add to nucleophilic carbon centers and facilitate protonation and deprotonation reactions to form surface acetate intermediates. The potential energy surfaces for the ethylene oxidation over Au–Ti^{4+} and Au–Au sites reported in Figure 4.7 all appear to be quite favorable with respect to the gas phase ethylene.

4.3.3 Density Functional Theory Simulations of the Inhibition of Ethylene Oxide Formation

Theory was also used to help explain the lack of detection of ethylene oxide on the Au/TiO_2 catalyst or in the gas phase. The calculated reaction paths and resulting energy diagrams for ethylene oxide formation on Ti^{4+} and Au sites are shown in Figures 4.7 and 4.8. The reaction proceeds by the migration of chemisorbed ethylene up onto an adsorbed atomic oxygen bound to a vicinal Ti^{4+} or Au site to form the Au- and Ti^{4+}-epoxides shown in Figure 4.8 with barriers of 1.54 and 1.01 eV, respectively. The barriers for epoxidation over Ti^{4+} and Au result in pathways that are considerably higher in energy (red paths in Figure 4.7) than the corresponding oxidation paths (blue paths in Figure 4.7) that lead to acetate. The results help to show that epoxidation is unlikely compared to acetate formation on Au/TiO_2 catalysts.

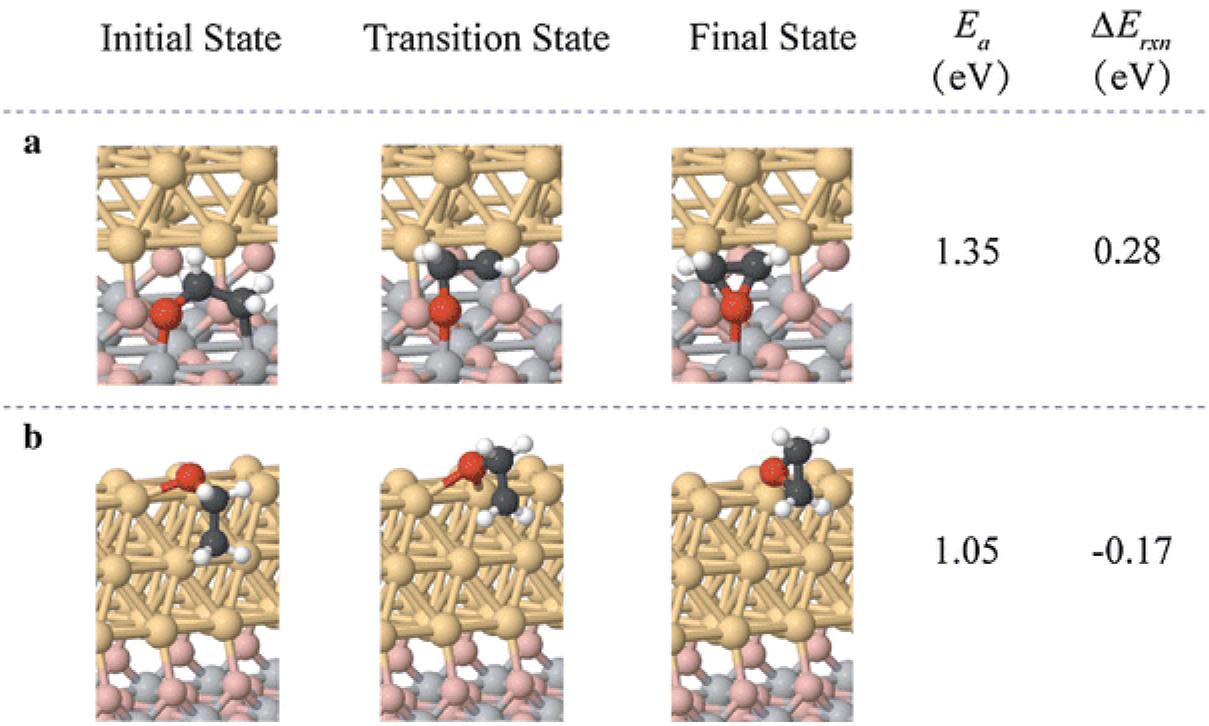

Figure 4.8 Formation of ethylene oxide on: (a) perimeter Ti site; (b) Au site.

4.3.4 Deuterium Kinetic Isotope Effect (DKIE) Study in the Partial Oxidation of Ethylene

During the ethylene partial oxidation on the Au/TiO_2 catalyst forming acetate, two C–H bonds are broken while one C–H bond is formed. It is therefore of fundamental interest to test the influence of deuterium substitution on the reaction kinetics. With such a goal in mind, the oxidation reaction as shown in Figure 4.2, using C_2D_4 in place of C_2H_4, was carried out (0.5 Torr C_2D_4 and 0.5 Torr O_2 mixture over the Au/TiO_2 catalyst at 370 K), where the DKIE was measured. As shown in Figure 4.9, deuterium substitution lead to IR shifts in the acetate/TiO_2 vibrational modes, which involve C–H motions. Due to the level of complexity in the fingerprint region of acetate/TiO_2, we used the half-peak area (high-frequency half) of the $\nu_{as}(CO_2)$ band to track the kinetic growth of acetate/TiO_2 species for both C_2H_4 and C_2D_4 reactants, as shown by the cross hatched regions in Figure 4.9.

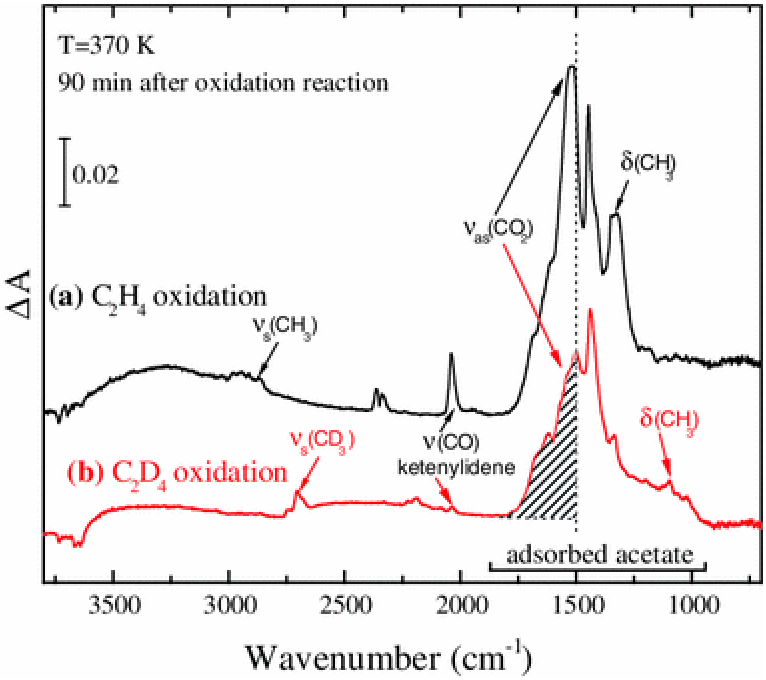

Figure 4.9 IR spectra of (a) C_2H_4 (black spectrum) and (b) C_2D_4 (red spectrum) partial oxidation at 370 K, after reaction has occurred for 90 min. The shadowed spectral region shows the mathematical integration region used in deriving the kinetics presented in Figure 4.10.

Figure 4.10a shows a plot of the integrated absorbance of half of the $\nu_{as}(CO_2)$ band for both C_2H_4 and C_2D_4 as a function of reaction time. The DKIE of ethylene partial oxidation to acetate is plotted in Figure 4.10b, where the ratio k_H/k_D is calculated using point-by-point differentiation of the numerical data shown in Figure 4.10a and subsequent 5-point averaging. The DKIE decays to near unity as the reaction slows down, which may be related to site blocking by the acetate species accumulated at the active sites. The observed initial DKIE value, ~3, is consistent with the results from Cant and Hall, where the DKIE value, 2.5, was found for propylene partial oxidation forming acrolein over a Au sponge.[29] Previous DKIE simulations were carried out for the partial oxidation reaction of acetate to form ketenylidene on the Au/TiO_2 catalyst to help confirm the measured DKIE value of ~4 for the reactions of CH_3COO and CD_3COO to Au_2=CCO product formation.[10] The measured DKIE value was found to be the result of a series of C–H bond breaking steps resulting in a higher rate of H-intermediate production.

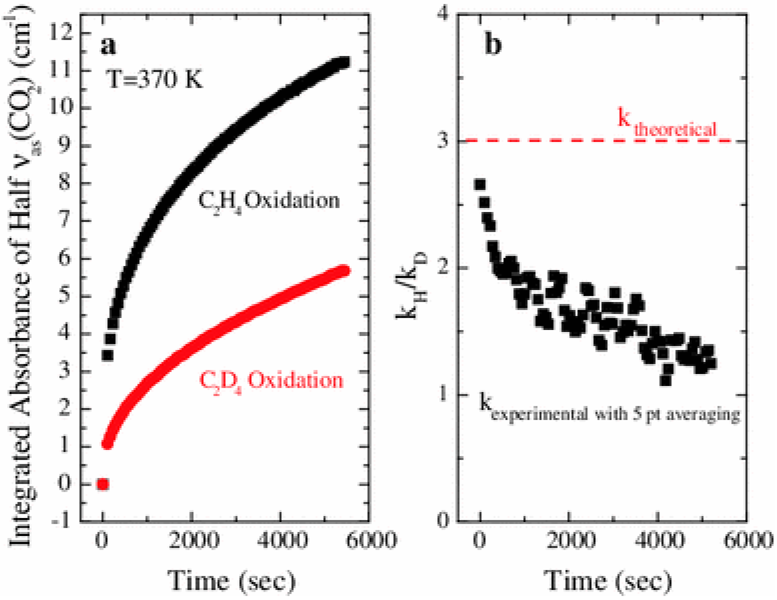

Figure 4.10 Plots of the deuterium kinetic isotope effect for C_2H_4 and C_2D_4 oxidation at 370 K. The initial $P_{ethylene}$= 0.5 Torr; the initial P_{O_2}= 0.5 Torr.

We have carried out similar DFT simulations here to rationalize the DKIE for ethylene oxidation to form the bound acetate intermediate. As was discussed in Section 4.3.2, the protonation of the $H_2C^*C(OH)O^*$ intermediate to produce the bound acetic acid is considered as the rate-determining step because of its relatively high activation energy. The DKIE, k_H/k_D, for the $H_2C^*C(OH)O^*$ protonation step is calculated based on the zero-point energy correction to the barrier. For the oxide perimeter site and Au site, the calculated k_H/k_D values are both ~3.4, which is consistent with the initial experimental DKIE measurement. This observation is consistent with the protonation of the $H_2C^*C(OH)O^*$ step as the rate limiting step of the reaction to acetate. However, it is hard to distinguish whether it is an early or late transition state from the DKIE value alone because of reaction symmetry as the H-transfer occurs between an O atom and a C atom. In this step, one O–H is breaking while the other C–H is forming; therefore, the early transition state should have a zero-point energy correction that is quite similar to the late transition state.

It is worth noting that the secondary oxidation product from acetate, gold ketenylidene, is also significantly kinetically retarded in the C_2D_4 experiment (Figure 4.9). This is because more C–H/C–D bond breaking steps are involved in the secondary oxidation steps to ketenylidene.

4.3.5 Nature of the Active Sites in the Partial Oxidation of Ethylene

The catalytic activity of Au/TiO_2 in the partial oxidation of unsaturated hydrocarbons presented here and in previous studies on the oxidation of CO to CO_2 and ethylene to ketenylidene is attributed to the unique dual $Au–Ti^{4+}$ sites that reside at the periphery of the Au/TiO_2 interface that readily bind and activate O_2 and to the highly reactive basic oxygen atoms that form on Au. We have shown previously that the adsorption of O_2 at the $Au–Ti^{4+}$ site results in the formation of a strongly bound and activated $Au–O–O–Ti^{4+}$ complex, which resembles reactive peroxide intermediates, and readily dissociates to generate O atoms at the interface. These weakly bound oxygen atoms acquire charge from the filled d-band of the Au thus resulting in negatively charged $O^{\delta-}$ species that are quite basic and weakly bound to Au. As a result, these species can readily carry out base-catalyzed nucleophillic addition reactions as was shown by Madix and Friend.[30-32] In addition, these basic oxygen atoms can also readily activate weakly acidic C–H bonds thus resulting in the formation of basic OH intermediates that can also carry out nucleophilic addition to the unsaturated carbon centers and activate weakly acidic C–H bonds.[28]

The weakly held basic O and OH groups that form readily promote the partial oxidation as is evident from the low activation barriers for the nucleophilic addition of O and OH to the unsaturated carbon centers as well as in the activation of the weakly acidic C–H bonds which comprise most of the elementary steps involved in the catalytic oxidation of ethylene to acetate shown in Figures 4.5, 4.6 and 4.7.

Previous reports on the partial oxidation over Au were carried out via processes that require the initial activation of O_2 or the addition of base in solution. The unique dual Au–Ti^{4+} perimeter sites, however, can directly activate O_2 at low temperatures and readily supply the O needed to carry out the partial oxidation thus avoiding the addition of base or the pre-activation of O_2.

4.4 Conclusions

The partial oxidation of ethylene to form acetate on a Au/TiO_2 catalyst was studied both experimentally and theoretically. The following results are found:

1. As shown by DFT calculations, O_2 dissociation is facile on the dual-perimeter Au–Ti^{4+} sites of Au/TiO_2 catalysts thus providing the atomic O on Au necessary for ethylene oxidation.
2. Ethylene reacts with the reactive oxygen atoms that form on Au/TiO_2 to produce acetate on the TiO_2 support at 370 K. No acetate formation occurs on the blank TiO_2 catalyst or the Au/SiO_2 catalyst.
3. No ethylene oxide on the catalyst surface or in the gas phase is detected by either FTIR or GC–MS techniques at temperatures up to 673 K. DFT simulations indicate that the reaction path to ethylene oxide involves a significantly higher barrier than the partial oxidation path to form acetate, thereby directing the reaction to the acetate.
4. The rate-limiting step for the partial oxidation of ethylene to acetate under these model conditions was found to be the protonation step in the species $H_2C^*CH(OH)O^*$ to produce a terminal CH_3 group.
5. The Au–Ti^{4+} sites appear to be responsible for the activation of O_2 at the interface to supply the reactive atom intermediates.

6. The adsorbed O atoms as well as OH intermediates that form on Au at the Au/TiO_2 interface are weakly bound to the surface, and as such, behave as bases that carry out the nucleophilic attack of bound ethylene intermediates as well as the activation of a range of weakly acidic C–H bonds.
7. An initial deuterium kinetic isotope effect of ~3 was obtained theoretically, and experiments comparing C_2H_4 to C_2D_4 suggest that this value is initially valid; then k_H/k_D decays to near unity as the reaction proceeds, which may be related to site blocking by the acetate species accumulated at the active sites.

References

1. Cheung, H.; Tanke, R. S.; Torrence, G. P. Acetic acid. *Ullmann's Encyclopedia of Industrial Chemistry;* Wiley: Weinheim, **2000**.

2. Sano, K.; Uchida, H.; Wakabayashi, S. A new process for acetic acid production by direct oxidation of ethylene. *Catalysis Surveys from Asia* **1999**, *3*, 55-60.

3. Chu, W.; Ooka, Y.; Kamiya, Y.; Okuhara, T. Reaction path for oxidation of ethylene to acetic acid over Pd/WO_3–ZrO_2 in the presence of water. *Catalysis letters* **2005**, *101*, 225-228.

4. Li, X.; Iglesia, E. Support and promoter effects in the selective oxidation of ethane to acetic acid catalyzed by Mo-V-Nb oxides. *Applied Catalysis A: General* **2008**, *334*, 339-347.

5. Li, X.; Iglesia, E. Synergistic Effects of TiO_2 and Palladium-Based Cocatalysts on the Selective Oxidation of Ethene to Acetic Acid on Mo–V–Nb Oxide Domains. *Angewandte Chemie International Edition* **2007**, *46*, 8649-8652.

6. Force, E. L.; Bell, A. T. Infrared spectra of adsorbed species present during the oxidation of ethylene over silver. *Journal of Catalysis* **1975**, *38*, 440-460.

7. Sachtler, W.; Backx, C.; Van Santen, R. On the mechanism of ethylene epoxidation. *Catalysis Reviews—Science and Engineering* **1981**, *23*, 127-149.

8. Rojluechai, S.; Chavadej, S.; Schwank, J. W.; Meeyoo, V. Catalytic activity of ethylene oxidation over Au, Ag and Au–Ag catalysts: Support effect. *Catalysis Communications* **2007**, *8*, 57-64.

9. Green, I. X.; Tang, W.; Neurock, M.; Yates, Jr., J. T. Localized Partial Oxidation of Acetic Acid at the Dual Perimeter Sites of the Au/TiO_2 Catalyst - Formation of Gold Ketenylidene. *Journal of the American Chemical Society* **2012**, *134*, 13569-13572.

10. Green, I. X.; Tang, W.; Neurock, M.; Yates, Jr., J. T. Mechanistic Insights into the Partial Oxidation of Acetic Acid by O_2 at the Dual Perimeter Sites of a Au/TiO_2 Catalyst. *Faraday Discussions* **2013**, *162*, 247-265.

11. Green, I. X.; Tang, W.; Neurock, M.; Yates, Jr., J. T. Spectroscopic observation of dual catalytic sites during oxidation of CO on a Au/TiO_2 catalyst. *Science* **2011**, *333*, 736-739.

12. Green, I. X.; Tang, W.; Neurock, M.; Yates, Jr., J. T. Low-Temperature Catalytic H_2 Oxidation over Au Nanoparticle/TiO_2 Dual Perimeter Sites. *Angewandte Chemie International Edition* **2011**, *50*, 10186-10189.

13. Basu, P.; Ballinger, T.; Yates, Jr., J. T. Wide temperature range IR spectroscopy cell for studies of adsorption and desorption on high area solids. *Review of Scientific Instruments* **1988**, *59*, 1321-1327.

14. Zanella, R.; Sandoval, A.; Santiago, P.; Basiuk, V. A.; Saniger, J. M. New preparation method of gold nanoparticles on SiO_2. *The Journal of Physical Chemistry B* **2006**, *110*, 8559-8565.

15. Liao, L. F.; Lien, C. F.; Lin, J. L. FTIR study of adsorption and photoreactions of acetic acid on TiO_2. *Physical Chemistry Chemical Physics* **2001**, *3*, 3831-3837.

16. Hasan, M.; Zaki, M.; Pasupulety, L. Oxide-catalyzed conversion of acetic acid into acetone: an FTIR spectroscopic investigation. *Applied Catalysis A: General* **2003**, *243*, 81-92.

17. Mattsson, A.; Osterlund, L. Adsorption and photoinduced decomposition of acetone and acetic acid on anatase, brookite, and rutile TiO_2 nanoparticles. *The Journal of Physical Chemistry C* **2010**, *114*, 14121-14132.

18. Ruiz, A.; van der Linden, B.; Makkee, M.; Mul, G. Acrylate and propoxy-groups: Contributors to deactivation of Au/TiO_2 in the epoxidation of propene. *Journal of Catalysis* **2009**, *266*, 286-290.

19. Liu, X.; Madix, R. J.; Friend, C. M. Unraveling molecular transformations on surfaces: a critical comparison of oxidation reactions on coinage metals. *Chemical Society Reviews* **2008**, *37*, 2243-2261.

20. Liu, X.; Friend, C. M. Competing Epoxidation and Allylic Hydrogen Activation: trans-β-Methylstyrene Oxidation on Au(111). *The Journal of Physical Chemistry C* **2010**, *114*, 5141-5147.

21. Liu, X.; Baker, T. A.; Friend, C. M. Effect of molecular structure on epoxidation of allylic olefins by atomic oxygen on Au. *Dalton Transactions* **2010**, *39*, 8521-8526.

22. Baker, T. A.; Xu, B.; Jensen, S. C.; Friend, C. M.; Kaxiras, E. Role of defects in propene adsorption and reaction on a partially O-covered Au(111) surface. *Catalysis Science & Technology* **2011**, *1*, 1166-1174.

23. Nijhuis, T.; Sacaliuc-Parvulescu, E.; Govender, N.; Schouten, J.; Weckhuysen, B. The role of support oxygen in the epoxidation of propene over gold–titania catalysts investigated by isotopic transient kinetics. *Journal of Catalysis* **2009**, *265*, 161-169.

24. Wendt, S.; Sprunger, P. T.; Lira, E.; Madsen, G. K.; Li, Z.; Hansen, J. O.; Matthiesen, J.; Blekinge-Rasmussen, A.; Laegsgaard, E.; Hammer, B.; Besenbacher, F. The role of interstitial sites in the Ti*3d* defect state in the band gap of titania. *Science* **2008**, *320*, 1755-1759.

25. Green, I. X.; Tang, W.; McEntee, M.; Neurock, M.; Yates, Jr., J. T. Inhibition at Perimeter Sites of Au/TiO_2 Oxidation Catalyst by Reactant Oxygen. *Journal of the American Chemical Society* **2012**, *134*, 12717-12723.

26. Roldan, A.; Torres, D.; Ricart, J. M.; Illas, F. On the effectiveness of partial oxidation of propylene by gold: A density functional theory study. *Journal of Molecular Catalysis A: Chemical* **2009**, *306*, 6-10.

27. Vaughan, O. P.; Kyriakou, G.; Macleod, N.; Tikhov, M.; Lambert, R. M. Copper as a selective catalyst for the epoxidation of propene. *Journal of Catalysis* **2005**, *236*, 401-404.

28. Zope, B. N.; Hibbitts, D. D.; Neurock, M.; Davis, R. J. Reactivity of the gold/water interface during selective oxidation catalysis. *Science* **2010**, *330*, 74-78.

29. Cant, N. W.; Hall, W. K. Catalytic oxidation. IV. Ethylene and propylene oxidation over gold. *Journal of Physical Chemistry* **1971**, *75*, 2914-2921.

30. Madix, R. J.; Auerbach, D. *Surface reactions;* Springer-Verlag New York: **1994**; Vol. 34.

31. Liu, X.; Xu, B.; Haubrich, J.; Madix, R. J.; Friend, C. M. Surface-mediated self-coupling of ethanol on gold. *Journal of the American Chemical Society* **2009**, *131*, 5757-5759.

32. Xu, B.; Liu, X.; Haubrich, J.; Friend, C. M. Vapour-phase gold-surface-mediated coupling of aldehydes with methanol. *Nature chemistry* **2010**, *2*, 61-65.

Chapter 5: Selective Catalytic Oxidative-Dehydrogenation of Carboxylic Acids—Acrylate and Crotonate Formation at the Au/TiO_2 Interface

(modified from *JACS*, **2014**, 136 (13), pp 5116-5120)

5.1 Introduction

The conversion of fatty acids derived from triglyceride-containing animal, vegetable, and algae oils into fuels and chemical intermediates requires catalytic deoxygenation, which is often carried out over supported Pd and other group VIII metal particles.[1-4] Long chain carboxylic acids can either undergo direct decarboxylation, which results in the formation of alkanes and CO_2, or a decarbonylation that produces olefins, CO, and water. The mechanisms for these reactions are still greatly debated and highly speculative. The Pd and Pt catalysts that are currently used are too active and unable to selectively produce α-olefins or other chemical intermediates in high yields.[1-3] In the present work, we use in situ IR spectroscopy, kinetics, and theory to show that Au nanoparticles supported on TiO_2 are highly selective in activating the C–H bonds at the C_2 and C_3 positions for linear organic acids (propionic and butyric acid) to form unsaturated carboxylate surface intermediates (Figure 5.1). The unique selectivity of Au/TiO_2 suggests that the sites and mechanism for the activation of organic acids are different from those active on supported Pd or Pt. These differences may provide clues for the design of catalytic engineering materials that are both highly active and selective.

Since Haruta's pioneering discovery[5] of the high oxidative catalytic activity for Au nanoparticles at low temperature and recent exciting high resolution electron microscopy studies,[6] well-defined kinetic in situ spectroscopic studies[7-9] and theoretical studies[10-12] have shown that the perimeter sites of Au nanoparticles supported on TiO_2 are responsible for the low temperature catalytic activity for the oxidation of H_2,[13,14] CO,[15-18] C_2H_4,[19] and acetic acid,[20,21] with reaction temperatures in the range 110–400 K. We have shown previously that the low temperature selective oxidation of C_2H_4 and acetic acid can be readily carried out over Au/TiO_2 catalysts, generating in both cases a ketenylidene intermediate on Au, $Au_2=C=C=O$.[19-21] In this paper, we report the observation of selective C=C double bond formation in higher carboxylic acids under oxidative-dehydrogenation conditions. The observed trend on Au/TiO_2 catalysts to selectively activate the C–H bonds at the C_2 and C_3 positions with respect to the COOH group in the organic acids, independent of alkyl chain length, is the result of the unique bifunctional characteristics of $Au–Ti^{4+}$ perimeter sites for the oxidative-dehydrogenation of carboxylic acids.

Fourier transform transmission infrared spectroscopy (FTIR) and quadrupole mass spectrometry (QMS) were used together with density functional theory (DFT) calculations to help identify the oxidation products of two carboxylic acids and to discern the most likely reaction path to form unsaturated carboxylic acids on Au/TiO_2. This is the first account of the production of acrylate from propionic acid and crotonate from butyric acid on a Au/TiO_2 catalyst. We also show that facile reduction of the C=C bond in unsaturated carboxylic acids can be achieved using H_2 or D_2 on the Au/TiO_2 catalyst containing the unsaturated carboxylate species.

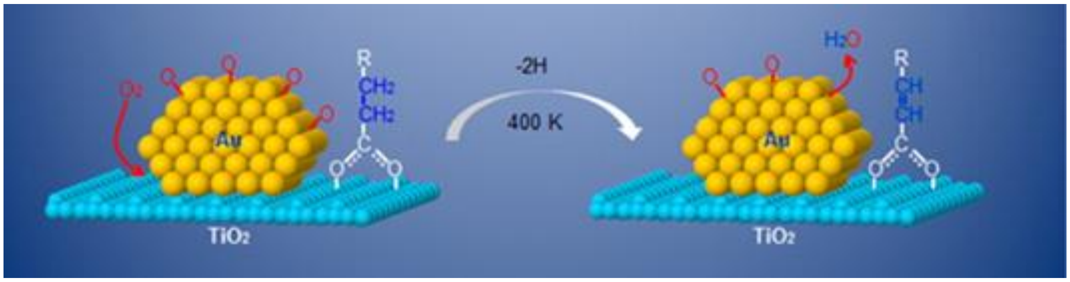

Figure 5.1 Schematic of oxidative-dehydrogenation of carboxylic acids to produce unsaturated acids on Au/TiO_2.

5.2 Experimental Procedures

A detailed description of the IR chamber is provided in Chapter 2.[22] Acrylic acid (99.5%, extra pure, stabilized) was acquired from Fisher Scientific. Propionic acid (≥99.5%, ACS reagent), propionic-2,3-$^{13}C_2$ acid (99 atom % ^{13}C), and butyric acid (≥99.5%, analytical standard) were acquired from Sigma-Aldrich and further purified using the freeze–pump–thaw method. Oxygen gas (99.998%, Research Purity), D_2 gas, and H_2 gas (99.9995%, Research Purity) were acquired from Matheson Tri-Gas, Inc. Gas and liquid purity analysis along with desorption experiments were performed using a quadrupole mass (QMS) analyzer attached to the IR cell. Additionally, a GC–MS spectrometer was employed to analyze the liquid carboxylic acids.

The catalyst was heated in vacuum to 473 K and held at that temperature for 20 min before every experiment to help clean the surface and to prepare the catalyst for reaction. Oxygen at a pressure of ∼18 Torr was then introduced to the catalyst at 473 K for ∼3.5 h in order to remove traces of accumulated impurity hydrocarbon species. The cell was evacuated for 10 min, and ∼2 Torr of H_2 was then introduced to the catalyst at 473 K for 10 min followed by evacuation for an additional 10 min. Finally, the catalyst was cooled to the desired reaction temperature of 400 K. Approximately 0.4 Torr of the desired carboxylic acid vapor was introduced into the cell followed by evacuation for 30 min at 400 K, forming a saturated layer of carboxylate species adsorbed on the TiO_2 support. One Torr of O_2 was then introduced into the cell, and over the course of 2.5 h, an FTIR spectrum was taken every minute during oxidation at the controlled sample temperature. Each FTIR spectrum takes 52 s and contains an average of 128 scans with a resolution of 2 cm^{-1}.

After oxidation of the desired acid followed by evacuation, 1 Torr of H_2 or D_2 was introduced into the cell at 400 K to carry out subsequent hydrogenation experiments, which were performed using IR spectroscopy or mass spectrometry. These experiments were performed immediately after catalytic oxidation of the carboxylic acid.

Density functional theory (DFT) calculations were carried out to examine the mechanism of acrylate formation and to determine the frequencies for adsorbed acrylate and crotonate species that form in order to compare with the experimental spectroscopic results. More details of the model structure and calculation can be found in the Chapter 3, Section 3.2.

5.3 Results and Discussions

5.3.1 Frequency Identification Using FTIR and DFT

During oxidation, an IR spectrum was taken every 60 s for 7810 s at 400 K. In order to capture the changes in the region below 1800 cm^{-1}, the oxidized propionate and butyrate spectra after 3070 s were measured by subtraction from their respective initial spectra before oxidation, as shown in Figure 5.2a.

Two characteristic absorbance bands formed at 1637 cm^{-1} and 1657 cm^{-1} during propionate and butyrate oxidation, respectively, on Au/TiO_2. These two bands are assigned to a >C=C< moiety at the C_2 and C_3 positions in both the bound propionate and butyrate species that form, respectively, converting them into acrylate and crotonate species. Others have assigned the C=C band for chemisorbed acrylate (CH_2=CHCOO*) and chemisorbed crotonate (CH_3CH=CHCOO*) on TiO_2[23,24] and other metal oxides[25,26] to similar frequencies near 1637 and 1659 cm–1, respectively. Other possible oxidation products were investigated and ruled out according to their C=O and C=C mode frequencies on TiO_2 (See Table 1 below).

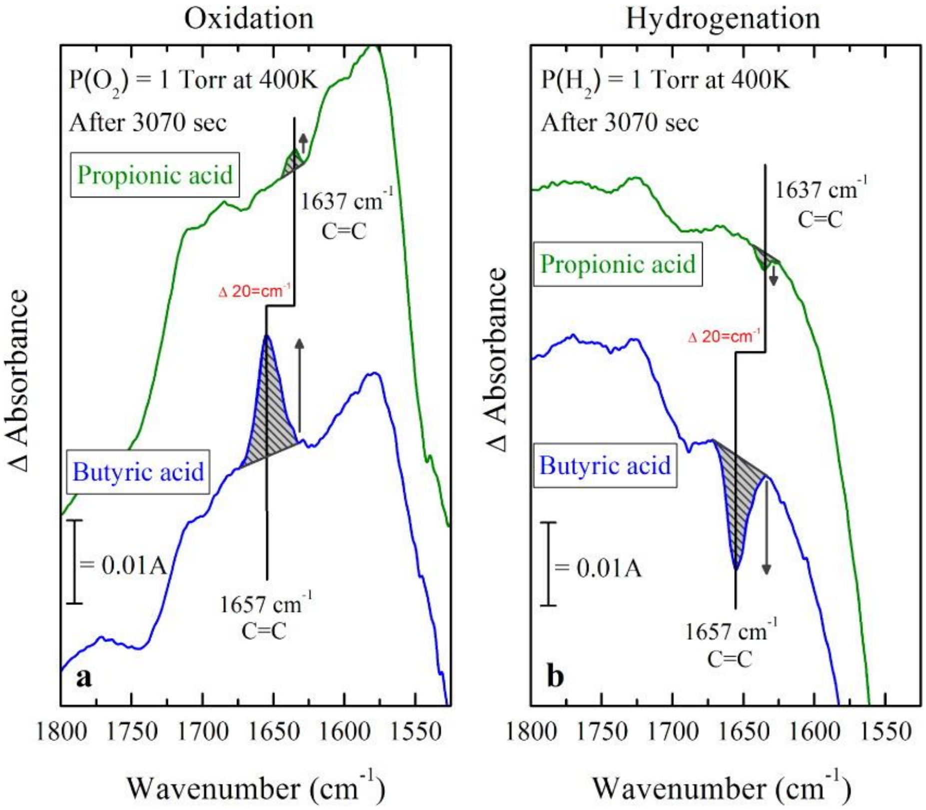

Figure 5.2 Developed spectra showing highlighted features in the C=C region of both propionic acid (green curve) and butyric acid (blue curve) after 3070 s of (a) oxidation and (b) subsequent hydrogenation on Au/TiO_2 at 400 K. The baseline in the selected (cross-hatched) features is drawn to guide the eye. The spectral features shown occur above an initial background, which has been subtracted. The spectral families associated with panel a are shown in Figures 5.3 and 5.4.

Table 1. Experimental IR Frequencies of C=C and C=O modes for Possible Oxidation Products on TiO_2

Molecule	**Frequency (cm^{-1})**	**Reference**
Acetone ($(CH_3)_2CO$)	1682	[16]
Acrolein (CH_2=CHCHO)	1647-1653	[16]
Acetic acid (CH_3COOH)	1532	[17]
Formic acid (HCOOH)	1555	[18]
Ethylene Oxide (C_2H_4O)	1268	[17]
Propanal (CH_3CH_2CHO)	1660, 1690 (sh), and 1730	[19]
Allyl alcohol (CH_2=$CHCH_2OH$)	1645	[16]
Lactic acid ($C_3H_6O_3$)	1676-1679	[20]
Acrylic acid (CH_2=CHCHOOH)	1635-1637	[16],[20]
Crotonic acid (CH_3CH=CHCOOH)	1657	[21]
Acrylic acid, this paper	1637	this paper
Crotonic acid, this paper	1657	this paper

In order to determine if the formation of the two unsaturated carboxylate species required the presence of Au, the oxidation experiments were repeated on a blank TiO_2 catalyst at 400 K. No acrylate or crotonate were formed on TiO_2 alone, as shown in Figures 5.3a and 5.4a. The oxidative-dehydrogenation activity, thus, appears to require Au sites. Previous results for the oxidation of CO, H_2, acetic acid, and ethylene showed that the activation and dissociation of O_2 occurs at the dual Au–Ti^{4+} site on the perimeter of Au nanoparticles and results in the formation of O adatoms bound to Au sites, which are rather basic and can participate in the activation of the C–H bonds of carboxylate intermediates bound to interfacial Ti^{4+} sites. Other groups[27] have also observed C–H bond activation due to oxygen at the Au/TiO_2 interface.

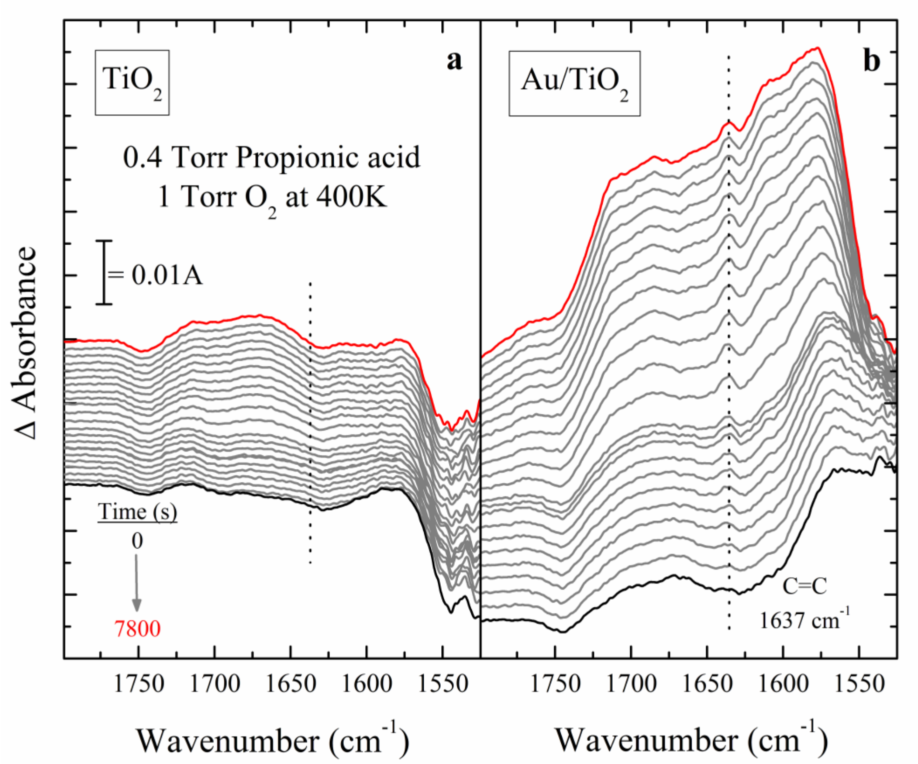

Figure 5.3 Difference IR spectra in the C=C region of both propionic acid on TiO_2 (a) and Au/TiO_2 (b) after 70 seconds (black curve) to 7810 seconds (red curve) of oxidation at 400K.

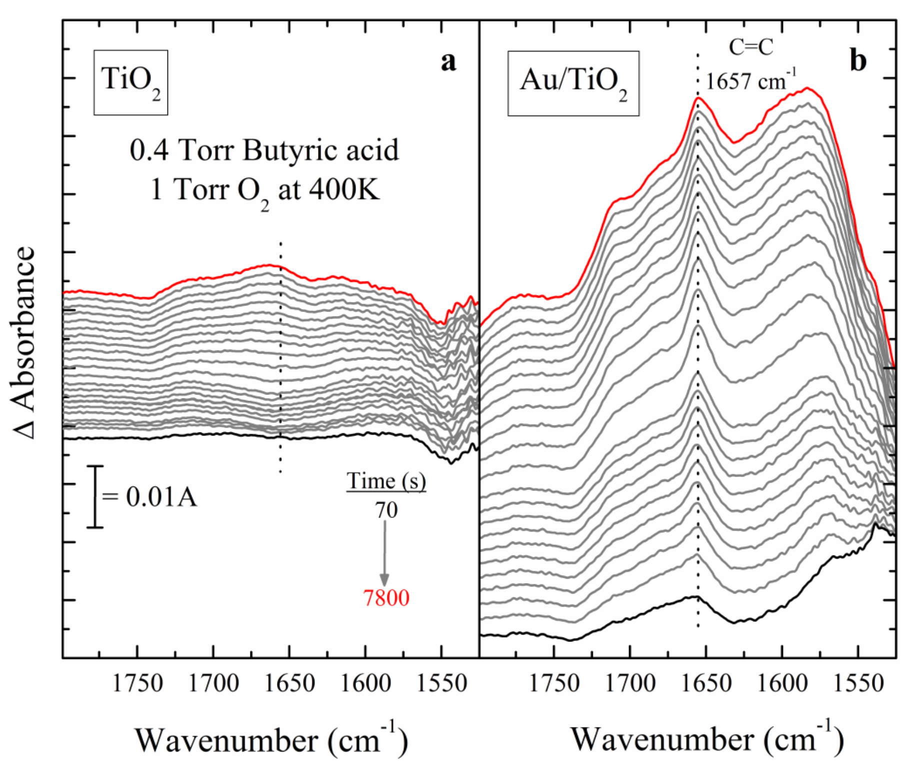

Figure 5.4 Difference IR spectra in the C=C region of both butyric acid on TiO_2 (a) and Au/TiO_2 (b) after 70 seconds (black curve) to 7810 seconds (red curve) of oxidation at 400K.

After the formation of these unsaturated carboxylate species, the cell was evacuated and one Torr of H_2 was introduced into the cell at 400 K for the same amount of time. Figure 5.2b shows the subtracted spectra for both the preoxidized propionate and butyrate on Au/TiO_2 after 3070 s in H_2. It can be seen that the same C=C absorption bands produced by the oxidative activation of the acid decrease in absorbance via reduction under H_2. The loss of these two bands is attributed to the hydrogenation of the unsaturated >C=C< bond, showing the reversibility of the oxidative-dehydrogenation and hydrogenation processes. To further verify that the 1637 cm^{-1} band is from >C=C< containing species (acrylate), 0.4 Torr of acrylic acid (CH_2=CHCOOH) was introduced onto the clean Au/TiO_2 surface at 400 K. Figure 5.5a shows bands at 1637, 1520, 1448, 1373, and 1271 cm^{-1}, which are attributed to acrylate species assigned to ν(C=C), $\nu_{as}(CO_2)$, $\nu_s(CO_2)$, δ(C–H), and ν(C–C), respectively.[23] The band at 1637 cm^{-1} assigned to the acrylate intermediate matches the ν(C=C) band formed during the oxidation of the surface propionate as shown in Figure 5.5b, establishing that oxidative-dehydrogenation of propionate is being observed specifically at the C_2 and C_3 positions of the acid. The loss of propionate during oxidation can be seen in Figure 5.5b with the negative bands around 1550–1500 cm^{-1} ($\nu_{as}(CO_2)$), 1460–1430 cm^{-1} ($\nu_s(CO_2)$), 1380 cm^{-1} ($\delta_s(CH_3)$), and 1300 cm^{-1} ($\delta(CH_2)$).[23] Unfortunately, the possible growth of other acrylate bands in these regions cannot be inferred; therefore, isotopic-labeling studies were performed.

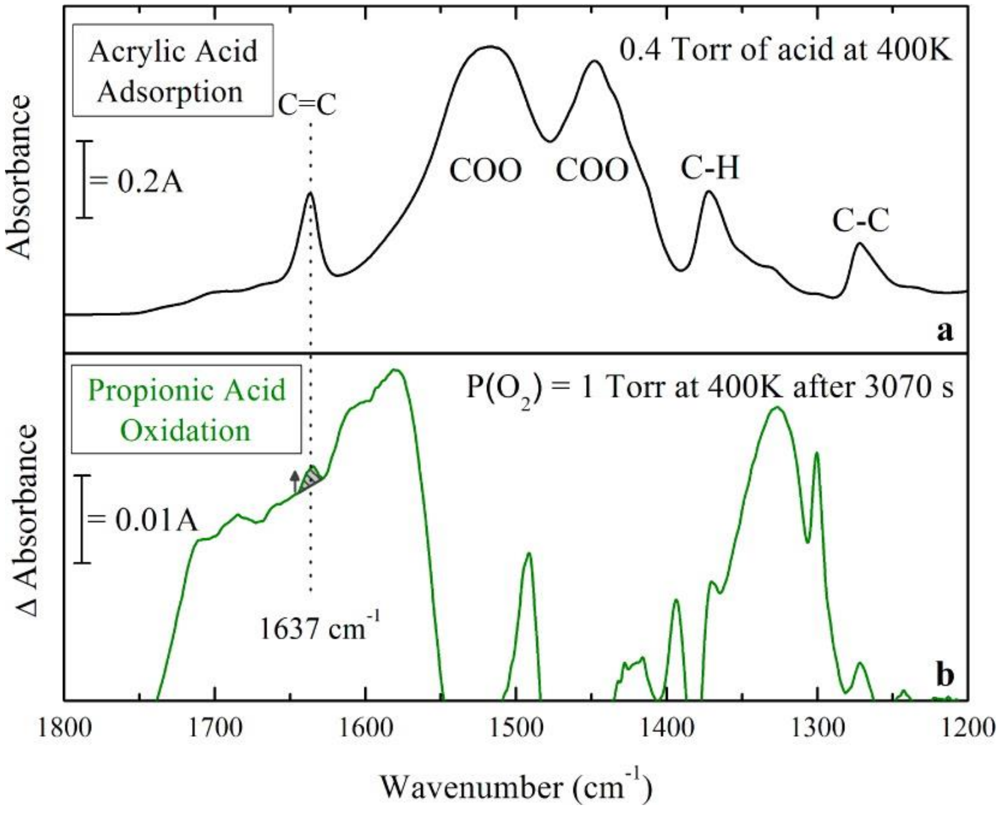

Figure 5.5 Comparison of (a) acrylic acid (black curve) and (b) propionic acid oxidation products (green curve from Figure 1a) on Au/TiO_2 at 400 K. The spectral features shown in (b) occur above an initial background.

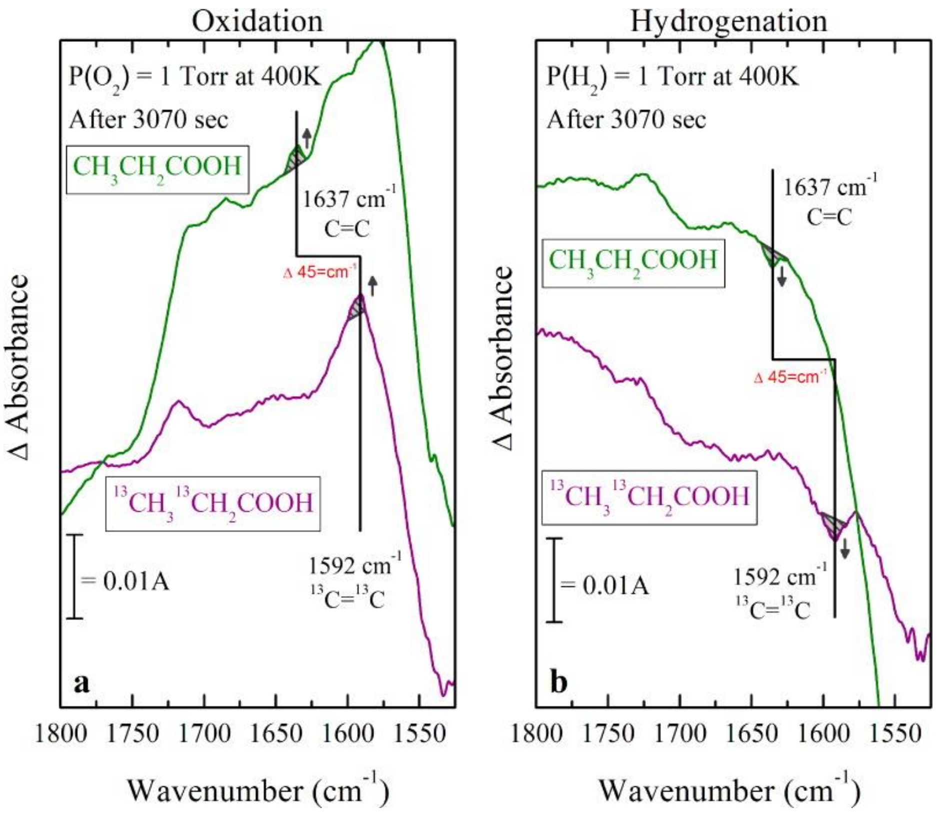

Figure 5.6 IR frequency shift comparison of the propionic acid (CH_3CH_2COOH) oxidation product (green curve) and the isotopically labeled propionic acid ($^{13}CH_3{}^{13}CH_2COOH$) oxidation product (purple curve) after 3070 s of (a) oxidation and subsequent (b) hydrogenation on Au/TiO_2 at 400 K.

Isotopically labeled propionic acid ($^{13}CH_3{}^{13}CH_2COOH$) oxidation experiments were also performed on Au/TiO_2 at 400 K. Figure 5.6a shows the difference spectra for both the propionate and ^{13}C-labeled propionate on Au/TiO_2 after 3070 s in O_2. The $^{13}C{=}^{13}C$ band is red-shifted by 45 cm^{-1} to 1592 cm^{-1}.

Our DFT calculation results indicate that the $^{12}C{=}^{12}C$ stretching frequencies for acrylate and $^{13}C_2$-acrylate appear at 1624 and 1576 cm^{-1}, respectively, as shown in Figure 5.7. The theoretical red shift between $^{12}C{=}^{12}C$ and $^{13}C{=}^{13}C$ frequencies is, therefore, 48 cm^{-1}, which is in very good agreement with the experimental difference of 45 cm^{-1} and well within the error of DFT. Subsequent hydrogenation experiments were performed as well, and both the $^{12}C{=}^{12}C$ and $^{13}C{=}^{13}C$ bands decrease in absorbance as shown in Figure 5.6b. These experiments and simulations provide convincing evidence that propionate dehydrogenates to acrylate under oxidation conditions.

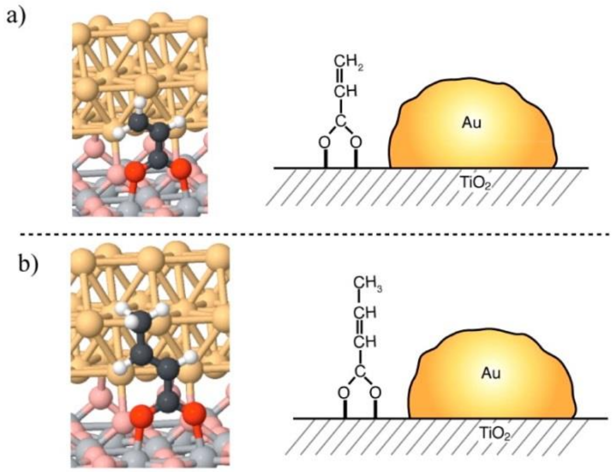

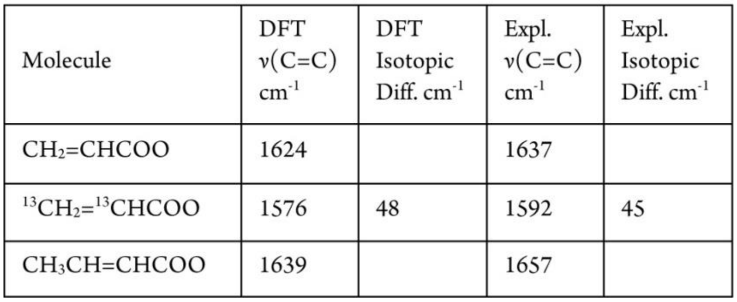

Molecule	DFT ν(C=C) cm^{-1}	DFT Isotopic Diff. cm^{-1}	Expl. ν(C=C) cm^{-1}	Expl. Isotopic Diff. cm^{-1}
CH_2=CHCOO	1624		1637	
$^{13}CH_2$=^{13}CHCOO	1576	48	1592	45
CH_3CH=CHCOO	1639		1657	

Figure 5.7 Structure of (a) acrylate and (b) crotonate bound to Ti4+ sites at the Au/TiO2 perimeter. Their calculated C═C bond vibrational frequencies are listed in the table along with the experimental frequencies and shifts.

Similarly, butyrate is found to convert into crotonate upon oxidative-dehydrogenation on Au/TiO_2. Figure 5.7 shows the DFT calculated C=C stretching frequency for crotonate, 1639 cm^{-1}, which is blue shifted by 15 cm^{-1} from the calculated acrylate C=C stretching frequency. This shift is consistent with the experimental shift of 20 cm^{-1} in comparing propionate and butyrate oxidation in Figure 5.2. It is likely that the second step in the oxidation mechanism after O_2 dissociation involves the oxidative activation of the C–H bond of the carboxylate at the C_2 site followed by the subsequent activation of the C–H bond at the C_3 site. These results are consistent with previous work by Green *et al.*,[21] where two H atoms were observed to be removed from the terminal methyl group on an acetate intermediate on TiO_2 by O atoms bound to neighboring Au sites in the initial steps in the oxidation of acetic acid at the Au/TiO_2 interface. This leads finally to the formation of the ketenylidene species, $Au_2C=C=O$, from acetic acid. The C–H bonds that sit α to carbonyl groups are weakly acidic and can be activated by basic oxygen intermediates that form on Au.[28,29]

5.3.2 Studies of Gas Phase Products Using QMS

After propionic acid oxidation, the vacuum cell was evacuated, and the catalyst was cooled down to 375 K for 30 min. Then, the catalyst was systematically heated up to 600 K at 0.5 K/s with the cell open to the QMS for analysis of gas products coming off the surface. To avoid over pressurizing the QMS, the catalyst was not heated higher than 600 K. As shown in Figure 5.8a, masses 72 and 71 start to desorb around 425 K and are assigned to acrylic acid (black and red curves). The inset in Figure 5.8a is an enlarged view of these two masses. The cracking pattern for propionic acid does not contain these masses; therefore, the most likely molecule is acrylic acid, which is consistent with the IR and DFT frequency identifications on the surface discussed above.

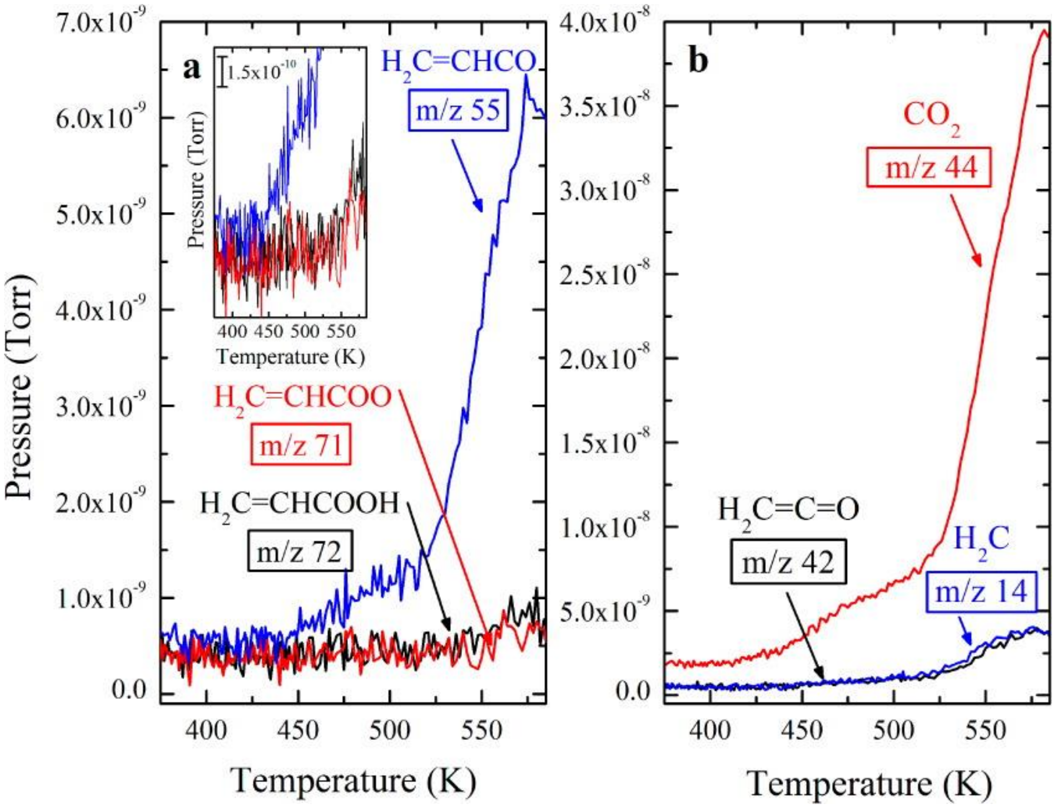

Figure 5.8 QMS desorption analysis of masses (a) 55 ($H_2C=CHCO$, blue), 71 ($H_2C=CHCOO$, red), and 72 ($H_2C=CHCOOH$, black) and (b) 14 (H_2C, blue), 42 ($H_2C=C=O$, black), and 44 (CO_2, red) after propionic oxidation on Au/TiO_2.

Other desorption products were also observed with masses at 14, 42, 44, and 55. Mass 55 ($H_2C=CHCO$) is attributed to a mixture of mass spectrometer cracking products of both acrylic acid and propionic acid.

Further oxidation occurs to form a ketene species ($H_2C=C=O$) and a CH_2^+ cracking product as shown in Figure 5.8b by masses 14 and 42. Lastly, the major product to be formed from the oxidation of propionic acid is CO_2 at mass 44. Therefore, the acrylic acid and ketene species are side products or intermediates that eventually form the fully oxidized product, carbon dioxide.

Another desorption experiment was performed after the addition of D_2 at 400 K to the catalyst, which had previously caused propionic acid oxidation. This experiment was designed to follow up on the hydrogenation experiment in Figure 5.2. After an hour in D_2, the cell was evacuated and the catalyst was cooled to 375 K. Similar to the desorption method mentioned above, the catalyst was heated up to 600 K and the QMS was used for gas analysis. Figure 5.9 shows masses at 75 ($CH_2DCHDCOO$) and 76 ($CH_2DCHDCOOH$), which are attributed to deuterated propionic acid (black and red curves) with 2 D atoms. Similarly, mass 59 is attributed to a mixture of propionic acid with the OH group replaced with a D atom (CH_3CH_2COD) and propionic acid without the OH group and containing 2 D atoms ($CH_2DCHDCO$). These mass assignments are consistent with the deuteration of the unsaturated molecules that were produced in the oxidation experiments. Therefore, in agreement with the disappearance of the C=C bands during hydrogenation, the appearance of these deuterated molecules is attributed to the deuteration of the unsaturated species produced in Figure 5.8a.

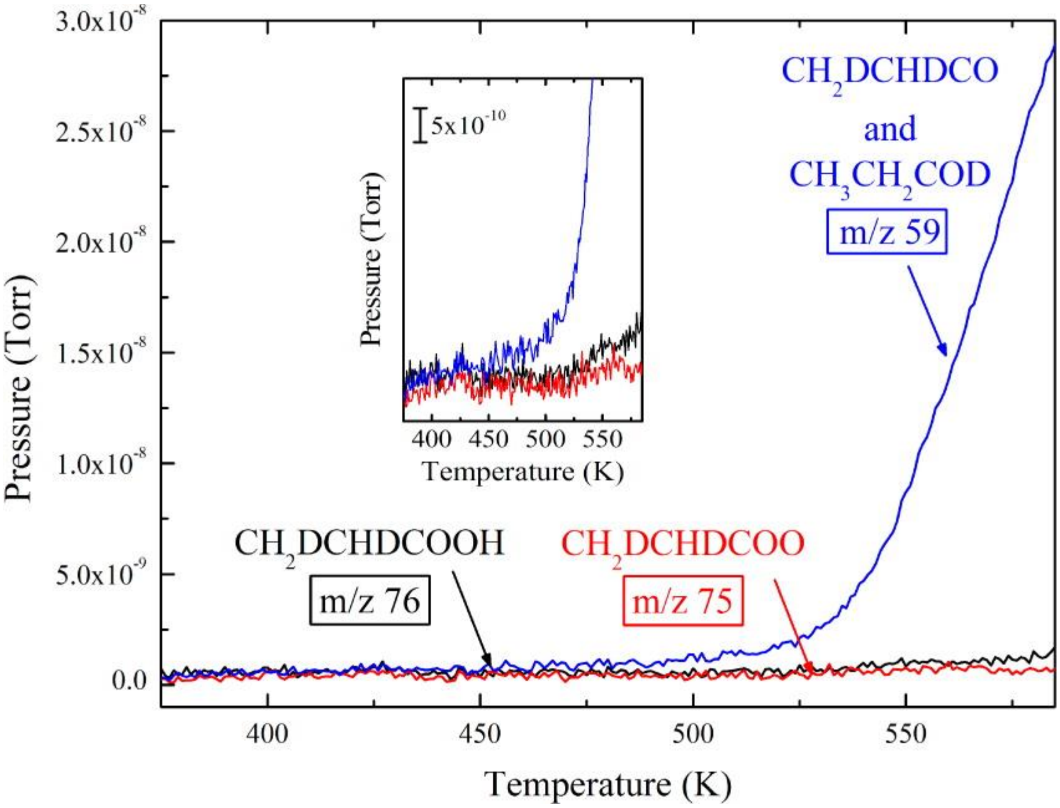

Figure 5.9 QMS desorption analysis of masses 59 ($CH_2DCHDCO$, blue), 75 ($CH_2DCHDCOO$, red), and 76 ($CH_2DCHDCOOH$, black) after the subsequent addition of D_2 to propionate + Au/TiO_2.

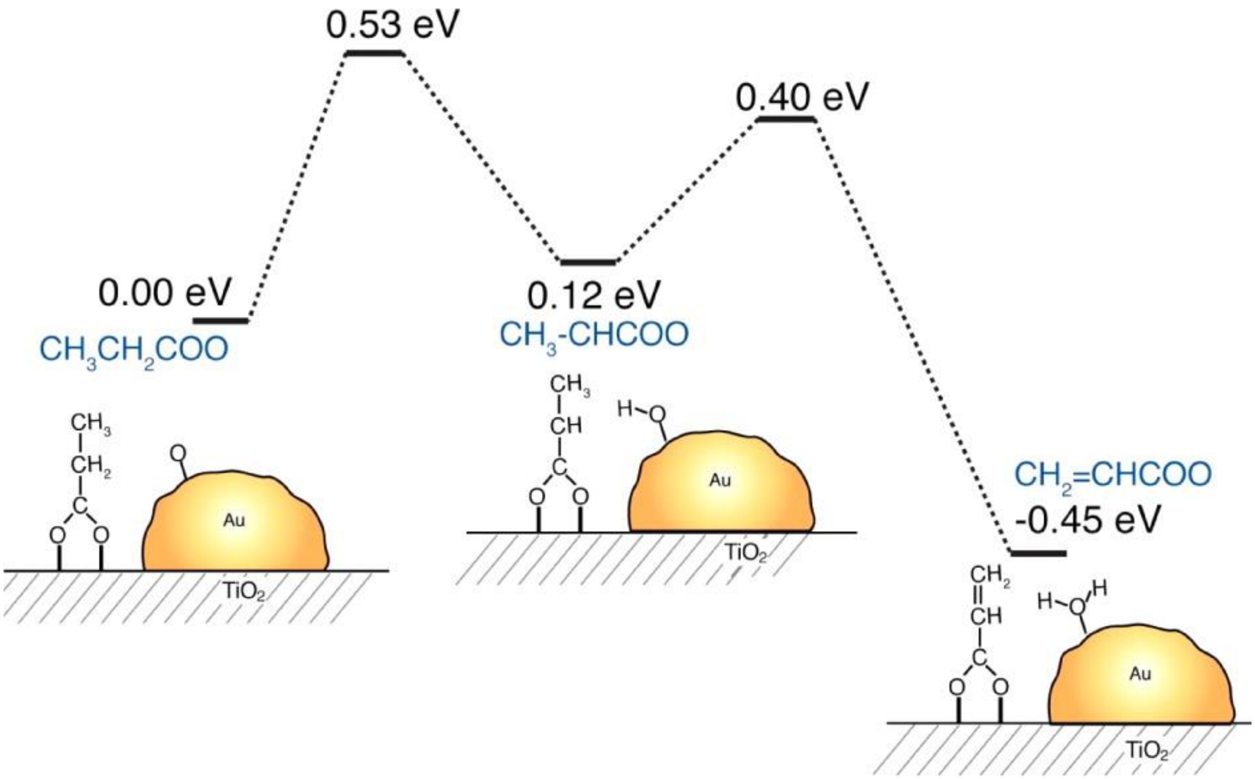

Figure 5.10 DFT-calculated potential energy diagram for the oxidative dehydrogenation of propionate at the Au/TiO_2 interface to form an acrylate surface intermediate.

5.3.3 DFT Energy Pathway to Form Acrylate on Au/TiO_2

The mechanism for the formation of acrylate from propionic acid was examined here by carrying out density functional theory calculations. The calculated potential energy diagram for this reaction is shown in Figure 5.10. The detailed atomic structures for all of the reactants, intermediates, and products reported in Figure 5.10 are presented in Figure 5.11. Previously, we showed that O_2 is activated at Au–Ti^{4+} site pairs at the Au/TiO_2 interface with a barrier of ~0.5 eV and results in the formation of adsorbed atomic oxygen (O*) on the Au sites at the Au/TiO_2 perimeter.[15] The atomic oxygen that results is weakly bound to Au and acts as a base that can effectively activate the C–H bonds involved in the oxidative dehydrogenation.[21] The influence of basic O* on Au in activating O–H as well as C–H bonds has been discussed previously.[27-31] The O–H bond of propionic acid is readily cleaved by the bridging oxygen sites on the TiO_2 surface, resulting in the formation of surface propionate intermediates at the Au/TiO_2 interface. A C–H bond at the C_2 position can then be activated by the basic O* species bound to nearby Au sites. The C_2–H bond is activated before the C_3–H bond, as it is weaker and more acidic than the C_3–H bond. Also, steric hindrance at the bulky CH_3 group decreases its reactivity according to DFT calculations. This steric repulsion effect may be partially compensated by a stabilization due to charge delocalization over the alkyl chain. The barrier to activate the C_2–H bond via the O* bound to Au was calculated to be 0.53 eV, resulting in the formation of the CH3CH–COO* species that is bound to Ti sites on the oxide and an OH* intermediate bound to a neighboring Au site. This OH* species is even more basic than O* and can subsequently activate the C_3–H bond of the CH_3CHCOO/Ti species with a barrier of only 0.28 eV, thus resulting in the formation of TiO_2-bound acrylate (CH_2=CH–COO/Ti) and H_2O bound to Au. The acrylate is 0.45 eV more stable than the original CH_3CH_2COO/Ti because of the formation of the C=C bond. All of the steps in this cycle involve activation barriers that range from 0.3 to 0.5 eV, thus indicating that the reaction can be carried out at moderate temperatures near 400 K as observed experimentally. Acrylate formation may occur at even lower temperatures; however, we chose 400 K as the ideal reaction temperature to observe all of the oxidation products for carboxylic acid oxidation on Au/TiO_2.

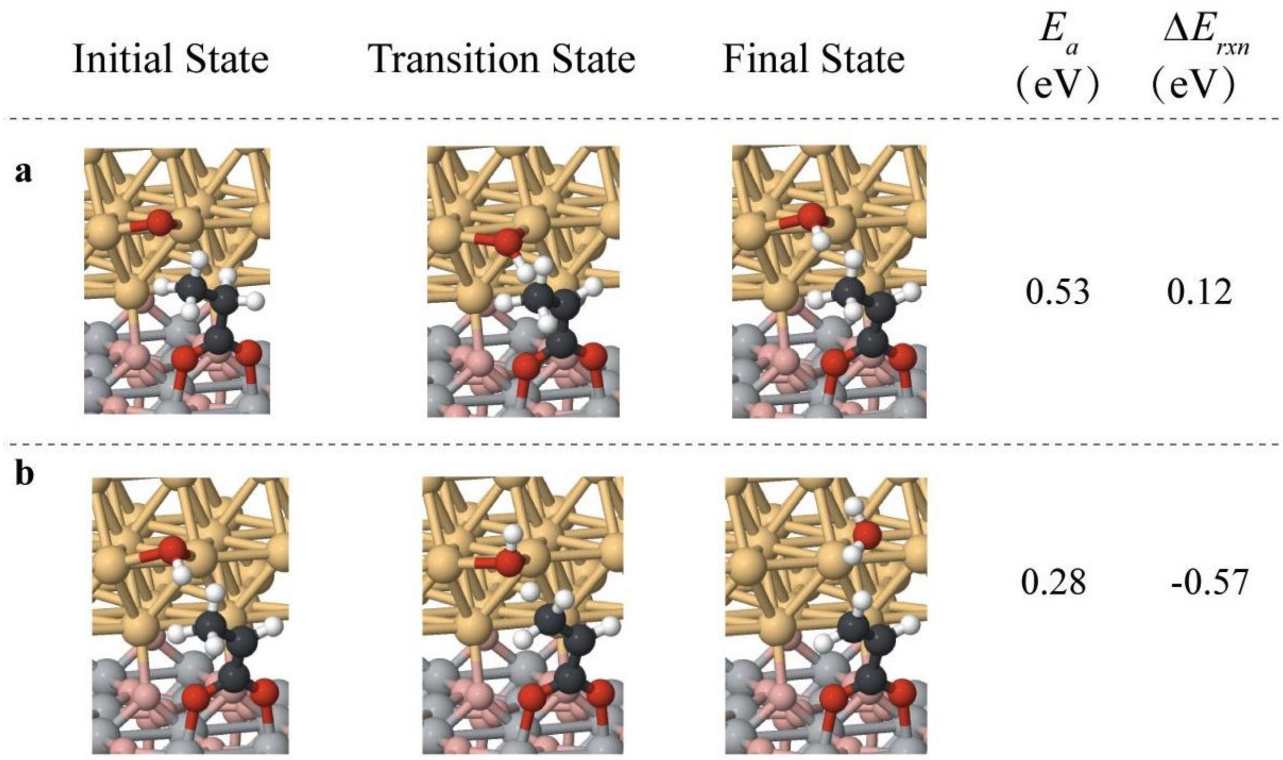

Figure 5.11 Detailed structure for acrylate formation steps at the Au/TiO_2 interface. The Au atoms and Ti atoms are shown in yellow and grey respectively, whereas the O in the TiO_2 lattice, adsorbed O, C atoms and H atoms are shown in pink, red, black and white respectively. E_a and ΔE_{rxn} refer to the activation barrier and reaction energy, respectively.

5.4 Conclusion

The oxidative-dehydrogenation of carboxylate intermediates formed via the dissociative adsorption of two organic acids over a Au/TiO_2 catalyst has been studied by transmission IR methods and density functional theory calculations. For both the C_2 and C_3 acids, the C–H activation of the alkyl backbone occurs first at the C_2 atom, followed by the subsequent C–H activation at the C_3 atom to form a C=C moiety. The dual Au–Ti^{4+} sites that exist at the perimeter of nominally 3 nm Au particles supported on TiO_2 appear to be the active sites as they can readily activate both O_2 (as well as the organic acid) to form Au–O surface species that can subsequently activate the C–H bonds. The activity and selectivity observed is consistent with other partial oxidation processes observed on these special sites.[30] DFT calculations of the energy pathway are consistent with the temperature required for the reaction and also provide theoretical confirmation of vibrational assignments, comparing ^{12}C- and ^{13}C-labeled species. Both acrylate and crotonate, unsaturated carboxylate species, and their corresponding acids are observed on the surface by IR spectroscopy and in the gas phase by mass spectrometry. Additionally, the Au/TiO_2 catalyst also catalyzes the hydrogenation of the unsaturated carboxylate species.

References

1. Bernas, H.; Eränen, K.; Simakova, I.; Leino, A.; Kordás, K.; Myllyoja, J.; Mäki-Arvela, P.; Salmi, T.; Murzin, D. Y. Deoxygenation of dodecanoic acid under inert atmosphere. *Fuel* **2010**, *89*, 2033-2039.

2. Immer, J. G.; Kelly, M. J.; Lamb, H. H. Catalytic reaction pathways in liquid-phase deoxygenation of C18 free fatty acids. *Applied Catalysis A: General* **2010**, *375*, 134-139.

3. Simakova, I.; Rozmysłowicz, B.; Simakova, O.; Mäki-Arvela, P.; Simakov, A.; Murzin, D. Y. Catalytic deoxygenation of C18 fatty acids over mesoporous Pd/C catalyst for synthesis of biofuels. *Topics in Catalysis* **2011**, *54*, 460-466.

4. Peng, B.; Zhao, C.; Kasakov, S.; Foraita, S.; Lercher, J. A. Manipulating Catalytic Pathways: Deoxygenation of Palmitic Acid on Multifunctional Catalysts. *Chemistry-A European Journal* **2013**, *19*, 4732-4741.

5. Haruta, M.; Tsubota, S.; Kobayashi, T.; Kageyama, H.; Genet, M. J.; Delmon, B. Low-Temperature Oxidation of CO over Gold Supported on TiO_2, α-Fe_2O_3, and Co_3O_4. *Journal of Catalysis* **1993**, *144*, 175-192.

6. Akita, T.; Kohyama, M.; Haruta, M. Electron Microscopy Study of Gold Nanoparticles Deposited on Transition Metal Oxides. *Accounts of Chemical Research* **2013**, *46*, 1773-1782.

7. Chen, M.; Goodman, D. The structure of catalytically active gold on titania. *Science* **2004**, *306*, 252-255.

8. Rodriguez, J.; Ma, S.; Liu, P.; Hrbek, J.; Evans, J.; Perez, M. Activity of CeO_x and TiO_x nanoparticles grown on Au(111) in the water-gas shift reaction. *Science* **2007**, *318*, 1757-1760.

9. Kotobuki, M.; Leppelt, R.; Hansgen, D.; Widmann, D.; Behm, R. Reactive oxygen on a Au/TiO_2 supported catalyst. *Journal of Catalysis* **2009**, *264*, 67-76.

10. Laursen, S.; Linic, S. Geometric and electronic characteristics of active sites on TiO_2-supported Au nano-catalysts: insights from first principles. *Physical Chemistry Chemical Physics* **2009**, *11*, 11006-11012.

11. Wang, J.; Hammer, B. Role of Au^+ in Supporting and Activating Au_7 on TiO_2(110). *Physical Review Letters* **2006**, *97*, 136107.

12. Hammer, B.; Norskov, J. Why gold is the noblest of all the metals. *Nature* **1995**, *376*, 238-240.

13. Green, I. X.; Tang, W.; Neurock, M.; Yates, Jr., J. T. Low-Temperature Catalytic H_2 Oxidation over Au Nanoparticle/TiO_2 Dual Perimeter Sites. *Angewandte Chemie* **2011**, *50*, 10186-10189.

14. Fujitani, T.; Nakamura, I.; Akita, T.; Okumura, M.; Haruta, M. Hydrogen dissociation by gold clusters. *Angewandte Chemie* **2009**, *121*, 9679-9682.

15. Green, I. X.; Tang, W.; Neurock, M.; Yates, Jr., J. T. Spectroscopic observation of dual catalytic sites during oxidation of CO on a Au/TiO_2 catalyst. *Science* **2011**, *333*, 736-739.

16. Green, I. X.; Tang, W.; McEntee, M.; Neurock, M.; Yates, Jr., J. T. Inhibition at Perimeter Sites of Au/TiO_2 Oxidation Catalyst by Reactant Oxygen. *Journal of the American Chemical Society* **2012**, *134*, 12717-12723.

17. Kung, M. C.; Davis, R. J.; Kung, H. H. Understanding Au-catalyzed low-temperature CO oxidation. *Journal of Physical Chemistry C* **2007**, *111*, 11767-11775.

18. Kung, H.; Kung, M.; Costello, C. Supported Au catalysts for low temperature CO oxidation. *Journal of Catalysis* **2003**, *216*, 425-432.

19. Green, I. X.; McEntee, M.; Tang, W.; Neurock, M.; Yates, Jr., J. T. Direct Formation of Acetate from the Partial Oxidation of Ethylene on a Au/TiO_2 Catalyst. *Topics in Catalysis* **2013**, *56*, 1512-1524.

20. Green, I. X.; Tang, W.; Neurock, M.; Yates, Jr., J. T. Localized Partial Oxidation of Acetic Acid at the Dual Perimeter Sites of the Au/TiO_2 Catalyst - Formation of Gold Ketenylidene. *Journal of the American Chemical Society* **2012**, *134*, 13569-13572.

21. Green, I. X.; Tang, W.; Neurock, M.; Yates, Jr., J. T. Mechanistic Insights into the Partial Oxidation of Acetic Acid by O_2 at the Dual Perimeter Sites of a Au/TiO_2 Catalyst. *Faraday Discussions* **2013**, *162*, 247-265.

22. Basu, P.; Ballinger, T.; Yates, Jr., J. T. Wide temperature range IR spectroscopy cell for studies of adsorption and desorption on high area solids. *Review of Scientific Instruments* **1988**, *59*, 1321-1327.

23. Chen, Y. K.; Lin, Y. F.; Peng, Z. W.; Lin, J. L. Transmission FT-IR study on the adsorption and reactions of lactic acid and poly (lactic acid) on TiO_2. *Journal of Physical Chemistry C* **2010**, *114*, 17720-17727.

24. Lochar, V.; Pytel, M.; Smolakova, L. FTIR Study of the Interaction of Crotyl Alcohol and Crotonic Acid with the Surface of SiO_2, TiO_2 and ZrO_2. *Scientific papers of the University of Pardubice, Series A* **2009**, *15*, 121-127.

25. Coast, R.; Pikus, M.; Henriksen, P. N.; Nitowski, G. A. Vibrational Spectroscopic Observation of Acrylic Acid Coadsorbed in Dissociated and Molecular Forms on Oxidized Aluminum. *Journal of Physical Chemistry* **1996**, *100*, 15011-15014.

26. Harrison, P. G.; Maunders, B. Tin oxide surfaces. Part 16.—Infrared study of the adsorption of formic acid, acrylic acid and acrolein on tin (IV) oxide, tin (IV) oxide–silica and tin (IV) oxide–palladium oxide. *Journal of the Chemical Society, Faraday Transactions I* **1985**, *81*, 1345-1355.

27. Camellone, M. F.; Zhao, J.; Jin, L.; Wang, Y.; Muhler, M.; Marx, D. Molecular Understanding of Reactivity and Selectivity for Methanol Oxidation at the Au/TiO_2 Interface. *Angewandte Chemie International Edition* **2013**, *52*, 5780-5784.

28. Madix, R. J.; Auerbach, D. *Surface reactions;* Springer-Verlag New York: **1994**; Vol. 34.

29. Liu, X.; Madix, R. J.; Friend, C. M. Unraveling molecular transformations on surfaces: a critical comparison of oxidation reactions on coinage metals. *Chemical Society Reviews* **2008**, *37*, 2243-2261.

30. Green, I. X.; Tang, W.; Neurock, M.; Yates, Jr., J. T. Insights into Catalytic Oxidation at the Au/TiO_2 Dual Perimeter Sites. *Accounts of Chemical Research* **2013**, *47*, 805-815.

31. Zope, B. N.; Hibbitts, D. D.; Neurock, M.; Davis, R. J. Reactivity of the gold/water interface during selective oxidation catalysis. *Science* **2010**, *330*, 74-78.

Chapter 6: Mechanistic Insights into the Catalytic Oxidation of Carboxylic Acids on Au/TiO_2: Partial Oxidation of Propionic and Butyric Acid to Gold Ketenylidene through Unsaturated Acids

(modified from *ACS Catalysis*, **2015**, 5, pp 744-753)

6.1 Introduction

Biomass, in the form of carbohydrates, oils, and fatty acids, can be converted into key chemical intermediates to replace nonrenewable fossil fuel resources used in the synthesis of different chemicals and fuels.[1] Recent studies on the decarbonylation and decarboxylation of model carboxylic acids over transition metal catalysts have generated significant interest because of their potential application in the conversion of fatty acids to olefins at low temperatures.[2-6] Experimental studies[4-7] and theoretical studies on model linear carboxylic acids[8,9] suggest that the decarboxylation proceeds via an initial activation and dehydrogenation of C_2–H and C_3–H bonds before undergoing C–O or C–C bond scission over Pd catalysts; however, only a few studies are found for carboxylic acid oxidation on Au-based catalysts.[10-12]

Green *et al*.[10,11,13] studied the oxidation of ethylene and acetic acid on a Au/TiO_2 catalyst and found that both molecules result in the formation of the partially oxidized gold ketenylidene species, $Au_2C=C=O$, via a sequence of kinetic steps involving the deprotonation of the acid at the Ti sites to form the acetate intermediate, the activation of two of the C–H bonds of the terminal CH_3 group by bound O* or OH* intermediates and the subsequent scission of the C–O bond at the bifunctional Ti–Au site to form the $Au_2C=C=O$ intermediate.

Exploratory studies on the oxidation of larger carboxylic acids such as propionic and butyric acid on a Au/TiO_2 catalyst were recently reported.[12] Here, we present detailed in situ FTIR observations of C–C bond cleavage at the second (C_2) and third (C_3) carbons, which reside at the α and β positions from the −COO group of both the propionate and butyrate species, followed by C–O bond cleavage in −COO to produce $Au_2C=C=O$ species at the Au/TiO_2 perimeter sites.

Density functional theory (DFT) calculations show that dehydrogenation at the C_α-C_β bond occurs before the C–C bond scission in a manner similar to the decarboxylation of propionic acid over the Pd(111) surface.[8,9] Detailed in situ FTIR isotopic kinetic experiments combined with DFT calculations help to elucidate the reaction mechanism for the production of the $Au_2C=C=O$ species from both C_3- and C_4-carboxylate species. The present study on the kinetics for the oxidative dehydrogenation and decarboxylation of propionic and butyric acid to produce ketenylidene on a Au/TiO_2 catalyst extends a very brief earlier report on the initial dehydrogenation of these acids.[12]

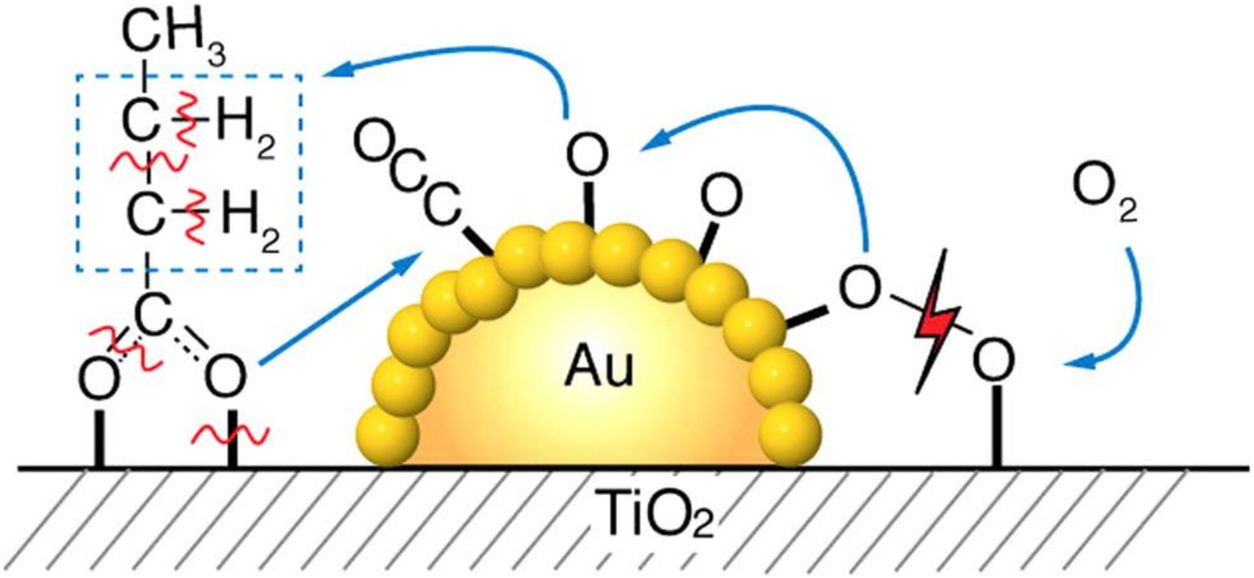

Figure 6.1 Schematic of $\geq C_3$ carboxylic acid oxidation on a Au/TiO_2 nanocatalyst at 400K.

6.2 Experimental Procedures

A high vacuum transmission IR cell with a base pressure of ~1×10^{-8} Torr was employed, and a detailed description is provided in Chapter 2.[14] Acetic acid (≥99.7%, ACS reagent), propionic acid (≥99.5%, ACS reagent), propionic-3,3,3-d_3 acid (99 atom % D), propionic-2,2-d_2 acid (98 atom % D), butyric acid (≥99.5%, analytical standard), and butyric-d_7 acid (98 atom % D) were acquired from Sigma-Aldrich and purified using the freeze–pump–thaw method. Gas and liquid purity analysis were performed using a quadrupole mass analyzer attached to the IR cell. The isotopically labeled propionic acid samples were also characterized using ^{1}H NMR analysis and an external GC/MS spectrometer (Thermo Finnigan Voyager MS with Trace 2000 GC) verifying their stated isotopic purity.

The catalyst was pretreated with ~18 Torr of O_2(g) at 473 K for ~3.5 h before each experiment to remove any hydrocarbon impurities. After evacuation of the O_2 gas, ~2 Torr of H_2(g) was introduced into the cell for 10 min, followed by evacuation. H_2(g) removes O adatoms that originated from O_2 pretreatment on Au and TiO_2 sites to form H_2O, which then desorbs from the surface at 473 K. The catalyst was then cooled to the desired temperature. Approximately 0.4 Torr of carboxylic acid vapor was introduced into the cell and then evacuated for 30 min. One Torr of O_2(g) was then introduced into the cell, and a FTIR spectrum was taken every minute for 2.5 h. Each FTIR spectrum took 52s and contained 128 scans at 2 cm^{-1} resolution. The $Au_2C=C=O$ absorbance increase was used to evaluate the kinetics of the oxidation process.

For the hydrogenation experiments, after the carboxylate species were oxidized, forming $Au_2C=C=O$, and the cell was evacuated, the catalyst was cooled to 292 K and exposed to 1 Torr of H_2(g) for 10 min at various temperatures. Hydrogenation of the unsaturated products on the surface was followed by FTIR.

First principle periodic plane wave DFT calculations implemented in the Vienna Ab Initio Simulation Program[15] were carried out to determine the activation energies and reaction energies associated with the reaction pathways. The results were used to examine proposed mechanisms for the oxidation of propionic acid over a model Au/TiO_2 interface. The structural model and calculations are described in more detail in Chapter 3, Section 3.2.

6.3 Results and Discussions

6.3.1 IR Frequencies of Carboxylic Acid Conversion to Acetate, Propionate, and Butyrate Along with Ketenylidene Formation at 400 K on the Au/TiO_2 Catalyst

The results for the oxidation of the three carboxylic acids (acetic acid, propionic acid, and butyric acid) carried out at 400 K on Au/TiO_2 are shown in Figure 6.2. For each experiment, 0.4 Torr of acid vapor was introduced into the cell for adsorption to saturation coverage, and the cell was then evacuated for 30 min. The black curves reported in Figure 6.2 correspond to the spectrum before oxidation, with the acid already present on the surface. Figure 6.2a (black curve) shows acetic acid (CH_3COOH) on Au/TiO_2 at 400 K. In agreement with previously reported assignments by Green *et al*.[10,11] and others,[16-18] acetic acid dissociates to form acetate (CH_3COO) species on TiO_2 with IR bands at 2936 ($\nu_s(CH_3)$), 1532 ($\nu_{as}(CO_2)$), 1454 ($\nu_s(CO_2)$), and 1338 ($\delta(CH_3)$) cm^{-1}. Similarly, propionic acid (CH_3CH_2COOH) dissociates to produce propionate (CH_3CH_2COO) species on TiO_2, as shown in Figure 6.2b (black curve) with major bands at 2981 ($\nu_{as}(CH_3)$), 2946 ($\nu_{as}(CH_3)$ in Fermi resonance/$\nu_{as}(CH_2)$), 2888 ($\nu_s(CH_3)/\nu_s(CH_2)$), 1523 ($\nu_{as}(CO_2)$), 1473 ($\delta_{as}(CH_3)$), 1430 ($\nu_s(CO_2)$), 1380 ($\delta_s(CH_3)$), and 1300 ($\delta(CH_2)$) cm^{-1}, which are in agreement with literature frequencies.[19]

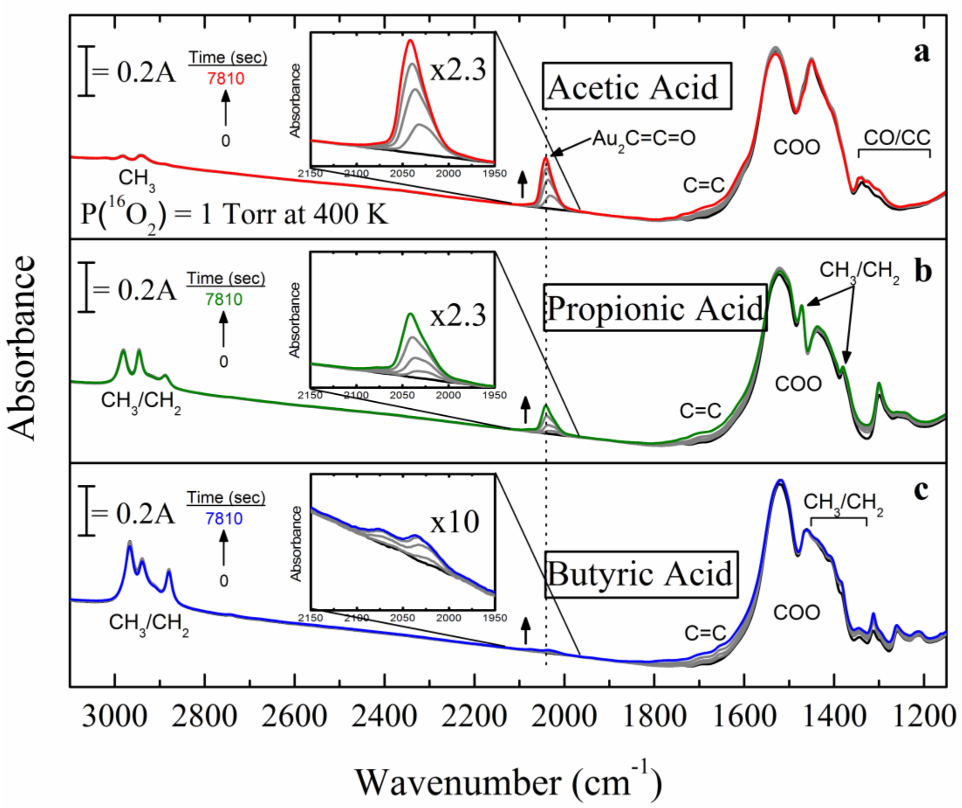

Figure 6.2 IR spectra comparison of (a) acetic acid, (b) propionic acid, and (c) butyric acid oxidation on Au/TiO_2 at 400 K for 7810 s. The black spectra were taken before adding O_2 to the IR cell, and the red (a), green (b), and blue (c) curves were taken after 7810 s in O_2.

Following the same trend, as shown in Figure 6.2c (black curve), the butyric acid ($CH_3CH_2CH_2COOH$) IR spectrum displays bands at 2967 ($\nu_{as}(CH_3)$), 2939 ($\nu_{as}(CH_3)$ in Fermi resonance/$\nu_{as}(CH_2)$), 2880 ($\nu_s(CH_3)/\nu_s(CH_2)$), 1522 ($\nu_{as}(CO_2)$), 1461 ($\delta_{as}(CH_3)$), 1408 ($\nu_s(CO_2)$), and 1382 ($\delta_s(CH_3)$) cm^{-1}, which are assigned to butyrate ($CH_3CH_2CH_2COO$) species on TiO_2.[20-22] The same bands mentioned above for all three acids were seen on the blank TiO_2 catalyst, confirming that the carboxylate species adsorb on the TiO_2 sites alone. All three of these carboxylic acids show a similar well-known trend, with the initial step in adsorption involving the deprotonation of the −COOH group[23,24] on TiO_2 sites, followed by adsorption of the carboxylate species, which provides a common starting point for the oxidation of these carboxylate species.

The next steps in the oxidation mechanism involve O_2 dissociation at the Au/TiO_2 interface to result in the formation of weakly bound O adatoms on Au that are negatively charged and act as a Lewis base in catalyzing the activation of weakly acidic C–H bonds, as described in our previous work.[12] The propionate (CH_3CH_2COO) and butyrate ($CH_3CH_2CH_2COO$) intermediates can react via an oxidative dehydrogenation of the C_α–C_β bonds to form surface acrylate ($CH_2{=}CHCOO$) and crotonate ($CH_3CH{=}CHCOO$) intermediates. These results are consistent with previous work by Green *et al.*[11] in which two H atoms were proposed to be sequentially removed from the methyl group of acetic acid by O adatoms during the first acetic acid oxidation steps on Au/TiO_2 to form the ketenyl CHCOO intermediate on Au.

Another IR band around 2040 cm^{-1} is observed to develop during the oxidation of acetate, propionate, and butyrate separately on Au/TiO_2 at 400 K, as shown in Figure 6.2 in the magnified inserts. This absorbance band was previously assigned to a gold ketenylidene species, $Au_2C{=}C{=}O$, by Green *et al*.[10,11] for acetic acid oxidation on Au/TiO_2. To produce this 2-carbon ketenylidene species from both propionate and butyrate, C–C bond breaking at the C_2–C_3 position must occur at a later stage in the oxidation process. All the experiments were repeated on the blank TiO_2 catalyst, and no ketenylidene species were formed. Because all three acids adsorb as carboxylate species on the TiO_2 support, the reaction likely takes place at the Au/TiO_2 perimeter to form C=C=O ketenylidene species, which are then adsorbed on Au sites.

Oxidation experiments were also performed using $^{18}O_2$ gas to verify the origin of the O atom in the final ketenylidene product. For both propionic and butyric acid, the main ketenylidene product was $Au_2C{=}C{=}^{16}O$, which is consistent with the C–C bond scission at the second and third carbons for both acids and the scission of one of the C–O bonds in the carboxylate on the TiO_2 support. The spectra are shown in Figure 6.3. The use of $^{18}O_2$ (g) led to very little or no formation of $Au_2C{=}C{=}^{18}O$. The possibility that the O atom comes from the TiO_2 lattice under vacuum conditions on Au/TiO_2 is also ruled out because before adding O_2 in each experiment, an IR spectrum was taken every minute for 30 min to monitor the changes on the surface. No ketenylidene was formed on the surface without O_2 gas being present in the cell. This observation is consistent with oxygen-induced activation of the C–H bonds, followed by C–O activation, leading to $Au_2C{=}C{=}O$.

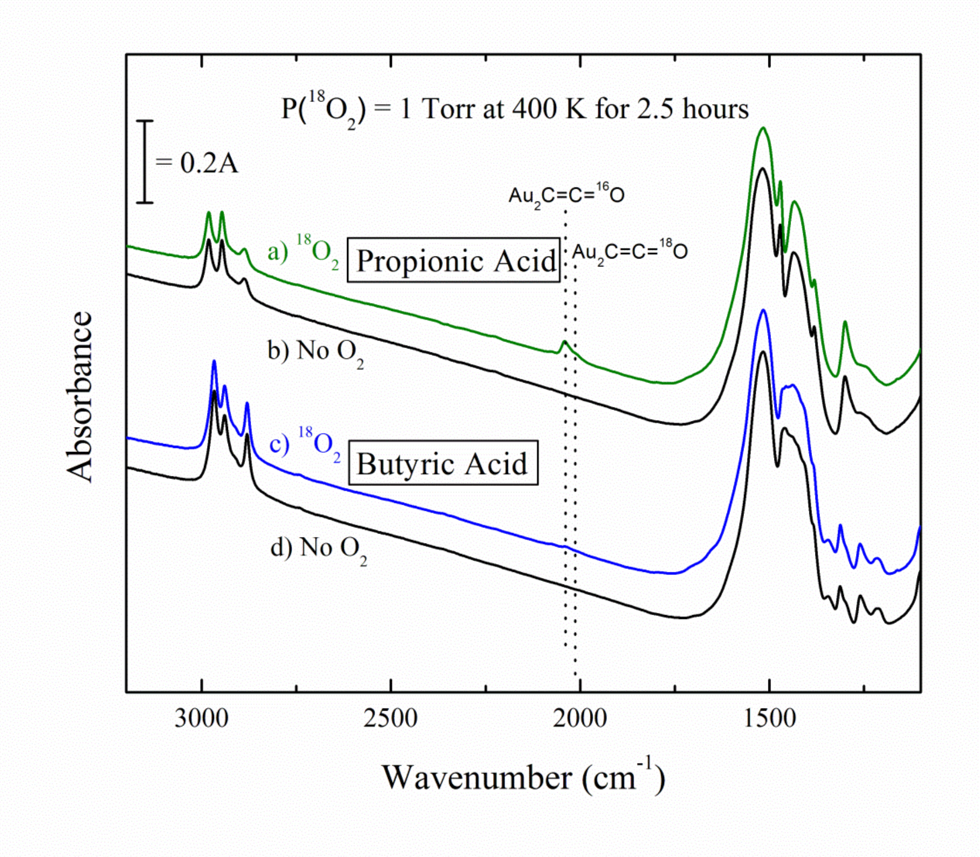

Figure 6.3 IR spectra of propionate (green curve) and butyrate (blue curve) oxidation using $^{18}O_2$ on Au/TiO_2 (a and c) and each carboxylate before oxidation (black curves) on Au/TiO_2 (b and d) at 400K.

6.3.2 *Kinetic Studies of Ketenylidene Formation from Acetate, Propionate, and Butyrate under Oxidizing Conditions*

Figure 6.4 displays the integrated absorbance at 2040 cm^{-1} of $Au_2C=C=^{16}O$ formation during oxidation over a period of 2500 s for all three acids at 400 K. Each set of experiments (I and II, performed to confirm reproducibility) in Figure 6.4a,b was carried out in a random order to ensure the integrity of the measurements. The second set of experiments in Figure 6.4b was also carried out to show the reproducible behavior of the catalyst after several cycles. The initial rates (black and white lines) of $Au_2C=C=^{16}O$ formation show a ~15-fold increase at 400 K for acetic acid compared with butyric acid for both sets of experiments. Propionic acid oxidation shows an intermediate behavior. This rate change in $Au_2C=C=^{16}O$ formation is likely due to changes in the activation enthalpy or the activation free energy to form the $Au_2C=C=O$ intermediate.

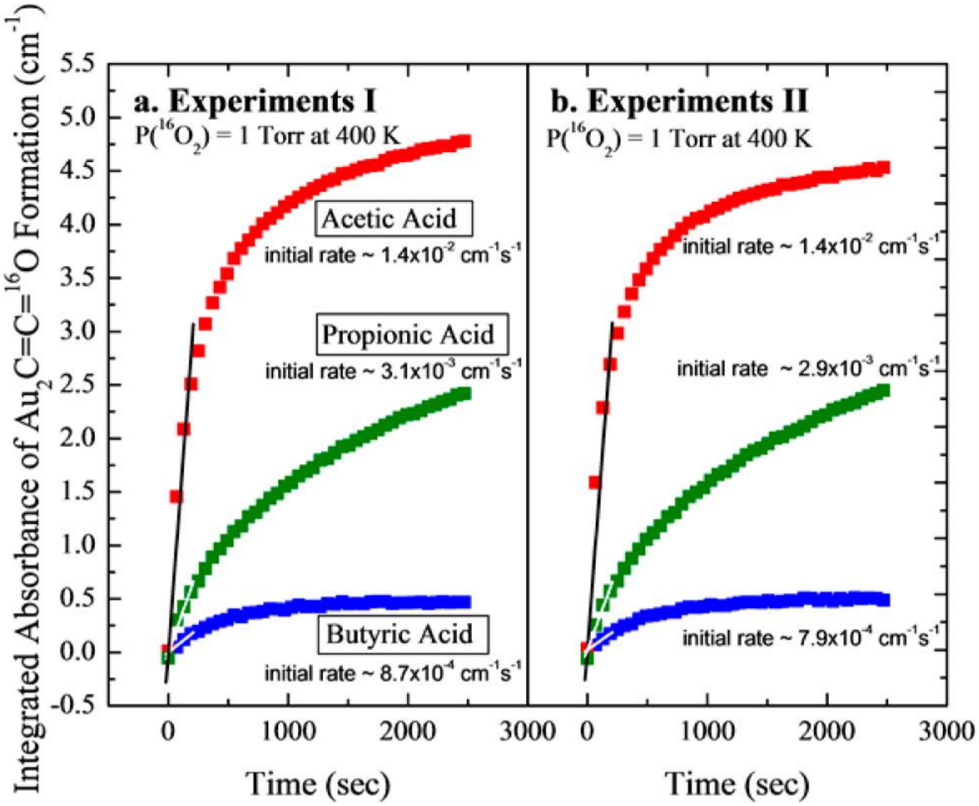

Figure 6.4 Two sets of kinetic studies of the $Au_2C=C=^{16}O$ formation from acetic acid (red curves), propionic acid (green curves), and butyric acid (blue curves) oxidation on Au/TiO_2 at 400 K. The black and white solid lines represent the initial rate fits for the experimental data.

To determine the reason for this trend, we carried out propionate oxidation experiments at various temperatures between 400 and 440 K and butyrate oxidation experiments at temperatures between 400 and 420 K, as shown in Figure 6.5a,b. This temperature range was chosen to avoid slow kinetics at 370 K (lowest tested temperature that shows $Au_2C=C={}^{16}O$ formation) and to avoid desorption or decomposition of the ketenylidene species at temperatures above 440 K. The initial rate of each reaction was fit to a first-order kinetic model to obtain a rate constant, k. Figure 6.5c shows the Arrhenius plots used to calculate the activation energies, E_a, for each acid. The acetic acid data were obtained from previous experiments performed by Green *et al*.[11] The slopes of the lines for ln(initial rate) vs 1/T (K^{-1}) for $Au_2C=C={}^{16}O$ formation from propionate and butyrate reported in Figure 6.5c were used to calculate activation barriers of 1.5 ± 0.2 eV for both 3- and 4-carbon carboxylate species, which are similar to the observed E_a of 1.6 ± 0.2 eV for $Au_2C=C={}^{16}O$ formation from acetic acid. The similarity in E_a values implies the change in rates in Figure 6.4 for the three carboxylates is not the result of simple differences in the apparent activation energy (E_a) in the $Au_2C=C={}^{16}O$ formation process, where barrier differences are proposed to govern the rates of the oxidation of the three carboxylate species.

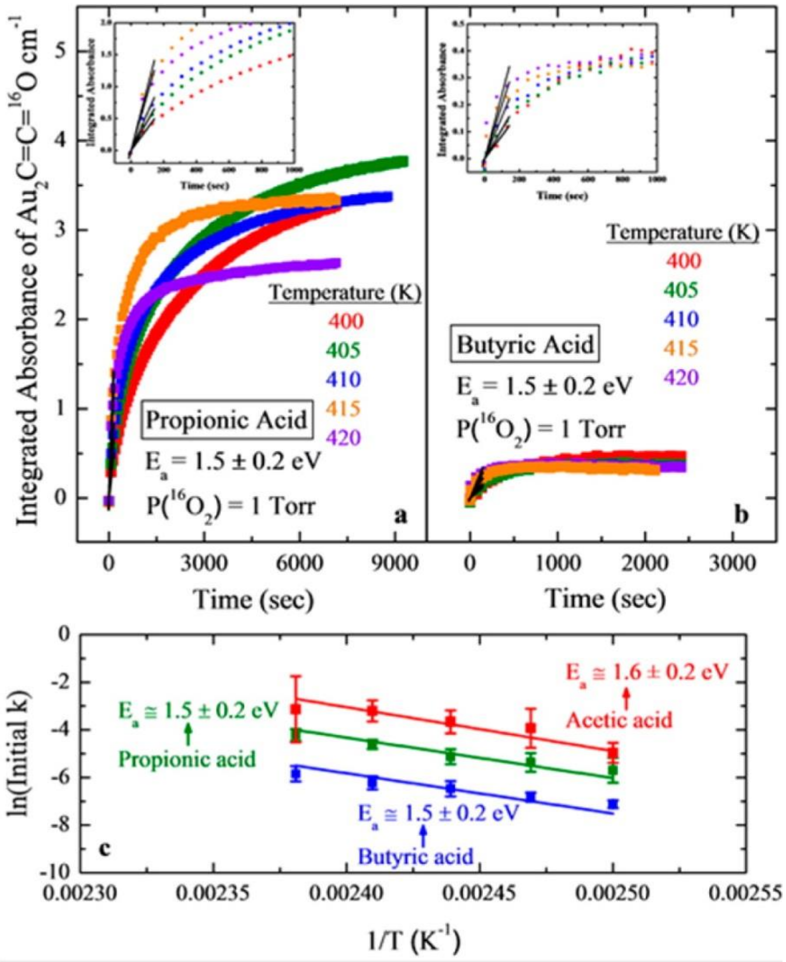

Figure 6.5 Integrated absorbance plots of Au$_2$C=C=^{16}O formation during oxidation at different temperatures are fitted to initial rate kinetics for (a) propionic acid and (b) butyric acid. (c) The activation energies of formation from acetic acid (red), propionic acid (green), and butyric acid (blue) are compared in the Arrhenius plot. Data for acetic acid were taken from ref [11].

The measured rate constants, shown in Figure 6.5, decrease in magnitude as one proceeds from acetate to propionate to butyrate while exhibiting similar activation energies. The reaction proceeds forward at slower rates as the alkyl group becomes more bulky. This observation indicates that the changes in rate are not due to changes in the enthalpies of activation but may be the result of entropic changes. We examine the changes in entropy and free energy in more detail in Section 6.3.5.

6.3.3 Deuterium Kinetic Isotope Effect (DKIE) Study of Propionate and Butyrate During Oxidation on the Au/TiO$_2$ Catalyst

To determine if C–H bonds are involved in the rate-determining step of the oxidative dehydrogenation reaction, we performed the same oxidation experiments at 400 K using deuterated propionic acid. Figure 6.6a shows the integrated absorbance of the $Au_2C=C=^{16}O$ formation as a function of time for both deuterated propionic acids (CD_3CH_2COOH (red curve) and CH_3CD_2COOH (blue curve)) and propionic acid (CH_3CH_2COOH (black curve)). The deuterated acid oxidation experiments were performed in exactly the same way as previously employed, with the CH_3CH_2COOH data taken from Figure 6.4 and redisplayed here. To accurately determine the k_H/k_D ratio, a 3-point slope at every data point was obtained for all acids, and the k_H/k_D ratio was evaluated at each point. The average k_H/k_D ratio is unity to within ±10% for both deuterated acids at all levels of completion of the reaction. For CD_3CH_2COOH and CH_3CD_2COOH, the kinetic involvement of D also does not change the rates, meaning that the activation step for conversion to $Au_2C=C=^{16}O$ does not involve C–H bond scission at either the second or third carbon atoms.

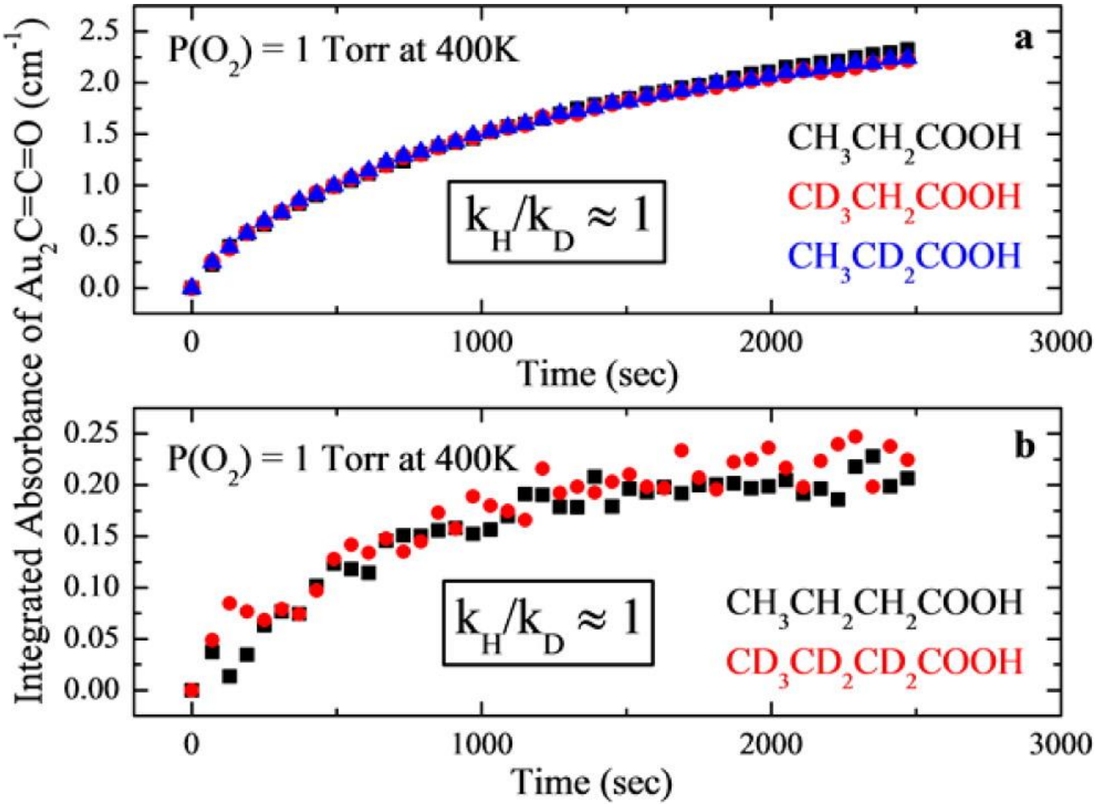

Figure 6.6 Kinetic plots of the integrated absorbance of $Au_2C=C=O$ formation from (a) CH_3CH_2COOH (black), CD_3CH_2COOH (red), and CH_2CD_2COOH (blue) oxidation on Au/TiO_2 at 400 K; (b) $CH_3CH_2CH_2COOH$ (black) and $CD_3CD_2CD_2COOH$ (red) oxidation on Au/TiO_2 at 400 K.

Similarly, Figure 6.6b displays the rates of $Au_2C=C=^{16}O$ formation for both fully deuterated butyric acid ($CD_3CD_2CD_2COOH$ (red curve)) and butyric acid ($CH_3CH_2CH_2COOH$ (black curve)). The average k_H/k_D ratio is unity for the deuterated butyric acid, as well. According to all of the plots, no DKIE exists for propionic acid with D labeling on either carbon atom or for fully deuterated butyric acid. This means that C–H bond scission is not involved in the rate-determining step in the catalytic oxidation of the larger acids to produce $Au_2C=C=O$. In contrast, for CH_3COOH to form $Au_2C=C=^{16}O$, a DKIE of ~4 was found.[11] Detailed theoretical and kinetic analyses showed that although C–O activation was the rate-controlling step for the selective oxidation of acetic acid, the C–H activation steps preceding the C–O scission were not quasi-equilibrated, thus resulting in kinetic differences between the rates of oxidation of deuterated and nondeuterated acetic acid to form $Au_2C=C=^{16}O$ and a DKIE value of ~4.[11]

6.3.4 Kinetic Studies of Ketenylidene Hydrogenation

To understand the later intermediate steps in the oxidation mechanism leading to $Au_2C=C=O$ formation, we approached the problem by starting with the final stable, observable surface-bound product, ketenylidene. Once the ketenylidene was formed from the oxidation of propionate and the O_2 was evacuated from the cell, the catalyst was cooled to 292 K and exposed to 1.0 Torr of H_2 for 10 min at various temperatures. The FTIR spectra are shown in Figure 6.7a of the $Au_2C=C=O$ species after 10 min in the temperature range of 292–350 K. The decreasing peak absorbance at 2040 cm^{-1} is attributed to the hydrogenation of ketenylidene to produce ketene ($H_2C=C=O$) in the gas phase. A temperature-programmed desorption experiment confirms the production of ketene in the gas phase. Figure 6.7b shows the normalized integrated absorbance plots of ketenylidene hydrogenation at various temperatures fitted to first-order kinetics to determine the E_a for hydrogenation. The Arrhenius plot in Figure 6.7 insert c yields $E_a = 0.21 \pm 0.05$ eV.

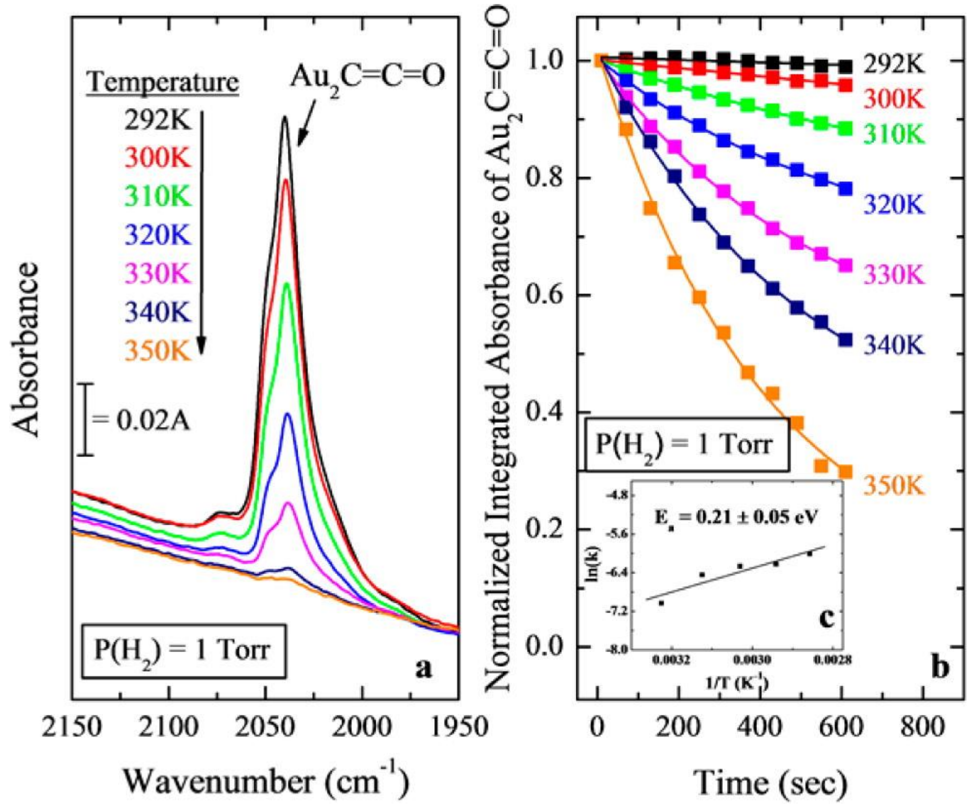

Figure 6.7 (a) IR spectra of $Au_2C=C=O$ after 10 min in 1 Torr of H_2 at various temperatures on Au/TiO_2. (b) Normalized integrated absorbance plots of $Au_2C=C=O$ hydrogenation at various temperatures. The solid lines represent the first-order kinetic fits for the experimental data. Insert (c) shows the Arrhenius plot and activation energy of ketenylidene hydrogenation.

This low activation barrier is consistent with a weak interaction between the ketene species and the Au surface. At the temperatures used in the oxidation experiments (400–440 K), this low activation barrier would allow for the $H_2C=C=O$ species to desorb from the surface before the final C=C=O species could form on the Au. Therefore, we conclude that after C–C bond scission, the last steps in the oxidation mechanism are the formation of either the C=C=O species or an intermediate HC=C=O species on Au which then dehydrogenates to form the C=C=O product chemisorbed on Au. The adsorbed ketene is not a precursor to $Au_2C=C=O$. These steps indicate that the C_α–H bonds must be activated before C–C and C–O bond scission, which is consistent with the early dehydrogenation steps to form C=C moieties at the second and third carbon atoms.[12]

6.3.5 *Density Functional Theory Simulations of Propionate C–C Bond Scission to Form Ketenylidene*

DFT calculations were carried out to examine plausible reaction pathways and the possible mechanism for the formation of ketenylidene from the propionate as well as the butyrate intermediates. The calculated energy diagram for ketenylidene formation from the adsorbed propionate is shown in Figure 6.8. As reported previously,[25] O_2 activation is thought to occur on dual Au–Ti^{4+} sites at the Au/TiO_2 interface. The activation energy for O–O bond breaking in the absence of CO at the Au–Ti^{4+} site was calculated to be 0.5 eV. The O adatoms that result can diffuse to other sites on the Au surface with diffusion barriers ranging from 0.2 to 0.7 eV.[26] O_2 can also be activated at defect sites such as a Ti interstitial,[27,28] which has an activation barrier similar to that at the Au–Ti^{4+} site. The atomic O that results on Au is weakly held and behaves as a base where it can carry out nucleophilic attack on the unsaturated C=C bonds and, in addition, activates weakly acidic C–H bonds.[29-34] These basic O species on Au were shown previously to play an important role in the oxidation of both ethylene and acetate on Au/TiO_2.[11,13]

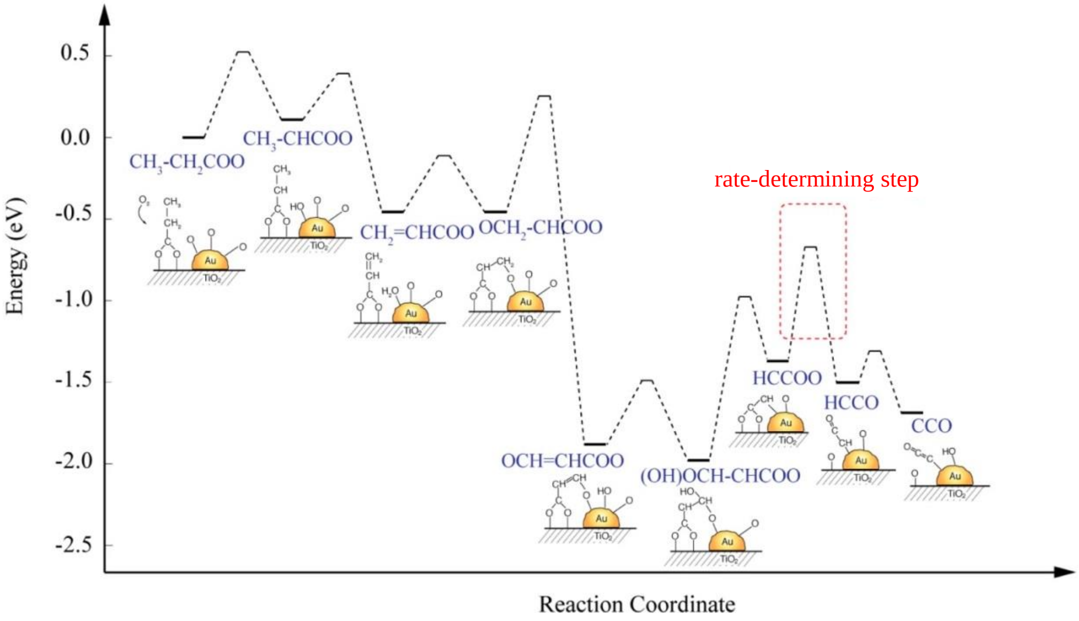

Figure 6.8 DFT-calculated reaction energy diagram for the oxidation of propionate to ketenylidene.

A range of different elementary reaction steps and possible mechanisms for producing ketenylidene from propionate were examined. Herein, we discuss only the lowest energy and most favorable path. The lowest energy route proceeds with the activation of the α-C–H bonds of $CH_3CH_2COO*^{Ti}$ by O (eq 6.1) or OH (eq 6.2) on Au with activation barriers of 0.53 and 0.28 eV, respectively, and reaction energies of 0.12 and −0.57 eV, respectively, resulting in acrylate ($CH_2{=}CH{-}COO*^{Ti}$) and H_2O. H_2O, which is weakly bound to Au with an adsorption energy of −0.08 eV, readily desorbs at 400 K.

$$CH_3CH_2COO*^{Ti} + O*^{Au} \rightarrow CH_3CHCOO*^{Ti} + OH*^{Au} \qquad (6.1)$$

$$CH_3CHCOO*^{Ti} + OH*^{Au} \rightarrow CH_2{=}CHCOO*^{Ti} + H_2O*^{Au} \qquad (6.2)$$

The $*^{Ti}$, $*^{Au}$, and $*^{TiAu}$ symbols used herein refer to the specific adsorption sites (Ti, Au, and bifunctional Ti–Au) at the Au/TiO_2 interface.

The initial C–H activation of propionate (0.46 eV) at the α-C–H bond to form $CH_3CHCOO*^{Ti}$ was found to be 0.4 eV more favorable than the activation of the same α-C–H bond of acetate (0.86 eV, Figure 6.9). The reaction energies for both reactions are endothermic and follow the same trend. The lower barrier and more favorable reaction energies for propionate are due to the stabilization that results upon activating a secondary C–H bond, as opposed to a terminal C–H bond. Although the subsquent activation of the β-C–H bond of $CH_3CHCOO*^{Ti}$ to form $CH_2{=}CHCOO*^{Ti}$ is also favored over the α-C–H bond of the CH_2COO*^{TiAu} intermediate to form $CHCOO*^{TiAu}$, the reaction energies for these steps are characteristically different in that the reaction to form the stable $CH_2{=}CHCOO*^{Ti}$ acrylate intermediate is exothermic by −0.57 eV, whereas the reaction energy to form the $CH{=}COO*^{Ti}$ product is actually endothermic. The lower barriers and the shift to exothermic reaction energies for C_3 over the C_2 intermediates are due to the stabilization that results in forming a terminal olefin in the acrylate product for C_3, C_4, and longer acids.

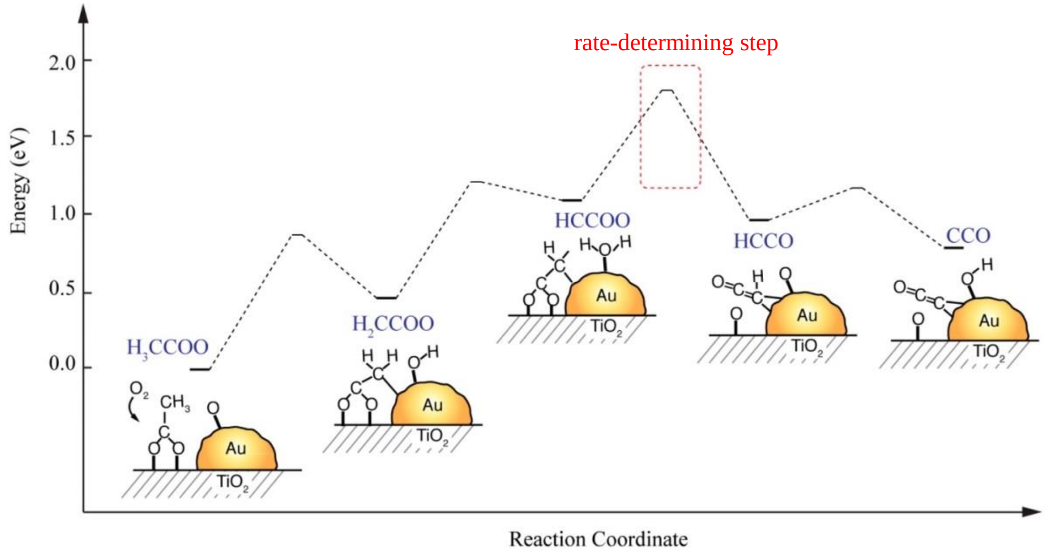

Figure 6.9 DFT-calculated reaction energy diagram for the oxidation of acetate to ketenylidene.

The reactivity of the acrylate ($CH_2{=}CHCO_2{*}^{Ti}$) product from propionate is quite different from that of the $CHCOO{*}^{TiAu}$ species from acetate. The later proceeds by the direct activation of the CO bond to form $HC{=}C{=}O{*}^{Au}$, which goes on to form the ketenylidene intermediate directly (Figure 6.9). The unsaturated C=C bond in acrylate, on the other hand, readily undergoes nucleophilic attack by the weakly held and basic O on Au to form $OCH_2–CH–COO{*}^{TiAu}$ (eq 6.3) with an activation barrier of 0.35 eV (Figure 6.8). A second O on Au can subsequently activate the C–H bond of the terminal $OCH_2–$ group to form $OCH{=}CHCOO{*}^{TiAu}$ and $OH{*}^{Au}$ (eq 6.4) with a barrier of 0.75 eV. The resulting $OH{*}^{Au}$ can then attack the terminal O=CH– group to form the $(OH)OCH–CHCOO{*}^{TiAu}$ (eq 6.5) intermediate with a barrier of 0.39 eV.

$$CH_2{=}CHCOO{*}^{Ti} + O{*}^{Au} \rightarrow OCH_2\text{-}CHCOO{*}^{TiAu} \qquad (6.3)$$

$$OCH_2\text{-}CHCOO{*}^{TiAu} + O{*}^{Au} \rightarrow OCH{=}CHCOO{*}^{TiAu} + OH{*}^{Au} \qquad (6.4)$$

$$OCH{=}CHCOO*^{TiAu} + OH*^{Au} \rightarrow (OH)OCH\text{-}CHCOO*^{TiAu} \qquad (6.5)$$

C–C bond activation takes place after the formation of (OH)OCH–CHCOO$*^{TiAu}$ (eq 6.6) and proceeds with a barrier of 1.00 eV and generates formic acid, HCOOH$*^{Au}$, as well as the HCCOO$*^{TiAu}$ products that form at the sites along the perimeter of Au/TiO_2. The C–C bond-breaking mechanism found herein is consistent with previous reports.[35,36] The carboxylate group (−COO$*^{TiAu}$) that anchors the (OH)OCH–C$^{(\alpha)}$HC$^{(\beta)}$OO$*^{TiAu}$ intermediate to the TiO_2 support sits β to the terminal acid ((OH)OC−) and facilitates the direct C–C bond scission and decarboxylation of the β-keto acid ((OH)OC−). The HCOOH$*^{Au}$ that forms binds weakly to a Au edge site and can readily desorb with an energy of 0.25 eV. The HCCOO$*^{TiAu}$ fragment that forms can subsequently undergo C–O bond scission (eq 6.7) with a barrier of 0.71 eV to form the HC=C=O$*^{Au}$ intermediate. This changes the binding mode for the HCCOO$*^{TiAu}$ reactant from a bidentate interaction involving terminal O–Ti and HC–Au interactions to a monodentate HC–Au interaction for the HC=C=O$*^{Au}$ product. The HC=C=O$*^{Au}$ can then react with O on Au to form the final $Au_2C{=}C{=}O$ product (eq 6.8) with a barrier of 0.21 eV.

$$(OH)OCH\text{-}CHCOO*^{TiAu} \rightarrow HCOOH*^{Au} + HCCOO*^{TiAu} \qquad (6.6)$$

$$HCCOO*^{TiAu} \rightarrow HC{=}C{=}O*^{Au} + O*^{Ti} \qquad (6.7)$$

$$HC{=}C{=}O*^{Au} + O*^{Au} \rightarrow C{=}C{=}O*^{Au} + OH*^{Au} \qquad (6.8)$$

The intrinsic activation barriers for all steps described above range from 0.21 to 1.00 eV, consistent with the fact that the carboxylic acid oxidation reaction readily occurs at a temperature of 400 K. To summarize, the reaction path reported here involves the activation of O_2 at the bifunctional Au–Ti^{4+} sites to generate weakly held O atoms on Au. These species are basic in character and, as such, aid in the activation of weakly acidic C–H bonds and readily undergo nucleophilic addition of oxygen to the unsaturated C=C bonds of acrylate and crotonate to form β-carboxylate acids, which promote the direct decarboxylation and C–O bond activation steps that occur at the interfacial sites for Au/TiO$_2$. The steps reported here were calculated to be the lowest energy path to form the ketenylidene.

A similar mechanism was examined for the selective oxidation and decarboxylation of the adsorbed butyrate intermediate, which is shown in detail in Figure 6.10. The results show energetics very similar to those found for the adsorbed propionate. Although the overall paths presented herein are consistent with experimental results, the relative ordering of the individual elementary steps and the exact nature of each step could be different. This should not, however, affect the overall conclusions.

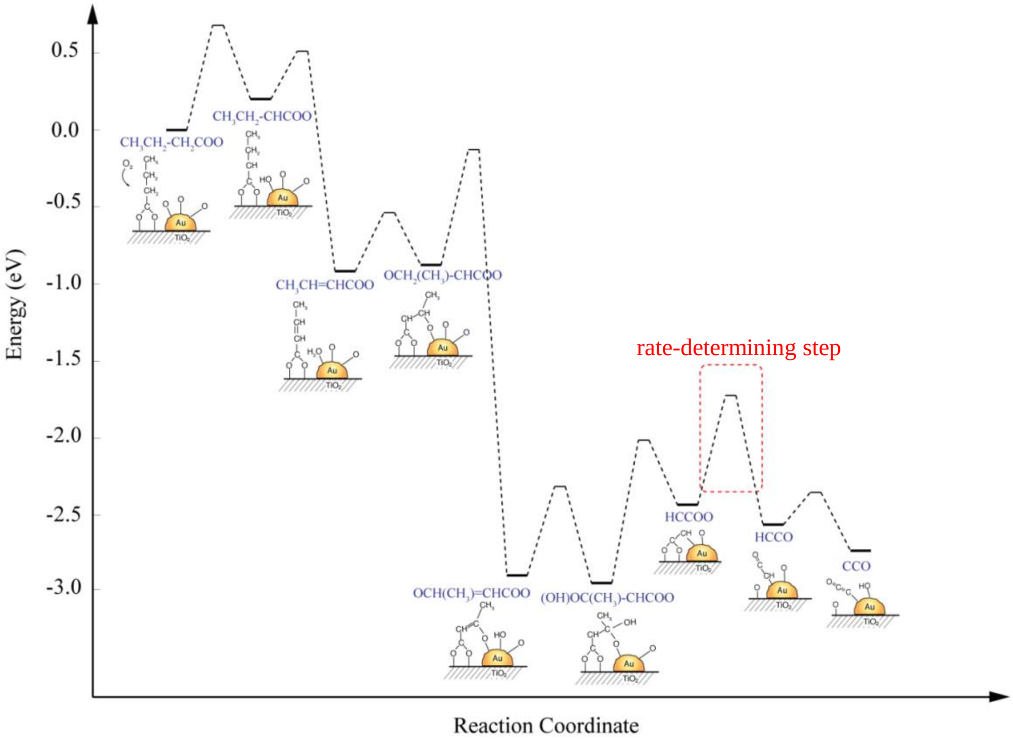

Figure 6.10 DFT-calculated reaction energy diagram for the oxidation of butyrate to ketenylidene.

The reaction energy diagram depicted in Figure 6.8 shows that the activation of propionate in general proceeds downhill via a sequence of intrinsic C–H activation and O and OH addition steps with relatively low intrinsic activation barriers between 0.5 and 0.75 eV to form the (OH)OCH–CHCOO$*^{TiAu}$ species. The (OH)OCH–CHCOO$*^{TiAu}$ intermediate resides in a deep energy well due to the high exothermicity of the preceding C–H activation steps involving the oxidative dehydrogenation of CH_3–CH–COO$*^{Au}$ to CH_2=CH–COO$*^{Au}$ and OCH_2–CHCOO$*^{TiAu}$ to O=CH–CHCOO$*^{TiAu}$, leading to the formation of very stable unsaturated olefinic or carbonyl groups. The resulting energies reported in Figure 6.8 suggest that the formation of (OH)OCH–CHCOO$*^{TiAu}$ is quasi-equilibrated. The barrier to hydrogenate OCH=CHCOO$*^{TiAu}$ back to form OCH_2–CHCOO$*^{TiAu}$ is 2.19 eV, which is over 1 eV higher than the forward apparent activation barriers needed to activate the C–C bond of (OH)OCH–CHCOO$*^{TiAu}$ (0.90 eV) or the C–O bond of HCCOO$*^{Ti}$ (1.21 eV) in the kinetically relevant step. Although the results here are similar to those for the partial oxidation of acetate (Figure 6.9) in that the kinetically relevant step involves the activation of the C–O bond, they are characteristically different in that they involve the formation of a stable quasi-equilibrated surface intermediate prior to C–O activation to form the ketenylidene, as opposed to the reactions of acetate that proceed through the formation of the much less stable HCCOO$*^{TiAu}$ intermediate.

A microkinetic model was constructed using the DFT-calculated adsorption and desorption energies, reaction energies, and activation barriers for the selective oxidation of propionic acid reported in eqs 1–8, along with preexponential values estimated from statistical mechanics and transition state theory. The resulting differential equations were solved to provide a more rigorous analysis of the resulting kinetics for the oxidation of propionic acid to form the ketenylidene. The simulations were carried out over a range of temperatures to calculate the apparent activation energy for ketenylidene formation to compare with the experiments. The results indicate that C–O activation and the availability of empty active sites control the rate of the reaction. The C–O activation step is the rate-limiting step because it has the highest energy with respect to the stable (OH)OCH-CHCOO species on the surface. The overall barrier for the kinetic simulation is higher than that from the energy diagram in Figure 6.8 because the availability of the empty site is considered in the kinetic simulations. An apparent activation energy of 1.58 eV was calculated from the microkinetic simulations, which is consistent with the value of 1.5 eV found experimentally.

As reported earlier, the large 15-fold increase in the experimental $Au_2C=C=O$ formation rates reported in Figure 6.4 in moving from the smaller acetic acid to the larger butyric acid is not the result of differences in the activation enthalpies because the apparent activation barriers are all within <0.1 eV for reactions involving the same rate-determining C–O activation for all three acids, as was shown experimentally and theoretically. The calculated barriers reported in Figure 6.8, however, refer only to changes in the electronic energies and do not include changes that result from changes in internal molecular motions in the adsorbed species or entropic changes.

To provide a more rigorous analysis and comparison of the three different acids, we instead examine the changes in Gibbs free energy barriers at 400 K for the formation of $Au_2C=C=O$. This involved calculating the translational, rotational, and vibrational partition functions for the reactants and products for the three acids. In our system, the translational and rotational parts have essentially no contributions, because the species involved are strongly adsorbed on the catalyst surface.[37] Therefore, the free energy barrier can be calculated from the contributions of the electronic and vibrational partition function. The relation between the reaction rate k and the free energy barrier ΔG can be written as

$$k \sim \frac{k_B T}{h} \exp(-\frac{\Delta G}{k_B T}) \qquad (6.9)$$

where T is the temperature, k_B is the Boltzmann constant, and h is the Planck constant. The $Au_2C{=}C{=}O$ formation rate ratio for acetic acid (k_1) and propionic acid (k_2) can be expressed by:

$$\frac{k_1}{k_2} = \exp(-\frac{\Delta G_1 - \Delta G_2}{k_B T}) \qquad (6.10)$$

where k_1 and k_2 are the rates for acetic acid and propionic acid, respectively, and ΔG_1 and ΔG_2 are the free energy barriers for acetic acid and propionic acid, respectively. The calculated $\Delta G_1 - \Delta G_2$ is −0.02 eV, which results in:

$$\frac{k_1}{k_2} = \exp\left(-\frac{-0.02}{k_B T}\right) \approx 2 \qquad (6.11)$$

This is consistent with the experimental data in Figure 6.4, in which $k_1/k_2 = 4.7$. It should be noted, though, that the energy differences here are on the order of 0.1 eV, which is less than the accuracy of DFT and within the experimental error limits.

6.3.6 *Density Functional Theory Simulations of DKIE of Unity for Propionate Acid Oxidation*

The absence of a DKIE in the experiments carried out herein on propionate and butyrate indicate that the C–H activation steps are not kinetically involved in the overall oxidation process. This is quite different from the results for acetate oxidation, which finds a DKIE value of ~4, which indicates that the C–H bond is kinetically relevant in the oxidation of the acetate. The rate of the oxidation of the larger carboxylate species as presented in Section 6.3.5 is controlled by the rate of C–O activation, in which the C–H activation steps are either equilibrated or occur after C–O activation. All of the C–H activation steps except for the last one involving $HCCO*^{Au}$ to $Au_2C{=}C{=}O$ occur before C–O bond activation that occurs in the rate-controlling step. The kinetic analyses presented earlier and the microkinetic simulations show that

(OH)OCH–CHCOO*^{TiAu} intermediate is quasi-equilibrated, and as such, the C–H activation steps involved in its formation do not contribute to the kinetics of ketenylidene formation. As a result, there should be no DKIE for propionic acid or butyric acid oxidation. Microkinetic simulations discussed in Section 6.3.5 were used to directly simulate the oxidation of H- and D-labeled propionate and reveal that the DKIE of the reaction is equal to 1. The concentrations of CH_3CH_2COO, CH_2=CHCOO, and C=C=O intermediates plotted vs time (Figure 6.11) indicate that the ketenylidene formation rates are the same for both the H-labeled propionate and D-labeled propionate, which further confirms the experimental absence of a DKIE for the higher carboxylate species.

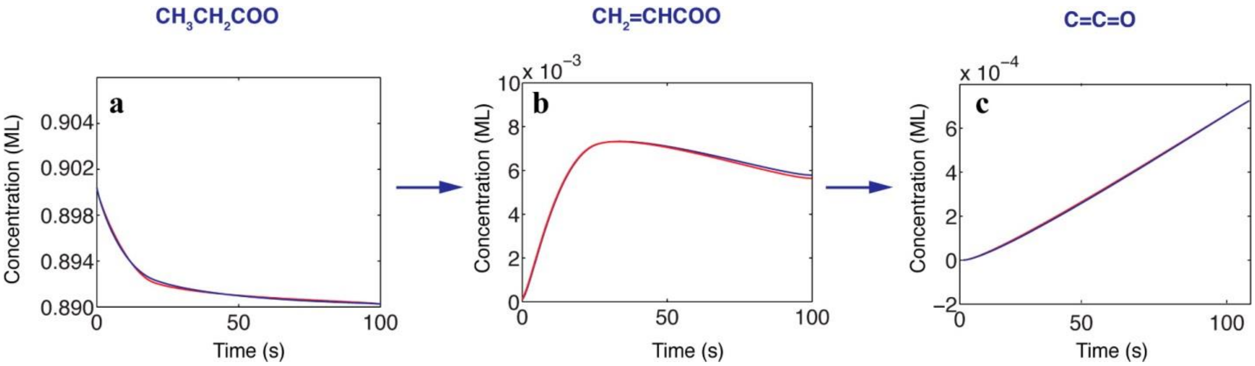

Figure 6.11 A comparison of surface concentrations of (a) CH_3CH_2COO (or CD_3CD_2COO), (b) CH_2=CHCOO (or CD_2=CDCOO), and (c) C=C=O intermediates at the Au–Ti^{4+} interface as a function of time derived from microkinetic simulations carried out for the partial oxidation of deuterium labeled and unlabeled adsorbed propionate.

Although acetate and propionate oxidative degradation are both controlled by C–O activation steps, they result in rather different DKIE values. The DKIE for acetate is ~4, which indicates a strong kinetic isotope effect. The DKIE for propionate, on the other-hand, is ~1, which would indicate the absence of a kinetic isotope effect. The differences are the result of differences in the overall reaction energies for C–H bonds that precede the C–O activation step. Acetate oxidation occurs via the activation of terminal C–H bonds of CH_3COO^{*Ti} to form H_2CCOO^{*TiAu} and

$HCCOO^{*TiAu}$ intermediates that are higher in energy and therefore formed by an endothermic process. As such, the reaction is not quasi-equilibrated. As a result, there are differences in the concentration of HCCOO* and DCCOO* intermediates that form on the surface and, thus, differences in the rate of oxidation for the deuterium labeled and unlabeled acetate, even though the reaction is controlled by the rate of C–O activation. The selective oxidation of propionate, on the other hand, rapidly equilibrates to form the stable $(OH)OCH{-}CHCOO^{*TiAu}$ intermediate that subsequently undergoes C–O activation in the rate-limiting step. As such, the C–H bond is not involved in any of the kinetically relevant steps and does not lead to any differences in the concentration of the propionate intermediates in these steps (as shown in Figure 6.11b,c); therefore, there are no kinetic isotope effects.

6.3.7 Theoretical Studies of Ketenylidene Hydrogenation

Subsequent DFT calculations were carried out to determine the site for hydrogen addition to the $Au_2C{=}C{=}O$ intermediate for H addition as well as the rates for hydrogenating the ketenylidene, as shown in Figure 6.12. Hydrogen was found to preferentially attack the terminal C atom of the C=C=O species bonded to the Au over that of the O atom or the central C atom. The second hydrogen also preferentially attacks the terminal C–Au moiety, resulting in the formation of the $H_2C{=}C{=}O$ intermediate that then desorbs from the surface. The results are consistent with the experimental results, which indicate that the $Au_2C{=}C{=}O$ species can be hydrogenated to form $H_2C{=}C{=}O$, which leaves the surface. However, because the $Au_2C{=}C{=}O$ species remains on the surface during the oxidation reaction and after evacuation, in contrast to ketene, $H_2C{=}C{=}O$, ketene does not appear to be an intermediate in the formation of $Au_2C{=}C{=}O$ because it would readily desorb before undergoing subsequent reaction.

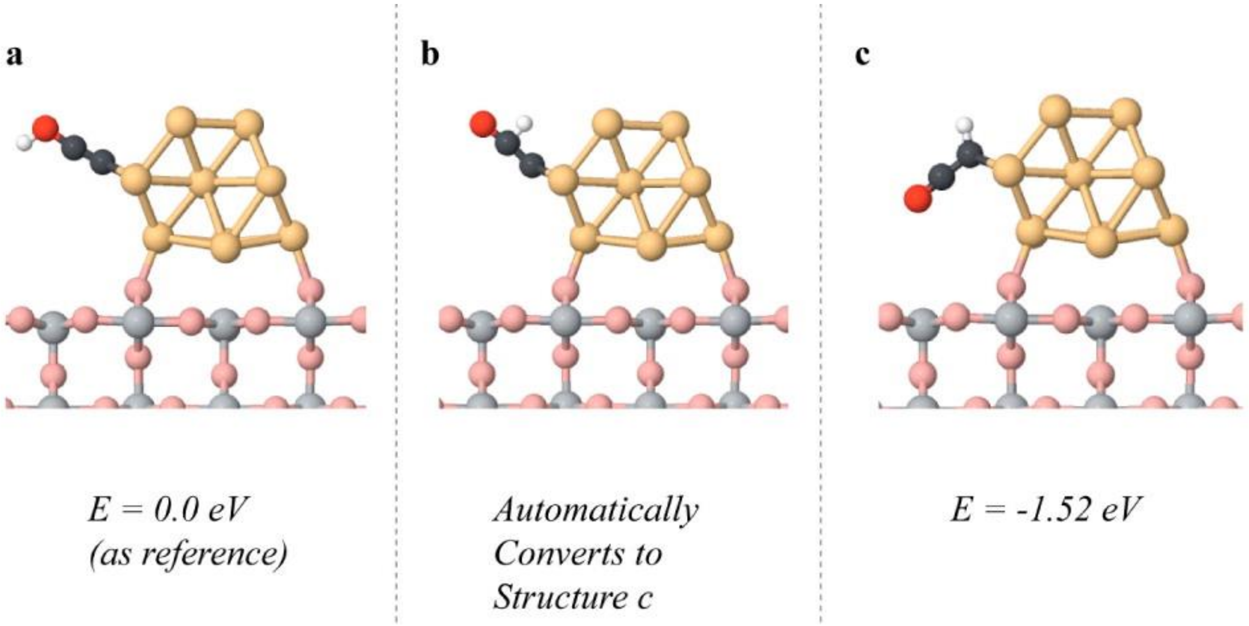

Figure 6.12 A comparison of the DFT calculated stabilities for the hydrogen addition to (a) the terminal O, (b) the central C, and (c) the end C bound to Au. The Ti atoms, the O in the TiO_2 lattice, adsorbed O, C atoms, and H atoms are shown in gray, pink, red, black, and white, respectively. The energies are reported in electron volts.

6.3.8 Pressure and Temperature Dependent Carboxylate Oxidation

The reaction temperatures and pressures for these experiments were chosen to conveniently observe the entire oxidation reaction, including intermediates and the final fully oxidized products. However, repeated experiments at higher O_2 pressures produce the same products but at faster rates, producing higher concentrations of fully oxidized products, such as CO_2 and H_2O. In addition, repeated experiments at higher temperatures also increase the rate of the reaction, with the reactant carboxylates on the surface being consumed until the Au/TiO_2 surface is clean again. The spectra for these experiments are shown in Figure 6.13.

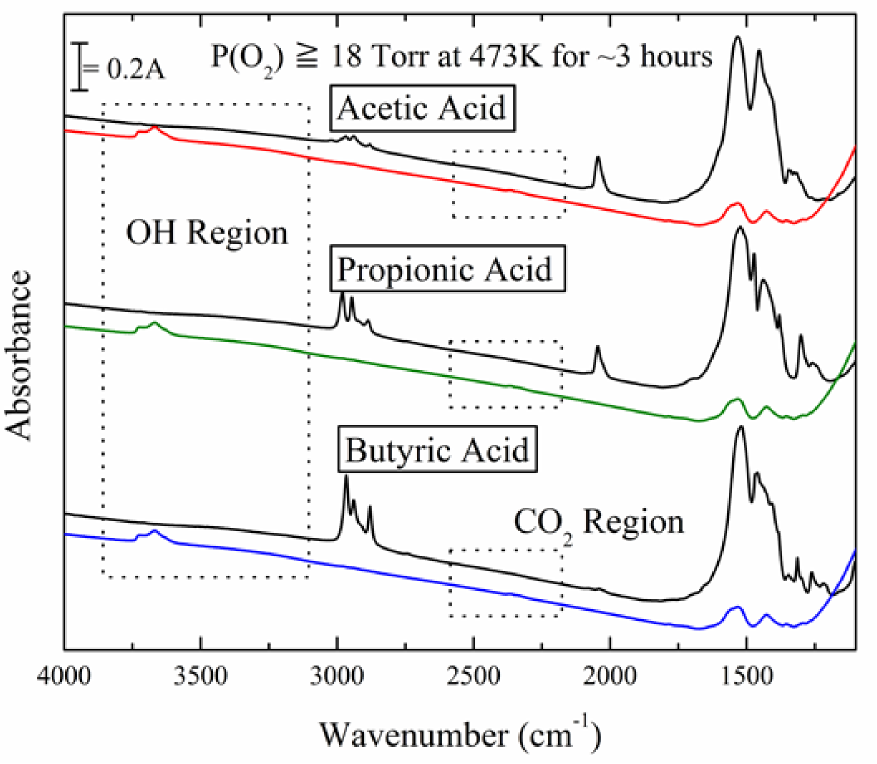

Figure 6.13 IR spectra of acetate, propionate and butyrate (black curves) oxidized on Au/TiO_2 at 1 Torr O_2 at 400K and each carboxylate after re-oxidation (red, green and blue curves) on Au/TiO_2 at 473K at ≥ 18 Torr O_2 after ~3 hours. These spectra show that the carboxylate species can be completely oxidized at high O_2 pressures and that $Au_2C=C=O$ species are also fully oxidized. The formation of traces of gas-phase CO_2 occurs as well as chemisorbed OH groups upon extensive oxidation.

6.4 Conclusions

The reaction paths and the catalytic sites necessary for the oxidative dehydrogenation of propionate and butyrate on the Au/TiO_2 catalyst surface to form $Au_2C=C=O$ species were examined using in situ IR spectroscopy, kinetic labeling studies, and density functional theoretical calculations. The results were compared with our previous studies on the oxidation of acetic acid over Au/TiO_2 to understand the changes in the reaction mechanism that occur with an increase in the chain length of the acid.

1. The oxidation of propionic and butyric acid proceeds via the dissociative adsorption of the acid on the TiO_2 substrate near the Au/TiO_2 interface to form the carboxylate intermediates (propionate and butyrate) and the activation of the O_2 at the dual Ti^{4+}–Au site (O_2 activation on low coordination Au sites on a Au particle requires a >1 eV barrier). Theoretical calculations suggest that the dehydrogenation of propionate and butyrate intermediates predominantly occurs at the C_α–C_β positions via weakly held basic O adatoms on Au to form acrylate and crotonate species, which is consistent with experimental results that show the formation of these same intermediates.[12]

2. The acrylate and crotonate intermediates can both undergo further oxidation and subsequent C–C and C–O scission to form the ketenylidene product. Theoretical results indicate that this can proceed via (i) nucleophilic addition of basic O or OH intermediates on Au to the unsaturated C=C bonds of acrylate and crotonate; (ii) C–C bond scission at the C_α-C_β position of the partially oxidized acrylate and crotonate intermediates at the dual Au–Ti^{4+} sites; (iii) C–O scission of the $HCCOO^{*TiAu}$ intermediate at the interfacial Au–Ti^{4+} sites; and (iv) O-assisted C–H activation of the HC=C=O*Au species to form the $Au_2C{=}C{=}O$ species.

3. Kinetic studies of $Au_2C{=}C{=}O$ formation for all three acids at 400 K produced a ~15-fold rate change between acetic and butyric acid. These changes do not appear in the measured activation barriers. Although theoretical simulations suggest that these differences may be due to the changes in entropy and the overall free energies of activation, the calculated energy differences are within the accuracy of density functional theory and its application, thus making it difficult to conclude that the differences are due solely to entropy.

4. Ketenylidene hydrogenation studies to produce $H_2C{=}C{=}O(g)$ rule out the possibility of an adsorbed $H_2C{=}C{=}O$ intermediate species because ketene is only weakly bound on Au/TiO_2 catalysts.

5. A DKIE of unity was determined experimentally and theoretically for propionate and butyrate oxidative dehydrogenation, providing evidence that dehydrogenation steps occur before C–O and C–C bond scission, at the α- and β-carbons of propionate and butyrate. These steps are equilibrated and do not contribute to a DKIE. The rate-limiting step involves C–O bond activation.

6. The oxidation of acetic acid that proceeds via C–H bond activation at its C_α (C_2) position is characteristically different from that for the C_3 and higher acids, which proceed via the dehydrogenation at both C_α–C_β (C_2–C_3) positions to form unsaturated carboxylates. The unsaturated carboxylates can readily undergo further oxidation and subsequent C–C and C–O rupture to form the $HCCOO^{*TiAu}$ intermediate. The acetate intermediate, however, has only C–H bonds at its C_α and therefore cannot form the unsaturated carboxylate or undergo C_α–C_β activation. Instead, for acetic acid, two of the C_α–H bonds are broken in a nonequilibrated process to directly form the same $HCCOO^{*TiAu}$ intermediate that results from the higher acids.

7. The measured activation barriers for the oxidation of acetic, propionic, and butyric acids are all controlled by the activation of the C–O bond and are quite similar. DKIE values, however, are quite different for the oxidation of acetic acid, which involves a strong kinetic isotope effect (DKIE ~ 4) versus propionic and butyric acids, which have negligible effects (DKIE ~ 1). The difference appears to be due to the fact that the $HCCOO^{*TiAu}$ intermediate

formed via the oxidation of acetic acid is nonequilibrated but the C_3 and higher acids proceed via the formation of a quasi-equilibrated $HCCOO*^{TiAu}$ intermediate.

References

1. Pietrangelo, A.; Hillmyer, M. A.; Tolman, W. B. Catalytic decarbonylation of biomass-derived carboxylic acids as efficient route to commodity monomers. *Green Chemistry* **2012**, *14*, 490-494.

2. Yang, X.; He, Z.; Zhou, X.; Xu, S.; Leung, K. Vibrational EELS and DFT study of propionic acid and pyruvic acid on Ni(100): Effects of keto group substitution on room-temperature adsorption and thermal chemistry. *Applied Surface Science* **2006**, *252*, 3647-3657.

3. Schulz, K. H.; Cox, D. F. Reaction pathways of C_3 carboxylates on copper (I) oxide (100): acrylic and propionic acid decomposition. *Journal of Physical Chemistry* **1992**, *96*, 7394-7398.

4. Xu, L.; Xu, Y. Activation of methyl acetate on Pd(111). *Surface Science* **2010**, *604*, 887-892.

5. Xu, L.; Xu, Y. Effect of Pd surface structure on the activation of methyl acetate. *Catalysis Today* **2011**, *165*, 96-105.

6. Davis, J.; Barteau, M. Hydrogen bonding in carboxylic acid adlayers on Pd(111): evidence for catemer formation. *Langmuir* **1989**, *5*, 1299-1309.

7. Holz, M. C.; Kähler, K.; Tölle, K.; van Veen, A. C.; Muhler, M. Gas-phase oxidation of 2-propanol over Au/TiO_2 catalysts to probe metal–support interactions. *Physica Status Solidi (B)* **2013**, *250*, 1094-1106.

8. Hansen, E.; Neurock, M. First-principles based kinetic simulations of acetic acid temperature programmed reaction on Pd(111). *The Journal of Physical Chemistry B* **2001**, *105*, 9218-9229.

9. Lu, J.; Behtash, S.; Heyden, A. Theoretical Investigation of the Reaction Mechanism of the Decarboxylation and Decarbonylation of Propanoic Acid on Pd(111) Model Surfaces. *The Journal of Physical Chemistry C* **2012**, *116*, 14328-14341.

10. Green, I. X.; Tang, W.; Neurock, M.; Yates, Jr., J. T. Localized Partial Oxidation of Acetic Acid at the Dual Perimeter Sites of the Au/TiO_2 Catalyst--Formation of Gold Ketenylidene. *Journal of the American Chemical Society* **2012**, *134*, 13569-13572.

11. Green, I. X.; Tang, W.; Neurock, M.; Yates, Jr., J. T. Mechanistic Insights into the Partial Oxidation of Acetic Acid by O_2 at the Dual Perimeter Sites of a Au/TiO_2 Catalyst. *Faraday Discussions* **2013**, *162*, 247-265.

12. McEntee, M.; Tang, W.; Neurock, M.; Yates, Jr., J. T. Selective Catalytic Oxidative-Dehydrogenation of Carboxylic Acids—Acrylate and Crotonate Formation at the Au/TiO_2 Interface. *Journal of the American Chemical Society* **2014**, *136*, 5116-5120.

13. Green, I. X.; McEntee, M.; Tang, W.; Neurock, M.; Yates, Jr., J. T. Direct Formation of Acetate from the Partial Oxidation of Ethylene on a Au/TiO_2 Catalyst. *Topics in Catalysis* **2013**, *56*, 1512-1524.

14. Basu, P.; Ballinger, T.; Yates, Jr., J. T. Wide temperature range IR spectroscopy cell for studies of adsorption and desorption on high area solids. *Review of Scientific Instruments* **1988**, *59*, 1321-1327.

15. Kresse, G. Dissociation and sticking of H_2 on the Ni(111),(100), and (110) substrate. *Physical Review B* **2000**, *62*, 8295.

16. Liao, L. F.; Lien, C. F.; Lin, J. L. FTIR study of adsorption and photoreactions of acetic acid on TiO_2. *Physical Chemistry Chemical Physics* **2001**, *3*, 3831-3837.

17. Hasan, M.; Zaki, M.; Pasupulety, L. Oxide-catalyzed conversion of acetic acid into acetone: an FTIR spectroscopic investigation. *Applied Catalysis A: General* **2003**, *243*, 81-92.

18. Mattsson, A.; Osterlund, L. Adsorption and photoinduced decomposition of acetone and acetic acid on anatase, brookite, and rutile TiO_2 nanoparticles. *The Journal of Physical Chemistry C* **2010**, *114*, 14121-14132.

19. Chen, Y. K.; Lin, Y. F.; Peng, Z. W.; Lin, J. L. Transmission FT-IR study on the adsorption and reactions of lactic acid and poly (lactic acid) on TiO_2. *The Journal of Physical Chemistry C* **2010**, *114*, 17720-17727.

20. Li, N.; Sun, S. In situ FTIR spectroscopic studies of the electrooxidation of C_4 alcohol on a platinum electrode in acid solutions Part I. Reaction mechanism of 1-butanol oxidation. *Journal of Electroanalytical Chemistry* **1997**, *436*, 65-72.

21. Weng, Z.; Ni, X.; Yang, D.; Wang, J.; Chen, W. Novel photopolymerizations initiated by alkyl radicals generated from photocatalyzed decarboxylation of carboxylic acids over oxide semiconductor nanoparticles: Extended photo-Kolbe reactions. *Journal of Photochemistry and Photobiology A.* **2009**, *201*, 151-156.

22. Sondag, A. H. M.; Raas, M. C.; Van Velzen, P. N. T. Contamination of aluminium oxide surfaces in ambient air investigated by FTIR MSR and TOF SIMS. Chemisorption of aliphatic carboxylic acids. *Chemical Physics Letters* **1989**, *155*, 503-510.

23. Thomas, A. G.; Syres, K. L. Adsorption of organic molecules on rutile TiO_2 and anatase TiO_2 single crystal surfaces. *Chemical Society Reviews* **2012**, *41*, 4207-4217.

24. Gutiérrez-Sosa, A.; Martínez-Escolano, P.; Raza, H.; Lindsay, R.; Wincott, P. L.; Thornton, G. Orientation of carboxylates on TiO_2(110). *Surface Science* **2001**, *471*, 163-169.

25. Green, I. X.; Tang, W.; Neurock, M.; Yates, Jr., J. T. Spectroscopic observation of dual catalytic sites during oxidation of CO on a Au/TiO_2 catalyst. *Science* **2011**, *333*, 736-739.

26. Green, I. X.; Tang, W.; McEntee, M.; Neurock, M.; Yates, Jr., J. T. Inhibition at Perimeter Sites of Au/TiO_2 Oxidation Catalyst by Reactant Oxygen. *Journal of the American Chemical Society* **2012**, *134*, 12717-12723.

27. Wendt, S.; Sprunger, P. T.; Lira, E.; Madsen, G. K.; Li, Z.; Hansen, J. O.; Matthiesen, J.; Blekinge-Rasmussen, A.; Laegsgaard, E.; Hammer, B.; Besenbacher, F. The role of interstitial sites in the Ti*3d* defect state in the band gap of titania. *Science* **2008**, *320*, 1755-1759.

28. Zhang, Z.; Lee, J.; Yates, Jr., J. T.; Bechstein, R.; Lira, E.; Hansen, J. Ø; Wendt, S.; Besenbacher, F. Unraveling the diffusion of bulk Ti interstitials in rutile TiO_2(110) by monitoring their reaction with O adatoms. *The Journal of Physical Chemistry C* **2010**, *114*, 3059-3062.

29. Xu, B.; Liu, X.; Haubrich, J.; Madix, R. J.; Friend, C. M. Selectivity Control in Gold-Mediated Esterification of Methanol. *Angewandte Chemie International Edition* **2009**, *48*, 4206-4209.

30. Liu, X.; Madix, R. J.; Friend, C. M. Unraveling molecular transformations on surfaces: a critical comparison of oxidation reactions on coinage metals. *Chemical Society Reviews* **2008**, *37*, 2243-2261.

31. Madix, R. J.; Auerbach, D. *Surface reactions;* Springer-Verlag New York: **1994**; Vol. 34, p 5-53.

32. Roldan, A.; Torres, D.; Ricart, J. M.; Illas, F. On the effectiveness of partial oxidation of propylene by gold: A density functional theory study. *Journal of Molecular Catalysis A: Chemical* **2009**, *306*, 6-10.

33. Zope, B. N.; Hibbitts, D. D.; Neurock, M.; Davis, R. J. Reactivity of the gold/water interface during selective oxidation catalysis. *Science* **2010**, *330*, 74-78.

34. Camellone, M. F.; Zhao, J.; Jin, L.; Wang, Y.; Muhler, M.; Marx, D. Molecular Understanding of Reactivity and Selectivity for Methanol Oxidation at the Au/TiO_2 Interface. *Angewandte Chemie International Edition* **2013**, *52*, 5780-5784.

35. Sim, W.; King, D. Mechanism of Acetone Oxidation on Ag {111}-p (4× 4)-O. *Journal of Physical Chemistry* **1996**, *100*, 14794-14802.

36. Mul, G.; Zwijnenburg, A.; van der Linden, B.; Makkee, M.; Moulijn, J. A. Stability and Selectivity of Au/TiO_2 and Au/TiO_2/SiO_2 Catalysts in Propene Epoxidation: An *In Situ* FT-IR Study. *Journal of Catalysis* **2001**, *201*, 128-137.

37. Laursen, S.; Linic, S. Geometric and electronic characteristics of active sites on TiO_2-supported Au nano-catalysts: insights from first principles. *Physical Chemistry Chemical Physics* **2009**, *11*, 11006-11012.

Chapter 7: Electric Field Changes on Au Nanoparticles on Semiconductor Supports – The Molecular Voltmeter and Other Methods to Observe Adsorbate Induced Charge Transfer Effects in Au/TiO_2 Nanocatalysts

(modified from *JACS,* **2015**, just Accepted)

7.1 Introduction

The electrical charge that results on supported metal nanoparticle catalysts under reaction conditions is important as it controls electron transfer and catalytic transformations that occur at the active sites on the surface of these particles. Understanding the mechanisms that control charge transfer and the activation of molecules at specific sites can aid in the design of more active and selective catalysts. Charge transfer can occur between adsorbates and different sites on the metal surface as well as between adsorbates and the support. The charge transfer that occurs between atomic sites on the surface with different metal atom coordination numbers provides one of the most prevalent routes whose mechanisms date back to early studies of the work function of atomically-smooth metal surfaces compared to atomically rough surfaces as developed by Smoluchowski,[1] Gomer[2] and by Lang and Kohn.[3,4]

In addition to the local charge distribution amongst metal sites, a metal particle residing on a semiconducting oxide support can also undergo a global charging effect as a result of its electronic interaction with the semiconductor support.[5] As shown in Figure 7.1, TiO_2 is a semiconductor with a bandgap on the order of 3.1 eV. TiO_2 is typically a non-stoichiometric oxide with a slight deficiency of O^{2-} ions. This leads to upward band bending at the TiO_2 surface and the TiO_2 is designated as n-type TiO_2 as a result of the extra negative charge that resides at surface oxygen vacancy defects.[5] These vacancy defects and the excess electron charge at the surface are easily observed in STM studies.[6] However, there are also oxygen vacancy-defect electron trap states in the TiO_2 bulk which are located above the Fermi level and slightly below the bottom of the conduction band which may be partially filled with electrons. These defect sites can participate in accepting or donating electrons to adsorbed donor or acceptor molecules that bind to TiO_2. Adsorbed donor molecules contribute electrons to TiO_2 causing bulk defect sites to become more occupied. In contrast, adsorbed acceptor molecules withdraw electrons from TiO_2 thus resulting in the loss of electrons from these bulk defect sites.[7] The adsorption of donor molecules contributes to a lowering of the extent of upward band bending, while adsorption of an acceptor molecule increases upward band bending.

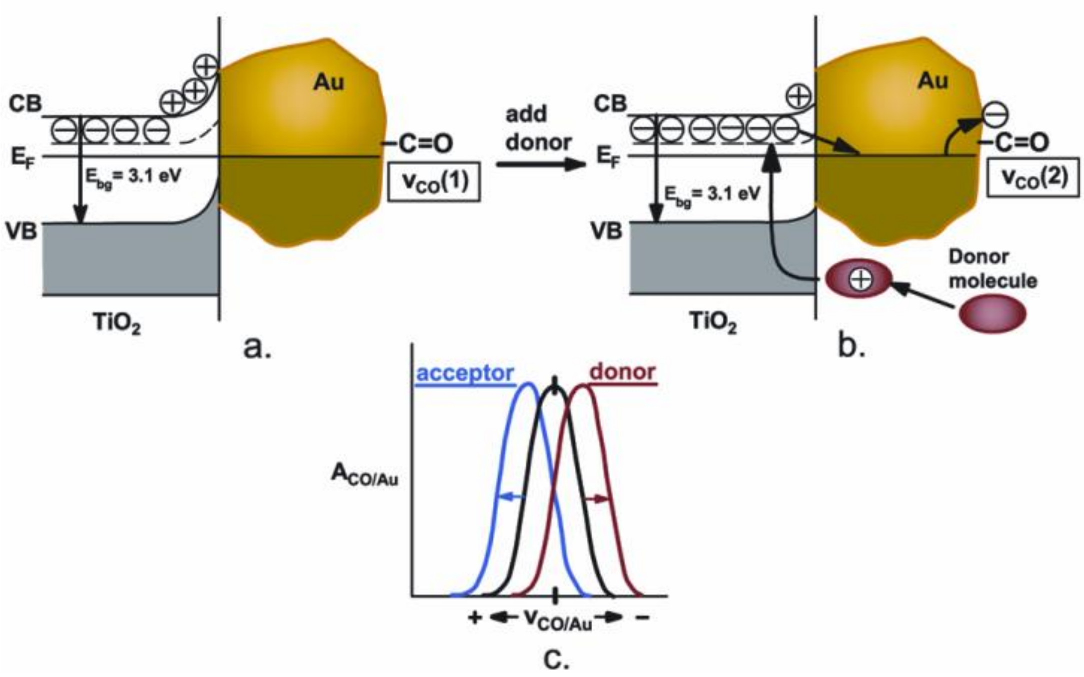

Figure 7.1 (a and b) Schematic energy levels for TiO_2 and a Au nanoparticle in contact with TiO_2. Electron donation from the donor molecule to a TiO_2 bandgap state is followed by partial electron transfer to the Au particle. Bandbending decreases with charge injection from the donor molecule to the support. In Figure 1c, a chemisorbed CO molecule shifts its ν_{CO} frequency in accordance with the change in electric field caused by changes in the electron surface density at the Au particle. The $\Delta\nu_{CO}$ change is driven in positive and negative directions by donor and acceptor molecules, respectively.

Au nanoparticles on TiO_2 also respond to charging and discharging of the TiO_2 bandgap defect states by themselves receiving or donating charge to the TiO_2 support depending on the occupancy of these bandgap states. The fractional negative charge on Au nanoparticles will be located at the outer surface of the Au particles as a result of Gauss's law.[8] Changes in the concentration of electron charges on the Au surface will change the electric field at the surface of the Au and the vibrational spectrum of the chemisorbed CO on Au will therefore shift its ν_{CO} negatively as electron density is added to the Au surface; in contrast, ν_{CO} will shift positively as electron density is removed. These ν_{CO} shifts measure the electric field on metals in accordance with the well-known Stark effect[9] often seen for adsorbates on charged metals.

In Figure 7.2, electron donation to the bandgap defect states in TiO_2[10] will influence the IR broadband absorbance of the background of the TiO_2 IR spectrum and this may be sensitively observed by transmission IR. An increase (or decrease) in electron occupancy in the bandgap states causes an increase (or decrease) in the background absorbance in the IR spectrum of the catalyst support. Figure 7.2 shows a schematic in which electrons are excited by IR photons from the TiO_2 bandgap states over a wide frequency range leading to excitation into the continuum of the TiO_2 conduction band (CB) states.

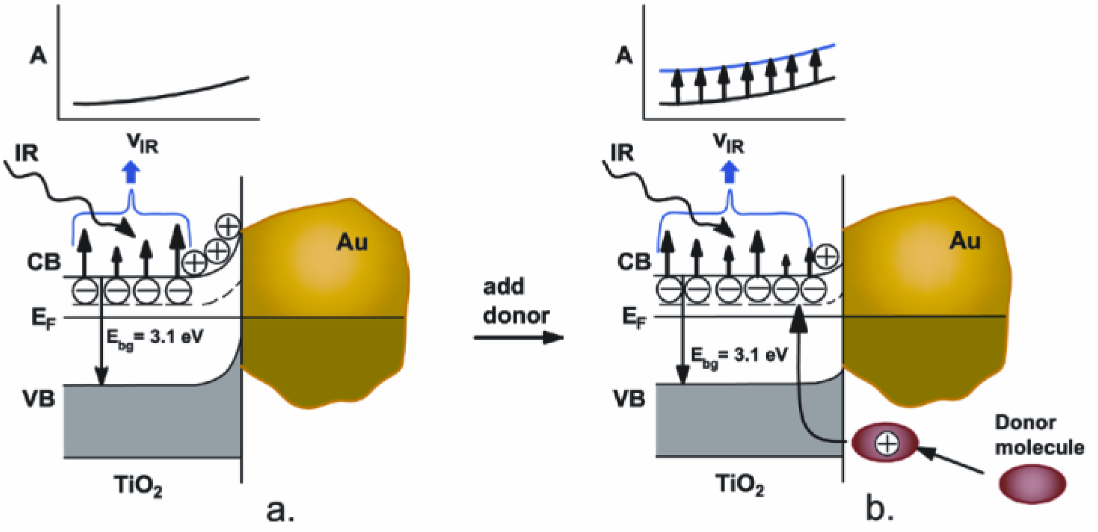

Figure 7.2 Adsorption of a donor molecule onto n-type TiO_2 results in a reduction in upward band bending and an increase in the population of the gap states near the bottom of the CB. This is detected by an enhancement of background absorbance of TiO_2 in the IR region as a result of IR excitation from the gap states into continuum CB states.

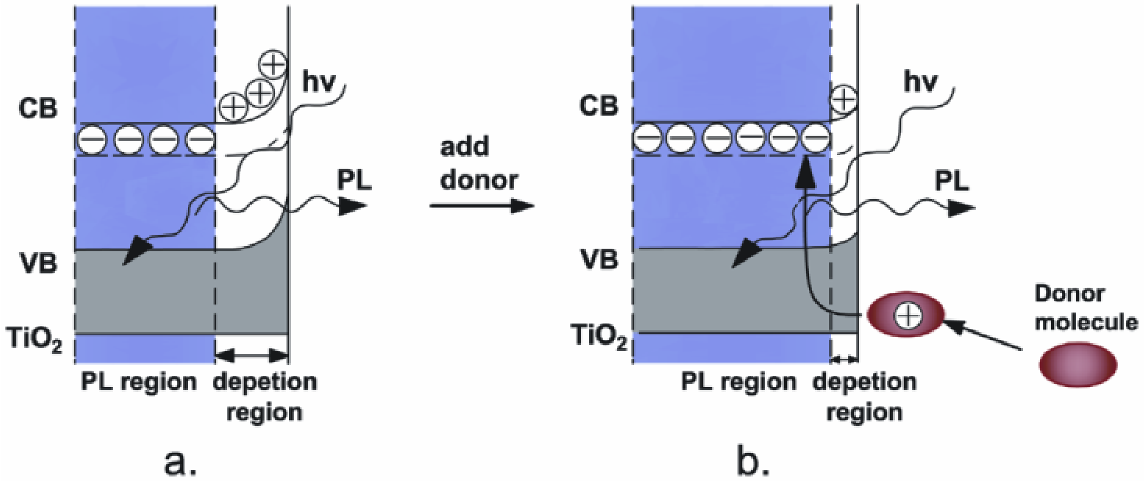

Figure 7.3 Schematic diagram showing the band bending influence of the adsorption of donor molecules on an n-type TiO_2 substrate. An increase in thickness of the PL source region by donor molecule adsorption causes the PL intensity to increase.

The role of the adsorption of donor and acceptor molecules on TiO_2 is schematically shown in Figure 7.3, where the extent of the TiO_2 bend banding that results from molecule adsorption is correlated with the intensity of emission of photoluminescence (PL) from the semiconductor TiO_2. The depth region associated with curved upward band bending leads to a rapid separation of photoexcited and oppositely moving electrons and holes, and therefore, prevents PL by electron-hole recombination in the depth region of the bent bands. This depth region of band bending is called the depletion region where activated negative and positive charge carriers rapidly move away from each other preventing recombination and PL emission. Photons incident on the TiO_2 surface can only produce PL from depths further beneath the depletion region as shown in the blue area in Figure 7.3. Hence, the reduction of both the degree of band bending and the width of the depletion region by adsorption of a donor molecule will be accompanied by an enhancement of the PL intensity.[11,12] The separate PL measurement of the opposite influence of electron donor and electron acceptor molecules on charge distribution in TiO_2 correlates well with the TiO_2 charging effects and subsequent electron transfer to Au nanoparticles as observed by other spectroscopic methods in Figure 7.1 and 7.2. It has been observed that small Au particles readily retard PL for Au/TiO_2 catalysts due to metal supported carrier particles being recombined in Au without photon emission.[13]

This chapter examines the small charging effects induced by physically-adsorbed molecules on a semiconducting TiO_2 support containing Au nanoparticles. Physically adsorbed donor or acceptor molecules influence the electronic properties of the TiO_2 support and this influence is rapidly passed to Au metal nanoparticles by charge transfer effects. The modified Stark effect has been measured previously for diatomic molecules such as chemisorbed CN on Ag electrodes and for CO on Pt, Au and other transition metal electrodes in electrolytes.[14-16] The large fields that exist in the electrical double layer of a few Å depth above the metal surface,[16] as well as for chemisorbed CO in vacuum,[14,17] and the sign and magnitude of the Stark shift that appear in these systems have been correlated to both the sign as well as the magnitude of the applied electrical field.[15,18] The Stark effect has been used recently, in addition to the field of electrochemistry, in the areas of nanomaterial antennas, sensors and plasmonic resonance studies.[19,20] In these studies, linear Stark shifts of CO are used to gauge the large local electric fields. The experiments reported here are carried out at temperatures where physical adsorption of the adsorbed donor or acceptor molecules occurs only on the oxide support. Relatively small charge effects on the support are observed with several independent spectroscopic methods, along with the associated Stark effect for adsorbed CO on Au.

The sign of the donor or acceptor charging effect measured on TiO_2 for the PL and IR behavior agrees in all three measurements. The agreement between three measurement methods for measuring the sign and magnitude of charge transfer from a physisorbed donor or acceptor molecule to the TiO_2 support and then to supported Au nanoparticles on TiO_2 leaves little doubt that small electron transfer effects are spectroscopically measurable on metal/semiconductor catalysts by multiple spectroscopies.

Other methods, such as surface-enhanced Raman spectroscopy (SERS) and picosecond laser flash photolysis experiments,[21-23] have also been used to measure electron transfer in nanomaterials, where the techniques themselves induce electron mobility. However, this article describes three unique methods that measure the electron transfer induced not by the light source, but by the adsorbed molecules on the surface. This effect may have a great importance on a catalyst, which is not being exposed to light - a catalyst being exposed to a metal oxide support which has been chemically modified for enhancement of catalytic activity.

The studies reported here provide insights as to how changes in oxide properties that result from changes in its chemical composition and its Lewis acidity or via adopting mixed (or doped) semiconducting oxides[24,25] influence the charge transfer into and out of the catalyst.

7.2 Experimental Procedures

7.2.1 Gases

CO (99.9% purity, Matheson Tri-Gas), CH_4 (>99% purity), C_2H_6 (99.999% purity, Matheson Tri-Gas), C_3H_8 (99.999% purity, Matheson Tri-Gas) and SF_6 (99.8% purity) were all further purified using a $N_2(lq)$ trap attached to a stainless steel high vacuum storage and transfer line before introducing each gas into the reaction cell.

7.2.2 IR measurements

The vacuum IR cell employed for these experiments has a base pressure of 1.0 x 10^{-8} Torr and is described in detail in Chapter 2.[26,27] Before every experiment, the Au/TiO_2 catalyst was heated to 680K in $O_2(g)$ for 30 minutes in order to remove any accumulated hydrocarbon impurities, and then cooled down to 105K. Approximately 60 mTorr of CO was introduced into the cell to achieve CO saturation adsorption and then 5 minutes later the CO(g) was evacuated for 10 minutes. The catalyst was then systematically heated up to 200K in order to desorb CO only from the TiO_2 support leaving CO chemisorbed on the Au nanoparticles. After 3 minutes at 200K, the catalyst was cooled down to the desired adsorption temperature used for the addition of modifier molecules. After 15 minutes at constant temperature, the desired donor or acceptor gas was added to the cell in incremental doses until saturation coverage was observed by FTIR of the donor or acceptor molecules on the TiO_2 or SiO_2 support. The FTIR spectrum was taken for each increment of gas added with an average of 128 scans at 2 cm^{-1} resolution. Once the catalyst was saturated with either the donor or acceptor molecule, an additional spectrum was obtained every minute for 10 minutes. Then, the catalyst was heated up in vacuum (or in partial pressure for CH_4) in 5K increments starting from the adsorption temperature in order to remove the adsorbates in small increments from the support. An IR spectrum was taken for each of these treatment temperatures as well, showing that CO IR line shifts and donor/acceptor absorption spectra exhibit reversible behavior in each case as donor or acceptor molecules are added or removed.

In addition to measuring the vibrational behavior of CO when influenced by the physisorbed donor or acceptor molecules used to modify the Au/TiO_2 catalysts, we employed the IR background shift (see Figure 7.2) which extends from about 4000 cm^{-1} to ~1000 cm^{-1} when varied electron transfer to or from the TiO_2 is caused by addition or removal of donor or acceptor molecules. It was found that this shift could be measured most easily by observations of the TiO_2 background intensity at 1900 cm^{-1} or over the 1800-2000 cm^{-1} region, where all vibrations of adsorbed species are missing.

7.2.3 PL measurements

Photoluminescence measurements were performed in an IR/PL stainless steel cell under high vacuum conditions. The base pressure of the cell was 2.0 x 10^{-9} Torr after bakeout. More detailed information about the IR/PL set up can be found elsewhere.[11] For the PL measurements, the 320 ± 10 nm (3.88 eV) excitation light was selected from a pulsed Xe source which focused power measured over time at the sample position of 9.1×10^{-5} J s^{-1} cm^{-2} (1.5×10^{14} photons cm^{-2} s^{-1}). The emitted PL light was collected by an R928 photomultiplier tube covering the range of 200-900 nm. The PL spectra were plotted employing a scan speed rate of 500 nm·min^{-1}. To minimize the specular reflection of the incident light from a CaF_2 window, all the spectra were collected 15° off a specular direction of the source light and a 390 nm cut off filter was employed.

Before each PL experiment, the TiO_2 sample was cleaned by heating in vacuum to 680 K and then introducing 0.8 Torr of O_2 for 25 min at 680 K to remove all hydrocarbon impurities. After evacuation of O_2 at 680 K, the sample was cooled down to ℓ–N_2 temperatures for PL measurements. During gas adsorption experiments, the excitation light was blocked by a shutter to avoid any influence of UV light. The surface was modified by sequential addition of known amounts of gas into the system. Following surface modification by electron donor or electron acceptor adsorbate molecules the surface was exposed to UV light for only 67 s to collect the PL spectra, and separate experiments show that this small UV exposure did not appreciably change the PL intensity.

7.2.4 DFT model and parameters

First principle density functional theory (DFT) calculations were carried out to gain insights into charge transfer between Au nanoparticles and the TiO_2 support and the changes in the CO frequency shifts for CO bound to Au/TiO_2 that occur upon the adsorption of donor and acceptor molecules on the TiO_2 support. A model Au/TiO_2 catalyst was constructed by bonding a gold nano-rod 3 atomic layers high and 3 atomic layers wide to the most stable rutile $TiO_2(110)$ surface. This supported gold nano-rod model has been used successfully in a number of previous theoretical studies to mimic the properties and reactivity of Au on different supports.[26,28-31] The TiO_2 support was modeled using a (2x3) and (4x3) surface unit cell comprised of three O-Ti-O tri-layers. A (4x3) Au/TiO_2 structure was used to calculate the effect of adsorbates on TiO_2 remote from the Au perimeter, while (2x3) Au/TiO_2 was used for the rest of calculations. The top half of the TiO_2 was fully relaxed whereas the bottom half was held fixed to the bulk TiO_2 lattice. More details about the calculations can be found in Chapter 3, Section 3.2.

7.3 Results

7.3.1 IR CO Frequency Shifts using Donor and Acceptor Adsorbate Molecules on Au/TiO_2

The first experiment is shown in Figure 7.4a displaying CO adsorbed on Au at 140K on a Au/TiO_2 catalyst before the addition of C_3H_8 donor molecules to TiO_2 (black curve). The absence of an absorbance band at 2179 cm^{-1} assigned to CO adsorbed on TiO_2 shows that CO is not adsorbed on the support following CO desorption at 200K.[31,32] The main absorbance band at ~2123 cm^{-1} is assigned to CO on metallic Au^0 sites and the shoulder at 2141 cm^{-1} is assigned to CO on $Au^{\delta+}$ sites.[31-34] From the width of the ν_{CO} band, it is likely that a superposition of CO frequencies exists characteristic of several different types of Au adsorption sites present on the Au nanoparticles. Incremental amounts of C_3H_8 were then added to the Au/TiO_2 catalyst at 140K. Based on C_3H_8 and other light alkane temperature programmed desorption experiments along with thermodynamic studies on Au (and Pt) single crystals and TiO_2 (and V_2O_3) oxides separately, C_3H_8 desorbs from Au below 140K and remains adsorbed on TiO_2 at the same temperature.[35-38] After each addition of C_3H_8 on TiO_2, an IR spectrum was taken as shown in

Figure 7.4a (grey curves). The major C-H stretch absorbance bands of propane on TiO_2 are 2964 cm^{-1} ($\nu_{as}(CH_3)$), 2944 cm^{-1} ($\nu_{as}(CH_2)$), and 2876 cm^{-1} ($\nu_s(CH_2)$) as shown in the insets of Figure 7.4.[39] Control experiments involving only C_3H_8 were performed on the pure TiO_2 catalyst as well, and the same C-H absorbance bands were observed indicating that the C_3H_8 molecules were adsorbed only on the TiO_2 support. The red curves in both the CO/Au and C_3H_8/TiO_2 IR regions represent the TiO_2 catalyst support saturated with C_3H_8 in Figure 7.4a. Saturation of the catalyst by C_3H_8 is determined by measuring the integrated absorbance of the C-H band intensity. Once the C-H bands stop growing even though more molecules are being added to the cell, the TiO_2 support is deemed to be saturated with C_3H_8 at 140K and ν_{CO} shifts are sensitive only to adsorbed C_3H_8. Multilayer formation is assumed not to occur because the temperature regime is for only monolayer coverage. As seen from the CO/Au IR bands, the frequencies for CO on both Au^0 and $Au^{\delta+}$ sites redshift toward lower frequencies as C_3H_8 is added to the TiO_2 support indicating partial electron transfer from the C_3H_8 to the support and then to the Au.

After C_3H_8 saturation (black curves in Figure 7.4b), the catalyst was heated in vacuum in 5K steps (grey curves) until the majority of the C_3H_8/TiO_2 was removed (red curves). As shown in Figure 7.4b, as C_3H_8 was removed from the TiO_2 surface, the CO/Au absorbance band blueshifts back to the original frequency, ~2123 cm^{-1}, observed before C_3H_8 adsorption. The reversibility of the CO frequency shifts suggests no chemical decomposition of the adsorbates and indicates that a reversible electron transfer occurs to and from the Au particles, induced by the weakly adsorbed C_3H_8 donor molecules on the TiO_2 support.

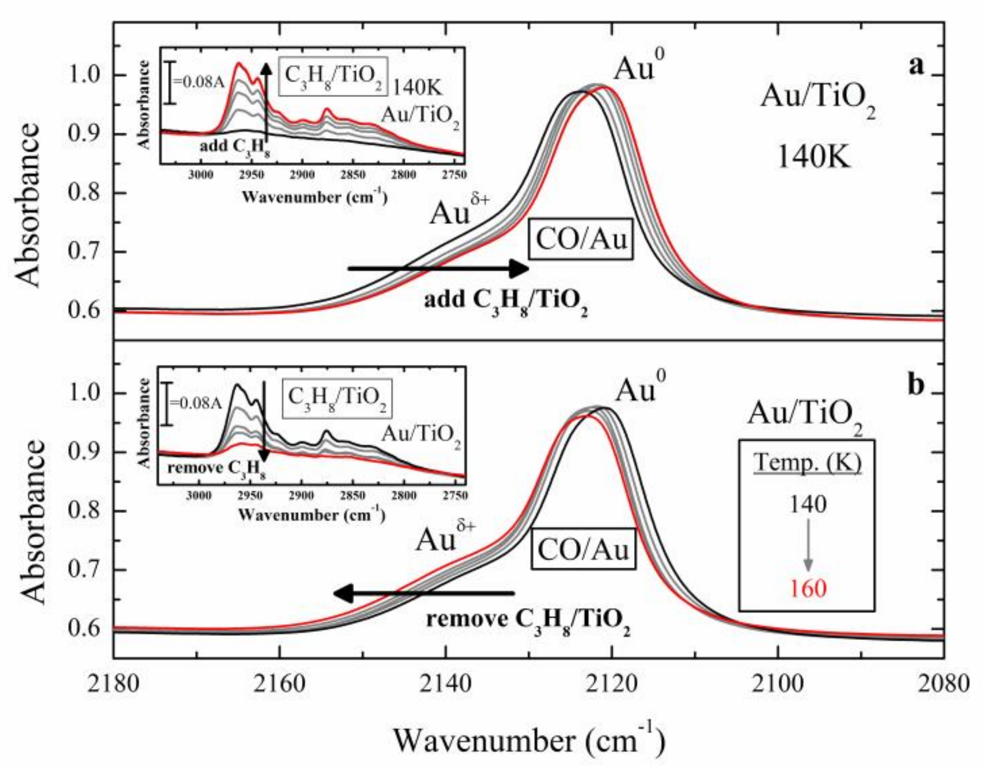

Figure 7.4 IR spectra of CO on Au as C_3H_8 (a) increases in coverage on TiO_2 to saturation (red curve) at 140K and (b) decreases in coverage on TiO_2 starting at saturation (black curve) and nearing complete desorption (red curve) after heating in small temperature intervals up to 160K. A reversible shift in the broad ν_{CO} feature is observed as caused by adsorption and desorption of C_3H_8 donor molecules on the TiO_2 support. The corresponding insets are the IR C-H stretching spectral region of physisorbed C_3H_8 on TiO_2 during (a) addition at 140K and (b) removal in the range of 140-160K. C_3H_8 exhibits reversible adsorption/desorption behavior.

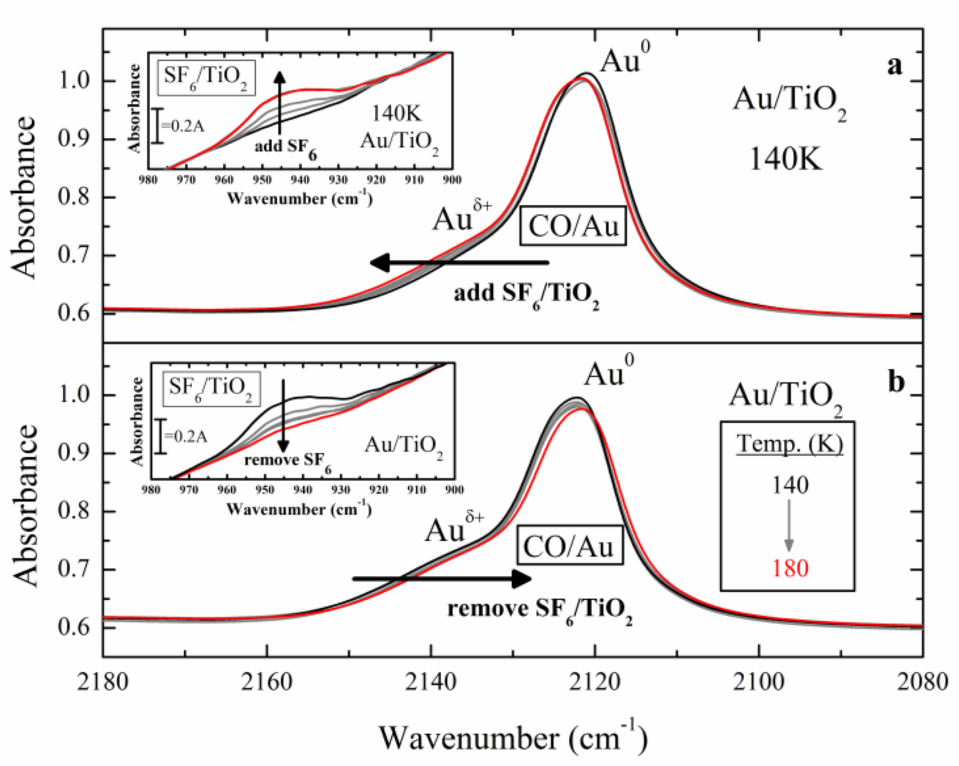

Figure 7.5 IR spectra of CO on Au as SF_6 (a) increases in coverage on TiO_2 to saturation (red curve) at 140K and (b) decreases in coverage on TiO_2 starting at saturation (black curve) and nearing complete desorption (red curve) after heating up to 180K. A reversible shift in the broad ν_{CO} feature is observed as caused by adsorption and desorption of SF_6 acceptor molecules on the TiO_2 support. The corresponding insets are the IR spectral region of SF_6 on TiO_2 during (a) addition at 140K and (b) removal in the range of 140-180K. SF_6 exhibits reversible adsorption/desorption behavior.

Similar experiments were performed using an acceptor molecule, SF_6, in order to produce an opposite electron transfer between Au and the TiO_2 support. Figure 7.5a shows the CO/Au absorbance bands before SF_6 adsorption (black curves) and after incremental additions of SF_6 (grey curves) until SF_6 saturation (red curves) occurs at 140K. The inset in Figure 7.5a displays an absorbance band of physisorbed SF_6 at 946 cm^{-1}. Gas phase SF_6 has a similar absorbance band at 948 cm^{-1} indicating only weak SF_6 binding to the Au/TiO_2 catalyst.[40] As with C_3H_8, SF_6-TPD experiments on Au single crystals and separately on metal oxides verify that SF_6 adsorbs only on TiO_2 under the experimental conditions employed here.[41,42] As shown in Figure 7.5a, when SF_6 is adsorbed on TiO_2, the CO/Au IR frequency shifts upward towards higher frequencies opposite to the effect observed when C_3H_8 adsorbs on TiO_2. Furthermore, when the catalyst is subsequently heated in 5K increments up to 180K starting from SF_6 saturation (Figure 7.5b, black curve) and ending with a clean TiO_2 surface (Figure 7.5b, red curve), the CO/Au IR frequency exhibits reversed redshifts toward lower frequencies opposite to the blueshift observed for C_3H_8 desorption.

In order to prove this IR shift phenomenon is not just specific to C_3H_8 and SF_6 molecules, similar experiments were performed using methane, CH_4, and ethane, C_2H_6 donor molecules. The experimental CO/Au IR frequency differences before and after molecular adsorption were plotted versus adsorbate coverage on Au/TiO_2 as shown in Figure 7.6a. Each centered maximum frequency of the CO on Au was subtracted from the frequency of the CO spectrum without donor or acceptor molecule adsorption to obtain the vibrational shifts. The CO spectral bands were fit to Lorentzian distribution functions to obtain the shift error bars shown in Figure 7.6a and 7.6b. Then, the integrated C-H or S-F absorbance band area for each spectrum was normalized to full-coverage spectra to yield the fractional coverage of the donor or acceptor adsorbate on the support. For CH_4, C_2H_6, and C_3H_8 adsorbed on Au/TiO_2, the maximum CO/Au IR shifts per monolayer of donor molecule are negative by ~1.0 cm^{-1} (Figure 7.6a, green squares), ~2.0 cm^{-1} (Figure 7.6a, blue squares) and ~2.8 cm^{-1} (Figure 7.6a, black squares), respectively. For SF_6 adsorbed on Au/TiO_2, the maximum CO/Au IR shifts are positive by ~1.0 cm^{-1} (Figure 7.6b, red squares).

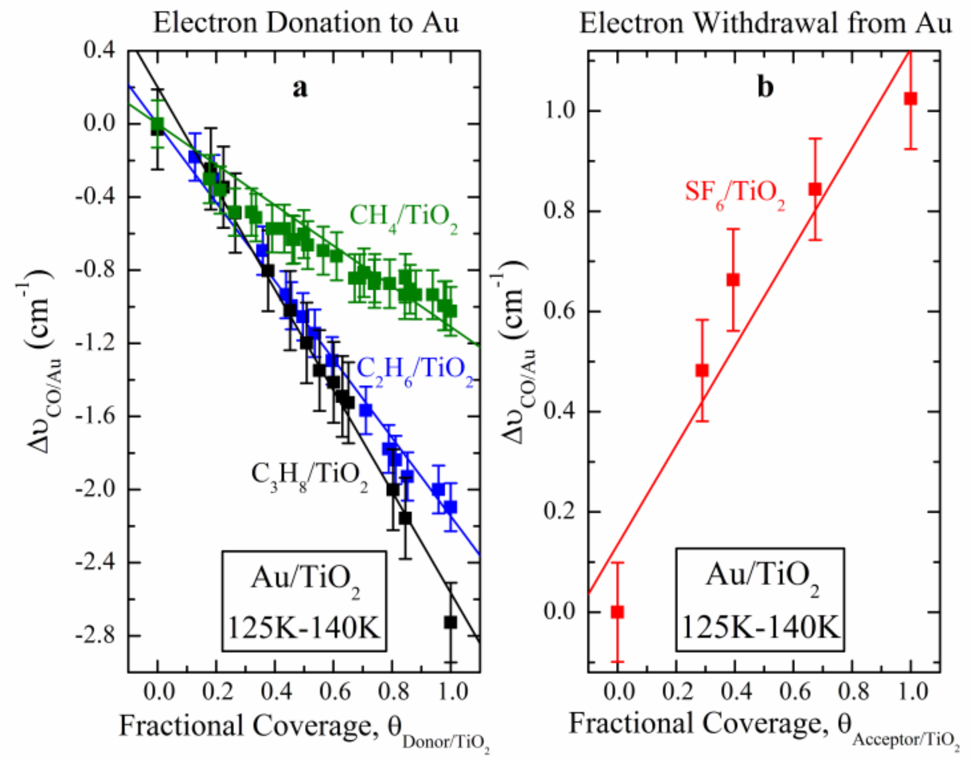

Figure 7.6 IR CO/Au frequency shifts vs adsorbate coverage on TiO_2 support for (a) donor molecules CH_4 (green squares), C_2H_6 (blue squares) and C_3H_8 (black squares) and (b) acceptor molecule SF_6 (red squares). The analytically determined errors in the measurements of $\Delta\nu_{CO/Au}$ are discussed in Section 7.3.1.

The overall absolute frequency shifts for SF_6 adsorption and desorption are smaller than for C_3H_8 induced frequency shifts. The small shifts for SF_6 compared to C_3H_8 are most likely due to the fact that Au/TiO_2 is an n-type semiconductor with an overall negative charge present on the surface before SF_6 adsorption. Thus, the negative charge character of the TiO_2 surface repels the electronegative SF_6 molecules and lowers the efficiency of electron transfer upon adsorption on TiO_2. If multilayer formation is possibly occurring, the effect is believed to be negligible compared to the effect of the molecules in direct contact with support surface.

In order to further eliminate the possibility of CO IR shifts being caused by nearby CO interactions with C_3H_8 or SF_6 on Au sites, identical experiments were done on a Au/SiO_2 catalyst

(Figure 7.7). Both the donor molecule, C_3H_8 (Figure 7.7a), and the acceptor molecule, SF_6 (Figure 7.7b), adsorb on SiO_2.

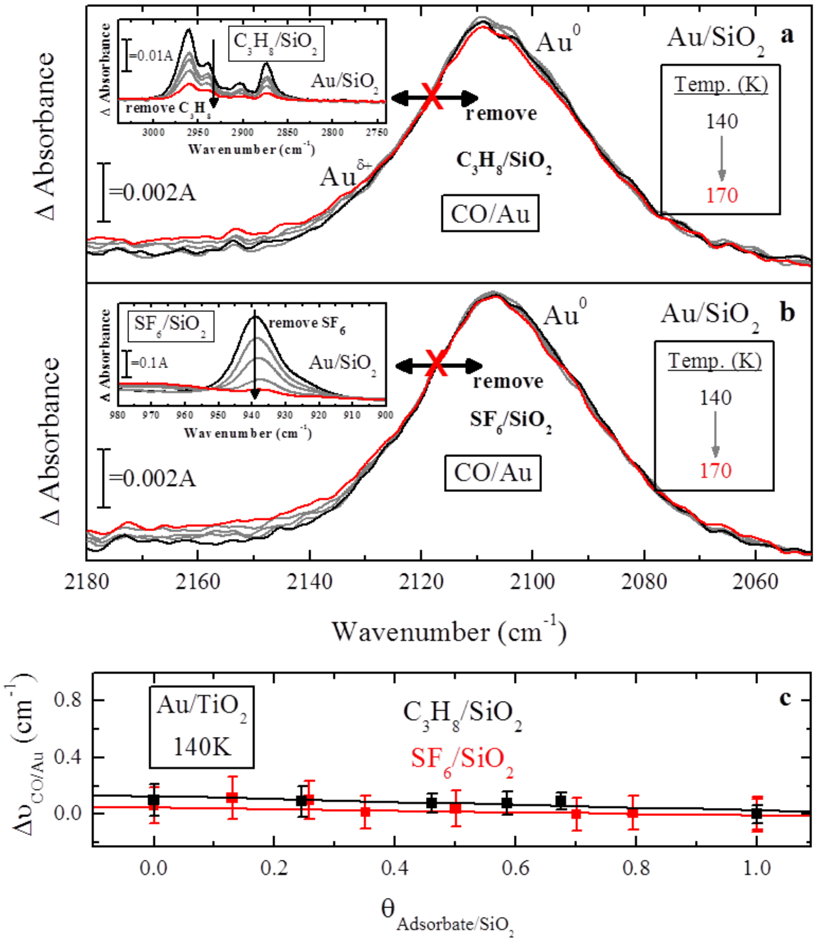

Figure 7.7 IR spectra of CO on Au/SiO_2 as (a) C_3H_8 and (b) SF_6 decrease in coverage on SiO_2 starting at saturation (black curve) and nearing complete removal (red curve) after heating up to 170K. The corresponding insets are the IR spectral region of (a) C_3H_8 and (b) SF_6 on SiO_2 during removal in the range of 140-170K. (c) The absence of IR CO/Au frequency shifts vs donor or acceptor molecule adsorption on SiO_2.

However, neither molecule induced a significant frequency shift in the CO/Au IR frequencies. For C_3H_8 and SF_6 adsorbed on Au/SiO_2, Figure 7.7c shows that the total $CO/Au/SiO_2$ IR shifts are very small or zero compared to measuring the CO frequency shifts on Au/TiO_2 (Figure 7.6). The absence of detectable CO/Au IR shifting on Au/SiO_2 compared to similar measurements on Au/TiO_2 show that the electron transfer interaction between Au and the support oxide requires that the oxide be a semiconductor with an appreciable level of charge carriers. Insulator covalent oxides, such as SiO_2, do not possess appreciable charge carriers to influence supported Au particles. Furthermore, the comparison of the results for Au/SiO_2 with those on Au/TiO_2 help to eliminate the possibility that $\Delta\nu_{CO}$ depends on donor/acceptor molecules on Au.

7.3.2 Electron Transfer to and from Au/TiO_2 as Observed from Defect Site Electron Population in the Energy Gap of TiO_2

It is well known that defect sites in the bulk, or on the surface of TiO_2, will interact with electron donor/acceptor molecules. The charge received or donated from adsorbed molecules causes a variation in the population of charge in these defect sites. The defect sites are close to the bottom of the conduction band in TiO_2. Therefore, when the sites are filled with electrons, they participate in the absorption of infrared radiation causing higher levels of electron excitation to occur from the defect into the TiO_2 conduction band. This absorption occurs over a broadband due to the energy continuum of conduction band states which may be occupied by IR excitation of defect-bound electrons and a broad background IR absorption from near 1000 cm^{-1} to 4000 cm^{-1} is observed. Similar effects have been seen by others on TiO_2.[43-46] This process has been observed also for ZnO[47] and is termed “metallization” as a result of the IR-induced electronic excitation into the continuum in the conduction band. Atomic H adsorbed on TiO_2 behaves as an electron donor resulting in additional electron occupancy of the defect states and a growth in the broad IR absorbance.[45,46] The IR absorbance due to electronic population of defect sites in single crystal rutile-TiO_2(110) has recently been attributed, in part, to the excitation of hydrogenic polaronic states which are associated with a series of sharp superimposed absorbance bands observed on top of the broad-band absorbance caused by defect bound electron excitation into the conduction band continuum.[48] This phenomenon is also observed for Au/TiO_2 catalysts during the adsorption of physically-absorbed donor or acceptor molecules on the TiO_2 support and is therefore coupled to Stark shifting of CO/Au species.

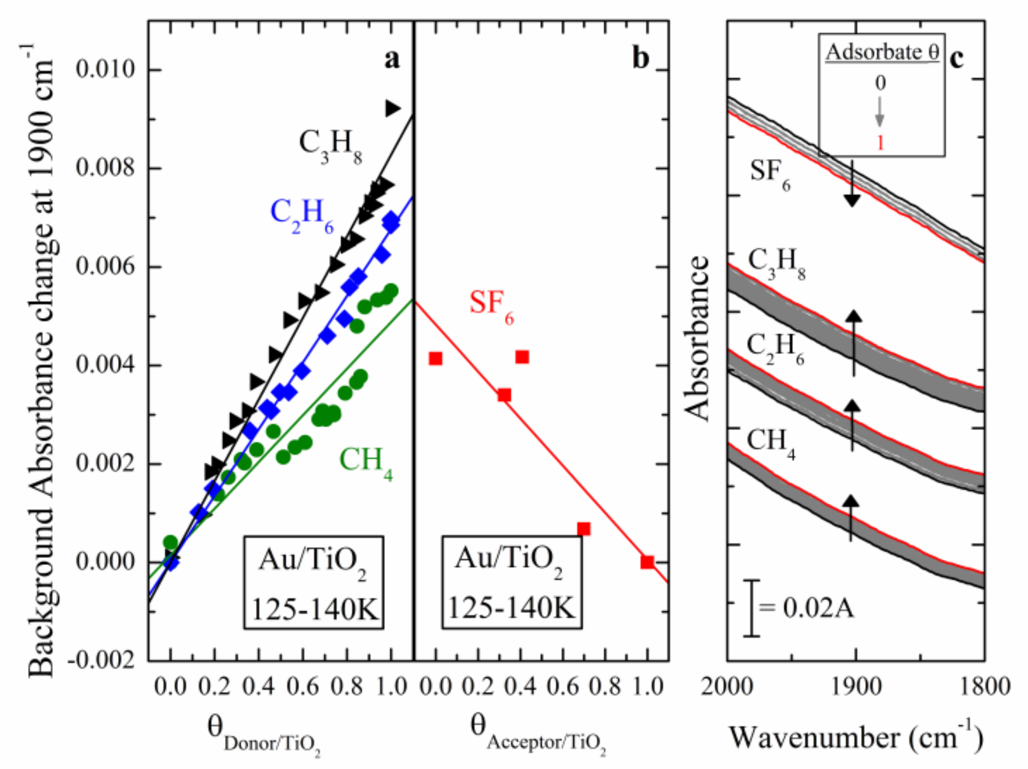

Figure 7.8 (a) The background IR absorbance changes measured at 1900 cm^{-1} for C_3H_8, C_2H_6 and CH_4 donor molecules. (b) The opposite shift occurs for the SF_6 acceptor molecule. (c) Partial spectra of the background absorbance over 1800-2000 cm^{-1} for adsorption of both donor and acceptor molecules.

Figures 7.8a and 7.8b show the shift of the background IR spectrum for Au/TiO_2 catalysts due to donor molecules as a function of the adsorption coverage of the donor molecules on TiO_2. The broad band responds by moving upward upon electron donation by the physically adsorbed molecules employed. This broad shift can be monitored by the motion of the background absorption as monitored by the changes in the band at 1900 cm^{-1}. Figure 7.8a shows the increase in the background absorbance at 1900 cm^{-1}, when three different donor molecules (CH_4; C_2H_6; C_3H_8) are systematically and separately adsorbed. Figure 7.8b shows the decrease in the background absorbance when an acceptor molecule (SF_6) is adsorbed on TiO_2. Figure 7.8c shows the observed spectral background over a broader region (1800-2000 cm^{-1}) as it shifts up or down when either donor or acceptor molecules are adsorbed on the Au/TiO_2 catalyst.

7.3.3 Redistribution of Electronic Charge in TiO_2 causing Band Bending by Donor or Acceptor Adsorbate Molecules – Photoluminescence Effects

The adsorption of donor or acceptor molecules on a semiconducting-TiO_2 surface produces a dramatic change in the intensity of photoluminescence (PL) from the surface as a result of band bending in the surface region.[11,12,49] TiO_2 is an n-type semiconductor where oxygen-vacancy surface defects result in the buildup of negative charge on the clean surface. This extra surface negative charge causes the conduction and valence band edges to bend upwards as shown in Figure 7.3.[5] Upward band bending increases the thickness of the depletion region associated with the curved upward bent bands. In the depletion region, PL is eliminated since the large motion in opposite directions of photo-generated electrons and holes sweeps the surface depletion region free of recombining charges before charge recombination (and associated PL) can occur. Hence, enhanced band bending may be detected from the change in PL intensity when donor or acceptor molecules are adsorbed.[11] When n-type TiO_2, with initially upward bent bands, adsorbs donor molecules, the bands bend downward resulting in an increase in PL intensity; the opposite band bending occurs for the adsorption of acceptor molecules on n-type TiO_2.

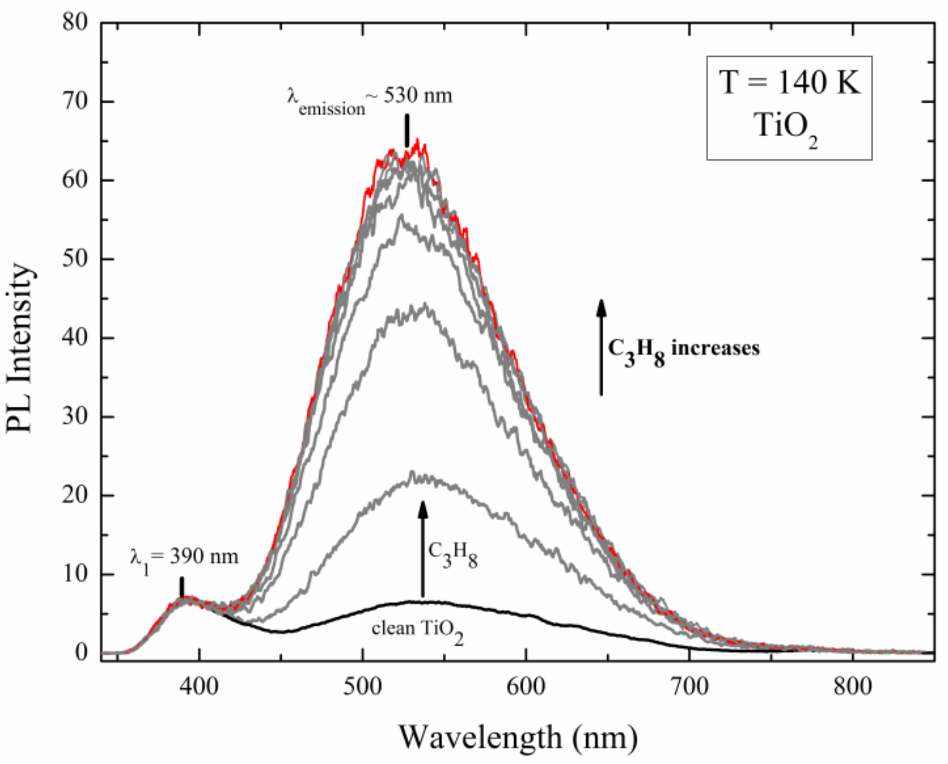

Figure 7.9 The photoluminescence (PL) intensity of a clean TiO_2 surface upon adsorption of C_3H_8 at 140K. The main peak at ~530 nm of a clean TiO_2 (black spectrum) increases upon addition of adsorbed C_3H_8 (gray spectra) reaching a saturation point (red spectra). The small light peak at λ_1 = 390 nm is due to a constant light reflection effect which is always present at a constant level and is disregarded.

Figures 7.9 and 7.10 show the behavior of the PL spectra and PL intensity, respectively, from clean powdered TiO_2 which has then been treated with physically-adsorbed C_3H_8 donor molecules or with physically-adsorbed SF_6 acceptor molecules. Figure 7.9 shows the change in the PL spectra of a clean TiO_2 surface upon adsorption of C_3H_8 at 140 K. The peak at ~ 530 nm corresponds to PL emission as a result of electron-hole recombination in TiO_2. The feature at 390 nm originates from a small portion of the reflected source light from a CaF_2 window and is invariant during the experiments. The resulting increase in PL intensity at ~ 530 nm for the donor-C_3H_8 molecule is consistent with reduction of the surface depletion region thickness. For acceptor SF_6 molecules, the surface depletion region grows thicker, causing diminished PL intensity.

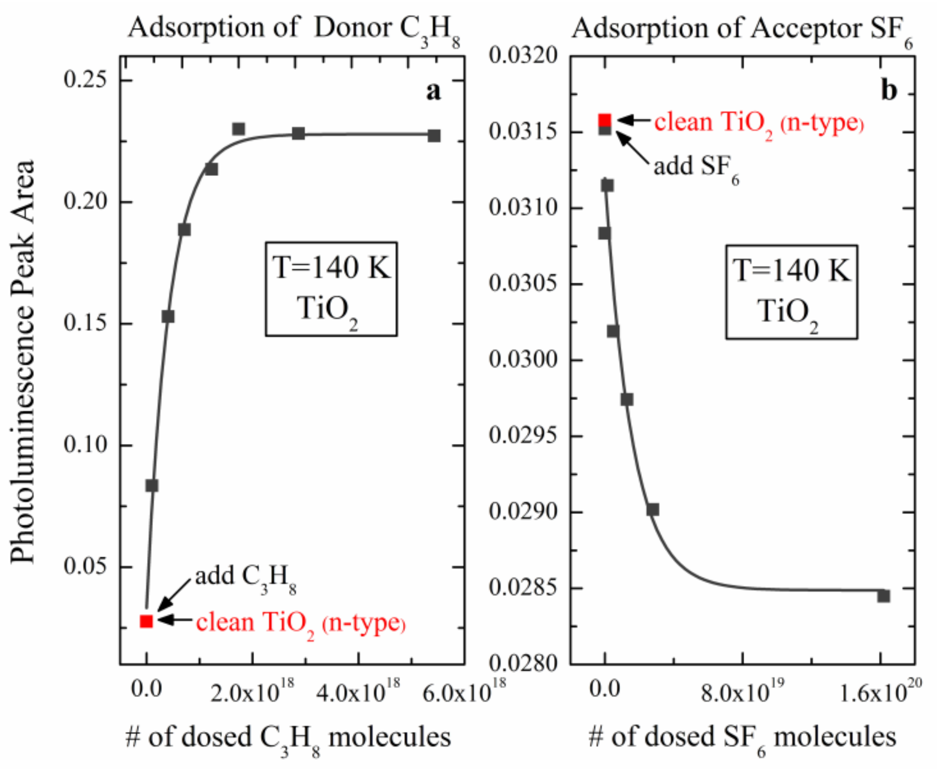

Figure 7.10 Opposite effects of van der Waals bound donor-C_3H_8 (a) and acceptor-SF_6 (b) molecules on the magnitude of photoluminescence intensity. (a) The results indicate that donor-C_3H_8 molecules reduce upward band bending in n-type TiO_2, causing an increase in PL intensity. (b) Conversely, acceptor-SF_6 molecules enhance upward band bending in n-type TiO_2, causing a decrease in PL intensity.

7.3.4 DFT Calculations of IR CO/Au Frequency Shifts by Donor and Acceptor Molecules Adsorbed on the TiO_2 Support

The adsorption of the CH_4, C_2H_6 and C_3H_8 donor molecules onto Ti sites on TiO_2 at the Au/TiO_2 perimeter result in theoretically calculated CO/Au frequency shifts that are negative by 2 cm^{-1}, 3 cm^{-1}, and 5 cm^{-1}, respectively (Figure 7.11bcd). A detailed analysis of charge density differences before and after the adsorption of the donor molecules on TiO_2 shows that the donor molecules induce an increase of electron density on the Au particle, resulting in negative charge on Au surface sites. The charge on the Au site to which CO is adsorbed is -0.02 e, -0.03 e and -0.04 e for CH_4, C_2H_6 and C_3H_8 adsorption on the TiO_2 support, respectively (Figure 7.11bcd). The CO/Au frequency shift for the SF_6 acceptor molecule adsorbed onto the TiO_2 support at the Au/TiO_2 interface is positive by 2 cm^{-1} (Figure 7.11e). The adsorption of SF_6 on TiO_2 induces a decrease in electron density on the Au particle, resulting in positive charge on Au sites. The charge on the Au site to which CO is bound increases from -0.02 e (CH_4) to +0.03 e if SF_6 is adsorbed on TiO_2 instead (Figure 7.11e). The trend of the calculated CO/Au frequency shift is consistent with all of our experimental observations for donor and acceptor molecules on TiO_2. As shown in Figure 7.12, a CH_4 donor adsorbate located further away from the Au perimeter induces a smaller IR CO/Au frequency shift; however, since shifts still occur, the electron transfer has to occur through the TiO_2 to the Au instead of through space from the donor or acceptor on the TiO_2 directly to the Au and adsorbed CO molecule. CH_4 that adsorbed ~6 Å away from the Au perimeter results in a negative $\Delta\nu_{CO}$ of 1 cm^{-1}, as shown in Figure 7.12b. The electron density perturbations caused by all of the donor molecules and by the SF_6 acceptor molecule are observed in the TiO_2 and this charge effect is transmitted through the TiO_2 to Au and then to the C-O bond of Au-CO species. The charge on the Au site to which CO is adsorbed on is -0.01 e in the case of CH_4 located ~6 Å away from the Au. CO molecules that are remote from the perimeter exhibit similar frequency shifts as those CO molecules adsorbed near the perimeter. As shown in Figure 7.12c, a frequency shift of - 5 cm^{-1} is found for CO on top sites of the Au/TiO_2 model. This shift is the same as the CO/Au frequency shift in Figure 7.11d where CO is adsorbed near the perimeter. Thus, electrons transfer to or from Au causes a field effect which is similar over the entire Au outer surface, i.e. a Stark effect.

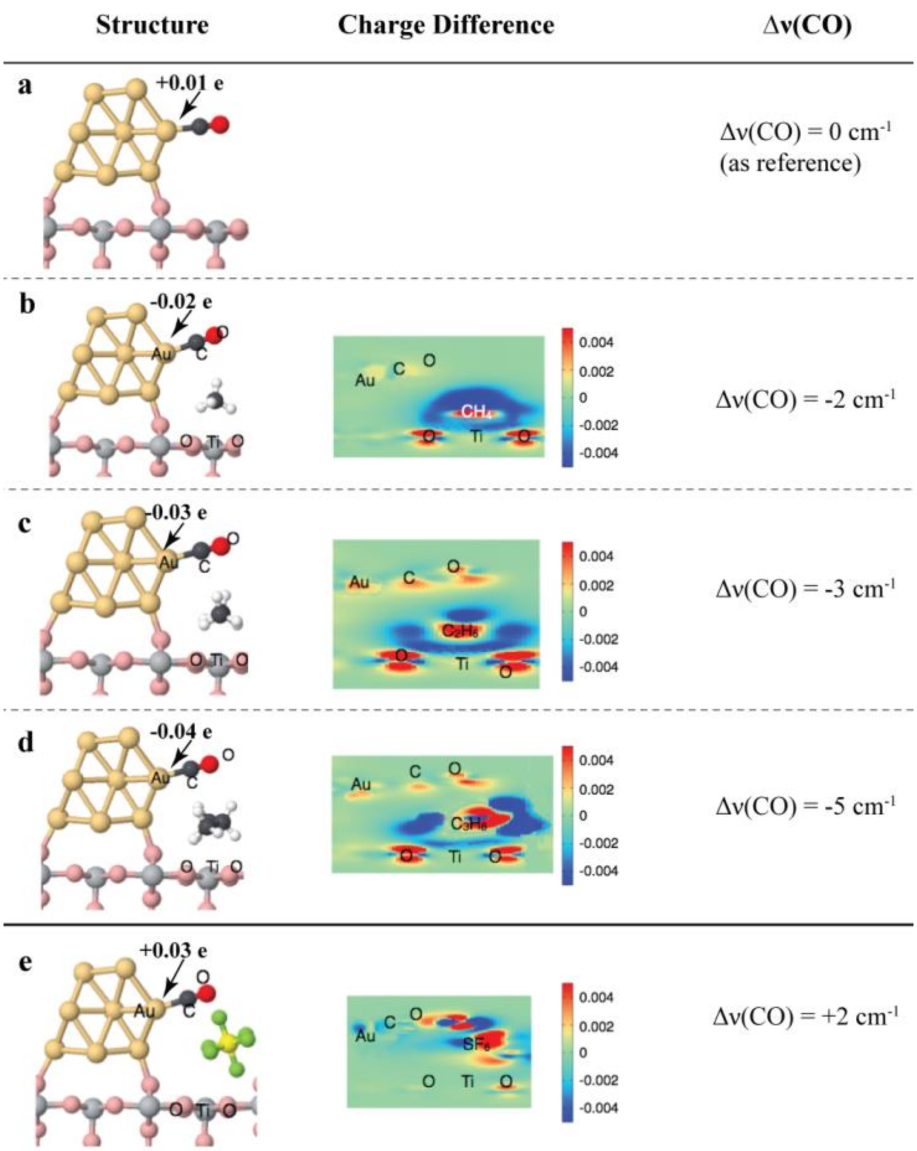

Figure 7.11 (a) Adsorption of CO on Au supported on TiO_2 and the resulting charge on the Au. CO frequency shift with the adsorption of (b) CH_4; (c) C_2H_6; (d) C_3H_8 and (e) SF_6. The charge on the Au atom is indicated in the figure. The Au atoms, Ti atoms, the O in the TiO_2 lattice, adsorbed O, C atoms, H atoms, F atoms and S atom are shown in gold, grey, pink, red, black, white, green and light yellow, respectively. Charge density differences before and after donor and acceptor adsorption are shown in the second column spatial figures. Orange and red indicate increasing of electron density while green and blue indicates decreasing electron density.

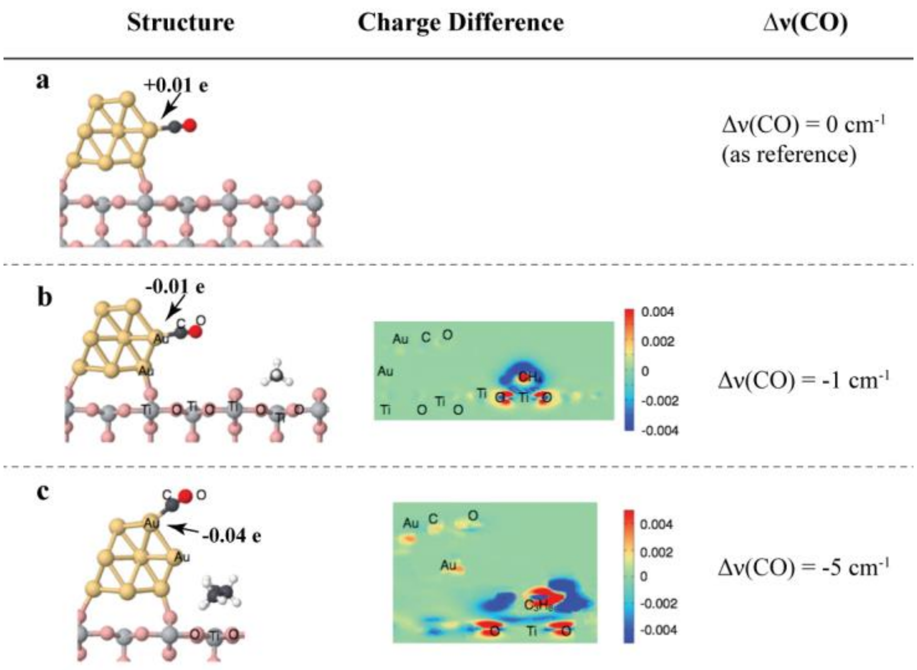

Figure 7.12 (a) Adsorption of CO on Au supported on TiO_2 and the resulting charge on the Au.CO frequency shift with the adsorption of (b) CH_4 that is remote from the perimeter; (c) C_3H_8 when CO is remote from the perimeter. The charge on the Au atom is indicated in the figure. Charge differences before and after CH_4 and C_3H_8 adsorption are shown in the second column spatial figure. Orange and red indicate increasing of electron density while blue indicates decreasing electron density.

7.4 Discussion

7.4.1 Three Spectroscopic Methods for Observing Charge Transfer Effects - Au/TiO_2 Catalysts

Three spectroscopic methods have been employed to understand the redistribution of electrons in a Au/TiO_2 catalyst due to the physisorption of donor or acceptor molecules on the TiO_2 support. Each method demonstrates that donor and acceptor molecules differ in the direction of electron transfer which is induced from TiO_2 to Au. While electron transfer into the semiconducting TiO_2 support is effective, similar donor and acceptor experiments with insulator SiO_2 supports are ineffective in producing electron transfer from the donor or acceptor molecules. Measurable $\Delta\nu_{CO}$ effects do not occur on Au/SiO_2.

For ~3 nanometer diameter Au particles bound to a TiO_2 support, the redistribution of electrons in the support may be determined by observing small spectroscopic shifts in the C-O stretching motion for chemisorbed CO on the Au surface. The average ~3 nm Au-Au particle separation is at least ~40 Å, based on a 0.15 fraction coverage of the TiO_2 particles as measured by TEM.[13] Beyond a Au particle-particle separation of ~6 Å, the inter-particle spectroscopic effect for adsorbed CO involves less than a 1 cm^{-1} shift in the ν_{CO}. Figure 7.13 shows a schematic diagram of the electron transfer effect from a donor and acceptor molecule to the TiO_2 support and then to and from the contacting Au nanoparticle containing chemisorbed CO molecules. This phenomenon is produced by a composite metal/semiconductor nanomaterial which we term a "molecular voltmeter" as schematically shown in Figure 7.13. Electrons transferred to or from the metal particle cause the CO frequency to shift to lower frequency (caused by donor molecules) or to higher frequency (caused by acceptor molecules), in accordance to a Stark shift.

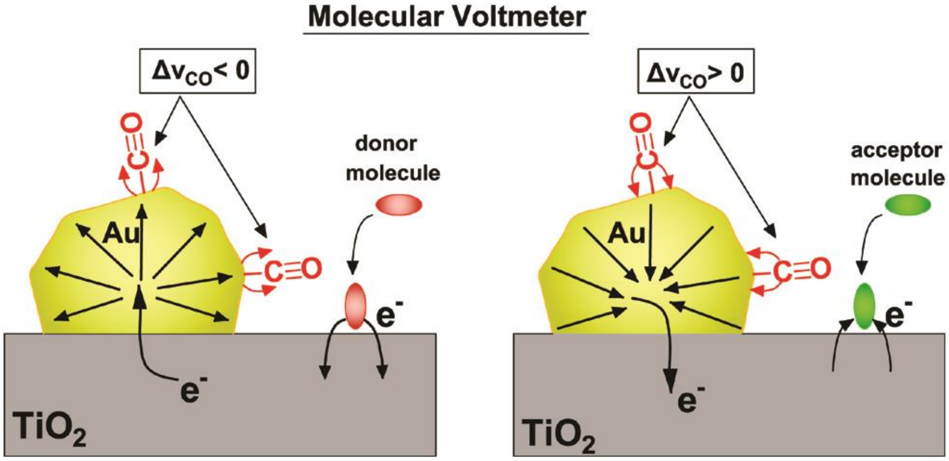

Figure 7.13 Schematic representation of the Molecular Voltmeter for the measurement of charge transfer from donor molecule (left) and acceptor molecule (right) to semiconducting TiO_2 support and then to a supported Au nanoparticle, using $\Delta\nu_{CO}$ for measurement. The Stark effect is related to electron donation to or withdrawal from frontier C-O orbitals and related to the k_{CO} force constant and the vibrational frequency, ν_{CO}.

A second effect related to electron donation or acceptance from a physisorbed donor or acceptor molecule has been studied on Au/TiO_2 catalysts and is schematically shown in Figure 7.2. Electron donors on TiO_2 will fill empty energy levels high in the bandgap region, which are due to the presence of empty lattice defect electron trap states. These levels are slightly below the bottom of the conduction band, such that the absorption of IR photons from an IR spectrometer is energetic enough to excite the trapped electrons to the conduction band. This excitation can be observed by means of the motion of the IR background upwards for TiO_2 or Au/TiO_2 samples. Conversely, electron acceptors adsorbed on the surface will remove electrons from these bandgap states, causing a reduction of the IR background intensity. The effect is seen over much of the IR region because IR excitation occurs from electron trap states in the bandgap into electron continuum states in the conduction band.

In addition to CO/Au frequency shifts and the variation of the background IR intensity, the donation or acceptance of electrons to or from a semiconductor such as TiO_2 may be visualized through bending of the conduction and valence bands and the influence of such band bending on PL intensity. As shown schematically in Figure 7.3, a donor molecule will become positive and will result in the decrease of the extent of upward-bending on an n-type TiO_2 surface causing the PL emission region to expand forward nearer to the TiO_2 surface; an acceptor adsorbed on n-type TiO_2 will cause the bands to bend further upward as additional negative charge is collected by the acceptor molecules causing the opposite effect on the thickness of the PL region and therefore decreasing the intensity of the PL signal. The change in band bending deduced by PL intensity is directly connected to the population change for trapped electrons in the bandgap states.

7.4.2 Electron Transfer from Adsorbate to TiO_2: Polarizability Correlation

The first step in the electron transfer process involves the interaction between the adsorbates and the TiO_2 support. The electric field at the TiO_2 surface induces electronic polarization created by δ^+ polarization of hydrogen atoms in the donor molecules when near the surface of TiO_2. This magnitude of the adsorbate molecule polarization in the surface electric field on TiO_2 is proportional to α, the polarizability of the absorbate. In Table 2 the Stark shifts of $CO/Au/TiO_2$ influenced by donor molecules of variable polarizability, α, are compared. It is observed that the $\Delta\nu_{CO}$ shift responds in close proportion to the polarizability of the donor molecules employed on the TiO_2 surroundings to the Au particles.

Table 2. Relative Shifts of $\nu_{CO/Au}$ Compared to Absorbance Background Shifts in TiO_2 Due to Charge Transfer and to Polarizability (α)

Donor Molecule	$\Delta\nu_{CO}$ Slope	α_{Donor} $(Å^3)^{50}$	$\Delta\nu_{CO}$ Slope/ $Å^3$	ΔIR Bkg Abs. Slope	ΔIR Slope/ $Å^3$
CH_4	-1.11 (±0.1)	2.59	0.43 (±0.04)	0.00425	0.0016 (±0.0001)
C_2H_6	-2.09 (±0.1)	4.47	0.47 (±0.02)	0.00664	0.0015 (±0.0001)
C_3H_8	-2.79 (±0.1)	6.29	0.44 (±0.02)	0.00875	0.0014 (±0.0001)

Another change noted in the IR spectra upon the adsorption of donor adsorbates onto the TiO_2 support is the increase in the IR background absorbance as shown in Figure 7.8. From previous studies,[44-46] this IR background absorbance increase (ΔIR) was attributed to electrons accumulating in discrete trap states just below the conduction band in TiO_2. Upon IR irradiation these electrons are excited into the conduction band continuum of states. We plotted the absorbance rise at 1900 cm^{-1} versus the donor coverage on TiO_2 and then calculated the linear slopes with respect to donor molecule coverage as shown in Figure 7.8a. The values are shown in Table 2 along with their corresponding ratios to donor molecule variable polarizability, α. Table

2 shows that both $\Delta\nu_{CO}/\text{Å}^3$ and $\Delta IR/\text{Å}^3$ are nearly the same for each different measurement, indicating that α is the driving force to the changes observed in both sets of spectroscopic measurements.

7.4.3 Electron Transfer from TiO_2 to Au: Behavior Uniformity of CO/Au IR Band

Once the electrons are transferred to or from the TiO_2, they move to or from the Au particles. In order to determine if the electron transfer is localized at the Au/TiO_2 interface or if the electrons are delocalized and transfer to the Au particle surface, the uniformity of the CO/Au IR frequency line shape as the adsorbates are added has to be determined. Each spectrum was analyzed using a best Lorenzian fit for the CO/Au IR absorbance band and the full width at half maximum (FWHM) was recorded verses adsorbate coverage (See Figure 7.14). In addition, for all the donor and acceptor adsorption and desorption experiments, the observation of the band shift at 3 levels of cutting the band absorbance (1/4, ½, ¾) shows clearly that a uniform shift of the overlapping v_{CO} lines is being observed, and a general shift of all lines is occurring. The FW accuracy is consistent with a uniform shift in the whole CO/Au IR line shape, meaning that slightly different CO bonding states respond uniformly to electron transfer from donor molecules to CO/Au. DFT calculations shown in Figures 7.11d and 7.12c are consistent with a uniform electron transfer to CO molecules on different Au sites.

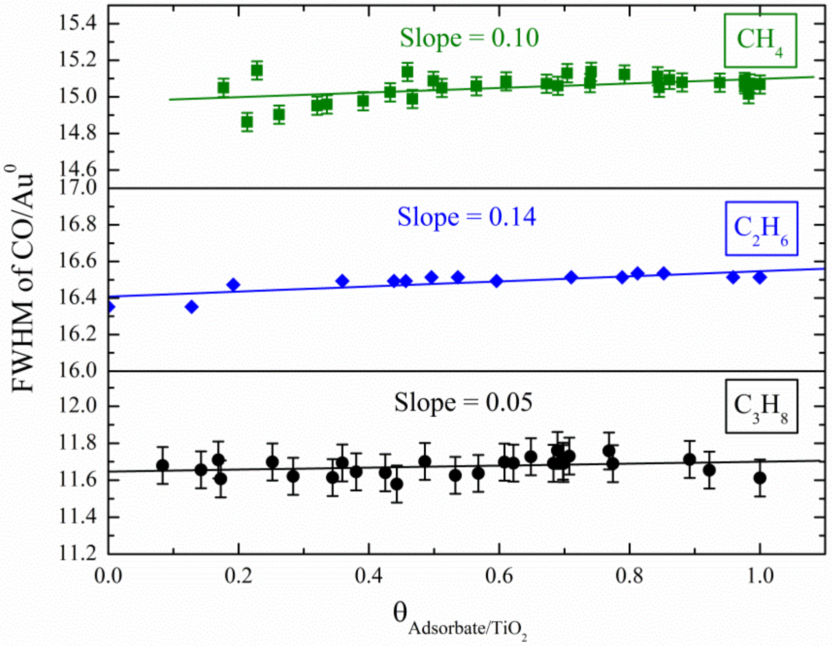

Figure 7.14 FWHM of the CO/Au absorbance band on a Au/TiO_2 catalyst vs donor coverage on TiO_2.

Deshlahra *et al.*[51] analyzed the uniformity of the CO IR line shape for their system, which involved an applied dc voltage from a bias power supply to shift the ν_{CO} on Pt/TiO_2, in a different way. We followed their formula by subtracting the IR shifted spectra from the spectrum before donor adsorption (in our case), and then integrated the sum of the positive and negative peaks, $A_{difference}$. This value was then divided by the integrated area of the spectrum before donor adsorption, A_{total}. Therefore, the IR CO/metal frequency shift can be quantified by this ratio as shown in equation (7.1),

$$F = \frac{A_{difference}}{A_{total}} \qquad (7.1)$$

where F is the fractional difference area.[51] We find F is linear verses donor coverage as seen in Figure 7.15, and the F slopes for each donor scale proportionally with α_{donor}. From this analysis combined with FW measurements and DFT calculations shown in Figure 7.12c, we conclude that electron transfer into the Au produces a delocalized Gauss distribution of charge at the Au surface, to within the experimental errors of this investigation.

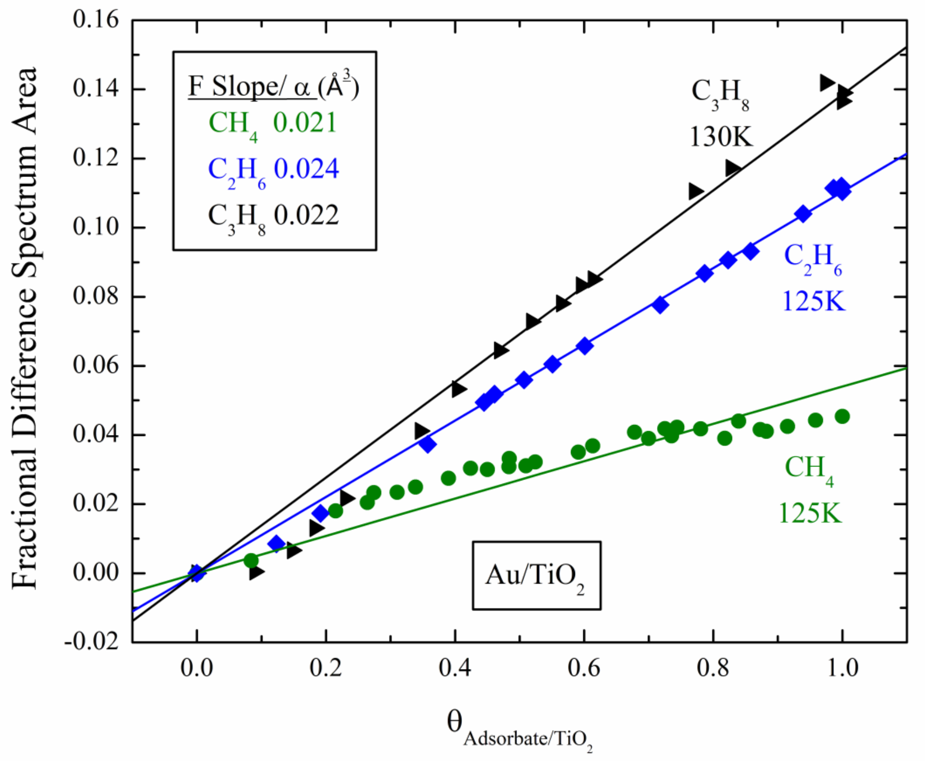

Figure 7.15 Fractional Difference Spectrum Areas, F, vs Donor Coverage for CH_4 (green diamonds), C_2H_6 (blue diamonds) and C_3H_8 (black triangles). The lines are linear fits to calculate the slopes. The inserted value of F slope/α is constant for the three donor molecules.

7.4.4 Stark Effect

The shift in the value of ν_{CO} can be envisioned as being due to the interaction of the chemisorbed CO molecule on a Au sphere with the transfer of donated electrons to the metal and then to the surface of the Au sphere, following the Gauss distribution of all added charge to the metal-sphere surface. The distribution of charge q over the low radius metal nanoparticle surface causes a high field at the sphere surface. The normal electric field strength E in vacuum near to the metal is given by equation (7.2);

$$E = \frac{q}{4\pi\varepsilon_0 r^2} \qquad (7.2)$$

where q is the surface electron charge, ε_0 is the permittivity of free space and r is the Au nanoparticle radius. Other measurements for CO adsorbed on a metal and exposed to various applied electric fields have yielded a Stark tuning rate of -8.6 x 10^{-9} cm^{-1}/(V/m).[52] This Stark tuning model yields a value of $\Delta\nu_{CO}$ ~6 cm^{-1} per electron distributed on the 3 nm diameter Au particle surface. Our measurements of $\Delta\nu_{CO}$ = 1 – 3 cm^{-1}/monolayer of the three alkane donor molecules indicates that the range of Au charge transfer/monolayer of alkane is from 0.2 – 1 electron/Au particle. The DFT results reported in Figure 7.11 which showed charge transfer from adsorbed alkanes to TiO_2 and the subsequent transfer of charge to the Au atoms at the surface of nanoparticles are in general agreement with the Stark charge calculated from $\Delta\nu_{CO}$. In addition, we found that the explicit addition and removal of charge to the Au/TiO_2 system without donor or acceptor molecules as is shown in Figure 7.16 also agrees closely with the Stark charge.

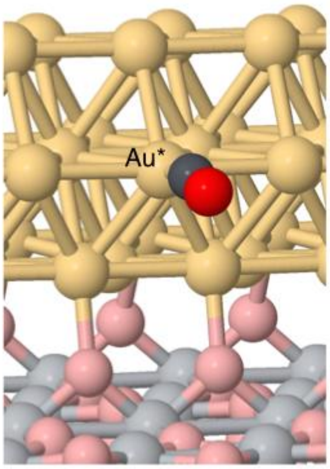

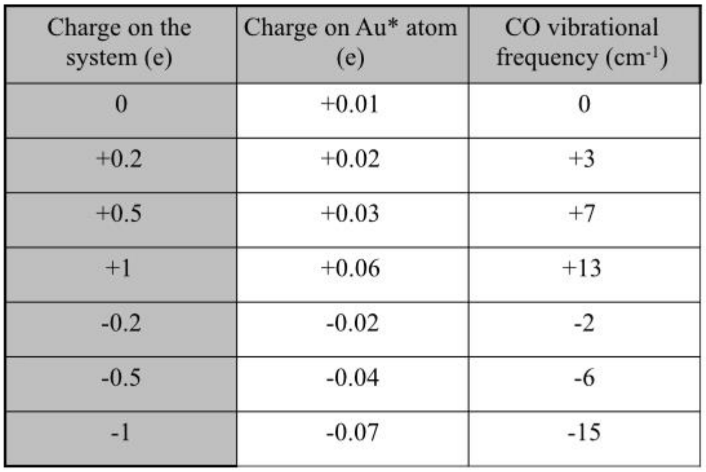

Charge on the system (e)	Charge on Au* atom (e)	CO vibrational frequency (cm^{-1})
0	+0.01	0
+0.2	+0.02	+3
+0.5	+0.03	+7
+1	+0.06	+13
-0.2	-0.02	-2
-0.5	-0.04	-6
-1	-0.07	-15

Figure 7.16 CO frequency shift on charged Au/TiO_2 system.

7.4.5 Support Effect: TiO_2 vs SiO_2

Our experiments have shown that semiconductor TiO_2 is effectively charged by either donor or acceptor molecules whereas insulator SiO_2 is not. The dielectric constant, κ, is 80 – 100 for TiO_2[53,54] and only 3.9 for SiO_2.[54] TiO_2 therefore contains significant charge carriers related to defect sites in the bulk, whereas SiO_2 contains few charge carriers, making SiO_2 less affected by charge transfer effects from donor or acceptor molecule adsorption, as shown in Figure 7.7. TiO_2 is therefore able to transfer charge to the surface of the Au nanoparticles, causing $\Delta\nu_{CO}$ effects, which are not observed for similar size Au nanoparticles on SiO_2. This observation verifies that CO molecules, adsorbed on Au nanoparticles, are sensitive "Molecular Voltmeters," which depend on the ability of the underlying semiconductor support to interact with polarizable molecules. CO dipole-dipole coupling[55,56] is not believed to cause this $\Delta\nu_{CO}$ effect because the Au particles are initially saturated with CO and monitored for 30 minutes with IR, and no $\Delta\nu_{CO}$ is observed. One other possibility that was not explored is the electric field changes due to a three-layer system[57] such as $CO/Au/TiO_2$, where the field changes to the TiO_2 might affect the CO molecule and not the Au. However, other molecules such as NH_3 adsorbed on TiO_2 caused different changes to the Au-CO IR absorbance band that could rule this idea out as well (not discussed here). Charge transfer to the support and hence to Au nanoparticles is believed to be observed by $\Delta\nu_{CO}$ shifts on Au nanoparticle detector sites.

7.5 Conclusions

1. IR and PL studies, on ~3 nm Au particles on TiO_2 indicate that charge transfer from inert donor or acceptor molecules on semiconducting TiO_2 results in charging or discharging of the Au nanoparticles.

2. Charging of Au nanoparticles can be measured by careful studies of the frequency shift of adsorbed CO molecules. The sign and magnitude of the value of $\Delta\nu_{CO}$ is consistent with the Stark effect producing a surface electric field on Au nanoparticles. This is shown by DFT studies of Au nanoparticle charging and CO frequency effects and agrees well with the known Stark effect sensitivity of adsorbed CO. DFT studies further show that electric field effects from donor or acceptor molecules to adsorbed CO molecules do not occur through vacuum but via charge transfer into the oxide and onto the metal. The Au/TiO_2 catalysts are termed “Molecular Voltmeter” devices.

3. The value of $\Delta\nu_{CO}$ is proportional to the known polarizability, α, of three donor molecules, CH_4, C_2H_6, and C_3H_8, which adsorb only on the TiO_2 support by van der Waals interactions. The opposite effect takes place for the acceptor molecule, SF_6. Donor molecules on TiO_2 result in CO redshifts and acceptor molecules result in CO blueshifts.

4. Charge transfer from physically adsorbed molecules to TiO_2 and then to Au nanoparticles occurs via electron storage in lattice defect states located in the TiO_2 bandgap near the bottom of the conduction band. The population of these defect electron trap states can be monitored by their broad IR excitation into the TiO_2 continuum. The magnitude of charge transfer effects from TiO_2 into Au correlates with the occupancy of these defect electron trap states.

5. Photoluminescence studies of C_3H_8 and SF_6 physisorbed molecules on pure TiO_2 confirm that these are electron donor or acceptor molecules which adsorb and desorb reversibly.

6. Charge transfer from donor or acceptor molecules on TiO_2, and from TiO_2 into Au depends upon significant carrier concentration changes associated with electron trap states in the TiO_2 semiconductor substrate. Insulator substrates (SiO_2) do not permit electron transfer processes.

References

1. Smoluchowski, R. Anisotropy of the electronic work function of metals. *Physical Review* **1941**, *60*, 661.

2. Gomer, R. Work Function in Field Emission. Chemisorption. *Journal of Chemical Physics* **1953**, *21*, 1869-1876.

3. Lang, N.; Kohn, W. Theory of metal surfaces: charge density and surface energy. *Physical Review B* **1970**, *1*, 4555.

4. Lang, N.; Kohn, W. Theory of metal surfaces: work function. *Physical Review B* **1971**, *3*, 1215.

5. Zhang, Z.; Yates, Jr., J. T. Band bending in semiconductors: chemical and physical consequences at surfaces and interfaces. *Chemical Reviews* **2012**, *112*, 5520-5551.

6. Mezhenny, S.; Maksymovych, P.; Thompson, T.; Diwald, O.; Stahl, D.; Walck, S.; Yates, Jr., J. T. STM studies of defect production on the TiO_2(110)-(1× 1) and TiO_2(110)-(1× 2) surfaces induced by UV irradiation. *Chemical Physics Letters* **2003**, *369*, 152-158.

7. Lüth, H. In Chapter 7: Space charge layers at semiconductor interfaces; *Surfaces and Interfaces of Solid Materials*, 3rd Ed; Springer: Berlin, **1997**; pp 316-371.

8. Ida, N. *Engineering electromagnetics;* Springer: **2004**; pp 173-281.

9. Brundle, C. *Vibrations at Surfaces (Studies in Surface Science and Catalysis);* Elsevier: **2000**; pp 60-64.

10. Wendt, S.; Sprunger, P. T.; Lira, E.; Madsen, G. K.; Li, Z.; Hansen, J. Ø; Matthiesen, J.; Blekinge-Rasmussen, A.; Lægsgaard, E.; Hammer, B. The role of interstitial sites in the Ti*3d* defect state in the band gap of titania. *Science* **2008**, *320*, 1755-1759.

11. Stevanovic, A.; Büttner, M.; Zhang, Z.; Yates, Jr., J. T. Photoluminescence of TiO_2: effect of UV light and adsorbed molecules on surface band structure. *Journal of the American Chemical Society* **2011**, *134*, 324-332.

12. Anpo, M.; Tomonari, M.; Fox, M. A. In situ photoluminescence of titania as a probe of photocatalytic reactions. *Journal of Physical Chemistry* **1989**, *93*, 7300-7302.

13. Stevanovic, A.; Ma, S.; Yates, Jr., J. T. Effect of Gold Nanoparticles on Photoexcited Charge Carriers in Powdered TiO_2-Long Range Quenching of Photoluminescence. *The Journal of Physical Chemistry C* **2014**, 118, 21275-21280.

14. Lambert, D. K. Vibrational Stark effect of adsorbates at electrochemical interfaces. *Electrochimica Acta* **1996**, *41*, 623-630.

15. Lambert, D. K. Vibrational Stark effect of CO on Ni(100), and CO in the aqueous double layer: Experiment, theory, and models. *Journal of Chemical Physics* **1988**, *89*, 3847-3860.

16. Korzeniewski, C.; Pons, S.; Schmidt, P.; Severson, M. A theoretical analysis of the vibrational spectrum of carbon monoxide on platinum metal electrodes. *Journal of Chemical Physics* **1986**, *85*, 4153-4160.

17. Lambert, D. Observation of the first-order Stark effect of CO on Ni(110). *Physical Review Letters* **1983**, *50*, 2106.

18. Angell, C. L.; Schaffer, P. C. Infrared Spectroscopic Investigations of Zeolites and Adsorbed Molecules. II. Adsorbed Carbon Monoxide1. *Journal of Physical Chemistry* **1966**, *70*, 1413-1418.

19. Banik, M.; El-Khoury, P. Z.; Nag, A.; Rodriguez-Perez, A.; Guarrottxena, N.; Bazan, G. C.; Apkarian, V. A. Surface-enhanced Raman trajectories on a nano-dumbbell: transition from field to charge transfer plasmons as the spheres fuse. *ACS Nano* **2012**, *6*, 10343-10354.

20. Li, L.; Steiner, U.; Mahajan, S. Single nanoparticle SERS probes of ion intercalation in metal-oxide electrodes. *Nano Letters* **2014**, *14*, 495-498.

21. Kamat, P. V.; Shanghavi, B. Interparticle electron transfer in metal/semiconductor composites. Picosecond dynamics of CdS-capped gold nanoclusters. *The Journal of Physical Chemistry B* **1997**, *101*, 7675-7679.

22. Choi, H.; Chen, W. T.; Kamat, P. V. Know thy nano neighbor. Plasmonic versus electron charging effects of metal nanoparticles in dye-sensitized solar cells. *ACS Nano* **2012**, *6*, 4418-4427.

23. Ikeda, K.; Suzuki, S.; Uosaki, K. Enhancement of SERS Background through Charge Transfer Resonances on Single Crystal Gold Surfaces of Various Orientations. *Journal of the American Chemical Society* **2013**, *135*, 17387-17392.

24. McFarland, E. W.; Metiu, H. Catalysis by doped oxides. *Chemical Reviews* **2013**, *113*, 4391-4427.

25. Metiu, H.; Chrétien, S.; Hu, Z.; Li, B.; Sun, X. Chemistry of lewis acid–base pairs on oxide surfaces. *The Journal of Physical Chemistry C* **2012**, *116*, 10439-10450.

26. Green, I. X.; Tang, W.; Neurock, M.; Yates, Jr., J. T. Spectroscopic observation of dual catalytic sites during oxidation of CO on a Au/TiO_2 catalyst. *Science* **2011**, *333*, 736-739.

27. Basu, P.; Ballinger, T.; Yates, Jr., J. T. Wide temperature range IR spectroscopy cell for studies of adsorption and desorption on high area solids. *Review of Scientific Instruments* **1988**, *59*, 1321-1327.

28. Molina, L.; Rasmussen, M.; Hammer, B. Adsorption of O_2 and oxidation of CO at Au nanoparticles supported by TiO_2(110). *Journal of Chemical Physics* **2004**, *120*, 7673.

29. Laursen, S.; Linic, S. Geometric and electronic characteristics of active sites on TiO_2-supported Au nano-catalysts: insights from first principles. *Physical Chemistry Chemical Physics* **2009**, *11*, 11006-11012.

30. Green, I. X.; Tang, W.; Neurock, M.; Yates, Jr., J. T. Low-Temperature Catalytic H_2 Oxidation over Au Nanoparticle/TiO_2 Dual Perimeter Sites. *Angewandte Chemie* **2011**, *50*, 10186-10189.

31. Green, I. X.; Tang, W.; McEntee, M.; Neurock, M.; Yates, Jr., J. T. Inhibition at Perimeter Sites of Au/TiO_2 Oxidation Catalyst by Reactant Oxygen. *Journal of the American Chemical Society* **2012**, *134*, 12717-12723.

32. Dekkers, M.; Lippits, M.; Nieuwenhuys, B. CO adsorption and oxidation on Au/TiO_2. *Catalysis Letters* **1998**, *56*, 195-197.

33. Chen, M.; Goodman, D. The structure of catalytically active gold on titania. *Science* **2004**, *306*, 252-255.

34. Hao, Y.; Mihaylov, M.; Ivanova, E.; Hadjiivanov, K.; Knözinger, H.; Gates, B. CO oxidation catalyzed by gold supported on MgO: Spectroscopic identification of carbonate-like species bonded to gold during catalyst deactivation. *Journal of Catalysis* **2009**, *261*, 137-149.

35. Schreiber, H.; McIntosh, R. Thermodynamic properties of hydrocarbons adsorbed on rutile II. *Canadian Journal of Chemistry* **1955**, *33*, 259-267.

36. Bandara, A.; Abu-Haija, M.; Höbel, F.; Kuhlenbeck, H.; Rupprechter, G.; Freund, H. Molecular adsorption on V_2O_3(0001)/Au(111) surfaces. *Topics in Catalysis* **2007**, *46*, 223-230.

37. Fichthorn, K. A.; Miron, R. A. Thermal desorption of large molecules from solid surfaces. *Physical Review Letters* **2002**, *89*, 196103.

38. Tait, S. L.; Dohnalek, Z.; Campbell, C. T.; Kay, B. D. n-alkanes on Pt(111) and on C(0001)⁄ Pt(111): Chain length dependence of kinetic desorption parameters. *Journal of Chemical Physics* **2006**, *125*, 234308.

39. Hägglund, C.; Kasemo, B.; Österlund, L. In situ reactivity and FTIR study of the wet and dry photooxidation of propane on anatase TiO_2. *The Journal of Physical Chemistry B* **2005**, *109*, 10886-10895.

40. Goyal, S.; Schutt, D.; Scoles, G. Vibrational spectroscopy of sulfur hexafluoride attached to helium clusters. *Physical Review Letters* **1992**, *69*, 933.

41. Rosenbaum, A.; Freedman, M.; Sibener, S. Vibrational properties of disordered mono-and bilayers of physisorbed sulfur hexafluoride on Au(111). *The Journal of Physical Chemistry A* **2006**, *110*, 5537-5541.

42. Ogawa, T.; Mochiji, K.; Ochiai, I.; Yamamoto, S.; Tanaka, K. Low-temperature synchrotron-radiation-excited etching of silicon dioxide with sulfur hexafluoride adsorption. *Journal of Applied Physics* **1994**, *75*, 4680-4685.

43. Yoshihara, T.; Katoh, R.; Furube, A.; Tamaki, Y.; Murai, M.; Hara, K.; Murata, S.; Arakawa, H.; Tachiya, M. Identification of reactive species in photoexcited nanocrystalline TiO_2 films by wide-wavelength-range (400-2500 nm) transient absorption spectroscopy. *The Journal of Physical Chemistry B* **2004**, *108*, 3817-3823.

44. Panayotov, D. A.; Burrows, S. P.; Yates, Jr., J. T.; Morris, J. R. Mechanistic studies of hydrogen dissociation and spillover on Au/TiO_2: IR spectroscopy of coadsorbed CO and H-donated electrons. *The Journal of Physical Chemistry C* **2011**, *115*, 22400-22408.

45. Panayotov, D. A.; Yates, Jr., J. T. n-Type doping of TiO_2 with atomic hydrogen-observation of the production of conduction band electrons by infrared spectroscopy. *Chemical Physics Letters* **2007**, *436*, 204-208.

46. Panayotov, D. A.; Yates, Jr., J. T. Spectroscopic detection of hydrogen atom spillover from Au nanoparticles supported on TiO_2: Use of conduction band electrons. *The Journal of Physical Chemistry C* **2007**, *111*, 2959-2964.

47. Willis, R. L.; Olson, C.; O'Regan, B.; Lutz, T.; Nelson, J.; Durrant, J. R. Electron dynamics in nanocrystalline ZnO and TiO_2 films probed by potential step chronoamperometry and transient absorption spectroscopy. *The Journal of Physical Chemistry B* **2002**, *106*, 7605-7613.

48. Sezen, H.; Buchholz, M.; Nefedov, A.; Natzeck, C.; Heissler, S.; Di Valentin, C.; Wöll, C. Probing electrons in TiO_2 polaronic trap states by IR-absorption: Evidence for the existence of hydrogenic states. *Scientific Reports* **2014**, *4*, 3808.

49. Anpo, M.; Chiba, K.; Tomonari, M.; Coluccia, S.; Che, M.; Fox, M. A. Photocatalysis on native and platinum-loaded TiO_2 and ZnO catalysts. Origin of different reactivities on wet and dry metal oxides. *Bulletin of the Chemical Society of Japan* **1991**, *64*, 543-551.

50. Boyd, R.; Kesner, L. Polarizability of polyethylene. *Macromolecules* **1987**, *20*, 1802-1806.

51. Deshlahra, P.; Schneider, W. F.; Bernstein, G. H.; Wolf, E. E. Direct Control of Electron Transfer to the Surface-CO Bond on a Pt/TiO_2 Catalytic Diode. *Journal of the American Chemical Society* **2011**, *133*, 16459-16467.

52. Lambert, D. Electroreflectance vibrational spectroscopy: A new surface analysis technique using diode lasers. *Studies in Surface Science and Catalysis* **1983**, *14*, 59-64.

53. Kim, S. K.; Kim, W.; Kim, K.; Hwang, C. S.; Jeong, J. High dielectric constant TiO_2 thin films on a Ru electrode grown at 250°C by atomic-layer deposition. *Applied Physics Letters* **2004**, *85*, 4112-4114.

54. Robertson, J. High dielectric constant gate oxides for metal oxide Si transistors. *Reports on Progress in Physics* **2006**, *69*, 327.

55. Persson, B. N. J. Vibrational interaction between molecules adsorbed on a metal surface: The dipole-dipole interaction. *Physical Review B* **1981**, *24*, 6954.

56. Schweizer, E.; Persson, B. N. J.; Tüshaus, M.; Hoge, D.; Bradshaw, A. M. The potential energy surface, vibrational phase relaxation and the order-disorder transition in the adsorption system Pt {111}-CO. *Surface Science* **1989**, *213*, 49-89.

57. Persson, B. N. J. Absorption of phonons by molecules adsorbed on metal surfaces. *Solid State Communications* **1979**, *30*, 163-166.

Appendix A: Installation, Optimization and Application of UV Fiber Optic

A.1 Installation of UV Fiber Optic Cable and Holder

Figure A.1 shows a schematic drawing of the IR cell, conflat (CF) flange connector tubes, and a fiber optic cable connected to a CF flange, which is placed inside the IR system under vacuum. The length of the fiber optic cable is 15.29 inches and is positioned precisely in line with the powdered, sample ~7 mm disk connected to the manipulator. In order to align the end of the cable with the sample, I designed a sample holder that would hold the end of the cable in line with the sample. Schematic diagrams of the dimensions of the precise sample placement inside the IR cell (left) and of the dimensions of the holder (right) are shown in Figure A.2. The actual sample holder is designed slightly differently than shown in Figure A.2, where the cable is held together by two, thin aluminum plates containing holes for maximum pumping volume instead of the thin beams shown. The reason for the design change was that the design below is a more complex machining process.

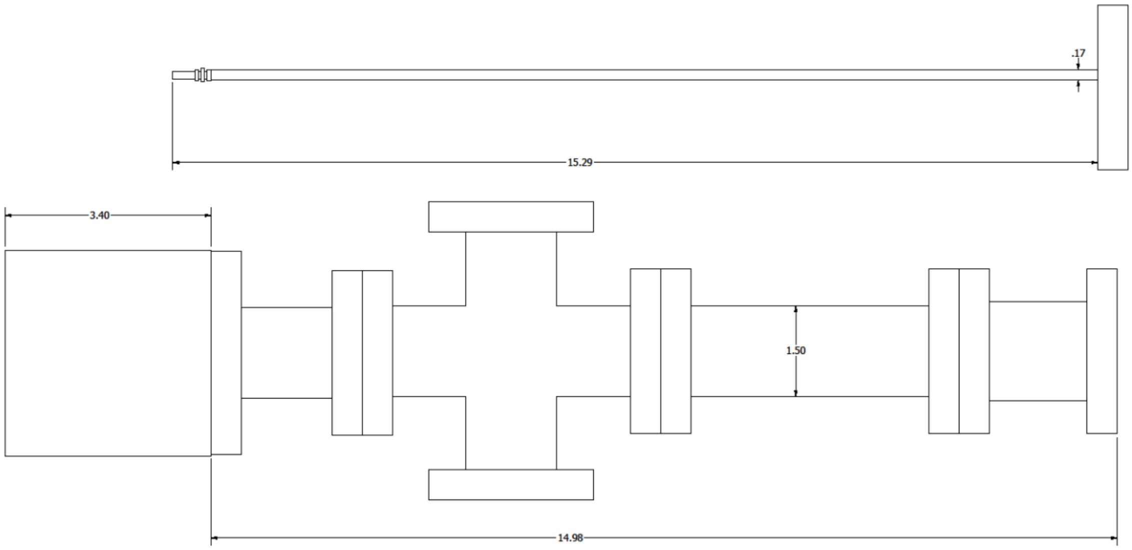

Figure A.1 Schematic of (top) a fiber optic cable connected to a CF flange and (bottom) the IR cell and CF flange connector tubes arranged to keep the fiber optic cable under vacuum. Dimensions are in inches.

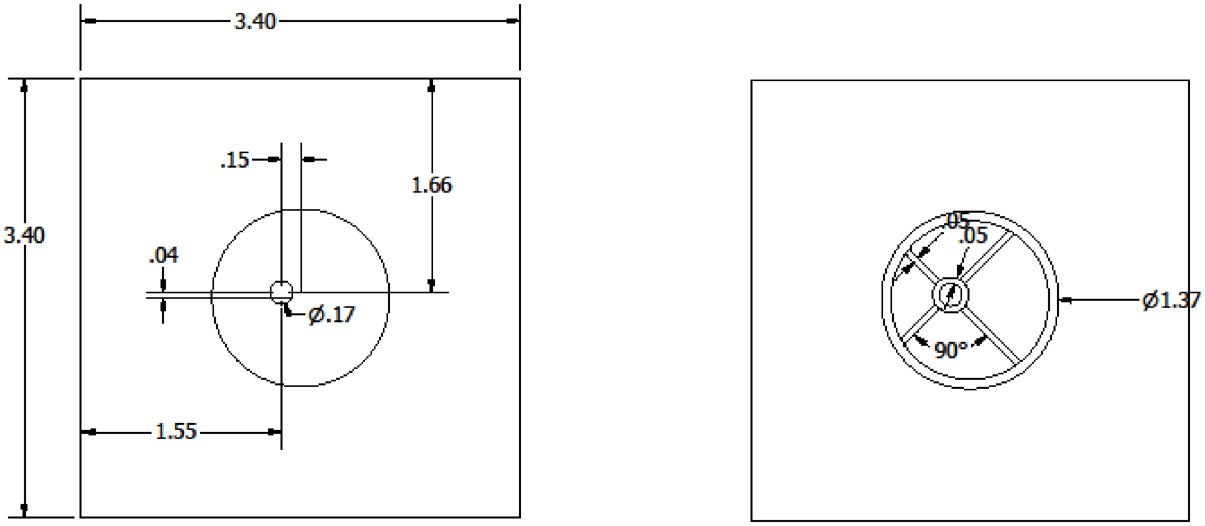

Figure A.2 Schematic of (left) the sample position in the IR cell from the view of the CF flange tube opening and (right) the sample holder original design and dimensions. Dimensions are in inches.

A.2 Calibration and Optimization of Light Intensity

Before the fiber optic cable was placed in vacuum, we calibrated and optimized the UV source lamp (Hg-arc lamp). The setup can be seen in Figures A.3, A.4, A.5 and A.6. Figure A.3 shows the full setup with the lamp (under the Al foil) connected to focus lens, a water filter, another focus lens and finally attached to a fiber optic cable. A close up of these individual components can be seen in Figure A.4. The water chiller for the water filter (left) and the lamp power supply (right) are shown in Figure A.5. Lastly, the cable was mounted to an XYZ manipulator mount, which was positioned next to a thermopile as shown in Figure A.6.

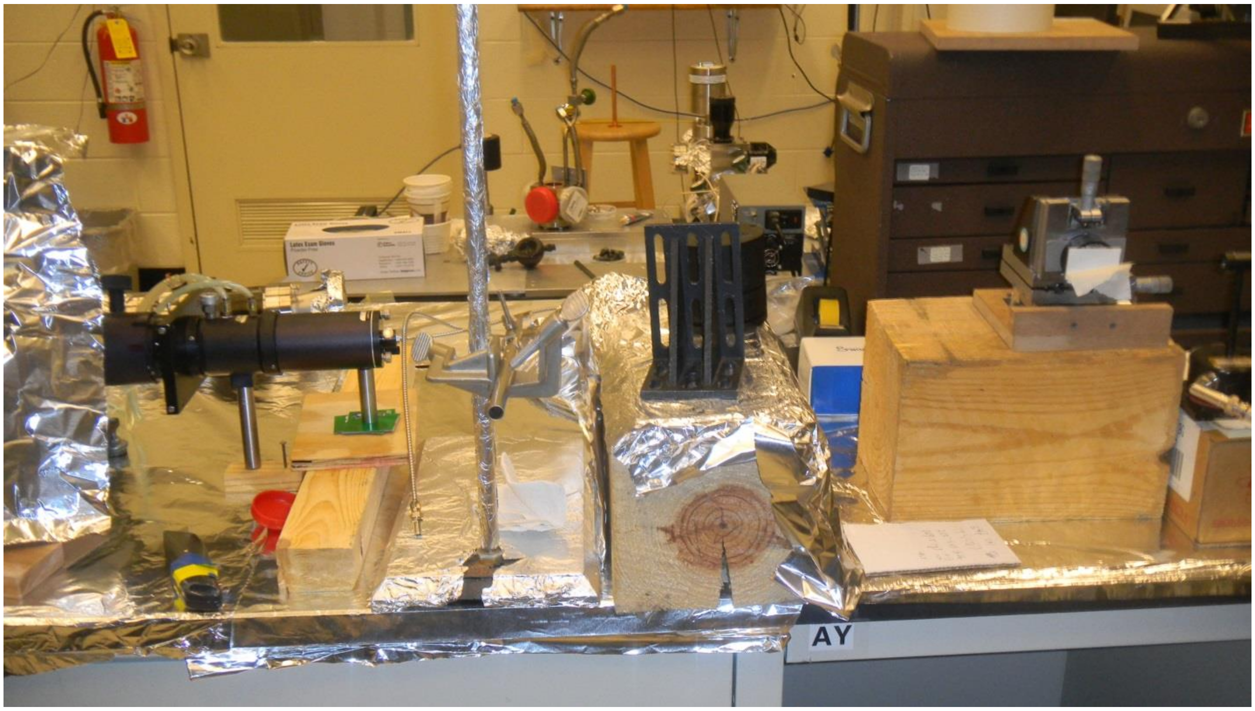

Figure A.3 Photograph of UV lamp and fiber optic cable calibration setup including focus lenses, a water filter, the fiber optic cable, an XYZ manipulator mount and a thermopile.

Figure A.4 Close up photograph of the UV lamp and fiber optic cable calibration setup including focus lenses, a water filter and the fiber optic cable.

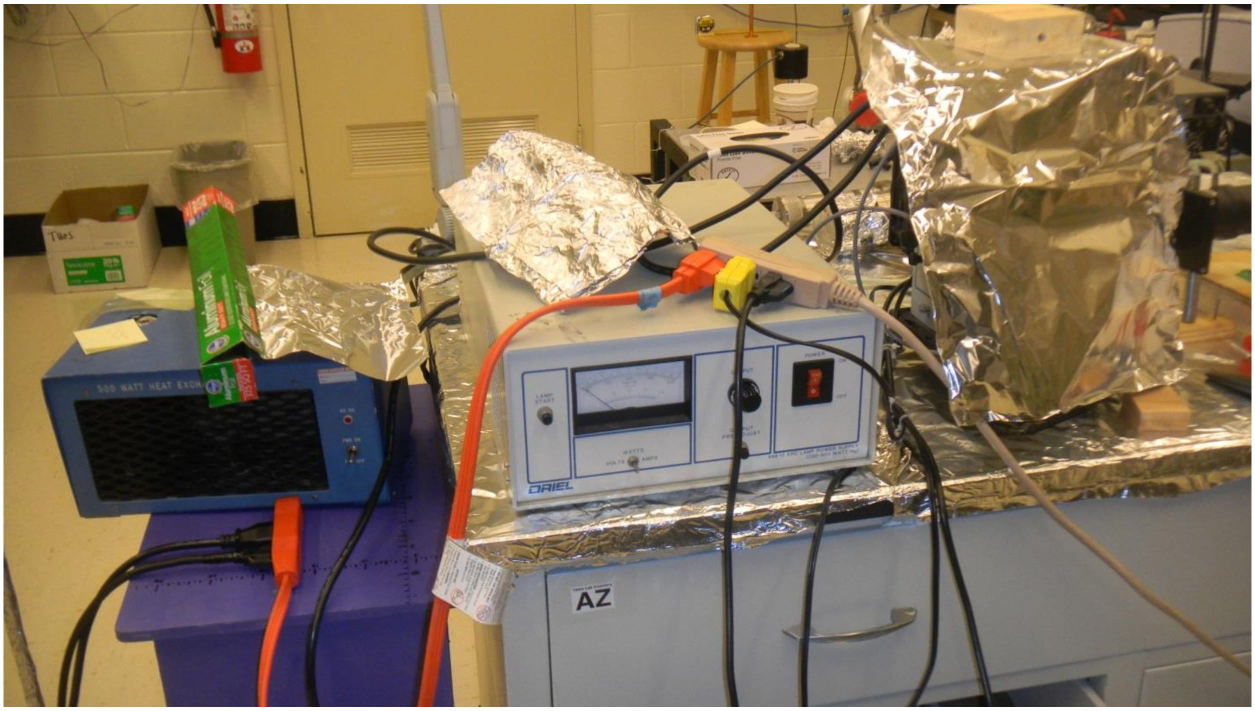

Figure A.5 Photograph of the water chiller (left), lamp power supply (center) and Hg arc lamp (right, under Al foil).

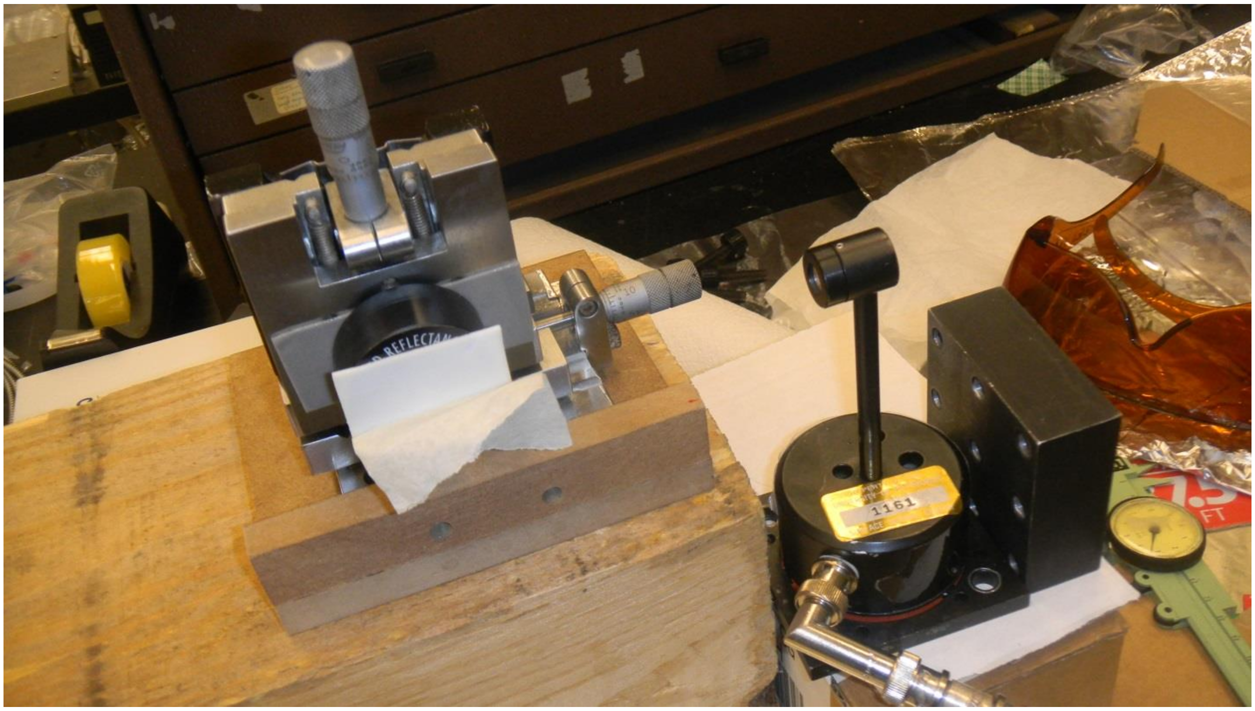

Figure A.6 Photograph of the XYZ manipulator mount and thermopile.

The thermopile was used for the calibration of the light intensity and lamp stability, and it contains a 2 mm × 2mm detector area. The detector calibration is 23.2 V/W with an upper limit of 0.1 W/cm^2. We tested three different distances from the end of the fiber optic cable to the thermopile: 2.2 cm, 3.0 cm and 3.5 cm. Figure A.7 shows the intensity of the light in mV vs. length (cm) in the direction from right to left of the IR cell. The range of detection that encompasses the whole sample (~7 mm disk) is shown when the cable distance is 3.0 cm away from the detector, with a spot size of ~7.5 mm. Thus, we positioned the holder in the IR cell so that the end of the cable would be 3 cm away from the sample, which creates a light spot size as large as the sample disk size.

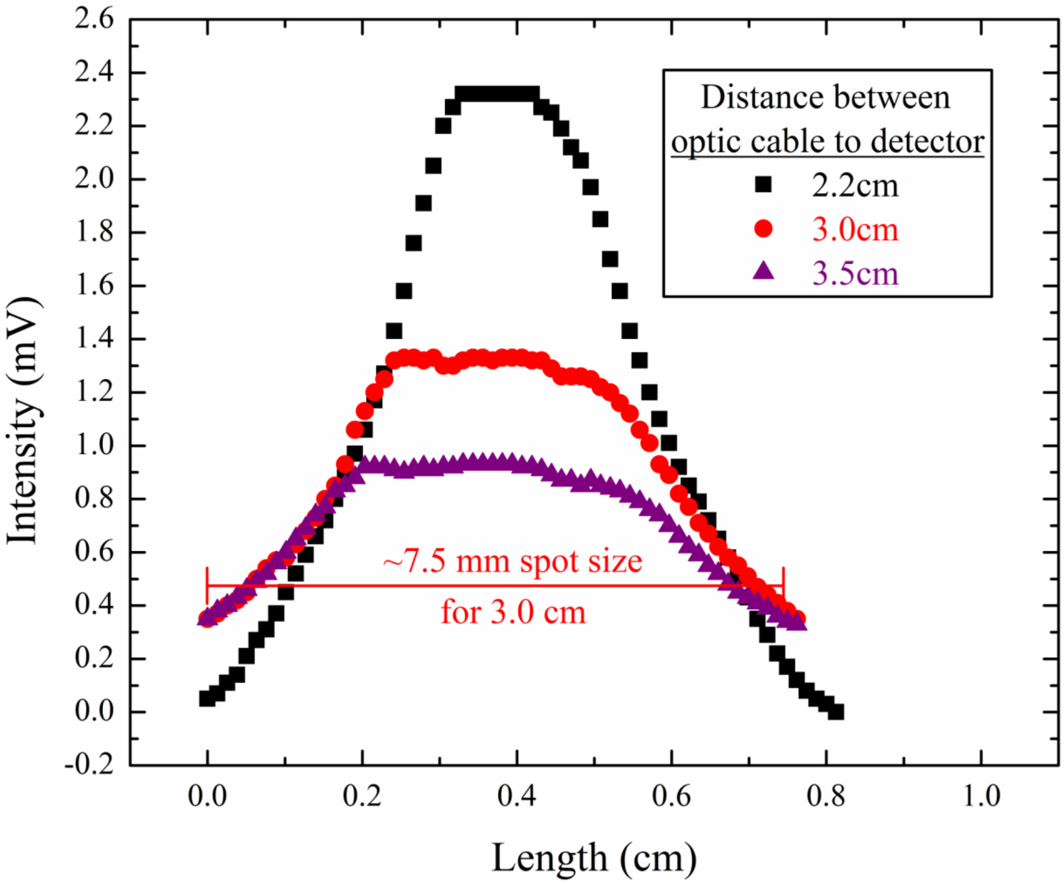

Figure A.7 Spot size determination using the intensity of the light coming out the fiber optic cable at different distances away from the detector: 2.2 cm (black curve), 3.0 cm (red curve) and 3.5 cm (purple curve).

In order to make sure the lamp intensity was stable, we measured the lamp intensity over several days as shown in Figure A.8 (grey lines). The lamp was stable within 10%. Three years later, I optimized the focusing lenses using the black dials on the lamp to increase the lamp intensity from ~.2-1.2 mV to ~1.4-4.5 mV. The intensity increased approximately five-fold as shown in the red, blue and green lines in Figure A.8.

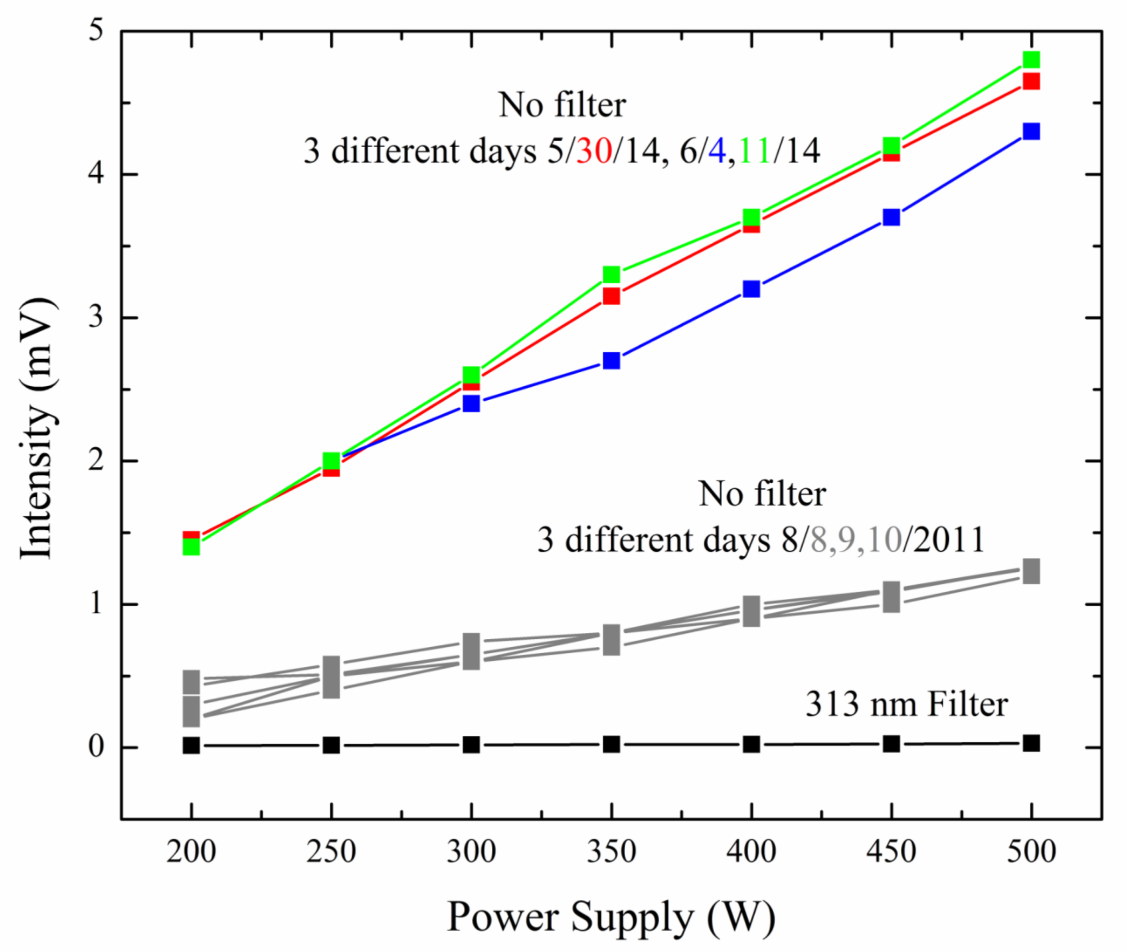

Figure A.8 Lamp stability and intensity optimization between 2011 and 2014.

A.3 Application: IR Background Absorbance Rise Due to UV Excitation of Electrons

Figure A.9 shows the change in the IR background absorbance rise before UV exposure and after UV exposure as a function of time on TiO_2 (black curve) and Au/TiO_2 (red curve). The process where IR light excites electrons in band gap states just below the conduction band (CB) into the CB is discussed in more detail in Chapter 7. Here, the photons coming from the He arc lamp with enough energy, greater than the band gap of TiO_2 (~3.2 eV), can excite electrons from the valence band (VB) into the CB and those bandgap states. Thus, more electrons populating the CB increases the IR background absorbance. Figure A.9 shows no change in the IR background before UV exposure and then a 0.025A increase after 1 hour of exposure on TiO_2. The IR background rise change was monitored at 1200 cm^{-1}.

When Au particles are supported on the surface of the TiO_2 particles, the UV light does not significantly affect the IR background absorbance. This is likely due to electron transfer from the TiO_2 CB to the Au particles, thus quenching the effect.

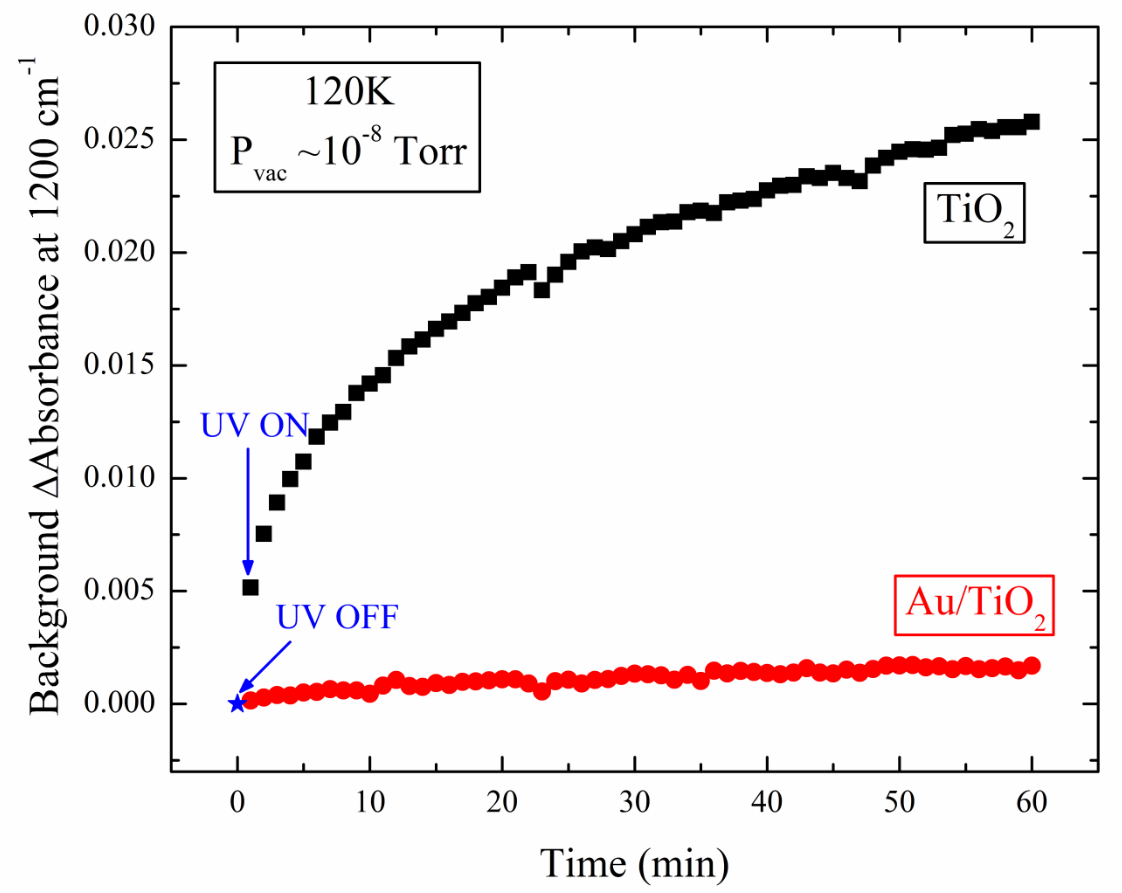

Figure A.9 IR background absorbance change before UV exposure (blue star) and after UV exposure on TiO_2 (black squares) and Au/TiO_2 (red circles).

Appendix B: GC-MS Sample Calibrations and Application

B.1 Calibration for Gas Sample Analysis for Ethylene Oxide

Gas and liquid samples are transferred to a Thermoquest CE Instruments Trace GC 2000 Series gas chromatography mass spectrometer (GC-MS) instrument with a 30 m GS-Q capillary column (Agilent Technologies, ID of 0.32 mm) for gas separation during the C_2H_4 oxidation experiment described in Chapter 4. Helium (Praxair, Ultralift) was filtered through a helium purifier and used as the carrier gas with a column flow rate set at 1.4 mL/min. The GC oven temperature program was set to 303 K for 10 minutes, and then heated at a rate of 5 K/min up to 373 K. Ions were detected in a Thermoquest Finnigan Voyager MS in electron impact positive ion (EI^+) mode with a scan range from 10-250. The GC-MS was calibrated against standard ethylene oxide (C_2H_4O) solutions in dimethyl sulfoxide (10^{-3}, $5x10^{-4}$, 10^{-4}, $5x10^{-5}$, and 10^{-5} M solutions using a 0.5 μL sample volume) as shown in Figure B.1(a). The number of C_2H_4O molecules detected for each concentration of the standard solution was acquired from the integrated area of the C_2H_4O elution peak for each gas chromatogram. One of the chromatograms, $5x10^{-4}$ M, is shown in Figure B.1(b) with its corresponding mass spectrum averaged over 11.65-11.97 minutes of C_2H_4O elution in Figure B.1(c). The limit of detection of the GC-MS was estimated to be ~$3x10^{12}$ molecules, corresponding to $3x10^{15}$ molecules in the gas phase in the IR cell.

Assuming an average Au particle size of ~3 nm and knowing the Au loading is ~8 wt%, we calculated the total amount of Au atoms at the perimeter to be ~10^{17} atoms in the 5 mg catalyst sample employed. If ~$3x10^{15}$ ethylene oxide molecules were detected in our experiment in the ~2.3 L cell volume the detection limit would correspond to only ~3% of the total perimeter sites on the catalyst.

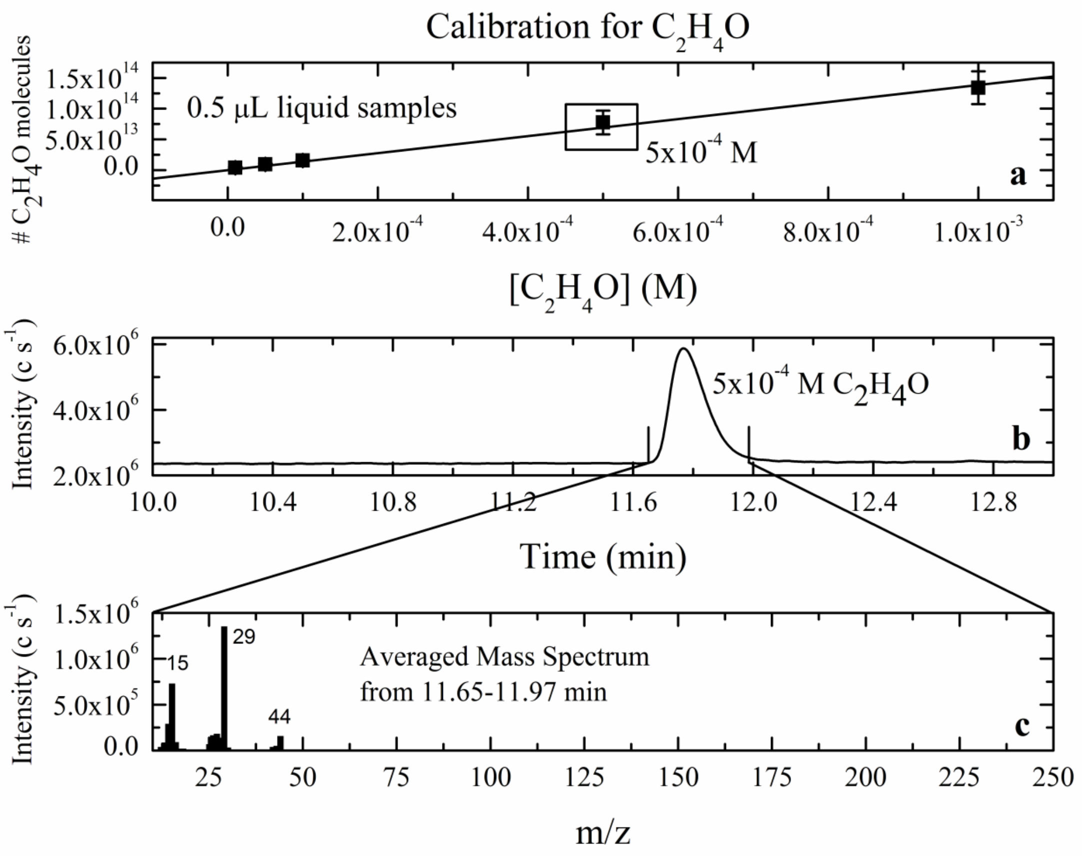

Figure B.1 Calibration of ethylene oxide in DMSO solution. (**a**). Calibration curve of ethylene oxide concentrations at 1x10^{-5} M, 5x10^{-5} M, 1x10^{-4}M, 5x10^{-4} M and 1x10^{-3} M. (**b**). Gas chromatogram of 5x10^{-4} M ethylene oxide solution which was used for (**a**). (**c**). Mass spectrum averaged over 11.65-11.97 minutes of ethylene oxide elution.

B.2 GC-MS Application: Identification of EUV-Driven Carbonaceous Film

(modified from *J. Phys. Chem. C*, **2013**, *117* (44), pp 23072–23081)

The present study has been motivated by the needs of extreme ultraviolet lithography (EUVL) that uses 92 eV photons to produce a pattern on a resist-coated wafer. Photon-induced reactions involving residual hydrocarbons and resist outgassing products in the vacuum system lead to a rapid build-up of a carbonaceous layer on the surface of expensive EUVL optics, reducing the optical transmission and the wafer throughput. In this investigation, we probe the chemistry of the 92 eV photon-induced decomposition of a long-chain hydrocarbon to produce a highly disordered, nonvolatile carbonaceous layer.

Experiments are performed on a carbonaceous layer grown by hydrocarbon photodecomposition on the surface of a *tri*-layer film structure (TiO_2/Si/Mo) fabricated on silicon. The structure is terminated by an amorphous 1.5 nm thick TiO_2 film and mimics the three top layers of optics designed for EUVL. A carbonaceous film (several nanometers thick and ∼1 mm in diameter) is grown by exposing the sample to the EUV beam at normal incidence at a *n*-tetradecane ($C_{14}H_{30}$) partial pressure of $\sim 10^{-5}$ Pa. For chemical analysis, the deposited C was partially dissolved and extracted with a 2 μL droplet of *n*-heptane and then also with a 2 μL droplet of benzene. The solution was subjected to GC-MS analysis. The GC-MS spectrometer (Thermo Finnigan Voyager with Trace 2000 GC, Rxi-17 column) was calibrated against standard solutions of anthracene and phenanthrene in heptane. While analysis of the extracted products is very informative, one must remember that only soluble molecules are observed.

The GC-MS spectra shown in Figure B.2a clearly display the presence of both phenanthrene and anthracene products and also show control experiments containing no evidence for phenanthrene or anthracene from extraction on the unirradiated area and from the pure solvent. It is clear that phenanthrene and anthracene products are observed from the irradiated area. Naphthalene was not observed in the extracts. The calibrated sensitivity of the GC-MS was $\sim 5 \times 10^{12}$ molecules in the 2 μL extracts in each case, and control GC-MS experiments are shown in Figure B.2b in order to compare retention times for both phenanthrene and anthracene standards.

The results of the GC-MS analysis lead to the conclusion that polycyclic aromatic hydrocarbon molecules are generated from *n*-alkane molecules by radiation damage and that the retention of the carbon chain length in this cyclization process is a characteristic feature of the reactions involved.

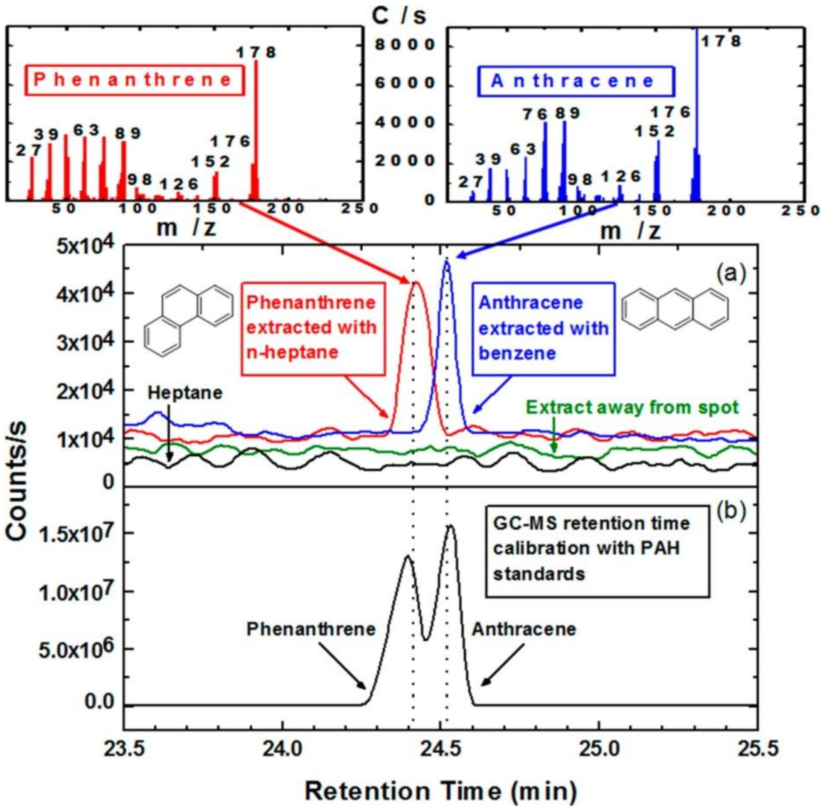

Figure B.2 GC-MS spectra of PAH compounds formed from *n*-tetradecane irradiation with 92 eV photons. (a) The carbonaceous deposit, measured by NEIS, was extracted sequentially with *n*-heptane and benzene to specifically dissolve phenanthrene and anthracene in the two extraction steps. (b) Standard GC-MS retention times. Both the retention times and the GC peak shapes agree well for phenanthrene and anthracene. The mass spectra agree with the literature for phenanthrene and anthracene and are very similar for the two molecules. Not shown are GC-MS spectra showing short chain (<C14) and long chain (>C14) hydrocarbons also produced by radiation damage of *n*-$C_{14}H_{30}$.

The number of PAH molecules extracted using 2 μL solvent droplets from the EUV-irradiated region is on the order of 1×10^{13} molecules, based on calibration of the GC-MS instrument. On the basis of the size of the carbonaceous deposit, this is a small fraction of the remaining insoluble carbon. The thickness of the carbonaceous spot is little affected by the solvent extraction process as measured by spectroscopic ellipsometry (not shown) performed after extraction. We speculate that the insoluble part of the carbonaceous deposit is mainly produced by cross-linking and consists of sp^2-carbon structures embedded in an sp^3-carbon disordered and amorphous network.

The fact that both phenanthrene and anthracene contain the same number of carbon atoms as *n*-tetradecane indicates that the radiation damage process causing C–H bond scission in *n*-tetradecane is more efficient than C–C bond scission. The cyclization of the carbon skeleton in a normal alkane is postulated to occur as a result of the radiation damage and a subsequent hydrogen abstraction process by atomic H, breaking multiple C–H bonds and leading to C=C bond formation plus 6-member ring closure as depicted by processes (B) and (C) in Figure B.3. Phenanthrene and anthracene are the only two isomers possible for the 14-carbon-fused-ring PAH molecules.

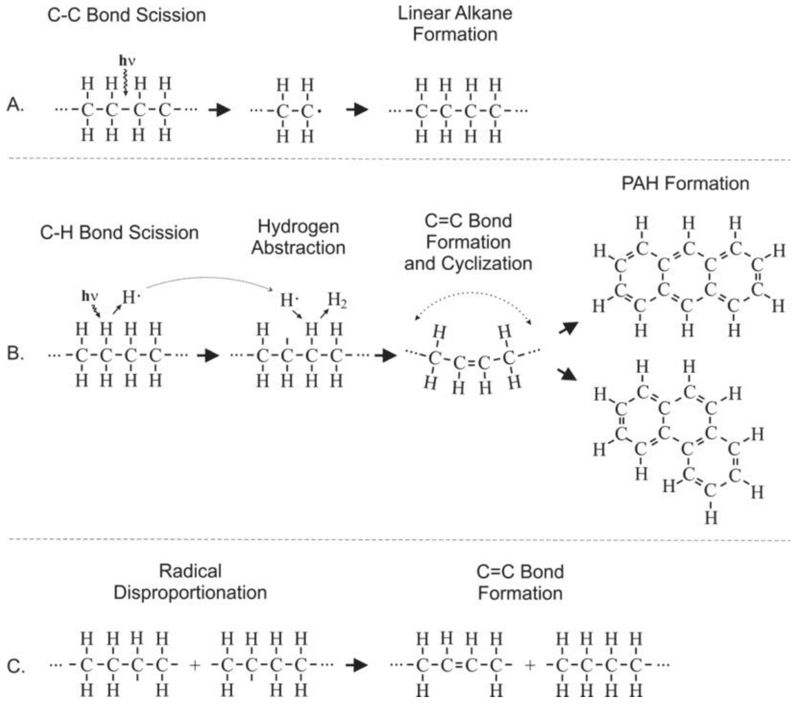

Figure B.3 Proposed major carbonaceous product reaction pathways deduced from VB and GC-MS spectroscopic measurements done after EUV irradiation of adsorbed *n*-tetradecane. (A) C–C bond scission and formation of other alkane fragments; (B) H atom abstraction to produce the C=C moiety and subsequent cyclization to form PAH molecules. (C) Radical–radical disproportionation to produce the C=C moiety which can cyclize as in (B).

Appendix C: Publication List

1. Monica McEntee, Wenjie Tang, Matthew Neurock, and John T. Yates, Jr., "*Lability of Lattice Oxygen in TiO_2—Mars van Krevelen Mechanism or Not?*" (In preparation).
2. Jun Wang, Monica McEntee, Wenjie Tang, Matthew Neurock, Arthur P. Baddorf, Petro Maksymovych, and John T. Yates, Jr., "*Formation of Au-CO Complex in Gold-assisted Catalysis for CO-oxidation*" (In preparation for J. Am. Chem. Soc.).
3. Monica McEntee, Ana Stevanovic, Wenjie Tang, Matthew Neurock and John T. Yates, Jr., "*Electric Field Changes on Au Nanoparticles on Semiconductor Supports – The Molecular Voltmeter and Other Methods to Observe Adsorbate Induced Charge Transfer Effects in Au/TiO_2 Nanocatalysts*" J. Am. Chem. Soc., **2015**, 137 (5), pp 1972-1982.
4. Monica McEntee, Wenjie Tang, Matthew Neurock, and John T. Yates, Jr., "*Mechanistic Insights into the Catalytic Oxidation of Carboxylic Acids on Au/TiO_2: Partial Oxidation of Propionic and Butyric Acid to Gold Ketenylidene through Unsaturated Acids*" ACS Catal., **2015**, 5 (2), pp 744-753.
5. Monica McEntee, Wenjie Tang, Matthew Neurock, and John T. Yates, Jr., "*Selective Catalytic Oxidative–Dehydrogenation of Carboxylic Acids – Acrylate and Crotonate Formation at the Au/TiO_2 Interface*" J. Am. Chem. Soc., **2014**, 136 (13), pp 5116–5120.
6. Nadir S. Faradzhev, Monica McEntee, John T. Yates, Jr., Shannon B. Hill, T.B. Lucatorto, "*EUV-Driven Carbonaceous Film Deposition and Its Photo-oxidation on a TiO_2 Film Surface*" J. Phys. Chem. C, **2013,** 117 (44), pp 23072-23081.
7. Isabel X. Green, Monica McEntee, Wenjie Tang, Matthew Neurock, and John T. Yates, Jr., *"Direct Formation of Acetate from the Partial Oxidation of Ethylene on a Au/TiO_2 Catalyst"*, Top. Catal., **2013**, 56 (15-17), pp 1512-1524.
8. Isabel X. Green, Wenjie Tang, Monica McEntee, Matthew Neurock, and John T. Yates, Jr., "*Inhibition at Perimeter Sites of Au/TiO_2 Oxidation Catalyst by Reactant Oxygen*", J. Am. Chem. Soc., **2012**, 134 (30), pp 12717–12723.